

CALL No.	
ACCESSION No. 259410	
INIT. CHECKED	FINAL CHECKED

UNIVERSITY OF CAPE COAST

THE EFFECT OF HOT ELECTRONS ON THE CONDUCTIVITY OF

CARBON NANOTUBES

BY

MATTHEW AMEKPEWU

Thesis submitted to the Department of Physics of the School of Physical Sciences, College of Agriculture and Natural Sciences, University of Cape Coast in partial fulfillment of the requirements for the award of Doctor of Philosophy degree in Physics

SEPTEMBER, 2015

SAM JONAH LIBRARY
UNIVERSITY OF CAPE COAST
CAPE COAST
Digitized by Sam Jonah Library

DECLARATION

Candidate's Declaration

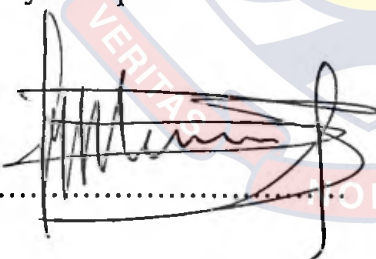
I hereby declare that this thesis is the result of my own original work and that no part of it has been presented for another degree in this university or elsewhere.

Signature:  Date: 16/09/2015

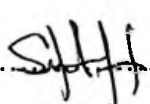
Candidate's Name: Matthew Amekpewu

Supervisors' Declaration

We hereby declare that the preparation and presentation of the thesis were supervised in accordance with the guidelines on supervision of thesis laid down by the University of Cape Coast.

Signature:  Date: 16/09/2015

Principal Supervisor's Name: Prof. Samuel Y. Mensah

Signature:  Date: 16/09/2015

Co-Supervisor's Name: Dr. Sulemana S. Abukari

ABSTRACT

The effect of hot electrons on the conductivity of undoped single walled achiral carbon nanotubes (CNTs) under the influences of applied dc field and dc-ac driven fields along the tube axis are theoretically considered. Semiclassical approach was adopted to solve Boltzmann's transport equation with and without the presence of the hot electrons source to derive the current densities. Plots of the normalized current density (J_z) versus applied dc field (E_z) with and without hot electrons reveal a negative differential conductivity (NDC) at strong electric fields. Also, NDC is observed for plots of J_z versus dc field of simultaneously applied dc-ac driven fields in quasi-static state (i.e. $\omega\tau \ll 1$, where ω and τ are frequency of ac field, and relaxation time respectively) with and without hot electrons. With strong enough axial injection of the hot electrons in either case, there is an upturn in the normalized current density resulting in a switch from NDC to positive differential conductivity (PDC). The upturn in normalized current density occurs near 50 kV/cm and 75 kV/cm for a zigzag CNT and an armchair CNT, respectively in the case when dc field is used while near 75 kV/cm and 140 kV/cm for a zigzag CNT and an armchair CNT, respectively when dc-ac driven fields in quasi-static state replaced the dc field. In this region of PDC in each case, the unwanted domain instability usually associated with NDC can be suppressed, suggesting a potential generation at low and high (room) temperatures of terahertz radiations which have enormous promising applications in very different areas of science and technology.

First and foremost, I would like to extend my deepest thanks and gratitude to my Principal Supervisor, Professor Samuel Y. Mensah and Co-Supervisor, Doctor Sulemana S. Abukari for their constant encouragement, enthusiasm and kindness. Without their substantial direction, patience and support, this work would never have been possible. Special thanks to Professor Kofi W. Adu, Mr. Kwadwo A. Dompseh, Mr. Rabiou Musah, Dr. Anthony Twum, and Mr. Philip K. Mensah for their regular sharing of ideas and support in my research. I would like to thank my dear wife, Mrs. Victoria Amekpewu and children, Ezra Amekpewu and Philemon Amekpewu for their love which have brought me a long way in my life. It gives me immense pleasure to express my deep sense of gratitude to my colleagues, Senior Members, at University for Development Studies especially Navrongo Campus for their constant encouragement and friendship. Also, I would like to thank the Abdus Salam International Centre for Theoretical Physics (ICTP) fellowship for their financial support. Furthermore, I would like to express my heartfelt gratitude to the Head of Department, Professor Moses Jojo Eghan, Senior Members and Senior Staff at Department of Physics, University of Cape Coast. Throughout my life as a graduate student, their regular support, advice and friendship has been a very vital factor in seeing this day. Last but not least, special thanks to the Dean of School of Physical Sciences, Professor David K. Essumang, for his moral support and encouragement.

DEDICATION

I dedicate this doctoral thesis to my dear wife, Mrs. Victoria Amekpewu and children, Ezra Amekpewu and Philemon Amekpewu.

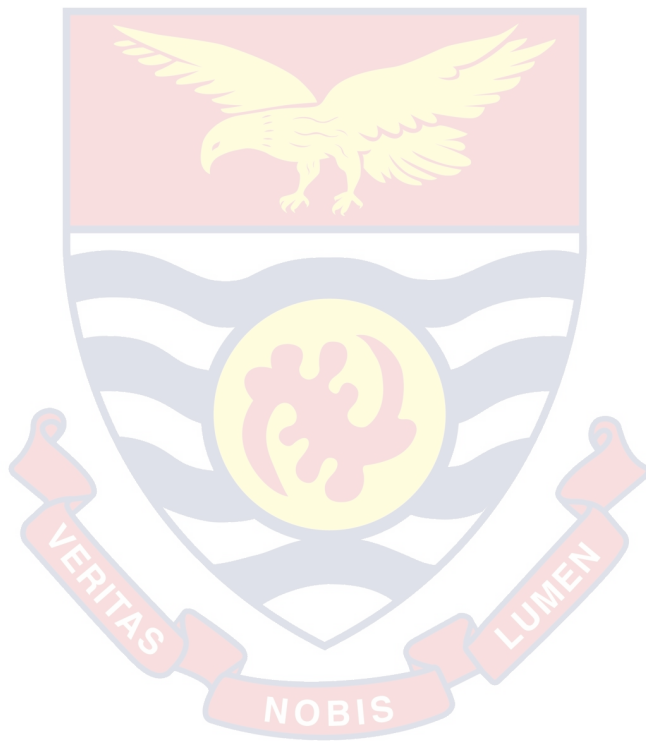
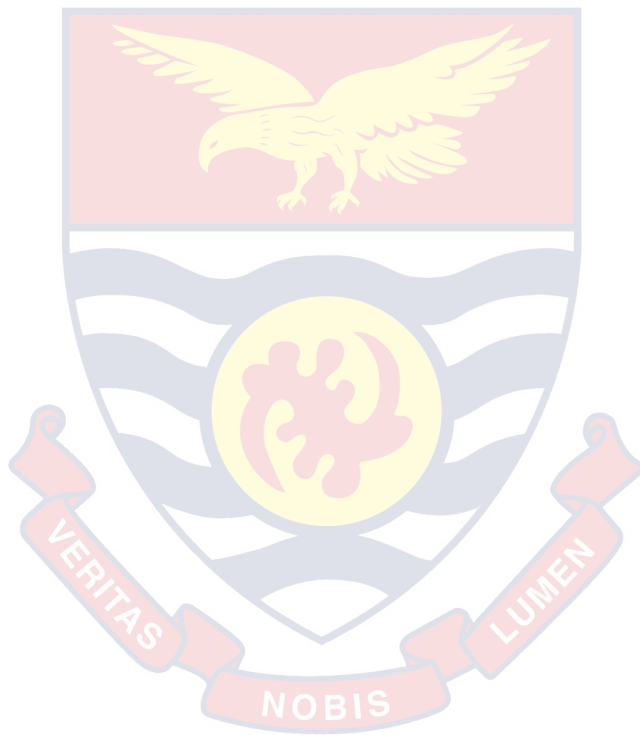


TABLE OF CONTENTS

	Page
DECLARATION	ii
ABSTRACT	iii
ACKNOWLEDGEMENTS	iv
DEDICATION	v
LIST OF TABLES	ix
LIST OF FIGURES	x
LIST OF PLATES	xviii
LIST OF ACRONYMS	xix
CHAPTER ONE: INTRODUCTION	1
Hot Electron	1
Hot Electron Device	3
Applications of Hot Electron and its Device	5
Research Objectives	5
Organization of work	7
CHAPTER TWO: CARBON NANOTUBES FUNDAMENTALS	9
Allotropes of Carbon	9
The Discovery of Carbon Nanotubes	15
Classification of Carbon Nanotubes	20

Synthesis Methods of Carbon Nanotubes	32
Graphite Sheet and Unit Cell of Carbon Nanotube	43
Energy Dispersion and Density of Electronic States in Carbon Nanotubes	60
Benefits of Carbon Nanotubes	85
 CHAPTER THREE: THEORETICAL MODELS OF CURRENT	
DENSITIES FOR CARBON NANOTUBES	122
Electron Transport in Carbon Nanotubes	122
Phenomenological Model of a Carbon Nanotube	123
Current density for zz-CNT in the absence of hot electrons source	126
Current density for zz- CNT in the presence of hot electron source	128
Current density for ac- CNT in the absence of hot electrons source	130
Current density for ac- CNT in the presence of hot electron source	131
High-Frequency Conductivity of zz-CNT in the Presence and Absence of Hot Electron Source	132
High-Frequency Conductivity of ac-CNT in the Presence and Absence of Hot Electron Source	133
 CHAPTER FOUR: RESULTS AND DISCUSSION	
Current density of a CNT as a function of the applied dc field	135
High-Frequency Differential Conductivity in a CNT	141
 CHAPTER FIVE: CONCLUSION AND RECOMMENDATIONS	
Summary	158

Conclusion	162
Recommendations	163
REFERENCES	164
APPENDICES	201
APPENDIX A	201
APPENDIX B	208
APPENDIX C	211
APPENDIX D	219
APPENDIX E	222
APPENDIX F	228
APPENDIX G	234



LIST OF TABLES

Table		Page
1	Comparison between SWCNT and MWCNT	22
2	Classification of Carbon nanotubes	31
3	Summary of the three main production methods for CNTs	42

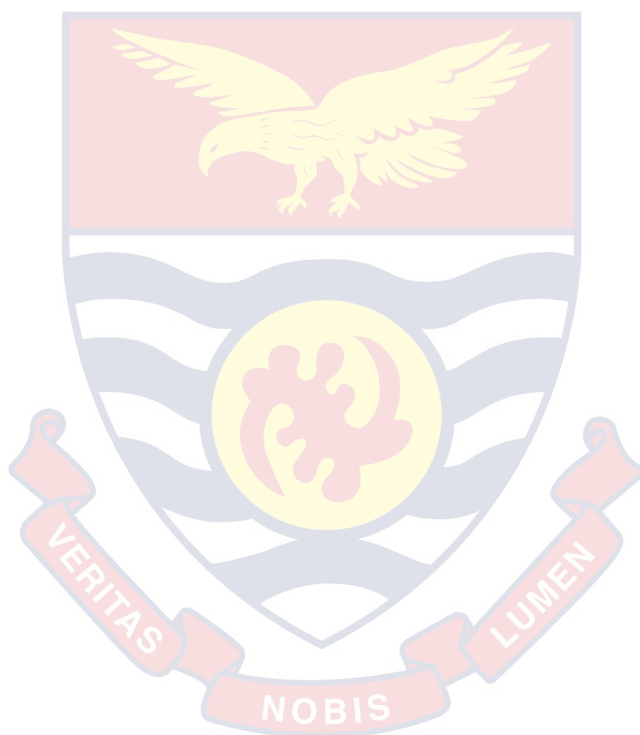


Figure	Page
1 The different hybridisations of carbon a) sp^1 , b) sp^2 , c) sp^3	10
2 (a) Structure of Diamond	12
(b) Structure of Graphite	12
(c) Structure of Fullerene	13
(d) Structure of Carbon Nanotube	14
3 Electron Micrographs of Multi-Walled Carbon Nanotubes	17
4 (a) Single-Walled Carbon Nanotubes	21
(b) Multi-Walled Carbon Nanotubes walls five	21
5 Hexagonal network of a graphene sheet with some essential lattice parameters	24
6 Unrolled sheet of Graphite or Graphene that can be rolled into the three types of Carbon nanotubes	25
7 Graphene showing atoms of metallic and semiconducting CNTs (n, m) which are denoted by the yellow and blue circles respectively	28
8 The Armchair and Zigzag Carbon nanotubes showing the atoms along the circumference of the tubes	29
9 (a) Structure of Armchair Carbon Nanotube: $n = m, \theta=30^\circ$	30
(b) Structure of Zigzag Carbon Nanotube: n or $m = 0, \theta=0$	30
(c) Structure of Chiral Carbon Nanotube: n or $m \neq 0$ and also $n \neq m, 0^\circ < \theta < 30^\circ$	30
10 (a) Schematic diagram of carbon arc-discharge method of producing CNTs	33

(b) Schematic diagram of laser-ablation method of producing CNTs	35
(c) Schematic diagram of CVD method of producing CNTs	37
11 Shows the chiral and the translation vectors in the case of the unrolled hexagonal lattice of a (4, 2) carbon nanotube	44
12 Real space with unit vectors (\hat{x}, \hat{y}) and reciprocal space with unit vectors (\hat{k}_x, \hat{k}_y) of length 2π	47
13 (a) The real space unit cell of graphite which contains points A and B	51
(b) The lattice vectors in reciprocal space	51
14 Unit Cell of Graphene containing 2 atoms/unit cell and unit vectors \mathbf{a}_1 and \mathbf{a}_2 in two equivalent zigzag directions	52
15 The real space vectors defining the nanotube (left) and the reciprocal Vectors defining the 2D Brillouin zone of the nanotube unit cell (right)	53
16 The 2D Brillouin zone of the carbon nanotube unit cell and Brillouin zone of the graphene sheet	56
17 (a) The reciprocal lattice vectors, \mathbf{K}_1 and \mathbf{K}_2 , for a $C_h = (4, 2)$ chiral nanotube	58
(b) The condition for metallic energy bands: if the ratio of the length of the vector YK to that of \mathbf{K}_1 is an integer, metallic energy bands are obtained	60
18 Simplified band structures of a (a) metal, (b) semiconductor and (c) a semi-metal	62
19 Energy band structure of the graphene layer	64

- © University of Cape Coast <https://ir.ucc.edu.gh/xmlui>
- 20 A graph of the energy $E(k_x, k_y)$ of valence and conduction states in graphene and (b) the hexagonal Brillouin zone of graphene 66
- 21 The graphene band structure near E_F showing Brillouin zone and zero-gap points 67
- 22 The momenta of the K points in the reciprocal lattice (right hand side) correspond to a motion along the 'zigzag' directions in the graphene sheet (left hand side. 68
- 23 (a) Band structure of graphene along several lines in the Brillouin zone Figure 69
(b) Sketch of Γ , M, and K which are points of high symmetry in the First Brillouin zone of 2D graphite 69
- 24 The lines which mark the momenta which are allowed states in the nanotube according to quantization condition 71
- 25 The graphene band structure near E_F , together with the quantization condition marked by dashed lines in the Brillouin zone 72
- 26 The quantization lines in the reciprocal lattice are spaced by $\Delta k = 2\pi/|C_h|$ and miss the K points by at least $\delta k = 1/3 \cdot \Delta k$ 74
- 27 Gap energies for tubes of different diameters 75
- 28 The band structure of (a) a metallic nanotube with chirality of (10, 10) and (b) a typical semiconducting nanotube with chirality of (14, 7) 76
- 29 The density of states for (a) typical metallic nanotube (10, 10) (b) typical semiconducting nanotube (14, 7) 78

30	The energy band diagram (left) and density of states (right) for a metallic (top) and a semiconducting (bottom) nanotube	79
31	Approximate one-dimensional energy dispersion of carbon nanotubes (left) and corresponding density-of-states (right)	81
32	(a) (5,5) Armchair metallic and (b) (5,0) Zigzag semiconducting nanotube, along with their associated density of states (DOS)	82
33	The DOS for metallic and semiconducting nanotubes using the tight binding k-space approach	82
34	Electronic 1D density of states per unit cell of a 2D graphene sheet for two (n,0) zigzag nanotubes	84
35	Schematic of vertical and horizontal interconnects in an Integrated circuit	85
36	Current density as a function of year and technology node in the ITRS roadmap	87
37	Time delays in integrated circuits as a function of technology node	88
38	Copper resistivity vs. interconnects line-width	89
39	The schematic of our fully suspended SWCNT p-n diode device	91
40	(a) I-V characteristics of a representative SWCNT diode with split gate separation of $4\ \mu\text{m}$ under different gate bias conditions	94
	(b) The extracted turn-on voltages show linear dependence on the split gate voltage V_{g2}	94
41	(a) The diode characteristics under constant V_{g1} of 4 V and varying V_{g2} from -2 to -9 V	95
	(b) The extracted turn-on voltages again show linear dependence on the amplitude of split gate voltage, $-V_{g2}$, but with a negative slope	95

42	(a) Carbon nanotube Field-Effect Transistors (CNTFET) © University of Cape Coast https://ir.ucc.edu.gh/xmlui	97
	(b) I-V characteristics for Carbon nanotube transistor	98
43	A three-terminal memory cell based on cantilever carbon nanotubes: (a) nonconducting state '0', (b) conducting state '1', and (c) scanning electron microscope (SEM) image	107
44	A three-terminal memory cell based on vertically aligned multiwalled carbon nanotubes: (a) nonconducting state '0', (b) conducting state '1', and (c) SEM image	109
45	A three-terminal memory cell based on suspended carbon nanotubes: (a) nonconducting state '0', (b) conducting state '1', and (c) Nantero's NRAM™	111
46	A three-terminal memory cell based on telescoping carbon nanotubes. an all-carbon memory cell with a CNT attached to the gate electrode: (a) in nonconducting state '0', and (b) in conducting state '1'. (c) SEM images of a memory cell with a flat gate electrode.	114
47	Schematic structure of nanotube flat panel display	118
48	The Samsung 4.5" full-color nanotube display	118
49	Resonant circuit connected to a s-SWCNT oscillator	120
50	A plot of normalized current density versus electric field for (a) (3, 0) zz-CNT and (b) (3,3) ac-CNT with axial injection of hot electrons ($\eta = 17.0 \times 10^{-9}$) and without hot electrons ($\eta = 0$), $T = 287.5$ K and $\nu = 1$ THz	136
51	A plot of normalized current density versus electric field for (a) (3,0) zz-CNT and (b) (3,3) ac-CNT as the nonequilibrium parameter η increases from 0 to 17.0×10^{-9} , $T=287.5$ K and $\nu =1$ THz	137
52	A plot of current density versus electric field for (a) (3,0) z-CNT and (b) (3,3) ac-CNT as the nonequilibrium parameter η further increases to 4.5×10^{-8} , $T= 287.5$ K and $\nu =1$ THz	139

- 53 A 3D plot of normalized current density (J_z) versus electric field (E_z) and nonequilibrium parameter (η) for (a) (3,0) zz-CNT and (b) (3,3) ac CNT, $T = 287.5 K$ and $\nu = 1 THz$ 140
- 54 A 3D plot of normalized current density (J_z) versus electric field (E_z) and nonequilibrium parameter (η) showing inversion of the differential conductivity in a nonequilibrium state for (a) (3,0) zz- CNT and (b) (3,3) ac- CNT, $T = 287.5 K$ and $\nu = 1 THz$ 140
- 55 A plot of normalized current density (J_z) versus frequency of ac field (ω) as the nonequilibrium parameter (η) increases from 0 to 4.5×10^{-9} for (a) (3,0)zz-CNT and (b) (3,3) ac-CNT, $T=287.5K$ and $\nu=1THz$ 142
- 56 A plot of normalized current density (J_z) versus frequency of ac field (ω) as the nonequilibrium parameter (η) further increases to 23.0×10^{-9} for (a) (3,0) zz-CNT and (b) (3,3) ac-CNT, $T= 287.5 K$ and $\nu=1THz$. 144
- 57 A 3D plot of normalized current density (J_z) versus frequency of ac field (ω) and nonequilibrium parameter (η) as η increases from 0 to 4.5×10^{-9} for (a) (3, 0) zz-CNT and (b) (3,3) ac-CNT, $T = 287.5 K$ and $\nu = 1 THz$ 145
- 58 A 3D plot of normalized current density (J_z) versus frequency of ac field (ω) and nonequilibrium parameter (η) as η further increases to 23.0×10^{-9} for (a) (3,0) zz-CNT and (b)(3,3) ac CNT, $T = 287.5 K$ and $\nu = 1 THz$ 145
- 59 A plot of normalized current density (J_z) versus normalized amplitude (β) of the high frequency ac electric field for (a) (3,0) zz-CNT and (b) (3,3)ac-CNT as the nonequilibrium parameter η increases from 0 to 2.0×10^{-9} , $T = 287.5 K$ and $\nu = 1 THz$ 146

60 A 3D plot of normalized current density (J_z) versus normalized amplitud (β) of the high frequency ac field and nonequilibrium parameter (η) for (a) (3,0) zz-CNT and (b) (3,3) ac-CNT , $T = 287.5$ K and $\nu = 1$ THz 147

61 A plot of normalized current density (J_z) versus applied dc-field (E_z) as non equilibrium parameter (η) increases 0 to 0.4×10^{-9} when $\omega \gg \nu$ or $\omega\tau \gg 1$ for (a) (3,0) zz-CNT and (b) (3,3) ac-CNT , $T = 287.5$ K $\omega = 10$ THz , $\nu = 1$ THz or $\tau = 1$ ps and $\omega\tau = 10$ 148

62 A plot of normalized current density (J_z) versus dc-field (E_z) as the nonequilibrium parameter η further increases to 3.0×10^{-9} , when $\omega \gg \nu$ or $\omega\tau \gg 1$ for (a) (3,0) zz-CNT and (b) (3,3)ac-CNT , $T = 287.5$ K , $\omega = 10$ THz , $\nu = 1$ THz or $\tau = 1$ ps and $\omega\tau = 10$ 150

63 A 3D plot of normalized current density (J_z) versus dc field (E_z) and nonequilibrium parameter (η) when $\omega \gg \nu$ or $\omega\tau \gg 1$ for (a) (3,0) zz-CNT and (b) (3,3)ac-CNT , $T = 287.5$ K , $\omega = 10$ THz , $\nu = 1$ THz or $\tau = 1$ ps and $\omega\tau = 10$ 150

64 A 3D plot of normalized current density (J_z) versus dc field (E_z) and nonequilibrium parameter (η) when $\omega \gg \nu$ or $\omega\tau \gg 1$ as the rate of hot electrons injection is further increased for (a) (3,0) zz-CNT and (b) (3, 3) ac- CNT, $T = 287.5$ K , $\omega = 10$ THz , $\nu = 1$ THz or $\tau = 1$ ps and $\omega\tau = 10$ 151

65 A plot of normalized current density (J_z) versus applied dc field (E_z) as the nonequilibrium parameter η increases from 0 to 13.0×10^{-9} when when $\omega \ll \nu$ or $\omega\tau \ll 1$ (i. e. quasi – static case), for (a) (3, 0) zz-CNT

and (b) (3, 3) ac-CNT, $T = 287.5 \text{ K}$, $\omega = 10^{-4} \text{ THz}$, $\nu = 1 \text{ THz}$ or
© University of Cape Coast <https://ir.ucc.edu.gh/xmlui>

$\tau = 1 \text{ ps}$ and $\omega\tau = 10^{-4}$

152

66 A 3D plot of normalized current density (J_z) versus dc field (E_z) and nonequilibrium parameter (η) when $\omega \ll \nu$ or $\omega\tau \ll 1$ (i. e. quasi), –static case for (a) (3, 0) zz-CNT and (b) (3, 3) ac-CNT, $T = 287.5 \text{ K}$, $\omega = 10^{-4} \text{ THz}$, $\nu = 1 \text{ THz}$ or $\tau = 1 \text{ ps}$ and $\omega\tau = 10^{-4}$ 155

67 A plot of normalized current density (J_z) versus applied dc field (E_z) as $\omega\tau \ll 1$ increases from 0.01 to 0.17 for (a) (3,0) zz-CNT and (b) (3,3) ac-CNT when $\eta = 0$ and $\eta = 0.9 \times 10^{-8}$, $\nu = 1 \text{ THz}$ or $\tau = 1 \text{ ps}$ 156



LIST OF PLATES

Plate		Page
1	A picture showing terahertz spectral range which lies between Microwave and Infrared in electromagnetic spectrum	6
2	A THz image revealing the knife concealed in the newspaper	6



LIST OF ACRONYMS

0D	Zero Dimensional
1D	One Dimensional
2D	Two Dimensional
3D	Three Dimensional
ac	alternating current
ac-CNTs	armchair Carbon Nanotubes
CMOS	Complementary Metal Oxide Semiconductor
CNTFETs	Carbon nanotube Field Effect Transistors
Co–Y	Cobalt- Yttrium
CVD	Chemical Vapor Deposition
dc	direct current
dc-ac	direct current- alternating current
DOS	Density of State
ESR	Equivalent Series Resistance
FAMOS	Floating-Gate Avalanche Metal-Oxide- Semiconductor
FETs	Field-Effect Transistors
GSI	GigaScale Integration
HRTEM	High Resolution Transmission Electron Microscopy or Microscope
IBM	International Business Machines
ICTP	International Centre for Theoretical Physics
ITO	Indium –Tin-Oxide
ITRS	International Technology Roadmap for Semiconductors

MOSFET © University of Cape Coast <https://ir.ucc.edu.gh/xmlui> Metal Oxide Semiconductor Field-Effect Transistor

MWCNTs Multi-Walled Carbon Nanotubes.

NDC Negative Differential Conductivity

NEC Nippon Electric Company

Ni-Co Nickel- Cobalt

Ni-Y Nickel- Yttrium

nm nanometre

NRAM Nonvolatile Random Access Memory

PDC Positive Differential Conductivity

RF PECVD Radio Frequency Plasma-Enhanced Chemical Vapour
Deposition

s-SWCNT Semiconductor Single Walled Carbon Nanotubes

STM Scanning Tunneling Microscopy

SWCNTs Single-Walled Carbon Nanotubes

TEM Transmission Electron Microscopy

THz Terahertz

XRD X-ray diffraction

zz-CNTs zigzag Carbon Nanotubes

CHAPTER ONE

INTRODUCTION

Hot Electron

Research in hot electrons, like any field in semiconductor research, has received a great deal of attention since the arrival of the transistor in 1947 [1]. Recently, it has become possible to fabricate semiconductor devices with submicron dimensions. Progress in miniaturization and the appearance of new functional materials over the years, have led device feature sizes to venture into the nanometre size regime [2,3]. Cost reduction, device functionality, and energy efficiency are the major driving forces in semiconductor and microelectromechanical system miniaturization [4]. However, as the dimensions of semiconductor devices shrink, the internal fields rise [5]. The miniaturization of devices has led to high field well outside the linear response region, where Ohm's law holds for any reasonable voltage signal [6]. In devices of such dimensions a few volts applied to the device result in the setting up of very high electric fields [1]. Thus electronic transport in the device becomes non-linear and can no longer be described using the simple equations of Ohm's law [1]. The physical understanding of the microscopic processes which underlie the operations of such devices at high electric fields is provided by research into hot electron phenomena [6]. Rapid development of submicrometer semiconductor devices, which may be employed in high-speed computers and telecommunication systems, further enhances the importance of hot electron phenomena [6].

hotter than the surrounding crystal lattice [1, 7] and these electrons are called hot electrons. The term “hot electrons” was originally introduced to describe nonequilibrium ensemble of high-energy electrons (or holes) in semiconductors [1, 8]. More broadly, the term describes electron distributions describable by the Fermi function, but with an elevated effective temperature. Hot electrons have an effective energy larger than the thermal Fermi energy $k_B T$ [7], where T is the lattice temperature and k_B is Boltzmann constant. Simply put, a hot electron is a high-energy electron which is not in thermal equilibrium with the lattice. The concept is very fruitful for semiconductors, where the mobility of charge carriers can be shown to depend on their effective temperature. In metals, however, electrons do not exhibit any pronounced variation of the mobility with their energy. As a result, heating of electrons in a metal does not affect the resistance, unless the change in the effective temperature is comparable with the Fermi temperature [9].

It is often possible to pump external energy such as irradiating intense laser light or applying electric field directly into the system of charge carriers. If the power input into the electronic system exceeds the rate of energy loss by that system to the lattice, then the charge carriers “heat up” and their velocity distribution deviates significantly from the equilibrium Maxwellian form [1]. A single volt across present-day submicron semiconductor devices introduces an electric field above 10kV/cm, which is generally enough to create hot electrons [7].

Hot Electron Device

Hot electron phenomena have become important for the understanding of all modern semiconductor devices [1, 10]. As the dimensions of semiconductor devices decrease drastically and the internal fields rise, a large fraction of carriers in the active regions of the device during its operation are in states of high kinetic energy. At a given point in space and time the velocity distribution of carriers may be narrowly peaked, in which case one speaks about "ballistic" electron packets [5, 11]. At other times and locations, the nonequilibrium electron ensemble can have a broad velocity distribution - usually taken to be Maxwellian and parameterized by an effective electron temperature $T_e > T$ [5], where T is the lattice temperature.

A number of devices have been proposed whose very principle is based on such effects [1, 5]. In many cases these effects are a nuisance that must be somehow cauterized, a typical example is the hot carrier injection into the gate dielectric in silicon field-effect transistors [1]. This unwelcome phenomenon gives rise to a degradation of transistor characteristics and may lead to circuit failure. Another well-known hot-electron effect in devices (with more benign consequences) is the saturation of drift velocity in high electric fields [1]. Velocity saturation is ubiquitous in modern semiconductor devices and is sometimes of central importance for their operation [1]. Thus, it is essential for the operation of all transit-time diode oscillators [1, 10].

Commercial utilization of hot electron phenomena began with the Gunn effect [12, 13] based on the intervalley transfer mechanism for a negative

Gunn diode is undoubtedly the best-known hot electron device, for which a mature technology has developed [16-18]. Another successful application of a hot-carrier effect has been made in nonvolatile memory devices. The floating-gate avalanche injection memory device FAMOS invented by Frohman-Bentchkowsky [19] bears conceptual similarity to some of the real-space-transfer devices. The FAMOS represents a p-channel MOSFET structure with a floating gate electrode. In the process of “writing” the memory, carriers, heated by the drain field, avalanche near the drain junction with hot electrons from the avalanche plasma injected into the floating gate. As the gate is charged, its potential is lowered and the p-channel conductance increases.

Two distinct classes of hot electron injection devices can be identified depending on which of the two hot electron regimes is essentially employed (the ballistic or the T_e regime) [5]. In the electron-temperature devices the heating electric field is applied parallel to the semiconductor layers with hot electrons then spilling over to the adjacent layers over an energy barrier. This process is quite similar to the usual thermionic emission-but at an elevated effective temperature T_e - and the carrier flux over a barrier of height ϕ can be assumed proportional to $\exp\left(-\frac{\phi}{k_B T_e}\right)$ [5]. Even though a small fraction of electrons - those in the high-energy tail of the hot carrier distribution function can participate in this flux, their number is replenished at a fast rate determined by the energy relaxation time, so that the injection can be very efficient. In the ballistic devices, electrons are injected into a narrow base layer at a high initial energy in the direction normal to the plane of the layer. Its performance is

limited by various energy-loss mechanisms in the base and by the finite probability of a reflection at the base-collector barrier [5].

Applications of Hot Electron and its Device

During the last decade, a new generation of hot electron superconducting sensors has been developed. These include submillimeter and THz mixers, direct detectors, and photon counters for the broad spectral range from microwaves to optical radiation and x rays [20]. Activity in the field of hot electron superconducting sensors is growing rapidly. These sensors have already demonstrated performance that makes them devices- of choice for many far-infrared (THz), infrared, and optical wavelength applications, such as plasma diagnostics, laser studies, ground-based and airborne heterodyne astronomy, single-photon-detection and quantum communications. Parallel development of compact cryocoolers and THz radiation sources opens hot electron sensors for satellite astronomy and communication applications [20].

Research Objectives

The general objective of this research work is to study the main influence of nonequilibrium hot electron phenomena in carbon nanotubes and to develop a comprehensive theoretical model to compute and investigate the effect of hot electrons on the conductivity of carbon nanotubes (CNTs). The main objective of the work is not only to probe the effect of hot electrons on conductivity of CNTs, but also to find out whether there is some useful application of the effect in very different areas of science and technology.

For instance, the useful application of the effect is to generate terahertz (THz) radiation which falls in between microwave radiation and infrared radiation in the electromagnetic spectrum as shown in plate 1

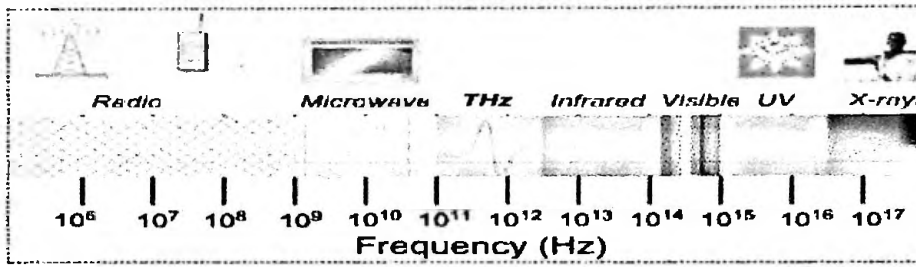


Plate 1: A picture showing terahertz spectral range which lies between Microwave and Infrared in electromagnetic spectrum

Although technology within each of these distinct bands in which terahertz radiation is sandwiched is well developed, the generation as well as detection of terahertz radiation has proceeded slowly, creating a “terahertz Gap”. Unlike X-ray, Terahertz radiation (i.e. T- ray) is non – ionizing and at modest intensities, safe to use on human beings. T-ray penetrates many common barrier materials enabling concealed object to be seen as shown in plate 2.



Plate 2: A THz image revealing the knife concealed in the newspaper

So the ultimate objective of the study is to generate terahertz radiation which
© University of Cape Coast <https://ir.ucc.edu.gh/xmlui>
apart from THz imaging has other useful applications that are relevance in
current-day technology, industry, and research.

The specific objectives of the work are stated as follows:

- i. to utilize the Boltzmann transport equation to derive mathematical expression of current density by adopting semiclassical approach for each achiral carbon nanotube under the influence of applied dc field as well as dc-ac driven fields with or without the presence of hot electrons source.
- ii. to investigate the behaviour of current density under the influence of either dc field or dc-ac driven fields with or without the presence of hot electrons with the aid of a graph in each case.
- iii. to compare the behaviour of current density in each case when hot electrons are absent and present in order to probe the effect of hot electrons on the conductivity of carbon nanotubes.
- iv. to finally find out whether the effect has any potential application like generation of terahertz radiation which is useful in different areas of science and technology.

Organization of work

Now a brief introduction of Hot electrons phenomenon and its applications as well as the research objectives have been given in chapter one, the rest of this thesis is organized into four parts. Chapter two is on the review of carbon nanotubes fundamentals which is crucial to deeper understanding of the research topic. Chapter three is the semiclassical approach in solving

Boltzmann's transport equations with and without the presence of the hot electrons source to derive comprehensive theoretical models of current densities for carbon nanotubes under the influences of dc field and dc-ac driven fields. Chapter four presents results and discussion after calculating and plotting various essential graphs showing effect of hot electrons on the conductivity of carbon nanotubes. Finally, chapter five provides an overall conclusion of this thesis. The results are analysed and some recommendations for the future research direction are offered.



CHAPTER TWO

CARBON NANOTUBES FUNDAMENTALS

This chapter will explore the literature on carbon nanotubes fundamental that is relevant to deeper understanding of the actual research work on the effect of hot electrons on the conductivity of carbon nanotubes. Many books and journal articles have previously reviewed most of the fundamentals of carbon nanotubes. The most useful books and journal articles that I have found to be vital for this review would be cited accordingly. The aim of this chapter is to report a short review of carbon nanotubes fundamentals starting from allotropes of carbon, arriving to the discovery, classification and synthesis methods of carbon nanotubes. Furthermore, reciprocal lattice, graphite sheet and unit cell of carbon nanotube, brillouin zone of graphene lattice, carbon nanotubes unit cell and carbon nanotubes would be reviewed briefly. Also the most relevant work performed on the energy dispersion relations and density of electronic states of carbon nanotubes are presented and this chapter will end with some benefits of carbon nanotubes.

Allotropes of Carbon

Since carbon nanotube is one of the allotropes of carbon, first and foremost, a short review of allotropes of carbon which is one aspect of fundamentals of carbon nanotubes crucial for better understanding of this work cannot be overlooked. To begin with, as stated by Dresselhaus et al.,[21], one distinct property of carbon atom is the many possible configurations of the

electronic states. Each free carbon has the electronic ground state configuration

© University of Cape Coast <https://ir.ucc.edu.gh/xmlui>

$1s^2 2s^2 2p^2$. The $1s^2$ orbital contains two strongly bound core electrons, and they are called core electrons. The four remaining electrons occupy the $2s^2 2p^2$ orbitals, and these more weakly bound electrons are called valence electrons.

In the crystalline phase, the valence electrons give rise to $2s$, $2p_x$, $2p_y$ and $2p_z$ orbitals, which are important in forming covalent bonds in carbon materials.

Since the energy difference between the upper $2p$ energy levels and the lower $2s$ level in carbon is small compared with the binding energy of the chemical bonds, one of $2s$ state electrons is excited to $2p$ state. As a result, the electronic

wave functions for these four valence electrons can readily mix with each other, thereby changing the occupation of the $2s$ and three $2p$ atomic orbitals so as to enhance the binding energy of the carbon atom with its neighbouring

atoms. The mixing of a single $2s$ electron with one, two or three $2p$ electrons is called sp^n hybridization with $n = 1, 2, 3$ [21]. The various bonding states

correspond to certain structural arrangements: sp bonding gives rise to chain structures, sp^2 bonding to planar structures and sp^3 bonding to tetrahedral structures as shown in figure 1. The element carbon can combine with itself

and other elements in three possible types of hybridisations namely; sp , sp^2 and sp^3 . Other group IV elements such as Si, Ge exhibit primary sp^3 hybridization.

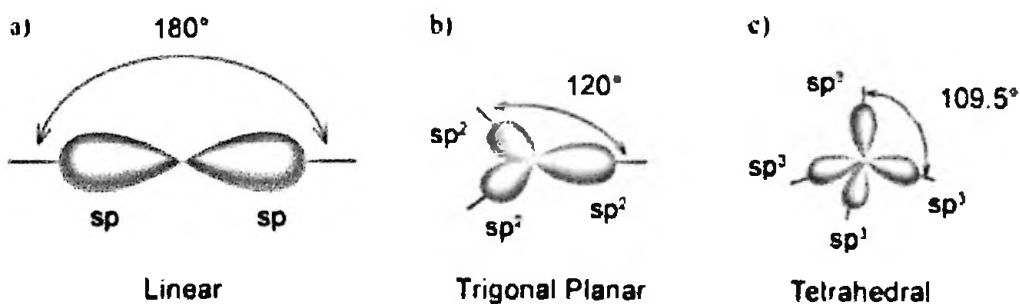


Figure 1: The different hybridisations of carbon a) sp^1 , b) sp^2 , c) sp^3 [21]

The sp^n hybridization is essential for determining the dimensionality of not only carbon-based molecules, but also carbon-based solids [23]. According to Saito et al., [23], carbon is the only element in the periodic table that has allotropes from 0 dimensions (0D) to 3 dimensions (3D). Graphite and diamond were the two most well-known allotropes of carbon prior to the discovery of fullerenes. Carbon atoms in the diamond are sp^3 -hybridized, forming a three-dimensional (3D) network by binding tetrahedrally to their four nearest neighbours as shown in figure 2(a). The structure of graphite consists of two inequivalent planar layers. In figure 2 (b), each carbon atom in a plane is bonded to three nearest neighbours in the plane via sp^2 orbitals. Because of the strong in-plane sp^2 bonds and very weak (van der Waals) interlayer bonds as shown in figure 2(b), graphite can be considered as a two-dimensional (2D) structure. The basic unit of this structure is one layer of carbon which is called graphene. Fullerenes C_{60} , the 0-dimensional (0D) molecules have a particular shape like a “soccer ball” (so-called “buckyball”) as shown in figure 2(c). These fullerenes are made up of 60 carbon atoms arranged in pentagonal and hexagonal rings. The discovery and subsequent synthesis in macroscopic quantities of fullerenes has initiated a new field in the chemistry and physics of carbon.

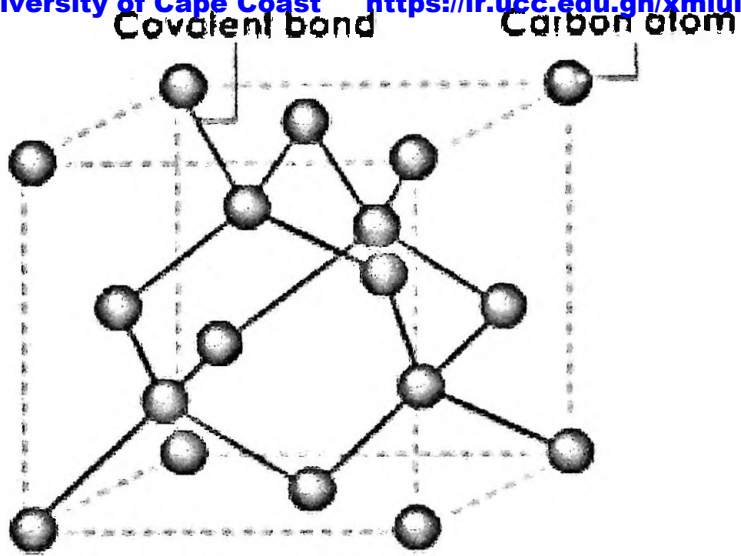


Figure 2: (a) Structure of Diamond [22]

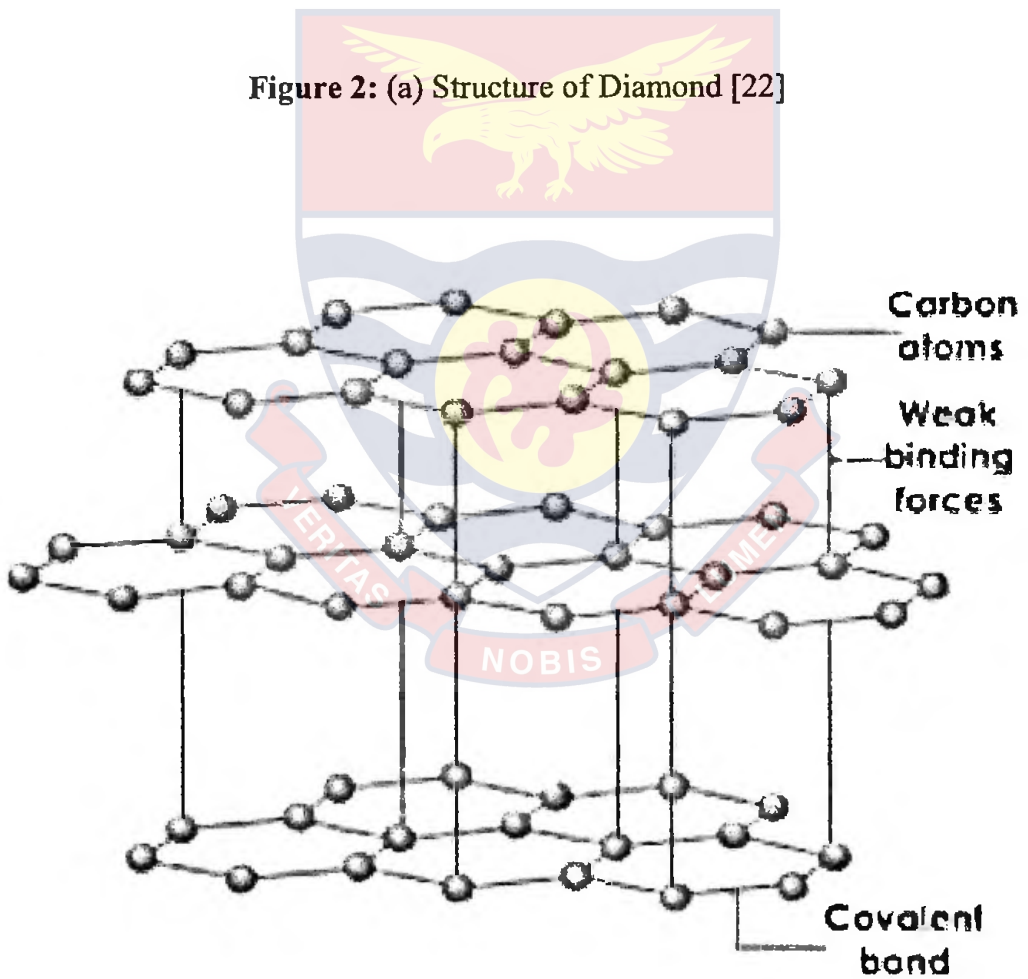


Figure 2: (b) Structure of Graphite [22, 23]

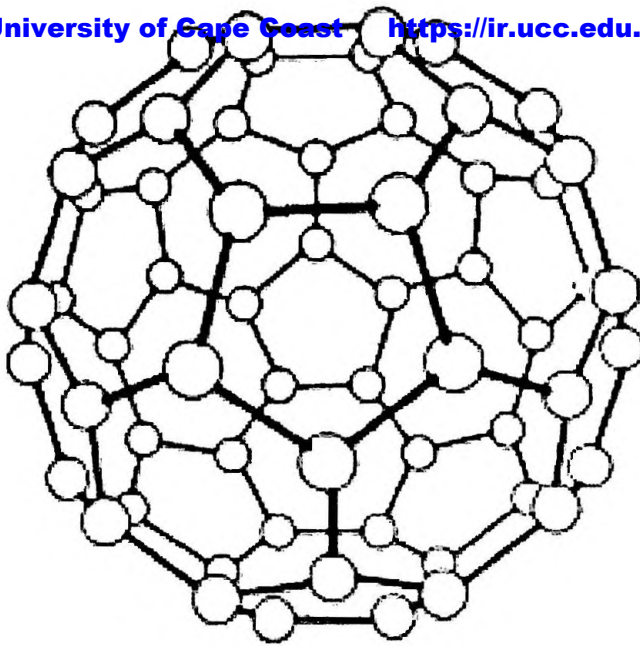


Figure 2: (c) Structure of Fullerene [24]

It is interesting that sp^2 hybridization which forms a two-dimensional (2D) graphite layer (or graphene), also forms (0D) fullerenes and (1D) carbon nanotubes. A carbon nanotube has a structure similar to a fullerene, but where a fullerene's carbon atoms usually form a sphere, a nanotube is always cylindrical and each end is typically capped with half a spherical fullerene molecule as shown in figures 2 (c) and (d). Carbon nanotubes are allotropes of carbon which are long, thin seamless hollow cylinders of graphite sheets, closed at each end with a hemispherical cap which contain precisely six pentagonal rings [24]. The diameter ranges from 1 nm and upwards, but up to an order of 100 μm long, their length-to-diameter aspect ratio is extremely high. CNTs can have a length-to-diameter aspect ratio of up to 28000000:1 which is significantly larger than any other material [25]. Their name derives from their unique size. A nanometre is one billionth of a metre, or about 100,000 times thinner than a human hair [26]. They can be viewed as single

molecules, regarding their small size, or as quasi-one dimensional crystals with translational periodicity along the tube axis. Simply put, a carbon nanotube exists as a large macromolecule of carbon, analogous to a sheet of graphite rolled into a cylinder. Graphite looks like a sheet of chicken wire, a tessellation of hexagonal rings of carbon sheets of graphite lay stacked on top on another, but they slide past each other and can be separated easily. However, when coiled, the carbon arrangement becomes very strong. In fact, nanotubes have been known to be up to hundred times as strong as steel [27]. They are light, flexible, thermally stable and chemically inert [28]. Nanotubes have an impressive list of attributes. They can behave like metals or semiconductors depending on the “twist” of the tube, can conduct electricity better than copper, can transmit heat better than diamond, and they rank among the strongest materials known [29] .

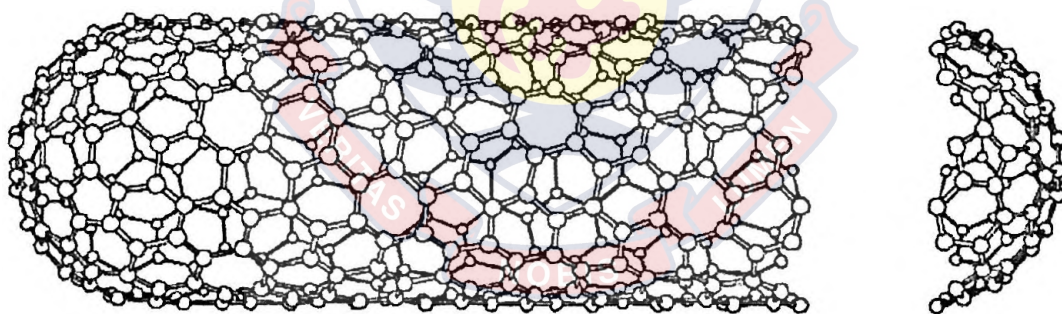


Figure 2: (d) Structure of Carbon Nanotube [24]

These large macromolecules are unique for their size, shape and remarkable physical properties. These intriguing structures have sparked much excitement in recent years and a large amount of researched has been dedicated to their understanding. Since the discovering of carbon nanotubes (CNTs) by Iijima in 1991 [30] , increasing attention has been attracted to this newly

[31, 32].

The notable properties of carbon nanotubes are summarised as follows:

- i. Carbon nanotubes can be metallic, or semiconducting depending on their diameter and rolling helicity [33, 34].
- ii. The energy gap of semiconducting carbon nanotubes can be varied continuously by varying the nanotube diameter. Here the band gap of semiconducting nanotubes decreases with increasing diameter [33, 35].
- iii. Nanotubes have high thermal conductivity (~ 2000 W/m/K, whereas copper has 400 W/m/K) [33, 36].
- iv. Individual carbon nanotubes are able to carry electrical current at significantly higher densities than most metals and semiconductors [33, 37].
- v. A nanotube device will consume less power than an equivalent Si device [33, 38]

These properties make carbon nanotube device a better choice than other molecular device [33].

The Discovery of Carbon Nanotubes

A brief review of the report on the discovery of carbon nanotube is the next to that of allotropes of carbon. According to Forró et al., [39], the last decade of the last century in condensed matter physics has been marked by the revival of carbon-based materials. Besides the conventional forms of carbon, the graphite and the diamond, new forms of carbon have been discovered:

University of Sussex in the UK and Richard Smalley from Rice University in the US were the first to observe the formation of the parent compound of fullerenes, which is C₆₀ molecule, after a series of experiments was performed using the vaporisation of carbon [24, 40]. This might have been the start to a new and promising branch of physics, but it was hardly a surprise to scientists all over the world and hence this fact was overlooked. Long before that, chemists and physicists had been wondering why the versatile carbon atom could only be found in two kinds of structures: graphite and diamond. There had been propositions by Roald Hoffmann, Orville Chapman as to what forms ought to be observable, but every attempt to create these structures had failed. So it was Kroto and Smalley who incidentally made the discovery while working on laser evaporation. In order to investigate this new state of carbon, a method was needed first to produce it in sufficient quantity. Wolfgang Krätschmer and Donald Huffman were successful in this with a carbon arc instead of a laser. Therefore, the full expansion of the activity concerning this material did not truly begin until the mass production of fullerenes was invented by Krätschmer and Huffman [41]. The great euphoria in the fullerene research started with the discovery of “high temperature superconductivity” in 1991, exceeding a critical temperature of 30K [42] upon alkali metal doping. The search for new carbon nanostructures, higher mass fullerenes has strongly motivated chemists and physicists.

After the world's first High-Resolution Transmission Electron Microscope (HRTEM) was developed at Arizona State University in 1971, carbon nanotubes which are fullerene-related structures were first

experimentally discovered in 1991 by the Japanese electron microscopist S. Iijima of NEC Fundamental Research Laboratory in Tsukuba, Japan [30, 43].
© University of Cape Coast <https://ir.ucc.edu.gh/xmlui>

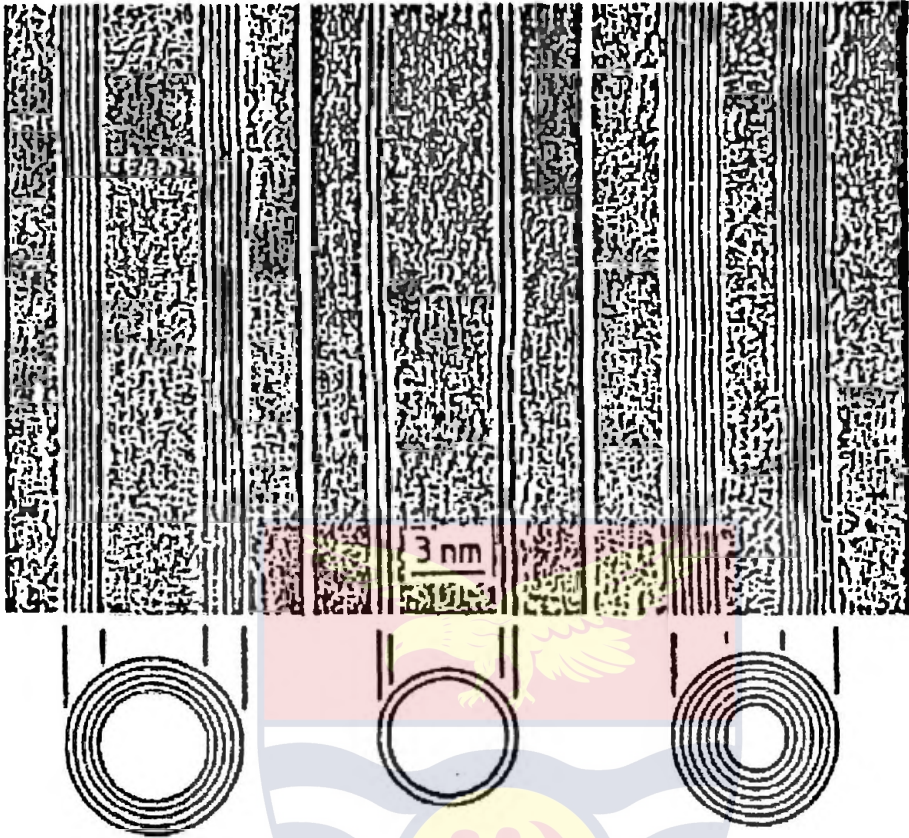


Figure 3: Electron Micrographs of Multi-Walled Carbon Nanotubes [30]

Using High Resolution Transmission Electron Microscopy (HRTEM), he examined electron microscope images of the soot deposited on the carbon cathode during the arc- evaporation synthesis of fullerenes. Iijima found that the central core of the cathodic deposit contained a variety of closed graphitic structures including nanoparticles and strange tube-like carbon structures [24, 30] of a type which had never previously been observed.

The new found strange tube-like carbon structures that consisted of several concentric tubes of carbon atoms, cylindrical in shape, exquisitely thin and impressively long were later called multiple-walled carbon nanotubes

(MWCNTs). These early structures had the form of cylinders within cylinders, nested inside each other like Russian dolls.

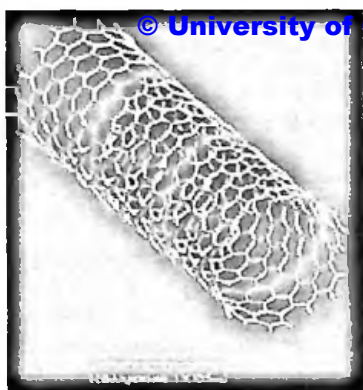
At the beginning, while the production and purification of these structures were not sufficiently elaborated, the research mainly consisted of “photography” that is of spectacular images obtained by High-Resolution Transmission Electron Microscopy (HRTEM) as shown in figure 3. Around 1994 some of these problems were solved, and paved the way to an explosion of research into the physical and chemical properties of carbon nanotubes in laboratories all over the world. Theoretical predictions about structure and electronic properties of CNTs followed quickly [36, 44-47]. Soon methods were developed to produce single-walled carbon nanotubes (SWCNTs), that is, nanotubes that consist of only a single sheet of graphite. In 1993, Iijima et al.,[48] and Donald Bethune et al.,[49] of IBM's Almaden Research Centre in California independently found that adding small amounts of transition-metal catalysts to the carbon electrodes could produce carbon nanotubes that were not nested together; that is, each nanotube was one macromolecule made of a single wall of carbon atoms. Because of their simple and well-defined structure, the single-wall nanotubes serve as model systems for theoretical calculations and for critical experimental studies [50]. Since then, the physical and electrical properties of carbon nanotubes have been studied extensively. This achievement was significant, because carbon nanotube transistors and circuits use such single-walled carbon nanotubes (SWCNTs). A short time later, Thomas Ebbesen and Pulickel Ajayan, from Iijima's laboratory, showed how carbon nanotubes could be produced in bulk quantities by varying the arc-evaporation conditions [48].

discovered 30 years earlier, but had not been fully appreciated at that time. It appears that the first carbon filaments of nanometre dimensions were prepared in the 1970s by Morinobu Endo, as part of his PhD studies at the University of Orleans in France. He grew carbon fibres about 7 nm in diameter using a vapour-growth technique. Indeed, he even observed some tubes consisting in only a single layer of rolled-up graphite, but these filaments were not recognized as nanotubes and were not studied systematically. At least two articles raise the question about pre Iijima carbon nanotubes. In an article reporting about the decade of discovery of nanotubes [51], it stated that nanotubes could have been unknowingly produced in the late nineteenth century by chemists experimenting on methane [52]. In 1960 Roger Bacon, working for the National Carbon Company, a division of Union Carbide Corporation report in a remarkably lucid and thorough account, his discovery of sub-micrometer diameter graphite whiskers grown in a dc carbon arc under high pressure (93 atm) of an inert gas [53]. These whiskers consisted of one or more concentric tube, each being in the form of a scroll, or rolled-up sheet of graphite layers. The fact that Iijima was using a procedure that generates a mixture of scrolls and tubes [54-56], suggests that, Bacon may also have done this. Wiles et al., (1978) found “mats of small fibres” on one electrode when sparks were passed between two graphite electrodes [57]. The scientists who investigated the growth of vapour grown carbon fibres may also have produced carbon nanotubes because they used the same technique with which carbon nanotubes are produced today [58]. In another article from Gibson [59], Davis is proposed as the one who saw the first nanotube in 1953 [60]. The writer

described thread-like carbon structures obtained from the reaction of Co and Fe_3O_4 at 450°C , which he suggested were 'similar' if not 'identical' to carbon nanotubes. These should not be seen as diminishing the importance of Iijima's work, who was the first to appreciate fully the nature and importance of these structures. That, is the first systematic study of carbon nanotubes was done by S. Iijima in 1991 who identified these carbon nanotubes using High-Resolution Transmission Electron Microscopy.

Classification of Carbon Nanotubes

A brief review of various forms of classification is very essential so far as better understanding of this work is concerned. There are various types of CNTs each having their own different properties [61]. When CNTs are synthesized, a bunch of different types of CNTs is produced. These CNTs can be well aligned or nestled depending on the synthesis method, the catalysts used and other reaction conditions such as temperature etc. If we look at the wall(s) of one CNT, then we can classify the CNT into single -walled carbon nanotubes (SWCNTs) and multi-walled carbon nanotubes (MWCNTs) [62] . A tube made of a single graphite layer rolled up into a hollow cylinder is called a single-walled carbon nanotube (SWCNT) and a tube comprising several, concentrically arranged cylinders is referred to as a multiwalled carbon nanotube (MWCNT). In figure 4, examples of a SCWNT and a MCWNT are shown.



a)

Figure 4: (a) Single-Walled

Carbon Nanotubes [63, 64]



b)

(b) Multi-Walled Carbon

Nanotubes walls five [63]

In general the multi-walled carbon nanotubes (MWCNTs) have a larger diameter than the single-walled carbon nanotubes (SWCNTs).

Single-wall nanotubes with only one single layer generally have a diameter of 1 to 5 nm. The properties of SWCNT are more stable than MWCNT so it is more favourable. MWCNT is a little bigger than SWCNT because MWCNT has about 50 layers. MWCNT's inner diameter is from 1.5 to 15 nm and the outer diameter is from 2.5 nm to 30 nm. Distances between the walls are mostly found to be between 0.1 and 0.4 nm [64]. Depending on the number of walls, CNTs may have different conductive properties. For example, MWCNTs have metallic conducting properties, whereas SWCNTs can have semiconducting properties as well as metallic conducting properties. This depends on the so-called chirality of the SWCNTs.

Both SWCNT and MWCNT are usually many microns long and hence they can fit well as components in submicrometer-scale devices and nanocomposite structures that are very important in emerging technologies. SWCNTs have better defined shapes of cylinder than MWCNTs, thus a

MWCNT has more possibilities of structure defects and its nanostructure is less stable. Most researchers focus on SWCNT and develop applications based on SWCNT due to the physical stability of SWCNT.

Table 1: Comparison between SWCNT and MWCNT [65]

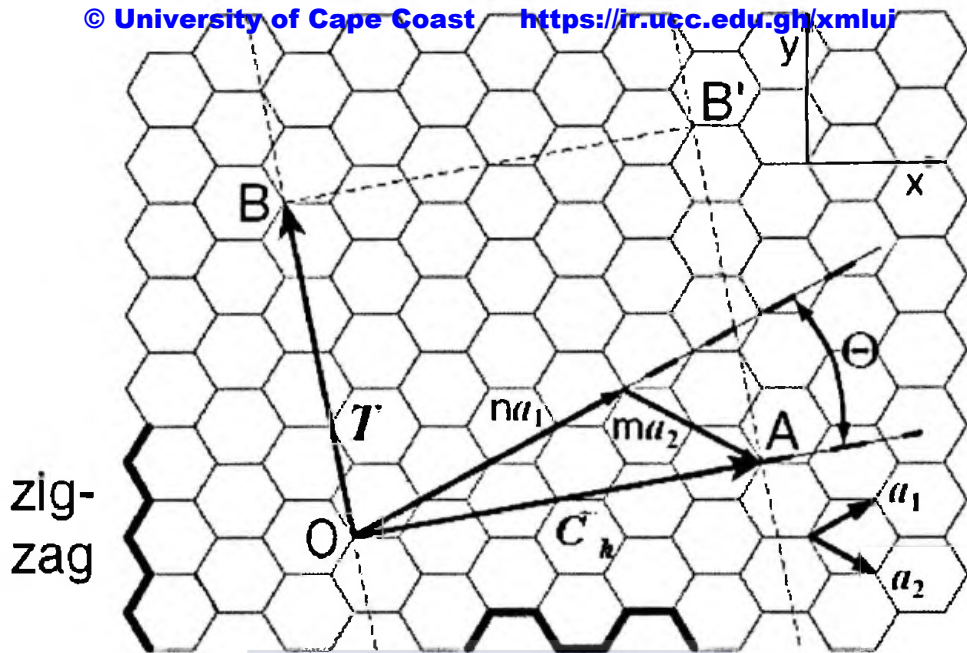
SWCNT	MWCNT
1. Single layer of graphene.	1. Multiple layer of graphene.
2. Catalyst is required for synthesis.	2. Can be produced without catalyst.
3. Bulk synthesis is difficult as it requires proper control over growth and atmospheric condition.	3. Bulk synthesis is easy.
4. Purity is poor.	4. Purity is high.
5. A chance of defect is more during functionalization.	5. A chance of defect is less but once occurred it's difficult to improve.
6. Less accumulation in body.	6. More accumulation in body.
7. Characterization and evaluation is easy.	7. It has very complex structure.
8. It can be easily twisted and are more pliable.	8. It cannot be easily twisted.

The second form of classification is common among both MWCNTs and SWCNTs and depends on the arrangement of carbon atoms in a given tube or how the two-dimensional graphene sheet is "rolled up". The primary symmetry classification of a carbon nanotube is as either being achiral (symmorphic) or chiral (non-symmorphic) [66]. An achiral carbon nanotube is defined by a

one. There are only two cases of achiral nanotubes:

- a) armchair nanotubes
- b) zigzag nanotubes

The names of armchair and zigzag arise from the shape of the cross-sectional ring, as shown at the edge of the nanotubes in figures 8 (a) and 8 (b). An armchair nanotube corresponds to the case of $n = m$, that is $C_h = (n, n)$ and a zigzag nanotube corresponds to the case of $m = 0$ or $C_h = (n, 0)$ [62]. Chiral nanotubes exhibit a spiral symmetry whose mirror image cannot be superposed on to the original one. All (n, m) chiral vectors other than (n, n) and $(n, 0)$ correspond to chiral nanotubes [67]. Because of the hexagonal symmetry of the lattice, we need to consider only $0 < |m| < n$ in $C_h = (n, m)$ for chiral nanotube. This classification depends on the geometric structure of CNTs described by the circumference vector or Chiral vector of the nanotube, C_h , whose magnitude represents the full circumference of the tube. It is defined by $C_h = na_1 + ma_2, n \geq m$ [23, 68] where a_1 and a_2 are unit vectors in the two-dimensional hexagonal lattice as shown in figure 5. The integers n and m denote the number of unit vectors along two directions in the hexagonal lattice of grapheme as shown in figure 5. This is often thought of as representing the number of carbon atoms around the circumference of the tube, and the number of atoms down the tube axis. Another important parameter is the chiral angle θ , which is the angle between C_h and a_1 .



armchair

Figure 5: Hexagonal network of a graphene sheet with some essential lattice parameters [23, 68]

The tube with index $(n, m) = (4, 2)$ is constructed when the dotted strip as shown in figure 5 is rolled up in such a way that point O matches point A, and point B matches point B'. θ denotes the chiral angle of a specific tube and varies between $0^\circ \leq \theta \leq 30^\circ$, the chiral vector C_h is perpendicular to the translational vector. Armchair carbon nanotubes are formed when $n = m$ and the chiral angle is 30° [68,69]. Zigzag carbon nanotubes are formed when either n or m is zero and the chiral angle is 0° [68, 69]. All other carbon nanotubes formed when $n \neq m$, n or $m \neq 0$ with chiral angles intermediate between 0° and 30° , are known as chiral carbon nanotubes [68,69].

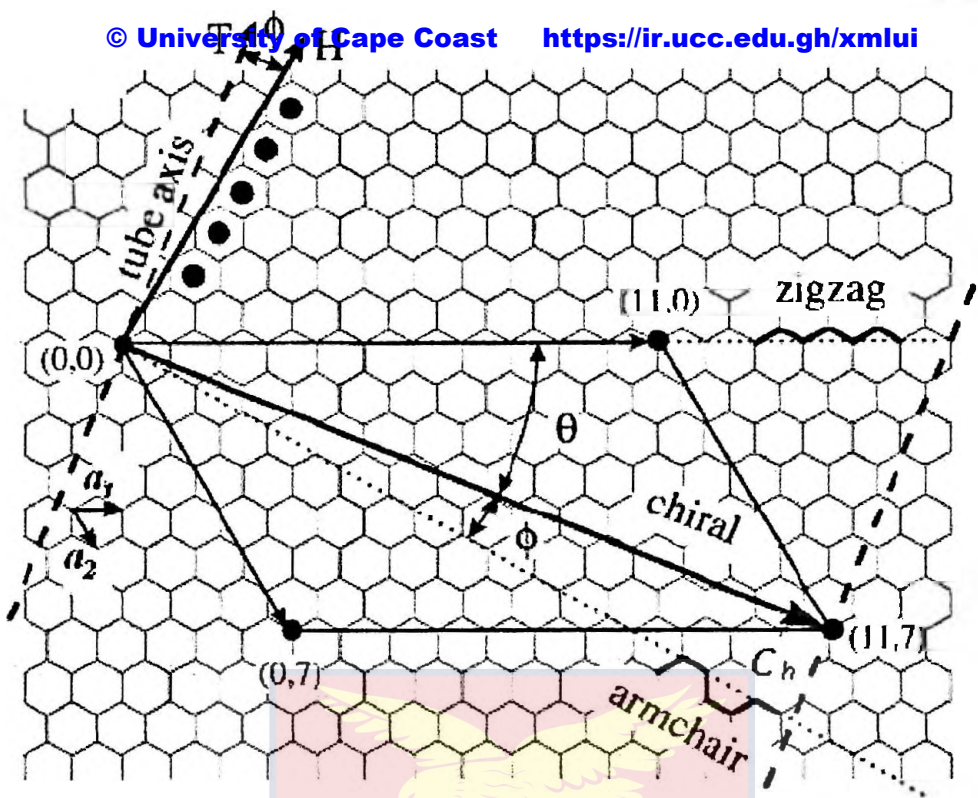


Figure 6: Unrolled sheet of Graphite or Graphene that can be rolled into the three types of Carbon nanotubes [69]

The chiral vector is a line that traces the CNT along its circumference from one carbon atom (we will call it the reference atom) back to itself. If we cut open the carbon nanotube along the tube axis and through the reference atom, we can imagine spreading out the nanotube into a graphene sheet that could exactly match a portion of an infinitely large graphene sheet. Figure 6 shows the hexagonal carbon network that can be thought of as the infinitely large graphene sheet. The dotted lines at the left and right represent the cut made along the CNT. Location (0, 0) represents the reference atom and is the location that the chiral vector C_h starts from. Although the chiral vector begins and ends on the same reference atom, end is represented by location (11, 7) in the graphene sheet as shown in figure 6. When the graphene sheet is

wrapped into a cylinder, chiral vector C_h which connects crystallographically equivalent points (0, 0) and (11,7) of the graphene lattice will both converge on the same reference atom. The unit vectors a_1 and a_2 both begin at one corner of a single hexagon and end two corners away in the same hexagon. Each hexagon corner in the hexagonal network represents one carbon atom in the physical graphene sheet. a_1 and a_2 point in the zigzag directions, or directions that make 30° angles with the armchair direction. Since a_1 and a_2 each transverse one whole hexagon, the coordinates (n, m) represent atoms that are n and m hexagons away from the reference atom in the a_1 and a_2 directions respectively. a_1 points in the indicated zigzag direction, 30° away from the armchair direction. If C_h lines up with the dotted zigzag line in figure 6 the resulting nanotube would be a zigzag CNT. The terms zigzag and armchair come from the patterns traced along the hexagons along those directions, as shown by the zigzag and armchair-like lines drawn in figure 6. The angles θ and ϕ always combine to form 30° [70].

The chiral angle and vector also play an important role in determining the important properties of nanotubes, besides being parameters used to discriminate between different types of carbon nanotubes. The properties of carbon nanotubes are also determined by their diameter, which depends on n and m . The nanotube diameter d is calculated using the formula given by

$$d = \sqrt{3a_{c-c}^2(m^2 + mn + n^2)} / \pi = C_h / \pi,$$

where a_{c-c} is the distance between adjacent carbon atoms in the flat sheet or

a_{c-c} is the  [University of Cape Coast](https://ir.ucc.edu.gh/xmlui) <https://ir.ucc.edu.gh/xmlui> $C-C$ bond length (0.142 nm) and C_h is the length of the

circumference or chiral vector C_h . The chiral angle, θ , on the other hand is

calculated using the formula given by [23] $\theta = \tan^{-1}(\sqrt{3}n/(2m+n))$

The translational vector T , which is perpendicular to the chiral vector, is expressed as [23], $T = [(2m+n)a_1 - (2n+m)a_2] / d_R$

The length T is the unit lattice length along the tube axis direction:

$$T = \sqrt{3}C_h / d_R = 3a_{c-c} \sqrt{n^2 + nm + m^2} / d_R$$

Here, d_R is the greatest common divisor of $(2n+m)$ and $(2m+n)$.

For example, let consider a (11, 8) tube: $2n+m=30$ and $2m+n = 27$ and $d_R = 3$.

or

$$d_R = \begin{cases} d & \text{if } n-m \text{ is not a multiple of } 3d \\ 3d & \text{if } n-m \text{ is a multiple of } 3d \end{cases}$$

And d is the highest common divisor of (n, m) . For example, let consider a

(11,8) tube : d is 1 and hence $d_R = 3$ since $11-8 = 3$ is a multiple of $3(1) = 3$

The number of hexagons N in a unit cell is given by [23],

$$N = \frac{2(n^2 + nm + m^2)}{d_R}$$

One of the most remarkable properties of a given (n, m) carbon nanotubes is that depending on their structure and diameter, conducting or semiconducting nanotubes are possible. The condition for metallic or conducting nanotubes is that $(2n+m)$ or equivalently $(n-m)$ is a multiple of 3 [71]. That is for a given (n, m) nanotube, if $2n+m=3i$ or $n-m=3i$ (where i is an integer), then the nanotube is metallic, otherwise the nanotube is a semiconductor. This leads to the cases that all armchair nanotubes are metallic

or conducting, if n is a multiple of 3. Figure 7 shows which carbon nanotubes (n, m) are predicted to be metallic and which are semiconducting, denoted by the black and red circles respectively. It can be seen from this diagram that approximately one third of carbon nanotubes are metallic or conducting while the other two thirds are semiconducting. These basic predictions from the theory have been verified using scanning tunnelling microscope studies.

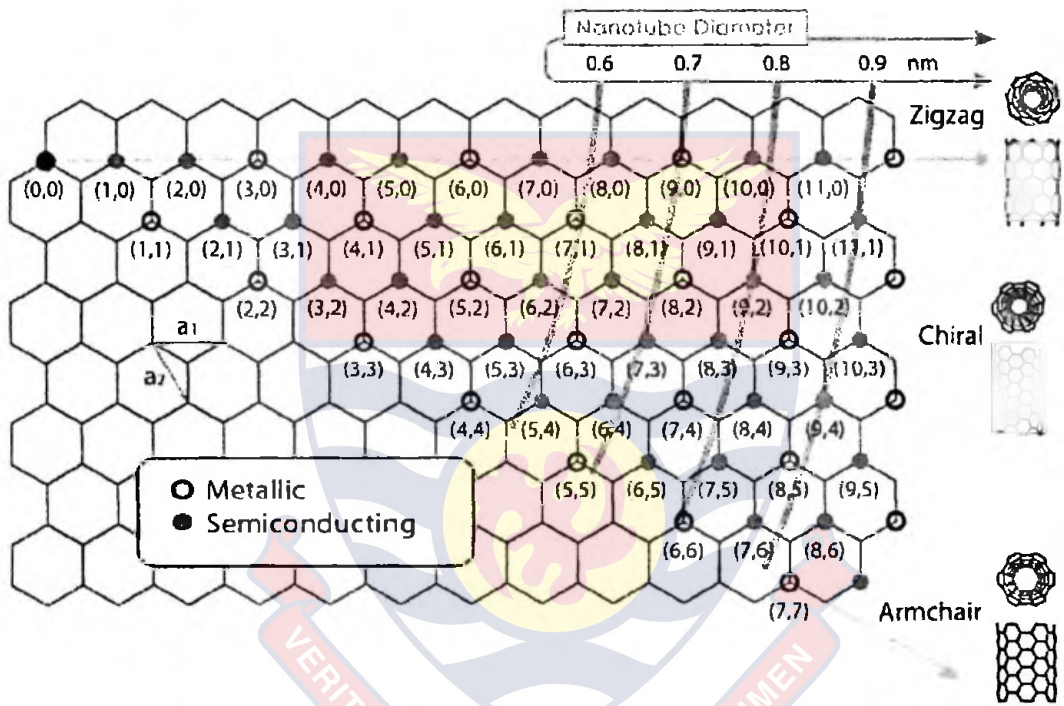
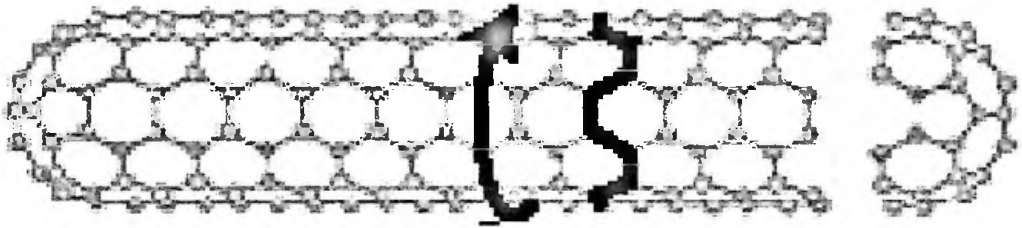


Figure 7: Graphene showing atoms of metallic and semiconducting CNTs (n, m) which are denoted by the black and red circles respectively [72]

Zigzag nanotubes correspond to $(n, 0)$ or $(0, m)$ and have a chiral angle of 0° , armchair nanotubes have (n, n) and a chiral angle, of 30° , while chiral nanotubes have general (n, m) values and a chiral angle of between 0° and 30° . Band-structure calculations show that the conductive properties of nanotubes depend strongly on the tube diameter as well as on the winding of the chiral

either n or m is zero, also referred to as the zigzag axis. Chiral nanotubes are formed when neither n nor m is zero and also $n \neq m$, hence it is general chiral (n, m) nanotube which corresponds to a chiral angle lying between $0^\circ < \theta < 30^\circ$.



C_h

Figure 9: (a) Structure of Armchair Carbon Nanotube: $n = m$, $\theta=30^\circ$ [23]

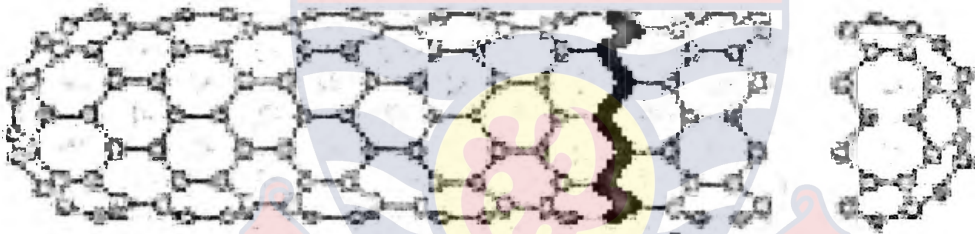


Figure 9: (b) Structure of Zigzag Carbon Nanotube: n or $m = 0$, $\theta=0^\circ$ [23]

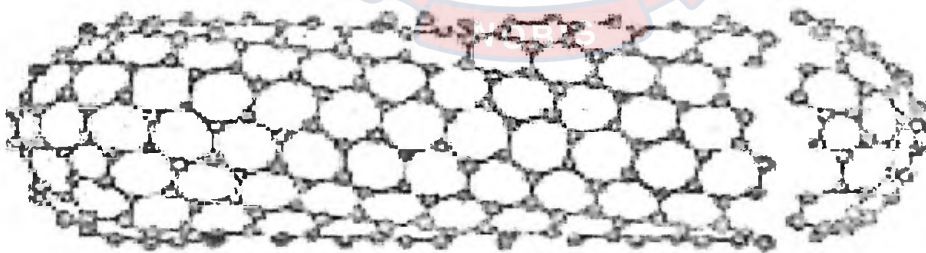


Figure 9: (c) Structure of Chiral Carbon Nanotube: n or $m \neq 0$ and also $n \neq m$, $0^\circ < \theta < 30^\circ$ [23]

There are two possible highly symmetric structures for carbon nanotubes, known as “zigzag” and “armchair” and these are illustrated in figures 9 (a) and (b) . In practice it is believed that most carbon nanotubes do not have these highly symmetric forms but have structures in which the hexagons are arranged helically around the tube axis as in figure 9 (c).

Of course, a carbon nanotube is not visible by bare eye, and a bundle of 100 of them is necessary to be spotted with the best optical microscope. Using Scanning Tunnelling Microscopy (STM) [74-76], the crystalline structure of the tubes was verified. Despite their small diameter, their length can be micrometers [77], which make nanotubes the (geometrically) most anisotropic molecules in the world.

Table 2: Classification of Carbon nanotubes [23]

Type of Carbon nanotubes	Armchair	Zigzag	Chiral
Chiral Vector, C_h	(n, n)	$(n, 0)$	(n, m)
Length of Chiral Vector, L	$\sqrt{3}na$	na	$a\sqrt{n^2 + nm + m^2}$
Chiral Angle, θ	30°	0°	$0 < \theta < 30^\circ$
Number of hexagon in a unit cell, N	$2n$	0	$\frac{2(n^2 + nm + m^2)}{d_R}$
Shape of cross-section	Cis- type: 	Trans-type: 	Mixture of cis and trans

Synthesis Methods of Carbon Nanotubes

Synthesis methods of CNTs have been addressed in many review, journal articles and books [43, 48, 49, 78-100]. Now part of a journal article by Sinha Niraj et al., in 2005 [78] on the mainstream synthesis methods of carbon nanotubes is mainly considered in this brief review since it will enhance better understanding of fundamentals of carbon nanotubes needed before the main research work. To begin with, there is a huge demand for quality carbon nanotubes both as research materials and for large scale industrial applications [101]. The carbon nanotubes examined by Iijima in 1991 were synthesized by arc-discharge method [43], but since then several other production methods have been developed. In this section we briefly described different successful methods for producing and purifying CNTs. The most common production methods used nowadays are: arc-discharge [43, 48, 49, 78-85] laser ablation [78, 86-89] and chemical vapour deposition [78, 90-100] methods.

Arc-Discharge Method

The arc discharge method generally involves the use of two high-purity graphite electrodes to generate an arc by dc current [43, 48, 49, 78-85]. Figure 10 (a) shows the schematic diagram of the arc-discharge method. The anode is either pure graphite or contains metals. In the latter case, the metals are mixed with the graphite powder and introduced in a hole made in the anode centre [78-85].

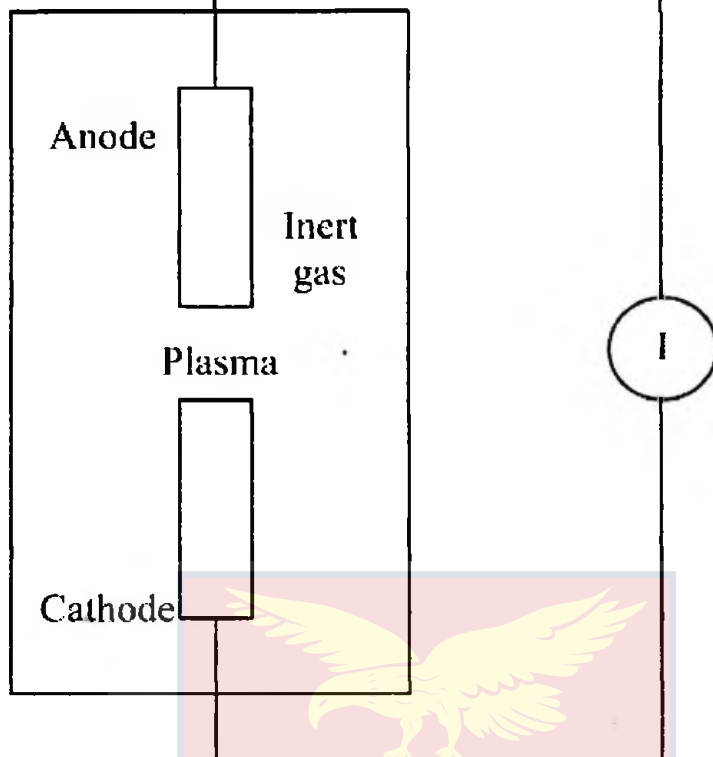


Figure 10: (a) Schematic diagram of carbon arc-discharge method of producing CNTs [78]

Initially, the two electrodes are kept independent. The electrodes are kept in a vacuum chamber and an inert gas is supplied to the chamber. The inert gas increases the speed of carbon deposition. Once the pressure is stabilized, the power supply is turned on (about 20 V). The distance between the electrodes is reduced until the flowing of a current (50–150 A). The positive electrode is then gradually brought closer to the negative one to strike the electric arc.

The electrodes become red hot, resulting in the evaporation of the carbon from the anode to form plasma. Once the arc stabilizes, the rods are kept about a millimeter apart while some of the plasma re-condenses as a hard cylindrical rod on the cathodic graphite. The central part of this deposit contains both CNTs and nanoparticles [78]. Once a specific length is reached, the power

supply is cut off and the machine is left for cooling. The two most important parameters to be taken care of in this method are: (i) the control of arcing current and (ii) the optimal selection of inert gas pressure in the chamber [78, 102].

The arc-discharge method produces high quality MWCNTs and SWCNTs [78]. MWCNTs do not need a catalyst for growth, while SWCNTs can only be grown in the presence of a catalyst. MWCNTs can be obtained by controlling the pressure of inert gas in the discharge chamber and the arcing current. In the case of MWCNT growth by the arc-discharge method, the by-products are polyhedron-shaped multilayered graphitic particles. For the first time, Ebbesen and Ajayan [80] synthesized high-quality MWCNTs having diameters in the range of 2–20 nm and lengths of several micrometers at the gram level. They applied a potential of ~18 V and a helium pressure of ~500 torr. Analysis by transmission electron microscopy (TEM) revealed that the carbon nanotubes consisted of two or more carbon shells. The MWCNTs produced by the arc-discharge method were highly crystalline and were bound together by strong van der Waals forces. Ijima and Ichihashi [48] used a gas mixture of 10-torr methane and 40-torr argon at a dc current of 200 A and a voltage of 20 V to synthesize SWCNTs with diameters ~1 nm. Carbon anode and Co, Ni, and Fe as catalysts were tried by Bethune et al., [49] They used a current of 95–105 A and a He pressure of 100–500 torr. The TEM analysis revealed that SWCNTs were obtained only with Co catalysts, and the diameters of CNTs were 1.2 ± 0.1 nm. Journet et al., [85] optimized the SWCNT growth by the arc-discharge method. They used a graphite cathode (16-mm diameter, 40 mm long), a graphite anode (6-mm diameter, 100 mm long), a mixture of

catalyst (Ni-Co, Co-Y, or Ni-Y), a helium pressure of 660 mbar, an arcing current of 100 A, and a voltage drop of 30 V between the electrodes. Scanning electron microscopy (SEM) revealed that the deposited material consisted of high amount of entangled carbon ropes of diameters 5–20 nm. Li et al., [83] used the modified arc-discharge method, which used FeS as a promoter, to synthesize SWCNTs. The diameters of CNTs were 5–20 μm and their length could reach 10 cm. As evaluated by SEM, thermogravimetric analysis, and Raman spectroscopy, the synthesized SWCNT fibers were 80% pure by volume.

Laser-Ablation Method

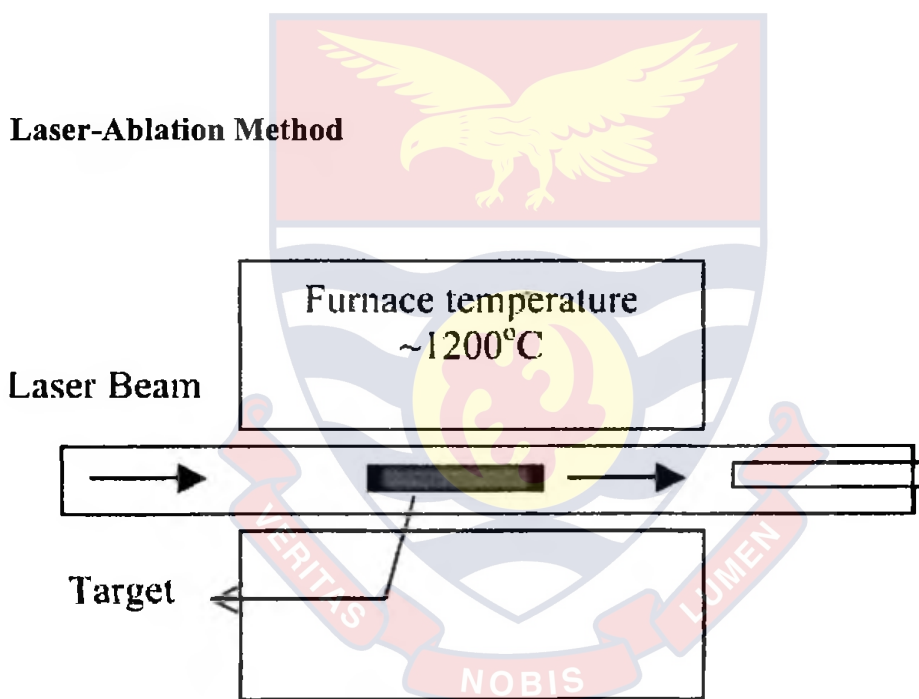


Figure 10: (b) Schematic diagram of laser-ablation method of producing CNTs [78]

In the laser-ablation method used by Thess et al., [86] for producing CNTs, intense laser pulses were utilized to ablate a carbon target.

The flow tube is maintained at a temperature of about 1200 $^{\circ}\text{C}$ by a tube furnace. The pulsed laser-ablation of graphite in the presence of an inert gas and catalyst formed SWCNTs at 1200 $^{\circ}\text{C}$. Figure 10 shows the schematic

diagram of the laser-ablation method. The X-ray diffraction (XRD) and TEM revealed that the SWCNTs produced by laser-ablation were ropes (or bundles) of 5–20 nm diameter and tens to hundreds of micrometers of length. Braidy et al., [87] synthesized SWCNTs and other nanotubular structures (graphite nanocages and low aspect ratio nanotubules) by pulsed KrF laser-ablation of a graphite pellet at an argon pressure of 500 torr, a temperature of 1150 °C, and a laser intensity of 8×10^8 W/cm². They observed that relatively high UV laser intensity was detrimental to the growth of SWCNTs. By using high vacuum laser-ablation, Takahashi et al., [88] synthesized multilayered MWCNTs having a tip angle of 15–20°. Graphite powder was dispersed on a Si (100) substrate and CNTs were grown selectively at high substrate temperature.

In general, some of the major parameters that determine the amount of CNTs produced are the amount and type of catalysts, laser power and wavelength, temperature, pressure, type of inert gas present, the fluid dynamics near the carbon target, etc. [103]. When synthesizing SWCNTs, the by-products in the case of the arc-discharge and laser-ablation methods are fullerenes, graphitic polyhedrons with enclosed metal particles, and amorphous carbon [103].

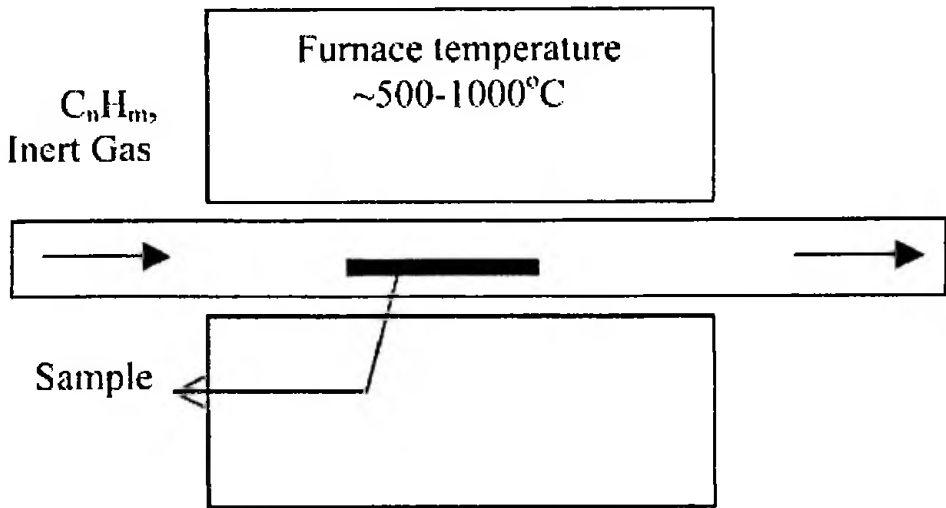


Figure 10: (c) Schematic diagram of CVD method of producing CNTs [78]

In the CVD method, CNTs are synthesized by decomposing hydrocarbons (the commonly used sources are methane, ethylene, and acetylene) at reaction temperatures below 1000 °C in a presence of metallic catalysts [78]. An energy source, such as electron beam or resistive heating is used to impart energy to them in the presence of metal catalysts (e.g. iron, cobalt, or nickel) . The key parameters that determine the yield and quality of the CNT are the nature of hydrocarbons, the catalysts and the growth temperature. The energy source breaks the molecule into reactive radical species in the temperature range of 550–750 °C. These reactive species then diffuse down to the substrate, which is heated and coated in a catalyst (usually a first-row transition metal such as Ni, Fe, or, Co), where it remains bonded. As a result, the CNTs are formed. Figure 11(c) shows the schematic diagram of the CVD method. Yacaman et al., [90] synthesized microtubules of up to 50 m

length of CNTs by catalytic decomposition of acetylene over iron particles at 700 °C. Li et al., [91] used iron nanoparticles (embedded in mesoporous silica) as catalyst for large-scale synthesis of aligned CNTs. The tubes were 50 μm long and well graphitized. Varadan and Xie [94] developed a CVD technique using microwave energy for synthesizing MWCNTs. They used acetylene as the hydrocarbon and cobalt as the catalyst at a temperature of 700 °C. MWCNTs prepared by this process had an average diameter of 20–30 nm and consisted of 26 layers. Park et al., [96] utilized a sequential combination of radio frequency plasma-enhanced CVD (RF PECVD) and thermal CVD to synthesize CNTs from acetylene and hydrogen gas mixture on stainless steel plates. Seidel et al., [99] synthesized dense networks of SWCNTs using Ni catalyst layers of 0.2 nm thickness by thermal CVD at temperatures as low as 600 °C. They proposed a growth model for CVD synthesis on the basis of their experimental observations that was based on the interaction between the catalyst and its support. According to them, the fast growth rates of SWCNTs during CVD synthesis can only be explained by surface diffusion of hydrocarbons on the catalyst support or along the CNTs. For the first time, metal (Fe)-encapsulated dendrimers were used as catalysts for low-temperature growth of CNTs by Vohs et al., [100]. MWCNTs were synthesized at 175 °C via decomposition of carbon tetrachloride in supercritical carbon dioxide by them. For synthesizing MWCNTs, most of the CVD methods utilize ethylene or acetylene as hydrocarbons. Chaisitsak et al., [30] observed that both SWCNTs and MWCNTs can be synthesized by optimizing the catalyst. By optimizing the growth conditions, SWCNTs of diameter 0.65 nm were synthesized by them at a substrate temperature of

660 °C. With regards to the effect of temperature, the density and growth rate of CNTs increase with an increase in temperature. Also, as the temperature increases, the CNTs tend to be vertically aligned. By using CVD, excellent alignment and positional control on the nanometer scale can be achieved in addition to controlling the diameter and the growth rate. A major drawback with the CVD method is that there are high defect densities in the MWCNT structures grown by this process. It is believed that it is most likely due to the lack of sufficient thermal energy for annealing CNTs because of relatively low growth temperature [104]. Between these two methods, the cost of producing CNTs by the arc-discharge method is less compared to the laser-ablation method. However, the main disadvantages with these processes are[78]: (i) tangled CNTs are synthesized by these processes that make the purification and applications of CNT samples difficult and (ii) these processes rely on evaporation of carbon atoms at temperatures 3000°C [104] . Apart from materials scale-up, controlled synthesis of aligned and ordered CNTs can be achieved by using CVD [105]. The microstructure of the CNT tips synthesized by the CVD technique have well-formed caps compared to other methods. The shapes of tips are more rounded and have higher radius compared to arc-discharge tube tips. However, they often have interrupted graphite layers. In applications such as scanning probe microscopies, tips are very important. Although CVD process appears technologically easier, the required quality of tips can be made by the arc-discharge method [106].

In all the above-mentioned preparation methods [43, 48, 49, 78-100], the nanotubes come with a number of impurities whose type and amount depend on the method used. The most common impurities are carbonaceous materials, whereas metals are the other types of impurities generally observed [102]. In the carbon arc-discharge method, the impurities can be purified by oxidation as the carbonaceous impurities have high oxidation rates. However, in this case, 95% of the starting materials are destroyed and the remaining samples require annealing at high temperature (~ 2800 °C) [107]. For purification by oxidation, generally two approaches are followed: (i) gas phase purification [107, 108] and (ii) liquid phase purification [109-111]. Ebbesen et al., [107] observed low yield of purification by gas phase oxidation. Therefore, liquid phase oxidation was tried by Hiura et al., [109] for more homogeneous oxidation. Kim et al., [111] used nitric acid, sulphuric acid, and their mixture as oxidants. As observed by SEM, purified SWCNTs of length less than $2\mu\text{m}$ were obtained. TEM confirmed that the SWCNTs were purified with little damage on the surface and metalcatalysts were efficiently removed. They characterized the size distribution with the field-flow fractionation (FFF) method. A purification technique for SWCNTs that are synthesized by the pulsed laser-ablation technique was proposed by Bandow et al., [112]. They used a cationic surfactant and trapped SWCNTs on a membrane filter. They observed 90% purity by weight after purification. For the SWCNTs grown by CVD of carbon monoxide, a purification process has been developed by Xu et al., [113]. The purification process included sonication, oxidation, and acid washing steps. After purification, the purity and yield were determined and

© University of Cape Coast <https://ir.ucc.edu.gh/xmlui>

estimated by them using TEM. MWCNTs grown by the CVD technique were subjected to wet and dry oxidation by Biro et al., [114] to remove impurities and traces of catalysts. It was observed that the $\text{KMnO}_4/\text{H}_2\text{SO}_4$ aqueous oxidation procedure was effective in reducing the Co catalyst while moderately damaging the outer wall of CNTs. Some other method have also been used to purify CNTs. Shelimov et al., [115] used ultrasonically assisted microfiltration for purifying SWCNTs from amorphous and crystalline carbon impurities and metal particles. SWCNTs with more than 90% purity were generated by this process. Dujardin et al., [116] boiled CNTs in nitric acid aqueous solutions to remove amorphous carbon and metal particles. Harutyunyan et al., [117] developed a scalable purification method for SWCNTs by using microwave heating in air followed by treatment with hydrochloric acid. Ko et al., [118] have developed a purification method for MWCNTs using microwave-assisted purification. They found by Raman spectroscopy and thermogravimetric analysis that a temperature of 180°C was suitable for the purification of CNTs. They observed that purification temperatures above 180°C decomposed the nanotubes, while temperatures below 180°C were not effective in removing defects. As a concluding remark, the above-mentioned purification methods change the structural surfaces of CNTs. As a result, there may be change in the electrical and mechanical properties of purified nanotubes. Therefore, the main thrust of the research should be in the area of producing purified CNTs in a single-step process to conserve the fascinating features of CNTs [78].

Table 3: Summary of the three main production methods for CNTs [43, 78, 119, 120]

Method	Arc-discharge	Laser-ablation	CVD
Pioneer	Iijima (1991) [43]	Guo et al.,(1995) [119]	Yacaman et al.,(1993) [120]
How	CNT growth on graphite electrodes during direct current arc-discharge evaporation of carbon in presence of an inert gas	Vaporization of a mixture of carbon (graphite) and transition metals located on a target to form CNTs	Acetylene decomposition over graphite-supported iron particles at 700 °C
Typical Yield	30 % to 90 %	Up to 70 %	20% to 100%
Types of CNTs	Both SWCNTs and MWCNTs	Only SWCNTs	Both SWCNTs and MWCNTs
Advantage	Can easily produce SWCNT, MWCNT. SWCNTs have few structural defect; MWCNTs without catalyst, Not too expensive, open air synthesis.	Primary SWCNTs with good diameter control and few defects. The reaction product is quite pure	Easiest to scale up to industrial production; long length, simple process, SWCNT diameter controllable, quite pure.
Disadvantage	Tubes tend to be short with random sizes and directions often needs a lot of purification	Costly method, because it requires expensive laser and high power requirement but is improving	CNTs are usually MWCNTs and often riddled with defect

advantages and disadvantages, but the chemical vapour deposition (CVD) method of synthesizing CNTs has the greatest potential of all the methods discussed [78]. Because CNTs grown by CVD have high yield, high purity, well aligned and even large scale synthesis is possible. By using the CVD method, different nanotubes (SWCNTs or MWCNTs) can be produced on different substrates. It has been found that the substrate/CNT interface interactions govern the alignment and type of CNT produced [78].

Graphite Sheet and Unit Cell of Carbon Nanotube.

The review of a graphite sheet (i.e. graphene) and unit cell of carbon nanotube are very important for deeper understanding of carbon nanotube fundamentals. A book written by Saito, R. et al., [23] on “Physical properties of carbon nanotubes” would be mainly utilized for this review. It has been reported that since the discovery of carbon nanotubes in the early 1990s [43], theoretical work has shown that various physical properties for example a metallic behaviour with high electrical conductivity, or semiconducting behaviour with relatively large band gaps should be strongly dependent on the nanotube chirality (the direction in which the graphite sheet or graphene was rolled up) and diameter [23, 121, 122]. This dependence is ultimately related to the way that the two-dimensional Brillouin zone of the graphite sheet (or graphene) is folded into the one dimensional Brillouin zone of the carbon nanotubes [123].

Figure 11 displays the chiral and the translation vectors on a graphite sheet or unrolled hexagonal lattice of a (4, 2) carbon nanotube [123].

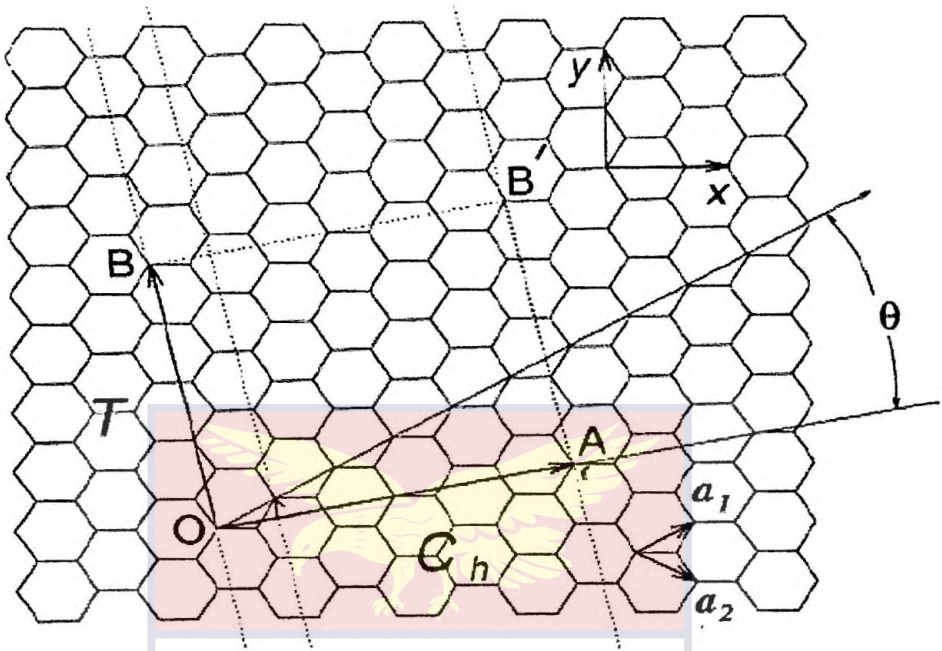


Figure 11: Shows the chiral and the translation vectors in the case of the unrolled hexagonal lattice of a (4, 2) carbon nanotube [123]

Choosing of the primitive lattice vectors a_1 and a_2 of the graphene sheet is the first thing we have to consider. These vectors define a parallelogram, which is called the primitive unit cell, and fill all space by the repetition of suitable crystal translations operations. So we can always make sure that we have chosen the right ones. There are many ways of choosing the lattice vectors, but some are more comfortable to work with than others. In figure 11, we have chosen a_1 and a_2 to be two secants of an isosceles triangle within two hexagons. In Cartesian coordinates (x, y) basis, the lattice vectors are [23]

$$a_1 = \left(\frac{\sqrt{3}a}{2}, \frac{a}{2} \right), \quad a_2 = \left(\frac{\sqrt{3}a}{2}, -\frac{a}{2} \right) \quad (1)$$

where a is the lattice constant given by $a = \sqrt{3} a_{c-c}$ denoting the nearest neighbour distance, $a_{c-c} = 1.42 \text{ \AA}$. Hence the value of a is given by

$$a = |a_1| = |a_2| = 2.46 \text{ \AA}$$

Another choice could be with an angle of 120 degrees instead of our 60 degrees. The two lattice vectors are now used to determine the roll up vector (also called the Chiral vector) given by [23]

$$C_h = na_1 + ma_2 \quad (2)$$

which determines the circumference of the carbon nanotube. Here n and m are the indices of the tube and for that reason it is obvious that (n, m) directly describes the size of the tube. Translation vector, T , describes the distance between two similar lattice points. Now, the two vectors C_h and T span a rectangle, which is called the 2D unrolled nanotube unit cell depicts various fundamental parameters of a CNT, and their relationships to graphene. This is the rectangle, we roll up in the chiral vector direction that forms the cylinder.

The side OB is put together with the side AB'. This define a CNT unit cell, that repeatedly put together forms the tube. The nanotube just created has no distortion of bond angles other than in the circumference direction, caused by the cylindrical curvature of the surface. This curvature, the chiral angle θ , the diameter $d = \frac{C_h}{\pi}$ and an applied magnetic field along the tubule axes have

influence of the electrical properties of the tube. The unit cell of the carbon nanotube is therefore defined as the rectangle formed by Chiral vector, C_h , and the one-dimensional translational vector T , as shown in figure 11.

Some aspect of the basic research work by Grove-Rasmussen Kasper in 2000 [124] especially on reciprocal lattice, brillouin zone of the graphene lattice, the 2D brillouin zone of the nanotube unit cell, boundary condition, and the 1D brillouin zone of the nanotube would be mainly considered in a brief review of reciprocal lattice and brillouin zone since these are relevant to carbon nanotubes fundamentals necessary for better understanding of this thesis

Reciprocal Lattice

Reciprocal space is also called Fourier space, k- space, or momentum space. In contrast to real space or direct space, the reciprocal space lattice is a set of imaginary points constructed in such a way that the direction of a vector from one point to another coincides with the direction of a normal to the real space planes and the separation of those points (absolute value of the vector) is equal to the reciprocal of the real inter planar distance. We are to find the lattice vectors in the reciprocal space given the real space lattice vectors. All calculations are done in Cartesian coordinates. The first Brillouin zone is found by Wigner-Zeits primitive unit cell [123]. In the following this zone is referred to as the Brillouin zone. The derivation of the reciprocal lattice vectors are first given generally. This approach is chosen because more than one set of reciprocal lattice vectors are to be calculated and the choice of real space lattice vectors are ambiguous. The general equation can be applied to the different kinds of real space lattice vectors connected with the carbon nanotube. The general relationship between a direct lattice vector, and reciprocal lattice vector is given by [125] :

where the \mathbf{a} 's are the basis vectors of the real or direct lattice. The \mathbf{b} 's are then called the fundamental vectors of the reciprocal lattice. Here δ_{ij} is the well-known Kronecker delta function defined such that [125]:

$$\delta_{ij} = \begin{cases} 1 & \text{if } i = j \\ 0 & \text{if } i \neq j \end{cases} \quad (4)$$

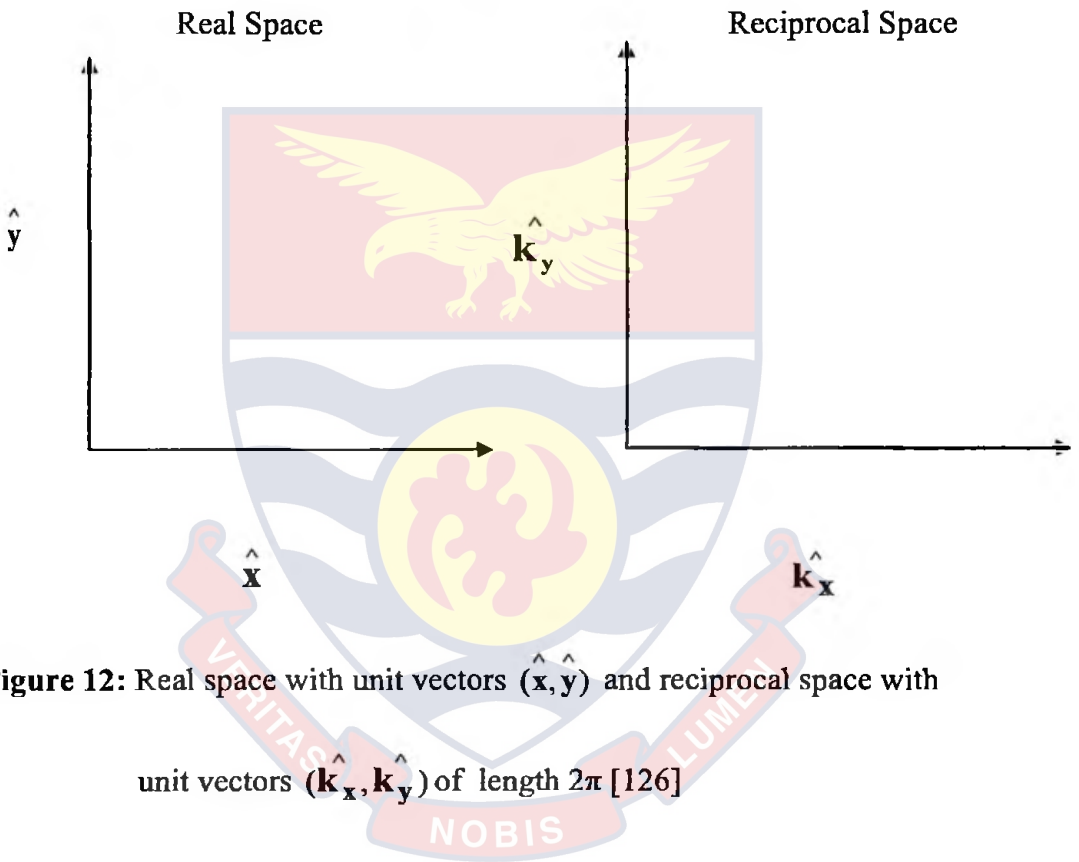


Figure 12: Real space with unit vectors (\hat{x}, \hat{y}) and reciprocal space with unit vectors (\hat{k}_x, \hat{k}_y) of length 2π [126]

Figure 12 shows how the unit vectors of the two-dimensional Cartesian coordinate system in real space which transform to the unit vectors in the reciprocal space according to equation (3). The \hat{x} unit vector is perpendicular to \hat{k}_y and vice versa. The unit lengths of the reciprocal vectors are 2π (not shown at figure 12). If the two real space vectors are not perpendicular, it is not possible to do the transformation to reciprocal space. In a three dimensional

lattice with real space vectors \mathbf{a}_1 , \mathbf{a}_2 and \mathbf{a}_3 , the reciprocal lattice vectors are

found by [127]

$$\mathbf{b}_1 = 2\pi \frac{\mathbf{a}_2 \times \mathbf{a}_3}{V_{\text{real}}}, \quad \mathbf{b}_2 = 2\pi \frac{\mathbf{a}_3 \times \mathbf{a}_1}{V_{\text{real}}}, \quad \mathbf{b}_3 = 2\pi \frac{\mathbf{a}_1 \times \mathbf{a}_2}{V_{\text{real}}} \quad (5)$$

where $V_{\text{real}} = \mathbf{a}_1 \cdot \mathbf{a}_2 \times \mathbf{a}_3$ is the volume of the box spanned by \mathbf{a}_1 , \mathbf{a}_2 and \mathbf{a}_3

These vectors obey equation (3) The length of a reciprocal lattice vector is given by [127]

$$|\mathbf{b}_i| = \frac{2\pi}{|\mathbf{a}_i|} \quad (6)$$

where i is 1, 2 or 3.

In our case we are only in two dimensions. This equation is only correct in special case where it is later used. $\mathbf{a}_3 = (0,0,1)$ and \mathbf{a}_1 is perpendicular to \mathbf{a}_2 in the plane orthogonal to \mathbf{a}_3

$$\mathbf{a}_1 = \begin{pmatrix} a_{1x} \\ a_{1y} \\ 0 \end{pmatrix}, \quad \mathbf{a}_2 = \begin{pmatrix} a_{2x} \\ a_{2y} \\ 0 \end{pmatrix}, \quad \mathbf{a}_3 = \begin{pmatrix} 0 \\ 0 \\ 1 \end{pmatrix}$$

The reciprocal lattice vectors of the plane are \mathbf{b}_1 and \mathbf{b}_2 . The volume spanned by the real space vectors are [124]

$$\begin{aligned} V_{\text{real}} &= \begin{pmatrix} a_{1x} \\ a_{1y} \\ 0 \end{pmatrix} \cdot \left[\begin{pmatrix} a_{2x} \\ a_{2y} \\ 0 \end{pmatrix} \times \begin{pmatrix} 0 \\ 0 \\ 1 \end{pmatrix} \right] = \begin{pmatrix} a_{1x} \\ a_{1y} \\ 0 \end{pmatrix} \cdot \begin{pmatrix} a_{2y} \\ -a_{2x} \\ 0 \end{pmatrix} \\ &= a_{1x} a_{2y} - a_{1y} a_{2x} \end{aligned}$$

$$b_1 = \frac{2\pi}{a_{1x}a_{2y} - a_{1y}a_{2x}} \begin{pmatrix} a_{2y} \\ -a_{2x} \\ 0 \end{pmatrix} \quad (7)$$

$$b_2 = \frac{2\pi}{a_{1x}a_{2y} - a_{1y}a_{2x}} \begin{pmatrix} -a_{1y} \\ a_{1x} \\ 0 \end{pmatrix} \quad (8)$$

The vector b_3 is not calculated, because it is irrelevant to our purpose. We are only working in two dimensions. Now for any choice of real space lattice vectors, the reciprocal lattice vectors can be calculated easily by equations (7) and (8). The Brillouin zone is obtained by finding Wigner-Zeits primitive cell. The above equations of the reciprocal lattice vectors are used to find the Brillouin zone of a general nanotube. In this derivation actually three Brillouin zones are in play.

These three are [124]

- i. The 2D Brillouin zone of the graphene sheet
- ii. The 2D Brillouin zone of the nanotube unit cell
- iii. The 1D Brillouin zone of the nanotube

It is very important to distinguish these three zones.

The 2D Brillouin zone of the graphene sheet is found by the real space lattice vectors of the graphene sheet (a_1, a_2) , equations (7) and (8). The same procedure is used in the 2D Brillouin zone of the nanotube unit cell, but now with the real space lattice vectors defining the nanotube (C_h, T) . Both cases give a two dimensional Brillouin zone. The 1D Brillouin zone of the nanotube is a result of the boundary condition, which arises when the graphene is made

to a tube. By using the zonefolding technique the dimension of the 2D Brillouin zone of the nanotube unit cell reduces to 1D Brillouin zone of the nanotube.

Brillouin Zone of The Graphene Lattice

The real space lattice vectors of the graphene sheet are given by equation (1) Thus using equations (7) and (8) the primitive reciprocal lattice vectors become [124]

$$\mathbf{b}_1 = \frac{2\pi}{a} \begin{pmatrix} 1 \\ \frac{1}{\sqrt{3}} \\ 1 \end{pmatrix}, \quad \mathbf{b}_2 = \frac{2\pi}{a} \begin{pmatrix} 1 \\ \frac{1}{\sqrt{3}} \\ -1 \end{pmatrix}$$

where a is the lattice constant

$|\mathbf{b}_{12}| = 4\pi/3a_{c-c}$ is a lattice constant in the reciprocal space [23].

In figure 14 2.3 the real lattice vectors and reciprocal lattice vectors are shown.

They define a 2D Brillouin zone with the shape of a hexagon.

Clearly \mathbf{a}_1 and \mathbf{a}_2 are perpendicular to \mathbf{b}_1 and \mathbf{b}_2 respectively. The hexagon is shown in k -space, but each pair of (\hat{k}_x, \hat{k}_y) corresponds to an energy value.

As mentioned above the choice of real space lattice vector is ambiguous.

Furthermore the coordinates of these vectors depend on the choice of coordinate system.

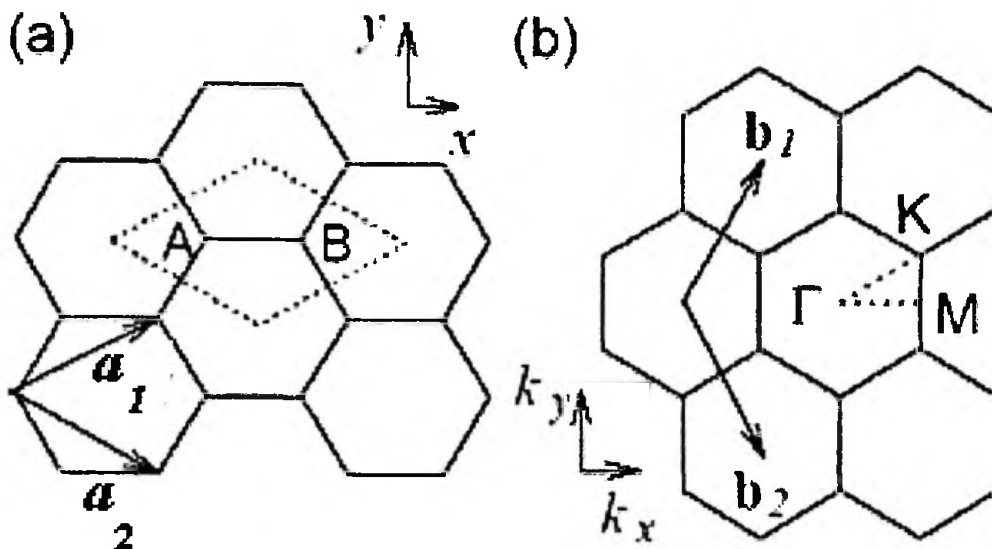


Figure 13: (a) The real space unit cell of graphite which contains points A and B and (b) the lattice vectors in reciprocal space[23]

Figure 13 shows the real space unit cell of graphite which is defined by the dotted line contains points A and B. and (b) the lattice vectors in reciprocal space[63]. The first Brillouin zone of graphene in (a) and (b) are shown as the dotted rhombus and shaded hexagon, respectively. \mathbf{a}_i and \mathbf{b}_i ($i = 1, 2$) are unit vectors and reciprocal lattice vectors, respectively. Γ , K and M are three high symmetry points and are defined as the centre, the corner and the centre of the edge of the Brillouin zone respectively. A and B are two inequivalent atoms in the unit cell as shown in figures 13 (a) and 14, and two Bloch functions are constructed from atomic orbitals for them to provide the basic functions for 2D graphite.

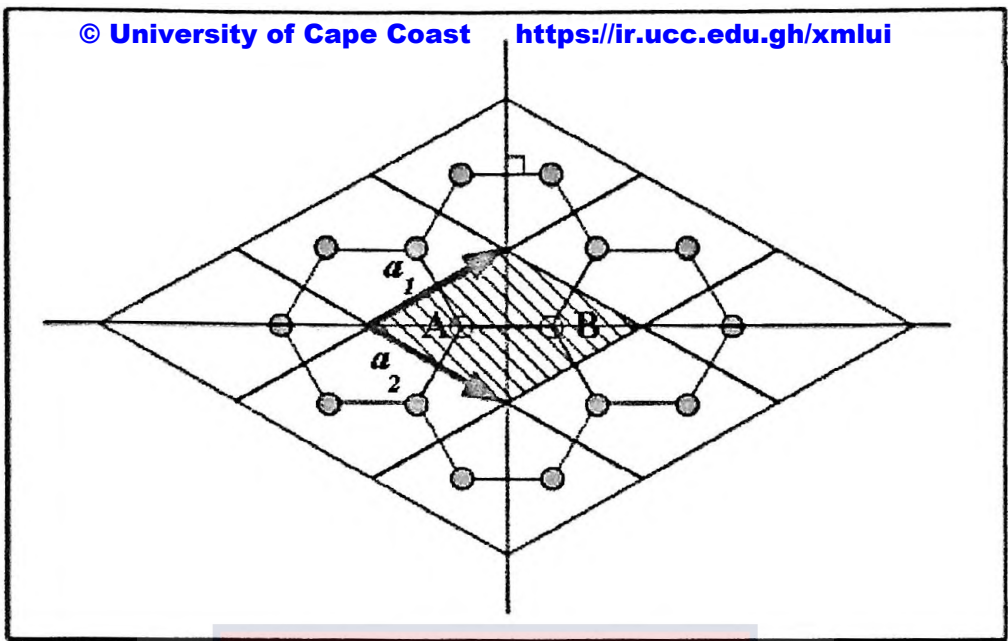


Figure 14: Unit Cell of Graphene containing 2 atoms/unit cell and unit vectors a_1 and a_2 in two equivalent zigzag directions [23]

The 2D Brillouin Zone of The Nanotube Unit Cell

If chiral vector C_h and translation vector T define a CNT real unit cell in 2D as shown in figure 11, then we may similarly assign two associated reciprocal vectors K_1 and K_2 respectively. The corresponding reciprocal lattice vectors K_1 (in the circumferential direction) and K_2 (along the direction of the nanotube axis) are calculated by the expression (3) giving [23, 124]

$$\begin{aligned}
 C_h \cdot K_1 &= 2\pi, & T \cdot K_1 &= 0 \\
 C_h \cdot K_2 &= 0, & T \cdot K_2 &= 2\pi
 \end{aligned}
 \tag{9}$$

Simple vector algebra gives [23, 124]:

$$K_1 = (-t_2 b_1 + t_1 b_2)/N \text{ and } K_2 = (m b_1 - n b_2)/N
 \tag{10}$$

where N denotes the number of hexagons in SWCNT unit cell,

$$N = (n^2 + nm + m^2)/dR \text{ and } t_1, t_2 \text{ are integers.}$$

Because of the translational symmetry of T wave vectors in the direction of K_2 are continuous for an infinitely long nanotube. In the circumferential direction there are N wave vectors iK_1 ($i = 0, 1, \dots, N - 1$), which means N discrete k vectors. Thus K_1 and K_2 define a CNT reciprocal unit cell in 2D. The length of the reciprocal vectors K_1 and K_2 are respectively $2\pi/C_h$ and $2\pi/T$ from equation (6). It is also clear from the expressions of K_1 and K_2 that the larger the CNT unit cell, the smaller the 2D reciprocal unit-cell. The transition from the 2D graphene to the 1D SCWNT results in a reduction of real space and reciprocal space.

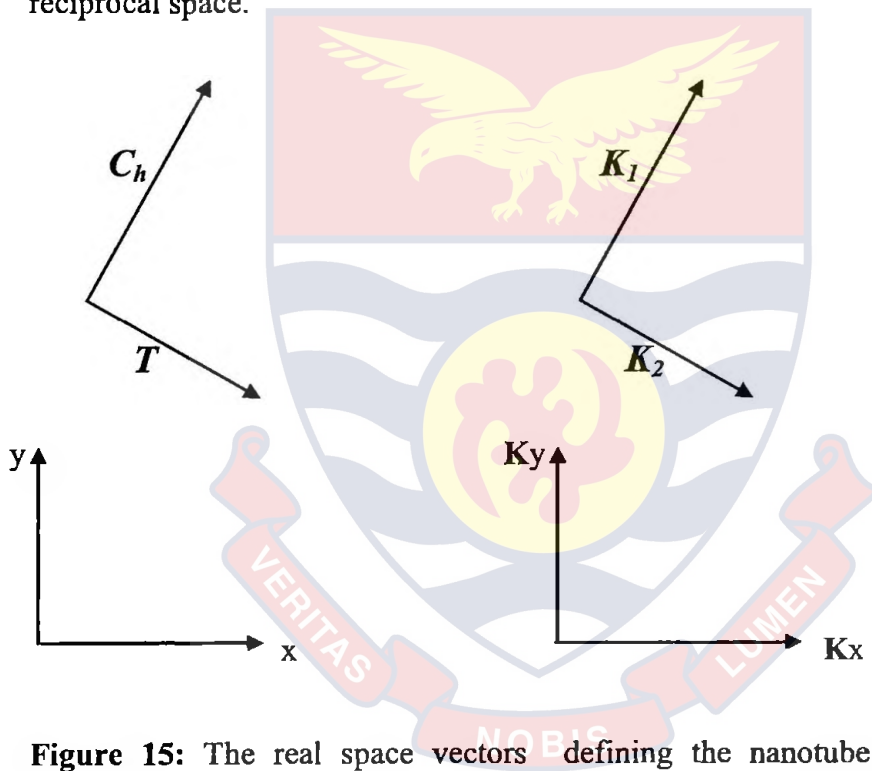


Figure 15: The real space vectors defining the nanotube (left) and the reciprocal Vectors defining the 2D Brillouin zone of the nanotube unit cell (right) [124]

In figure 15, the four vectors are shown. Here in the case of an unspecified chiral tube, the reciprocal lattice vectors of the nanotube unit cell in Cartesian coordinates are given by equations (7) and (8) The Brillouin zone depicted in figure 15 is the rectangle which has the area spanned by the two reciprocal

lattice vectors. The larger the area of the nanotube unit cell gets the smaller the area of the Brillouin becomes, because the reciprocal vectors are proportional to the reciprocal length of the unit vectors. In the chiral case even for small values of n and m , the area of the real space carbon nanotube unit cell becomes large and thereby reducing the 2D Brillouin of the nanotube unit cell.

Boundary Condition

When the nanotube 2D unit cell is folded to a cylinder only a discrete set of wave-vectors along the reciprocal vector \mathbf{K}_l in the reciprocal space are allowed [123]. This results in a number of quantization lines in the reciprocal space which represent the allowed pairs of (k_x, k_y) . The condition on k_x and k_y is dependent on the choice of real space lattice vectors and the choice of coordinate system. Hence we first derive it generally. The expression derived can then be used with another choice than ours. The periodic boundary condition is a result of the required periodicity along the circumference of the Bloch wave-function express as [124]

$$\psi(x + C_h) = \psi(x)$$

where $\psi(x)$ is the Bloch wave function of the graphene sheet and x is along the circumference. This gives rise to the following equation [124]

$$C_h \cdot \mathbf{k} = 2\pi i \quad (11)$$

where $C_h = na_1 + ma_2$ is the chiral vector defining the nanotube, \mathbf{k} the wave-vector and i an integer. Restrictions are later made on i . We write the relation in Cartesian coordinates to express the dependence between k_x and k_y .

$$\left(n \begin{pmatrix} a_{1x} \\ a_{1y} \end{pmatrix} + m \begin{pmatrix} a_{2x} \\ a_{2y} \end{pmatrix} \right) \cdot \begin{pmatrix} k_x \\ k_y \end{pmatrix} = 2\pi i$$

$$(na_{1x} + ma_{2x})k_x + (na_{1y} + ma_{2y})k_y = 2\pi i \quad (12)$$

The last equation shows a linear dependence between k_x and k_y and gives the pairs of (k_x, k_y) , which are allowed in the reciprocal space. When the tube is made only a subset of wave-vectors in k-space are allowed. Because of the linear dependence we speak about quantization lines. Using the defined real space lattice vectors a_1 and a_2 (i.e. equation (1)), the relation becomes [124]

$$\left(n \frac{\sqrt{3}a}{2} + m \frac{\sqrt{3}a}{2} \right) k_y = 2\pi i - \left(n \frac{a}{2} + m \left(-\frac{a}{2} \right) \right) k_x$$

$$(n+m)k_y = \frac{4\pi i}{\sqrt{3}a} - \frac{n-m}{\sqrt{3}} k_x \quad (13)$$

$$k_y = \frac{4\pi i}{\sqrt{3}a(n+m)} - \frac{n-m}{\sqrt{3}(n+m)} k_x \quad (14)$$

Equation (13) expresses the boundary condition and is true for all n and m . Two particular simple cases appear for $n = m$ (armchair nanotube) and $n = 0$ (zigzag nanotube). In the armchair case the quantization condition is [124]

$$k_y = \frac{4\pi i}{\sqrt{3}a(n+n)} = \frac{2\pi i}{\sqrt{3}an}$$

which corresponds to horizontal lines, while the lines are vertical $k_x = \frac{2\pi i}{an}$ in the zigzag case. These two cases are often used as illustrative examples in articles. It is worth a remark that the (n, n) and $(n, 0)$ nanotubes are not in the same symmetry area i.e. between the 30 degrees. It is more obvious to look at the $(n, 0)$ zigzag nanotubes, which are equivalent to the $(n, -n)$ tubes, together with the (n, n) armchair nanotubes. They are defining a symmetry area, where

all nanotubes can be constructed. In the following we will use equation (14)

Two different nanotubes are shown at figure 16. The dashed lines are the allowed pairs of wave-vectors according to the periodic boundary condition and the rectangle is the 2D Brillouin zone of the nanotube unit cell.

Only the lines near the Brillouin zone of the graphene sheet are depicted. The spacing between the lines is $\frac{2\pi}{C_h}$, because the allowed wave-vectors \mathbf{k} are the projection on C_h of length 2π times an integer as in equation (3).

This is exactly the reciprocal lattice vector \mathbf{K}_1 . The edge of the Brillouin zone of the nanotube unit cell parallel to the quantization lines is half the distance of the vector \mathbf{K}_1 . The vector \mathbf{K}_2 is along the lines perpendicular to \mathbf{K}_1 and defines the edge of the Brillouin zone of the nanotube unit cell in that direction. The angle between the lines and the k_x -axis is determined by equation (14)

In the (9,0) zigzag case the slope of the lines is $-\frac{1}{\sqrt{3}}$, which is a line with an angle to the k_x -axes of -30 degrees as in figure 16 (a)). The (5,5) armchair has

$k_y = \frac{2\pi i}{5\sqrt{3}a}$, which is a constant. Thus the horizontal lines in figure 16 (b)

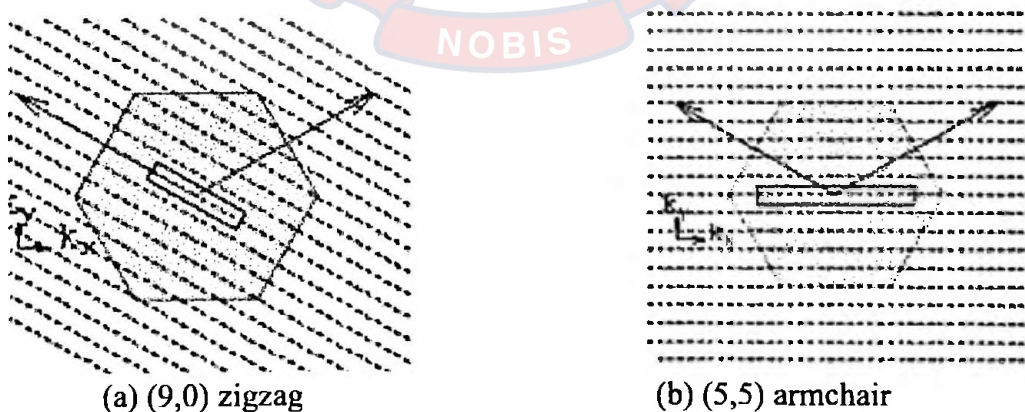


Figure 16: The 2D Brillouin zone of the carbon nanotube unit cell and Brillouin zone of the graphene sheet [124, 126]

The 2D Brillouin zone of the carbon nanotube unit cell (blue rectangular) compared with the Brillouin zone of the graphene sheet is shown in figure 16. The dashed lines represent the allowed values of k_x and k_y . Only one line crosses the Brillouin in zone of the tubes unit cell.

The 1D Brillouin Zone of The Nanotube

By using the periodic boundary conditions in the circumferential direction imposed by chiral vector C_h , the wave-vector K_1 associated with the C_h direction becomes quantized in a CNT, while the wave vector K_2 associated with the direction of the translational vector T along the nanotube axis remains continuous for a nanotube of infinite length. The quantization conditions imposed on the circumference vector give a quantization of the reciprocal vector iK_1 ($i = 0, 1, \dots, N-1$). The momentum vector along the tube length K_2 is continuous in the range of $(-\pi/T, \pi/T)$ for an infinitely long nanotube. This gives rise to a set of k vectors that are parallel to T . These k vectors will result in cross-sections of the graphene electron dispersion. These cross sections result in the appearance of various subbands in a CNT. The band structure is obtained along the K_2 vector. Figure 17 a shows the reciprocal lattice vectors, K_1 and K_2 , for a $C_h = (4, 2)$ chiral nanotube. The wave-vectors of a carbon nanotube are indicated by the parallel lines since K_1 is discrete and K_2 is continuous. The length of all the parallel lines is $2\pi/T$ which is the length of the one-dimensional first Brillouin zone. Thus, the set of one dimensional (1D) energy dispersion relations of a carbon nanotube is made up of slices of the 2D energy band structure of graphite [85]. The reciprocal lattice structure of 2D graphite, and how the carbon nanotube fits into that structure is as shown below.

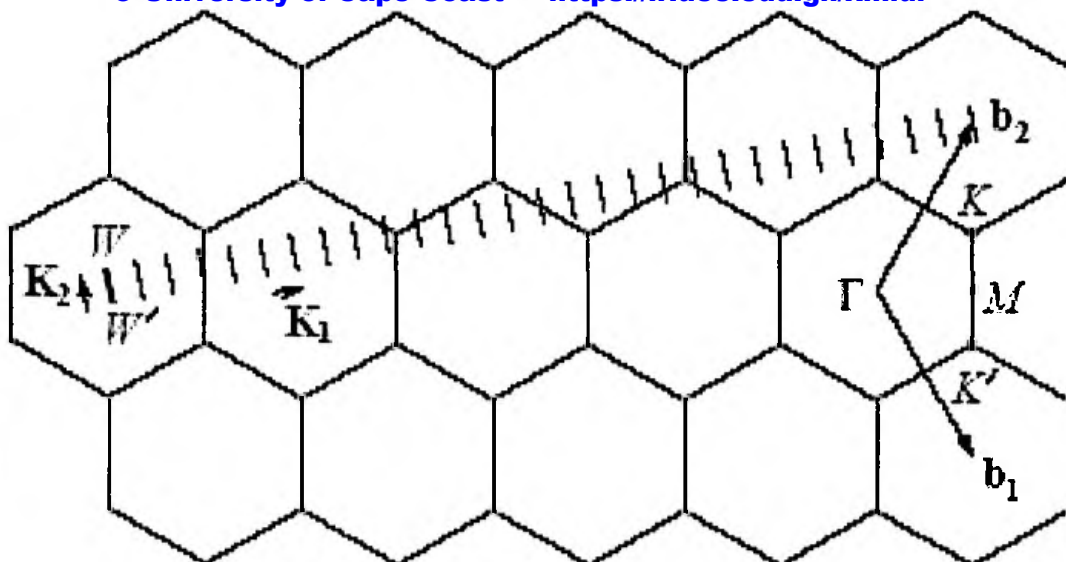


Figure 17: (a) The reciprocal lattice vectors, K_1 and K_2 , for a $C_h = (4,2)$ chiral nanotube [23]

Figure 17 (a): shows the reciprocal lattice vectors, K_1 and K_2 , for a $C_h = (4,2)$ chiral nanotube. The vectors K_1 and K_2 are reciprocal lattice vectors corresponding to C_h and T , respectively. The line segment WW' , which is parallel to K_2 , represents the Brillouin zone of the nanotube. The figure corresponds to $C_h = (4,2)$, $T = (4, -5)$, $K_1 = (5b_1 + 4b_2)/28$, $K_2 = (4b_1 - 2b_2)/28$ [23]. In this figure, each hexagon represents a Brillouin zone of 2D graphite. The Brillouin zone represents a line of reciprocal vector K_2 . The first, and some of the extended Brillouin zones of the nanotube are shown in figure 17(a). The reciprocal lattice vectors of the 2D graphite are b_1 and b_2 , while K_1 and K_2 are the reciprocal nanotube lattice vectors corresponding to C_h and k , respectively. The line segment WW' represents the first Brillouin zone of a carbon nanotube. Points Γ , M , K , and K' are points of high symmetry in the

Brillouin zone of 2D graphite. This figure shows the nature of the quantization of the wave vectors of a carbon nanotube in the form of a series of parallel Brillouin zones. Total number of Brillouin zones equals number of hexagons in tube's unit cell. Hence the transition from the 2D graphene to the 1D SWCNT results in a reduction of real and reciprocal space. These N distinct wave - vectors result in N pairs of 1D energy dispersion relations for the carbon nanotube.

Figure 17 (b): illustrates the condition for obtaining metallic versus semiconducting CNTs. The condition for obtaining a metallic energy band is that the ratio of the length of the vector YK to that of K_1 as in figure 17 (b) is an integer [23].

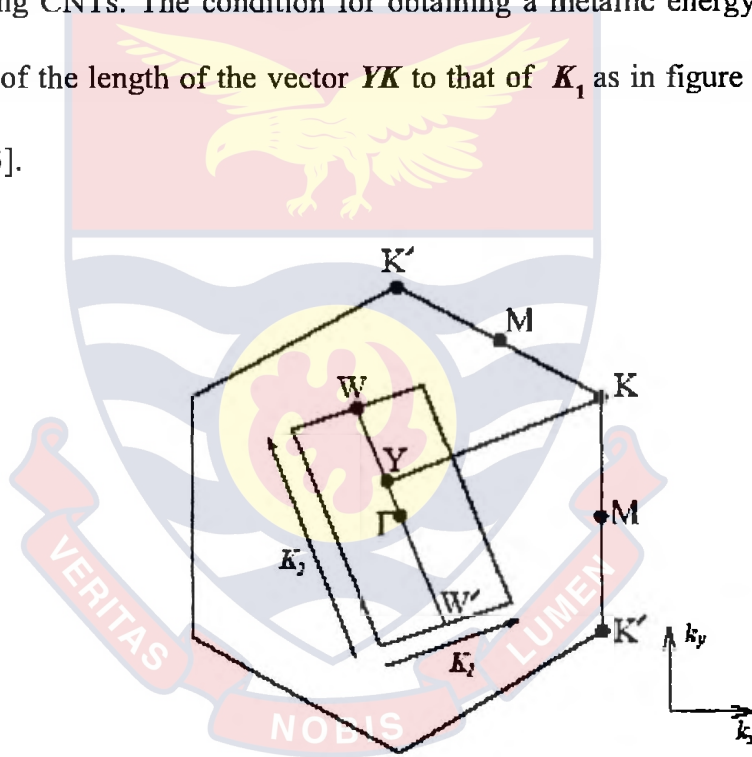


Figure 17: (b) The condition for metallic energy bands: if the ratio of the length of the vector YK to that of K_1 is an integer, metallic energy bands are obtained [23]

$$YK = \frac{(2n+m) K_1}{3} \quad (15)$$

If the vector YK is an integer multiple of vector K_1 , we will have a CNT band line intersecting the graphene K point. This is because, in the extended zone scheme, CNT band lines are spaced $|K_1|$ apart. However a case in which YK is a non-integer multiple of K_1 does not correspond to a CNT band line, and the CNT will be semiconducting. That is, if none of the Brillouin zones are passing through the K points of graphene inverse lattice unit cell, thus the tube is semiconducting. The condition for metallic nanotubes is that $(2n+m)$ or equivalently $(n-m)$ is a multiple of 3. In particular, the armchair nanotubes denoted by (n, n) are always metallic, and the zigzag nanotubes $(n, 0)$ are only metallic when n is a multiple of 3.

Energy Dispersion and Density of Electronic States in Carbon Nanotubes

The energy dispersion and density of electronic states in carbon nanotube are briefly reviewed under the following:

- i. Typical energy dispersion relations for metal, semiconductor and semimetal
- ii. Graphene sheet energy dispersion relation
- iii. Energy dispersion relation of the 1D nanotube
- iv. Density of states (DOS)

The most useful books and journal articles found to be vital for this review are cited accordingly.

Semimetal

Before starting with the band structure of graphene, we would briefly mention the principal band structures of solids. One could distinguish between metals, semiconductors, insulators, and semi-metals. Important for this differentiation is whether the Fermi level (E_F) lies in the conduction band, the valence band, or within a band gap [128]. The Fermi level is defined as the energy at which the probability of occupation of the electron states is 1/2. In solids, the valence band is the band with the highest range of electron energies where the electrons are present at zero temperature (0K) [128]. In contrast, the conduction band is the band in which the electrons are free to be accelerated under the influence of an applied electric field. It is, therefore, located at higher energies than the valence band. Both bands are separated by a band gap E_g . A metal is characterized by the position of the Fermi level within the conduction band, which is, therefore, also the valence band. Metals conduct electricity easily because there are so many electrons with easy access to adjacent conduction states. A semiconductor, in contrast to a metal, is characterized by a finite band gap between a filled valence and an empty conduction band at 0K. In an undoped (intrinsic) semiconductor the Fermi level lies in the middle of the band gap in figure 18(b). An excitation of the electrons in the valence band is necessary to transfer them into the conduction band and to allow electronic transport in a semiconductor. Therefore, in semiconductors, electrons need an energy boost from light or electric field to jump the gap to the first available conduction state as shown in figure 18(b). The amount of energy needed depends on the separation between the two levels. Doping the semiconductor

will shift the Fermi level either towards the valence band or towards the conduction band, making the semiconductor p-type or n-type, respectively. In a p-type semiconductor holes are the majority carriers and electrons the minority carriers, whereas in an n-type semiconductor it is vice versa. If the band gap becomes too large one obtains an insulator, where excitations of electrons into the conduction band become very unlikely.

A particular case is a semi-metal, which is neither a distinct metal nor a real semiconductor. In a semi-metal the Fermi level is degenerated to a single point – the Fermi point (K-point) in figure 18(c). The valence band of a semi-metal is almost completely filled whereas the conduction band is almost completely empty. The graphite is a semimetal that just barely conducts, because without the external boosts such as external electric field or light, only a few electrons can access the narrow path to a conduction band.

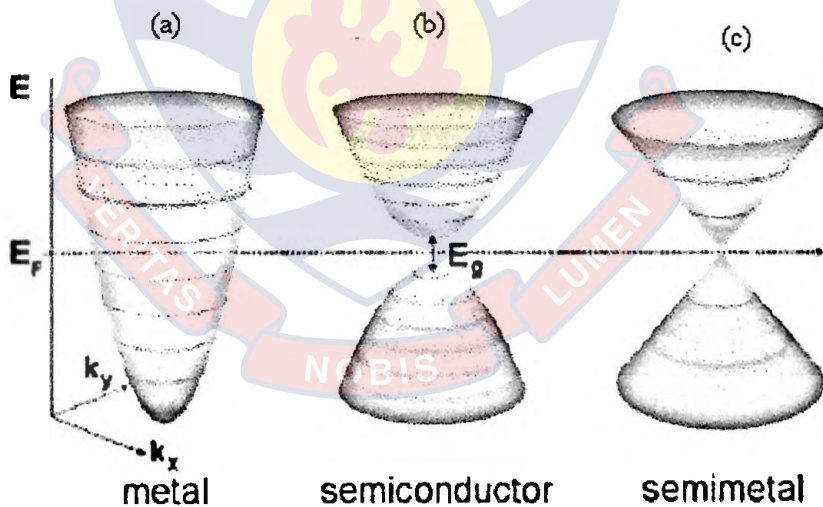


Figure 18: Simplified band structures of a (a) metal, (b) semiconductor and (c) a semi-metal [128, 129]

Electrical properties of a material depend on the separation between the collection of energy states that are filled by electrons (below Fermi level) and the additional “conduction” states that are empty and available for electrons to hop into (above Fermi level). The Fermi level E_F in a metal lies within the conduction band, whereas in a semiconductor within the band gap E_g between valence and conduction bands. In a semi-metal the valence and conduction bands touch at a point called the Fermi point. The axis k_x and k_y define the vectors in reciprocal space.

Graphene Sheet Energy Dispersion Relation

Before we are able to find the energy dispersion relation of the carbon nanotube, we need the energy dispersion relation of the graphene sheet. To determine the energy band structure of carbon nanotubes, it is convenient to start by calculating the energy band structure of a graphite sheet by the tight-binding approximation [130, 131] and then to superimpose the periodic boundary conditions of nanotubes along the circumferential direction. The theoretical calculation of graphitic electronic structure was pioneered by Wallace as early as 1947 [132]. In order to characterize the binding within the basal planes, he used a “tight-binding approximation”. With this approximation, the electronic structure is calculated by separating the interaction within each basal plane (covalent) from in-plane interactions (van der Waals). Such a separation is justified due to the weak interaction that exists between graphene sheets. The unit cell in real space of graphene contains two carbon atoms as shown in figure 13(a). Each carbon atom in the graphene sheet has four valence electrons. The first three electrons form a strong sp^2 σ -bond

with its ~~University of Cape Coast~~ <https://ru.academia.edu/UniversityofCapeCoast> which are in the same plane, with angles of 120° and are at energies -2.5 eV which lie far below the Fermi level and do not contribute to the electrical conduction. The fourth valence electron, however, is located in the π orbital which lobes is perpendicular to the plane of the graphene sheet, which is slightly below the Fermi Level; therefore, this electron is predicted to control electrical conduction and transport properties. This corresponds to the valence band of the energy diagram. The anti-bonding π orbital (π^* orbital) is slightly above the Fermi level, which corresponds to the conduction band in an energy diagram shown in figure 19. Hence, the electronic properties of graphene and carbon nanotubes are well described taking into account the energy dispersion of the π -electrons only [133-135].

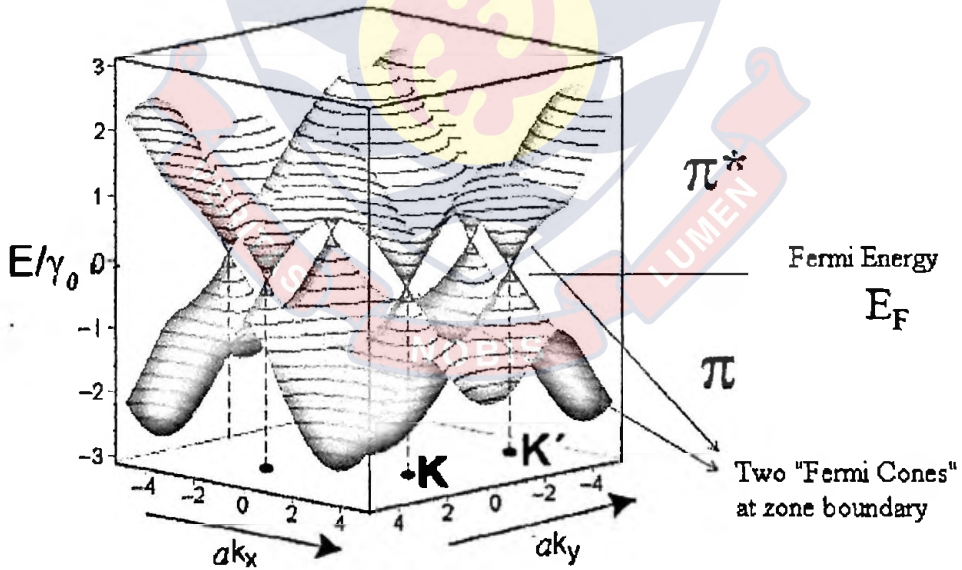


Figure 19 : Energy band structure of the graphene layer [23]

The energy dispersion relation for the π -electrons of the graphene sheet can be calculated in a tight-binding approximation yielding a bonding (-) and anti-bonding (+) energy band given by [132] :

$$E(k_x, k_y) = \pm \gamma_0 \left[1 + 4 \cos\left(\frac{\sqrt{3}k_x a}{2}\right) \cos\left(\frac{k_y a}{2}\right) + 4 \cos^2\left(\frac{k_y a}{2}\right) \right]^{\frac{1}{2}} \quad (16)$$

where $\gamma_0 \approx 3.0\text{eV}$ is the energy overlap integral between nearest neighbours and $a = 0.246\text{ nm}$ is the in - plane lattice constant. This equation yields two bands resulting from bonding and anti-bonding states between the two atoms in the unit cell. Figure 20 (a) shows a three-dimensional plot of the energy dispersion $E(k_x, k_y)$, as follows from equation 16. The conduction and valence bands touch and are degenerate at six K points; these six points define the vertices of the first Brillouin zone, as shown in figure 20 (b). That is the vanishing energy gaps at six points coincide with the corners of the hexagonal Brillouin zone. The Fermi surface is thus reduced to six points, two of which, the K and K' points, are inequivalent , where the conduction and valence bands meet or where the anti-bonding and bonding bands touch . At $0K$, the lower bonding bands are completely filled and the upper bands are empty, so graphite is classified as a zero-gap semiconductor.

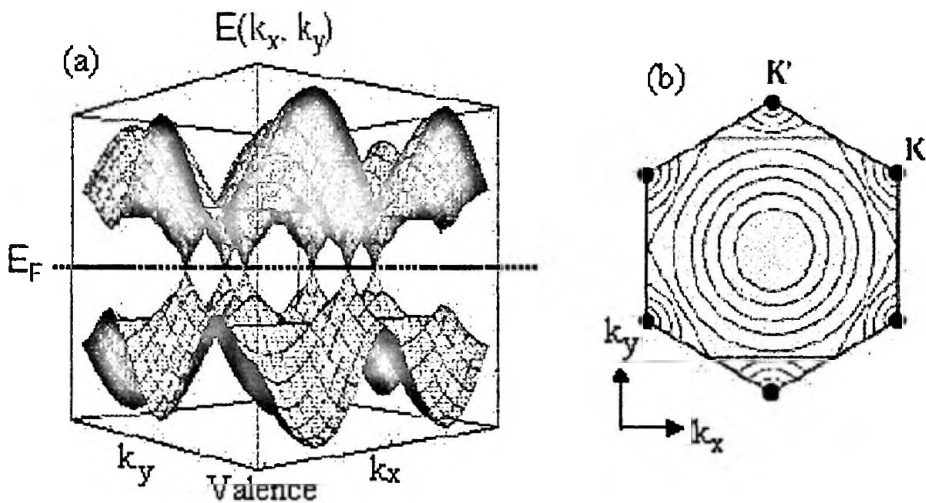


Figure 20: (a) A graph of the energy $E(k_x, k_y)$ of valence and conduction states in graphene and (b) the hexagonal Brillouin zone of grapheme [23]

Figure 20(a) shows Energy dispersion for graphite. The three-dimensional graph of the energy $E(k_x, k_y)$ of valence and conduction states in graphene plotted as a function of wave-vector \mathbf{k} is shown in figure 20(a). The hexagonal Brillouin zone of graphene with energy contours schematically drawn for the bonding band is also shown in figure 20(b). The Fermi level is reduced to the six corner points, indicated by black dots.

The π and π^* bands touch at the K points. Because there are two electrons in the unit cell, the π band (valence band) is completely filled and π^* band (conducting band) is empty. The valence and conduction states meet at singular points in \mathbf{k} -space called K points. Dispersion around these points is conical. The Fermi energy E_F is reduced to six points where the bonding and antibonding bands touch [118]. Energy contours for the bonding band are drawn in the first Brillouin zone in figure 20(b). The antibonding band is similar. Also indicated are the gapless Fermi points at the corners by black

dots. Two Dirac cones are obtained by lattice transformations along b_1 and b_2 . The energy dispersion in the vicinity of these points is approximately radially symmetric within the k_x, k_y plane. Equation (16) can be simplified in these regions to

$$E - E_F = \frac{\sqrt{3}}{2} a \gamma_0 |k - k_F| \quad [136-138]$$

Energy dispersion for 2D graphene where π and π^* bands touch at the K points and the hexagonal Brillouin zone of 2D graphene is illustrated in figure 21.

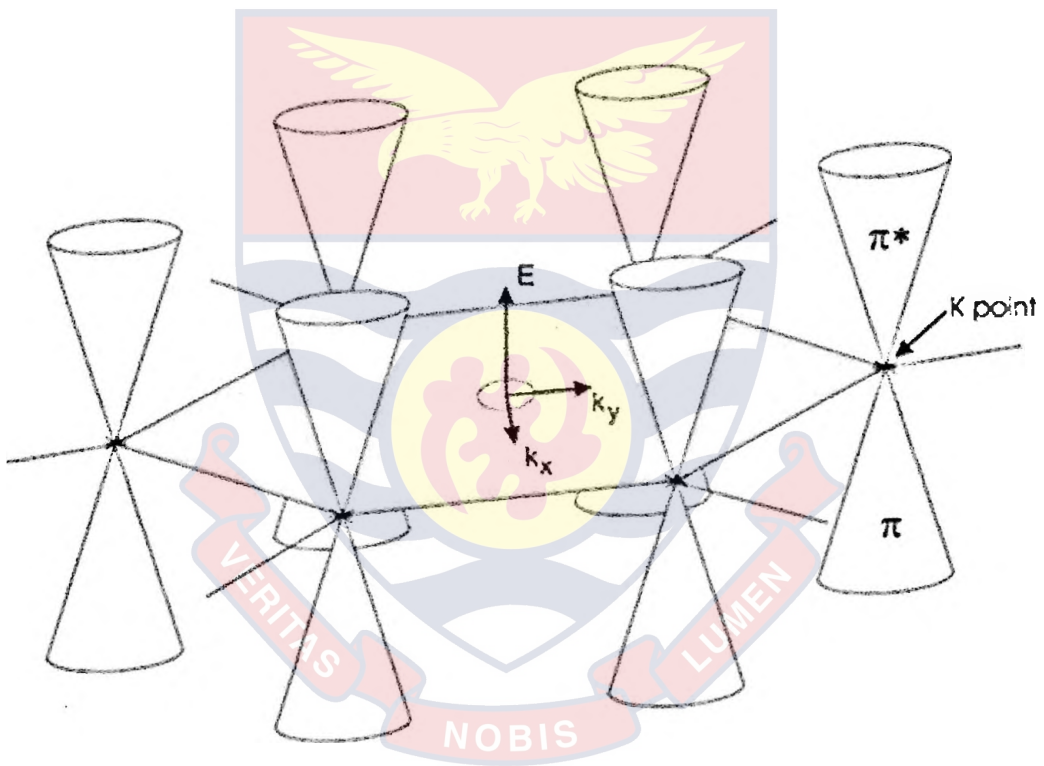


Figure 21: The graphene band structure near E_F showing Brillouin zone and zero-gap points [139]

Figure 21 shows the graphene band structure near E_F . The cones represent the π and π^* electronic bands near the Fermi level, touching in the corners of the hexagonal Brillouin zone and the black dots called K-points are zero-gap

points. The bands of the cones of the Brillouin zone and form 'cones' above and below the Fermi level. They can be described by [139]

$$E(k) = E_F \pm \hbar \cdot v_F \cdot |k - k_F|$$

where k_F is the momentum at a K point and $v_F = |v(k)| = |\hbar^{-1} \cdot dE/dk| \approx 10^6$ m/s. This description holds for a range of several hundred meV around the Fermi level [140]. The states at the K points can be visualized very easily.

In figure 22 (a) the six momenta belonging to the K points are retransferred into the real lattice from reciprocal lattice space as shown in figure 22(b). They correspond to a motion along the 'zigzag' directions in the graphene lattice as in figure 22(a). This is reasonable, as the zigzag directions offer the most direct path for current transport if transport is imagined as moving an electron from bond to bond.

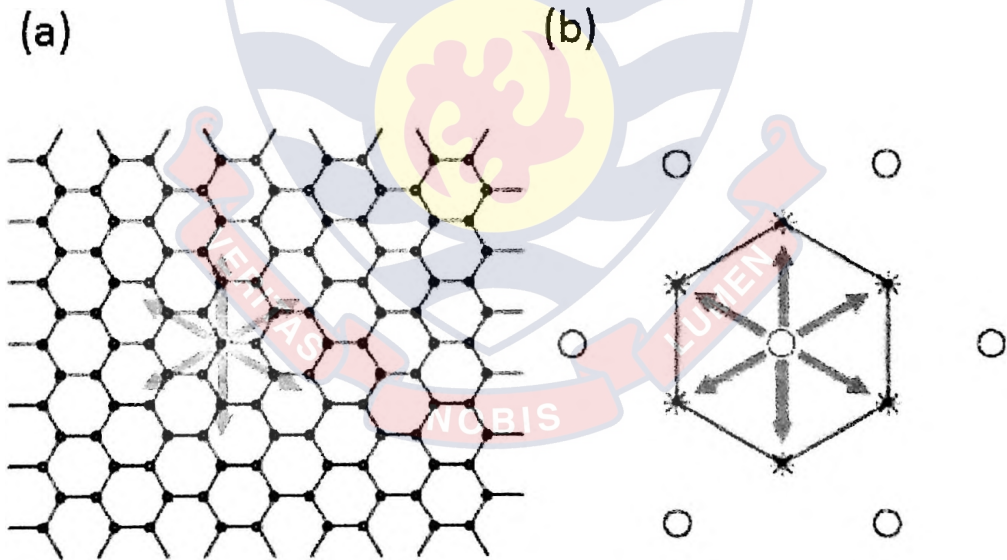
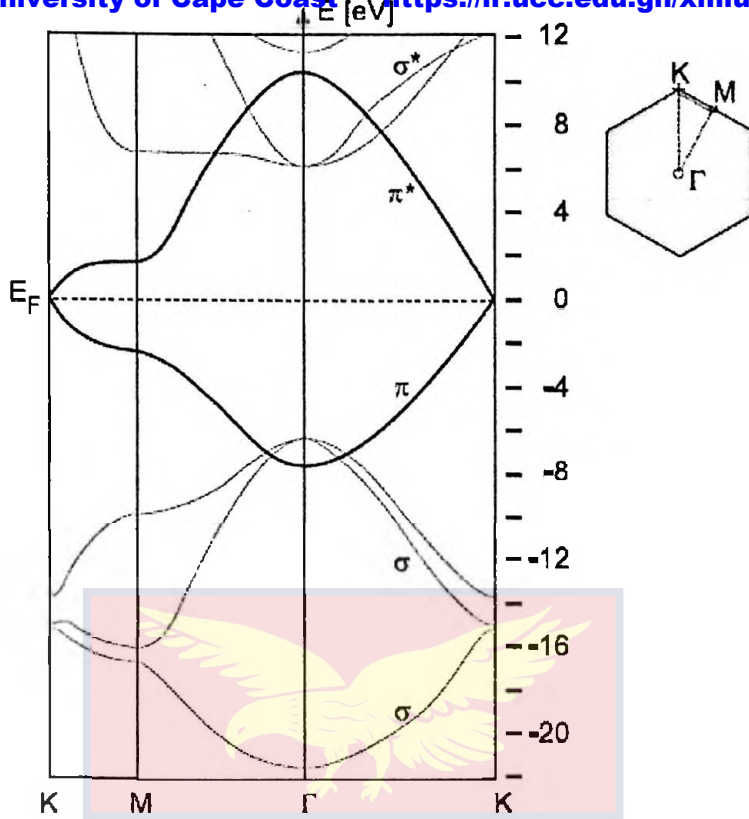


Figure 22: The momenta of the K points in the reciprocal lattice (b) which correspond to a motion along the 'zigzag' directions in the graphene sheet (a) [139]



Wave Vector (k)

Figure 23: (a) Band structure of graphene along several lines in the Brillouin zone [139]

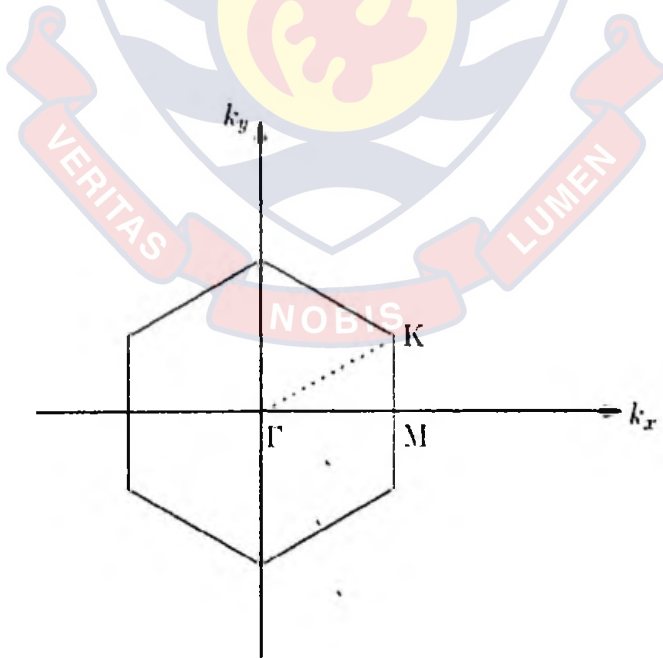


Figure 23: (b) Sketch of Γ , M, and K which are points of high symmetry in the First Brillouin zone of 2D graphite [23]

Figure 23(a) shows band structure of graphene along several lines in the Brillouin zone [141]. The σ and bands are derived from the sp^2 hybrid orbitals forming the in-plane bonds. The π and π^* bands (emphasized) result from the delocalized p orbitals. Since every carbon atom supplies one electron in its p orbital, the bonding π band is completely filled, while the antibonding π^* band is completely empty. These electronic bands touch each other at the K point that is in the corners of the Brillouin zone and thus the Fermi level is pinned there, making graphene a zero gap semiconductor [139].

Energy Dispersion Relation of The 1D Nanotube

The folding of the graphene layer to form a CNT introduces an additional level of quantization due to the confinement of electrons around the circumference of the nanotube [142]. The component of the wave-vector k is constrained by imposing the periodic boundary or quantization condition

$$C_h \cdot k = 2\pi i \quad (i = 0, 1, 2, \dots)$$

along the circumferential direction as shown in equation (2.11). Thus, in going from a 2D graphene sheet to a 1D CNT, each graphene band is split into a number of 1D subbands indexed by i . The number of available energy modes in the circumferential direction is quantized. The electrons are only free to move in an axial direction. This quantization along the circumferential direction gives rise to discrete numbers of parallel equidistant lines in the direction of the tube axis, representing the allowed k modes in the reciprocal space of the grapheme [139].

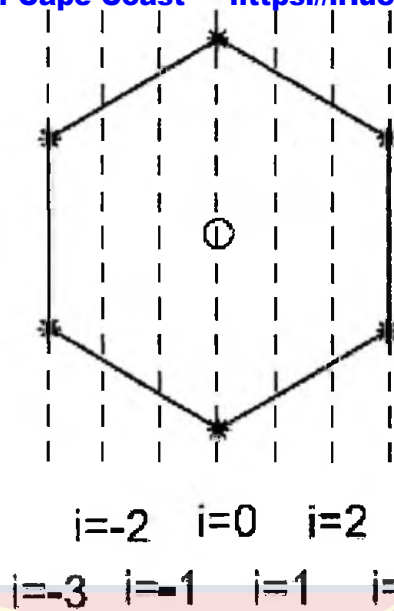


Figure 24: The lines which mark the momenta which are allowed states in the nanotube according to quantization condition in equation (11) [139]

In figure 24, the dashed lines cutting through the Brillouin zone in the reciprocal lattice mark the momenta which are allowed states in the nanotube according to quantization condition in equation (11). The dashed lines mark the momenta which satisfy the quantization condition and are thus allowed states in this special nanotube. The only degree of freedom for the electronic momentum left is along the tube axis. The momentum around the circumference is quantized.

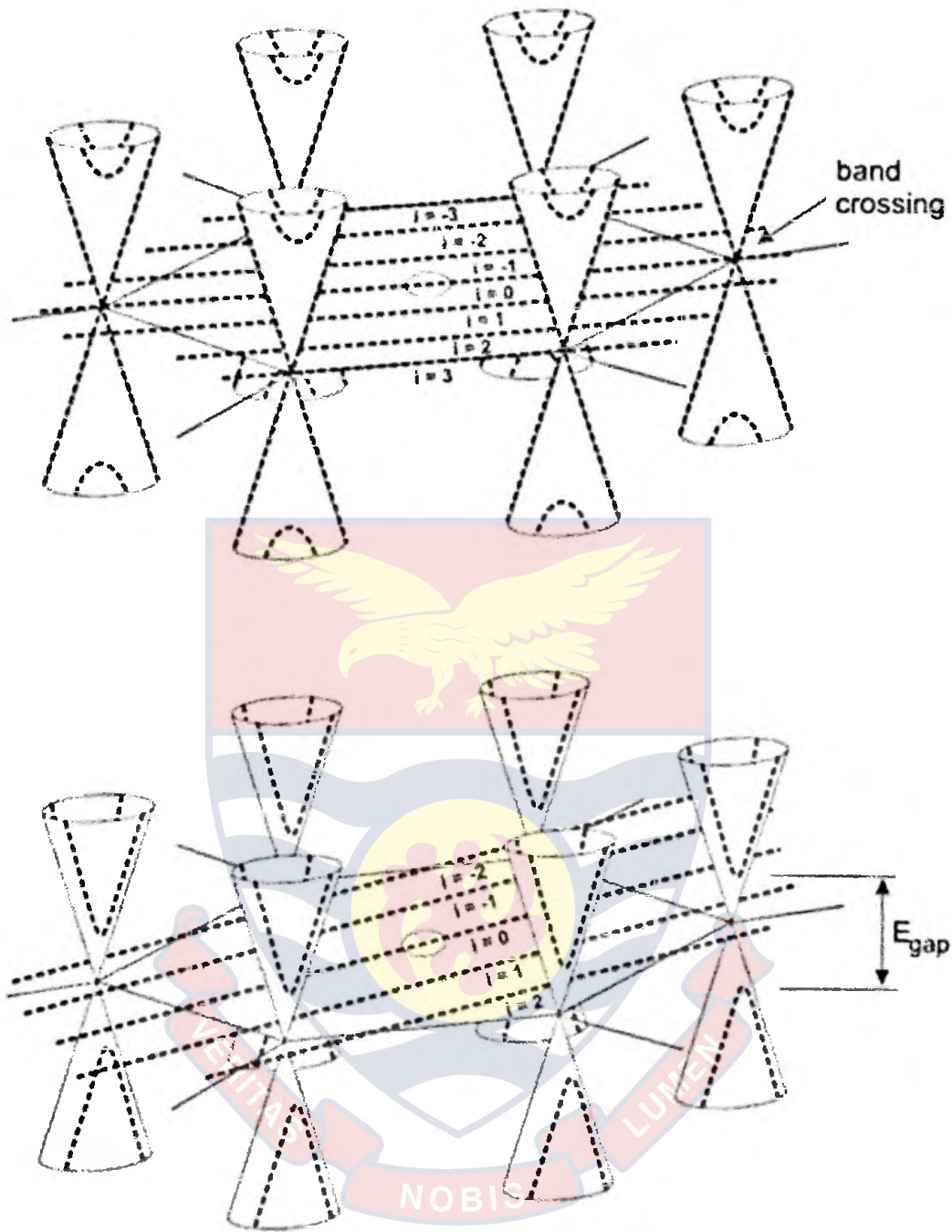


Figure 25: The graphene band structure near E_F together with the quantization condition marked by dashed lines in the Brillouin zone [129]

Figure 25 shows the graphene band structure near E_F , together with the quantization condition marked by dashed lines in the Brillouin zone.

The resulting subbands in the π and π^* bands (cones) are marked by the dotted lines. The upper figure shows a situation, where the K points are included in one of the quantization lines ($i=0$ and $i=\pm 3$), hence the belonging subbands are touching (or crossing) at the Fermi level and the tube is metallic. In the lower figure, the quantization lines miss the K points and a finite energy gap between the subbands results.

It further shows how the quantization condition results in semiconducting and metallic tubes when applied to the graphene band structure. If the quantization lines include the K points, the tube is metallic (i.e. there are allowed states at the Fermi level), while if the quantization misses these points, an energy gap between the subbands results. As can be seen, the closer the quantization is to the K points, the smaller the energy gap will be. When the diameter of the tube is increased, the interval between quantization lines for different subbands i shrink and the lines draw closer to the K points, so the gap decreases. Using the quantization condition in equation (16), one can compute how close (or how far) the K points are missed by the subbands. For a metallic tube, this distance is zero, at least for one sub band-K point combination.

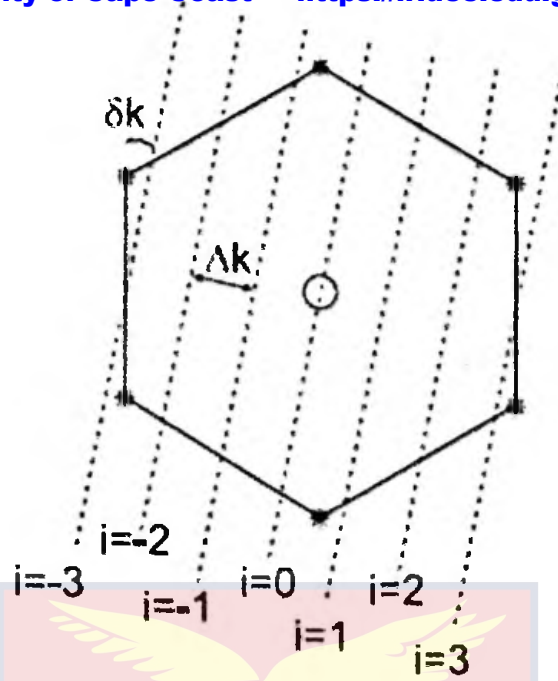


Figure 26: The quantization lines in the reciprocal lattice are spaced by $\Delta k = 2\pi/|C_h|$ and miss the K points by at least $\delta k = 1/3 \cdot \Delta k$. [139]

For the semiconducting tubes the minimum distance between a subband and a

K point as shown in figure 26 turns out to be $\delta k = \frac{1}{3} \cdot \frac{2\pi}{|C_h|} = \frac{1}{3} \cdot \Delta k$

where Δk is the separation of the quantization lines in the reciprocal space.

Due to the linear dispersion relation around the K points, the energy gap for the semiconducting tubes turns out to be [139]

$$E_{\text{gap}} = 2 \hbar v_F \delta k = \frac{2}{3} \hbar v_F \frac{2\pi}{|C_h|} = \frac{4}{3} \frac{\hbar}{d} v_F \quad (17)$$

The gap energy scales inversely with the diameter d of the tube. Figure 27 visualizes the dependence of the gap energy on the tube diameter.

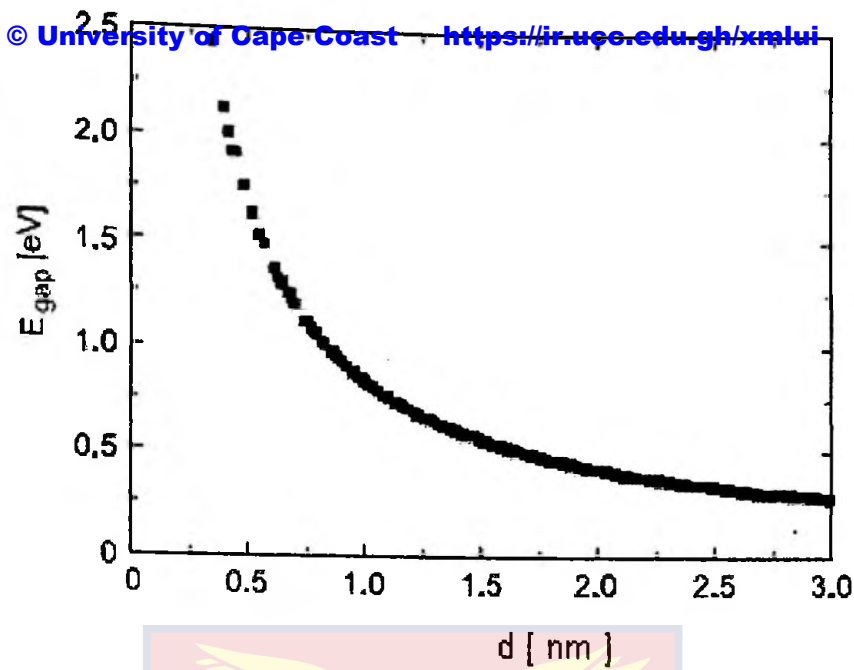


Figure 27: Gap energies for tubes of different diameters [139]

One third of the tubes are metallic (the ones fulfilling $n-m = 3i$), hence they have zero energy gap. The gaps of the other two thirds of the tubes decrease with increasing diameter according to equation (17). Each quantization line corresponds to a one-dimensional channel for conduction along the nanotube. In the case of an armchair nanotube the quantization condition is $n\sqrt{3}k_x a = 2\pi i$ ($i = 0; 1; 2 \dots n$) and the allowed k -lines run in the (vertical) k_y direction. For zigzag nanotubes the condition $nk_y a = 2\pi i$ ($i = 0; 1; 2 \dots n$) applies and the allowed k -lines are in the (horizontal) k_x direction. The dispersion relations for armchair and zigzag nanotubes can be obtained by inserting these quantization conditions in equation 16, to yield [145].

$$E_{armchair}(k_y) = \pm \gamma_0 \left[1 + 4 \cos\left(\frac{\pi i}{n}\right) \cos\left(\frac{k_y a}{2}\right) + 4 \cos^2\left(\frac{k_y a}{2}\right) \right]^{\frac{1}{2}} \quad (18)$$

$$E_{\text{zigzag}}(k_x) = \pm \gamma_0 \left[1 + 4 \cos\left(\frac{\sqrt{3}k_x a}{2}\right) \cos\left(\frac{\pi i}{n}\right) + 4 \cos^2\left(\frac{\pi i}{n}\right) \right]^2 \quad (19)$$

where $a = \sqrt{3}a_{c-c}$ is the lattice constant.

Band structures of typical metallic and semiconducting carbon nanotubes, which have similar diameters of ~ 1.3 nm are plotted in figure 28 (a) and (b).

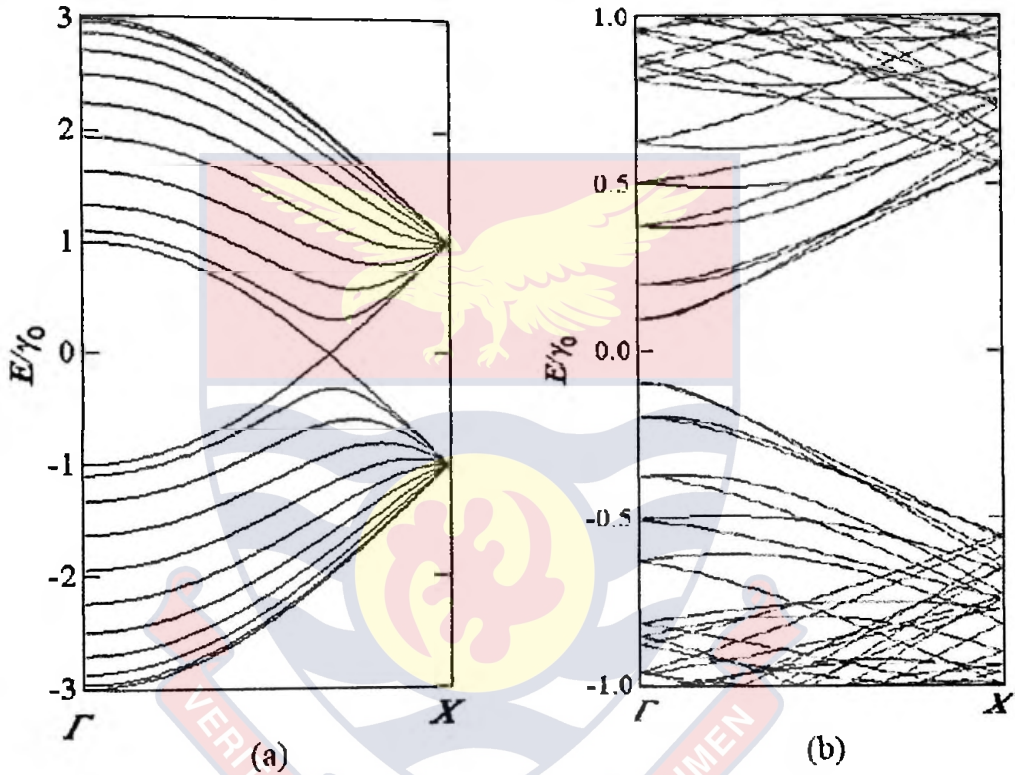


Figure 28: The band structure of (a) a metallic nanotube with chirality of (10, 10) and (b) a typical semiconducting nanotube with chirality of (14, 7) [23]

The 1D density of states (DOS) in units of (states/C-atom)/eV is

calculated by [146]
$$D(E) = \frac{T}{2\pi N} \sum_{\pm} \sum_{i=1}^N \int \frac{1}{\left| \frac{dE_i^{\pm}(k)}{dk} \right|} \delta(E_i^{\pm}(k) - E) dE \quad (20)$$

where the summation is taken for the N conduction (+) and valence (-) 1D bands. T is the magnitude of the translation vector T shown in figure 11 and $E_i^{\pm}(k)$ is the 1D energy dispersion relations of a CNT. Since the energy dispersion near the fermi energy is linear [132], the density of states of metallic nanotubes is constant at the Fermi energy and is inversely proportional to the diameter of the tube [147].

$$D(E_F) = \frac{a}{2\pi^2 \gamma_0 dt} \quad (21)$$

It is clear from equation 20 that the density of states becomes infinity at the points where the energy dispersion relation becomes flat as a function of k . One dimensional van Hove singularities (vHs) appear in the density of states, which are known to be proportional to $(E^2 - E_0^2)^{-1/2}$ at both the energy minima and maxima ($\pm E_0$) of the dispersion relations for carbon nanotubes. These are important for determining many solid state properties of carbon nanotubes, such as the spectroscopy studies of SWCNTs with scanning tunnelling microscope and optical absorption. The DOS of typical metallic nanotube (10,10) and nanotube semiconducting (14, 7) can be numerically calculated this way as clearly shown in figure 29 (a) and (b), respectively, as well as, the van Hove singularities. The vHs are the peaks which can be used to determine the magnitude of the band gap for the semi-conducting tubes. The differences

between the highest-lying valence band singularity and the lowest-lying conduction-band singularity in the 1D electronic density of states have been calculated by Mintmire and White [138], and White and Todorov [148] and are given by

$$E_{11}^M(d_t) = 6a_{c-c}\gamma_0 / d_t \text{ and } E_{11}^S(d_t) = 2a_{c-c}\gamma_0 / d_t \quad (22)$$

where the superscript M and S denotes metallic and semiconducting, respectively. Around a K point, the energy gap approximately has a linear dependence on $k = |k|$ measured from K point. Within the small k approximation, we can derive the energy difference of the first pair of van Hove singularities in the 1-dimensional DOS for metallic and semiconducting nanotubes as shown in equation (22)

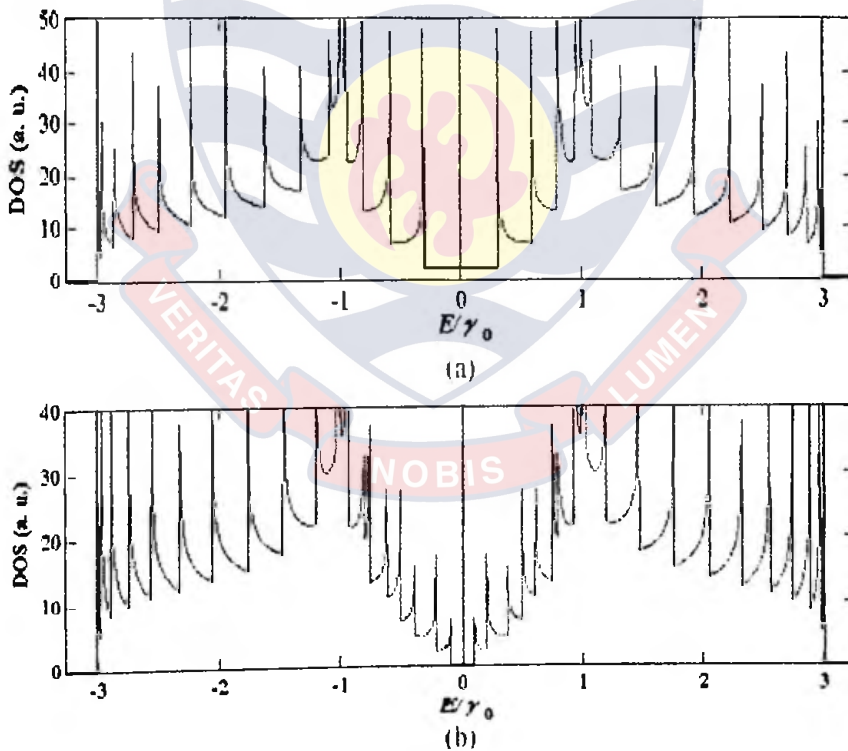


Figure 29: The density of states for (a) typical metallic nanotube (10, 10) (b) typical semiconducting nanotube (14, 7) [149]

Figure 29 shows the density of states for (a) typical metallic nanotube (10, 10) (b) typical semiconducting nanotube (14, 7). For the semiconducting nanotube, the gap between the first pair of van Hove singularities is half of that of the metallic nanotube, which has a similar diameter. For the semiconducting tube the DOS is zero at the Fermi level. For all nanotubes, vHs arise at each band edge due to the low dimensionality of the material [149].

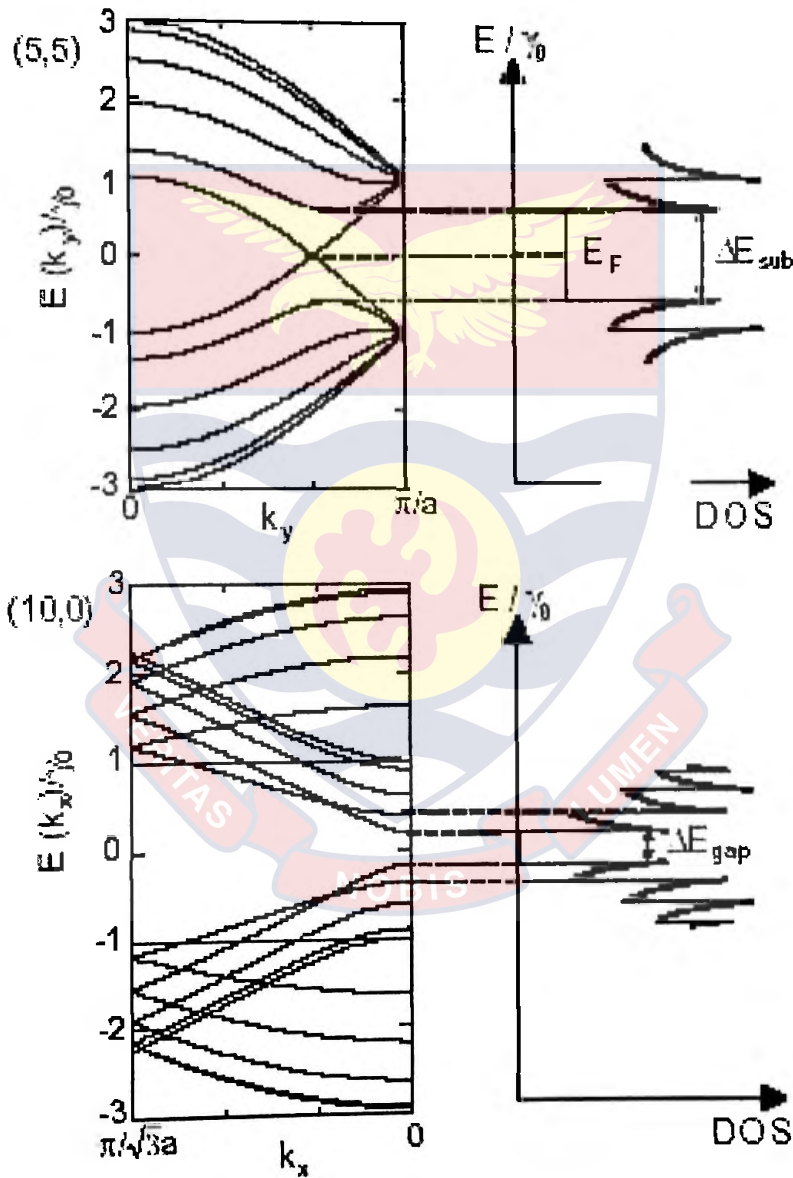


Figure 30: The energy band diagram (left) and density of states (right) for a metallic (top) and a semiconducting (bottom) nanotube [23]

The k_x ; k_y of figure 30 (Left) shows two normalized energy dispersion diagrams plotted as E/γ_0 against k that follow from equations (18) and (19) for a (5, 5) and a (10, 0) nanotube and the density of states corresponding to metallic and semiconducting nanotubes respectively. This figure shows the energy band diagram (left) and density of states (right) for a metallic (top) and a semiconducting (bottom) nanotube. The energy dispersion diagrams are calculated with equations (18) and (19) for a (5,5) and (10,0) nanotube respectively. The energy is divided by the energy overlap integral γ_0 . In the density of states (DOS) diagrams, a series of sharp peaks appear which are the subband onsets. The energy differences between the first two singularities near the Fermi level are indicated for the metallic and the semiconducting case by ΔE_{sub} and ΔE_{gap} respectively.

The right figure of figure 34 schematically shows the density of states (DOS) that can be derived from the energy dispersion diagrams shown in the left figure. The linear crossing energy bands near the Fermi level yield a small constant DOS for the armchair nanotube. At energies away from the Fermi energy, the next subbands lead to van Hove singularities at the onset due to the one-dimensional nature of the subbands. The energy separation between the first singularities above and below the Fermi level is here defined as ΔE_{sub} . The DOS for a semiconducting nanotube also consists of a series of sharp Van Hove singularities. In this case however, there is an energy gap ΔE_{gap} . For chiral nanotubes, the unit cell $T \times C_h$ is typically an order of magnitude larger than for achiral nanotubes. It has been argued that a large number of subbands and therefore also many singularities in the DOS may be expected [150]. However, it has been found that near the Fermi level a universal DOS exists

that scales with diameter and depends, to first order, only on the metallic or semiconducting character of a nanotube [136-138]. The DOS for a chiral nanotube with the same diameter is therefore similar to that of a zigzag or an armchair nanotube.

Figure 31 shows: approximately one-dimensional energy dispersion relations and corresponding density of states for (a) metallic carbon nanotubes and (b) semiconducting carbon nanotubes respectively. The number of subbands depends on the chiral vector. The energy at the Fermi level is zero.

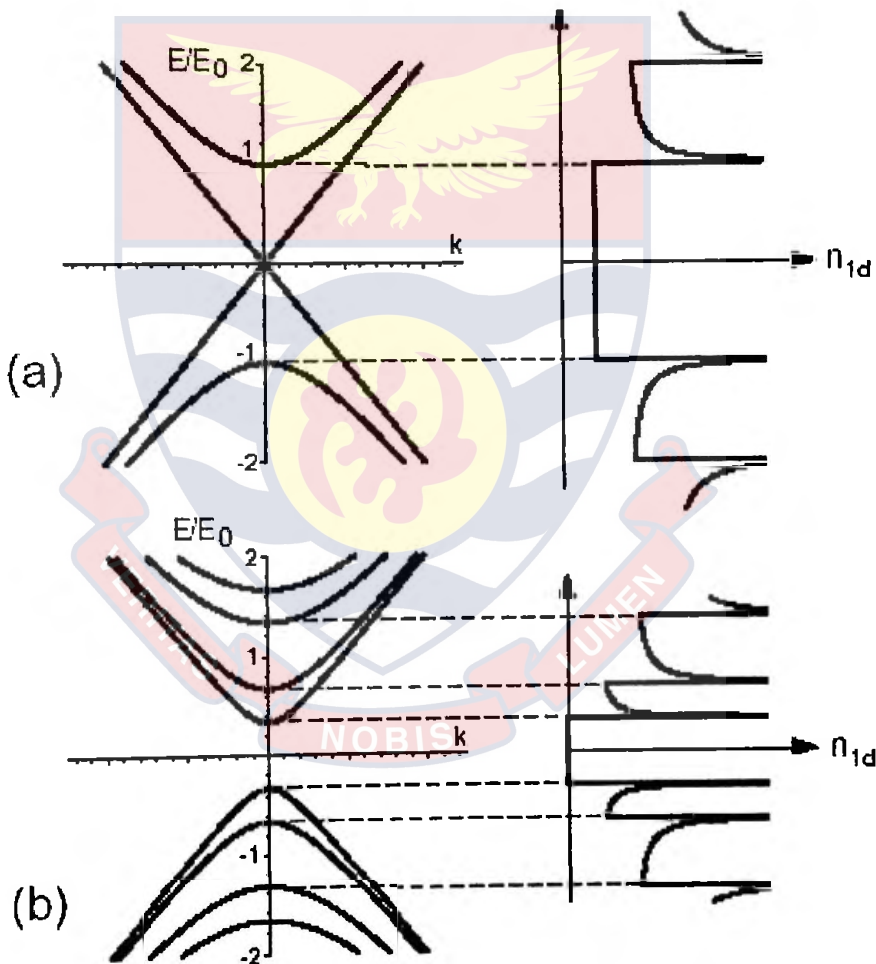


Figure 31: Approximate one-dimensional energy dispersion of carbon nanotubes (left) and corresponding density-of-states (right) [23]

(a) (5,5) Armchair Tube Metal

(b) (5,0) Zigzag Tube Semiconductor

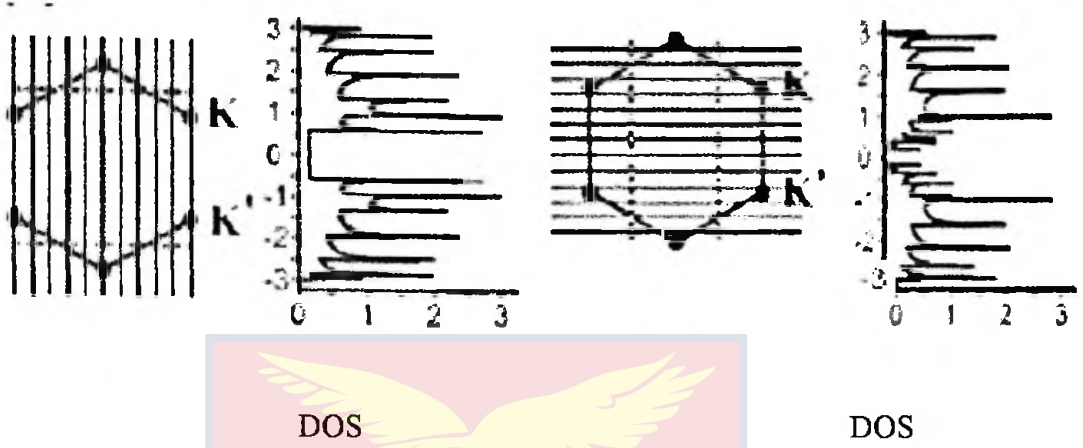


Figure 32: (a) (5,5) Armchair metallic and (b) (5,0) Zigzag semiconducting nanotube, along with their associated density of states (DOS) [23]

There are two kinds of nanotubes: metallic and semiconducting one. A tube is metallic, if $2n+m$ is a multiple of three.

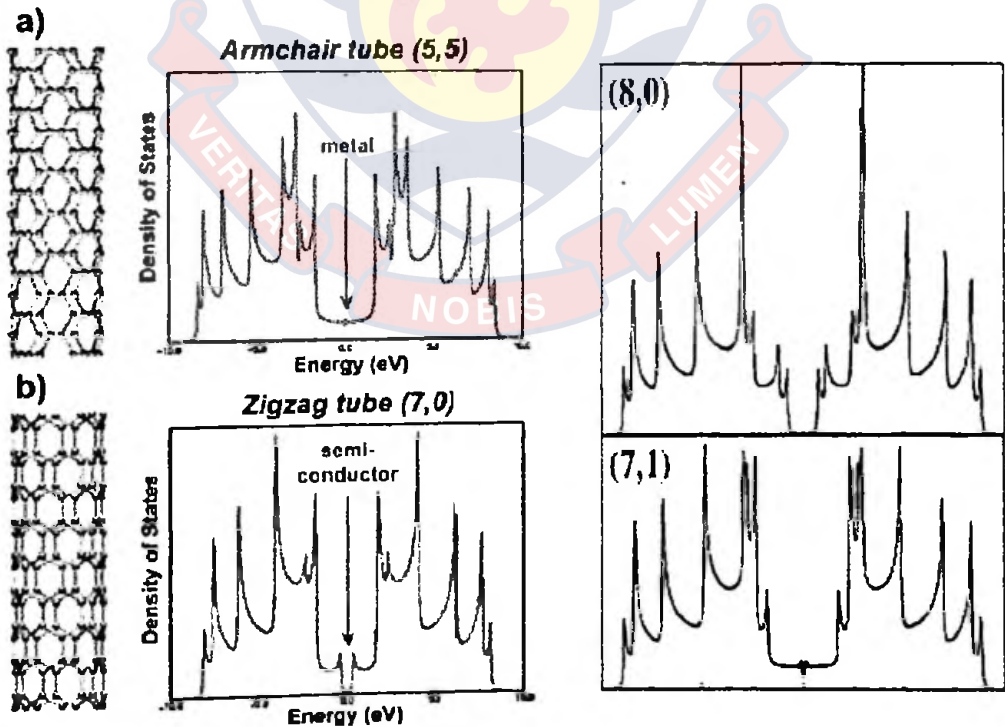
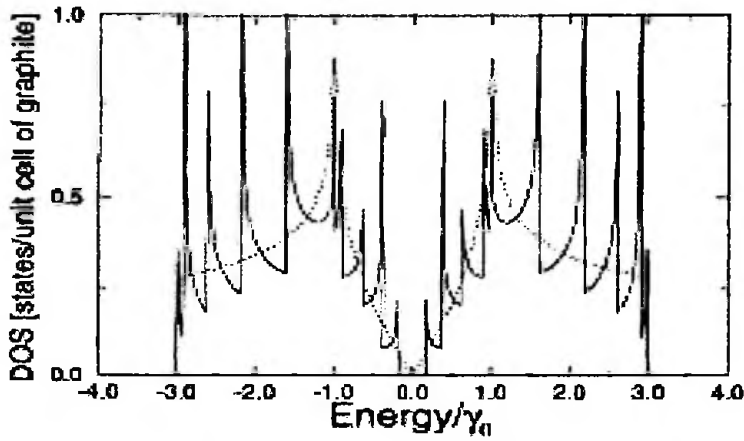


Figure 33: The DOS for metallic and semiconducting nanotubes using the tight binding k-space approach [23]

Density of states (DOS) exhibiting the valence (negative values), the
© University of Cape Coast <https://ir.ucc.edu.gh/xmlui>

conduction band (positive values) and the Fermi energy (centred at 0eV) for (a) a metallic armchair (5,5) tube, which shows electronic states at the Fermi energy (characteristic of a metal); (b) a zigzag tube (7,0) revealing semiconducting behaviour caused by the energy gap located between the valence and conduction band (characteristic of semiconductors) are shown in figure 33. The (8,0) zigzag tube is a large-gap semiconductor, the (7,1) chiral tube has a tiny gap and will behave as a metal at room temperature. The spikes shown in the DOS of the tubules are called Van Hove singularities and are the result of the one dimensional quantum conduction, which is not present in an infinite graphite crystal. We see that the density of states near the Fermi level E_F (located at $E = 0$) is different for metallic and semiconducting nanotubes. The density of states at E_F has a value of zero for semiconducting nanotubes, but is non-zero (and small) for metallic nanotubes. The condition for a (n,m) carbon nanotube to be metallic is that $m - n$ be a multiple of three [133]. An equivalent condition is that $2n + m$ be a multiple of three [135]. Thus, a carbon nanotube can be either metallic or semiconducting, depending on its diameter and its chiral angle. Also of great interest are the singularities in the 1D density of states, corresponding to extrema in the $E(k)$ relations.



(b) $(n,m)=(9,0)$

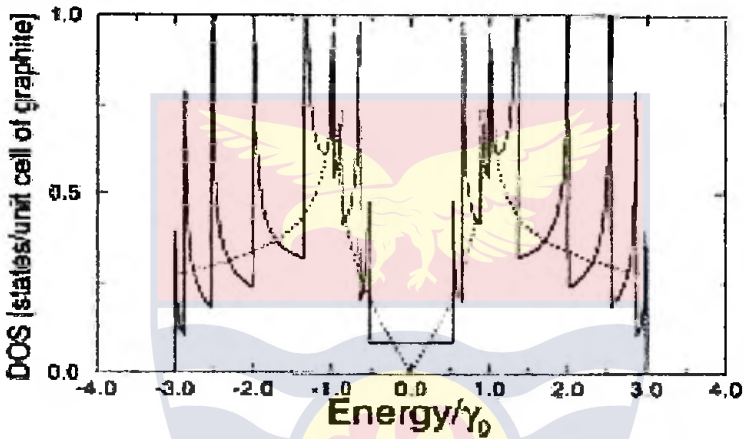


Figure 34: Electronic 1D density of states per unit cell of a 2D graphene sheet for two $(n,0)$ zigzag nanotubes [150]

Figure 34 shows electronic 1D density of states per unit cell of a 2D graphene sheet for two $(n,0)$ zigzag nanotubes. The $(10,0)$ nanotube which has semiconducting behaviour is shown in figure 34 (a) and the $(9,0)$ nanotube which has metallic behaviour is shown in figure 34(b). Also shown in the figure is the density of states for a 2D graphene sheet (dotted curve) [133]. Due to the large length-to-diameter ratio for the nanotubes, the electron motion is normally confined to the tube axis, and therefore, for small diameter nanotubes, the one-dimensional (1D) density of electronic states exhibits sharp singularities below and above the Fermi level E_F as shown in figure 34.

Benefits of Carbon Nanotubes

© University of Cape Coast <https://ir.ucc.edu.gh/xmlui>

Now the review of fundamentals of carbon nanotube ends after considering some benefits of carbon nanotubes. These quasi-one dimensional allotrope of carbon are subject of many theoretical [135, 151-155] and experimental [126,156-163] studies. Carbon based nanostructure materials exhibit unique mechanical, electrical, and optical characteristics [164]. It is a material with extraordinary properties and with a wide variety of possible applications [23, 70, 165]. A few applications of carbon nanotubes (CNTs) range from quantum wire interconnects [166] , diodes and transistors for computing [167] , to high power electrochemical capacitors [168] , data storage devices[169], field emitters for flat panel displays [170 ,171] and terahertz oscillators[172] .

Quantum Wire Interconnects

Robertson J., et al., [173] defined interconnects as the metal wires which pass current between the transistors and are oriented both vertically and horizontally as shown in figure 35.

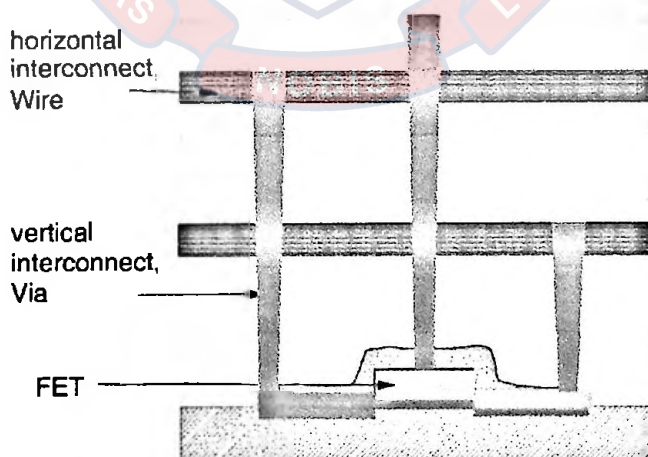


Figure 35: Schematic of vertical and horizontal interconnects in an integrated circuit [173]

According to Naeemi A. et al., [174], as the conventional copper interconnect feature sizes shrink, the surface roughness [175] as well as its resistivity increases due to surface and grain boundary scatterings. Furthermore, wires especially power and ground lines are becoming more and more vulnerable to electromigration because of rapid increases in current densities [176]. In contrast, carbon nanotubes exhibit ballistic flow of electrons with electron mean free paths of several microns and are capable of conducting very large current densities [177]. Carbon nanotubes are therefore proposed as potential candidates for power and signal interconnection [178,179]. In a journal article by Noemi A. et al., [174], the performances of copper wires and nanotube interconnects are compared. The results offer important guidance regarding the nature of carbon nanotube technology development needed for improving interconnect performance.

Robertson J. et al., [173] state reasons why carbon nanotube technology development is needed for improving interconnect performance as follows. There is a need at the 22 nm node and beyond to consider replacing Copper as the interconnect. First, the current density carried by the interconnects will exceed the maximum current density of 6.0×10^6 A/cm² that copper can carry before it could fail due to electromigration [173] as shown in figure 36.

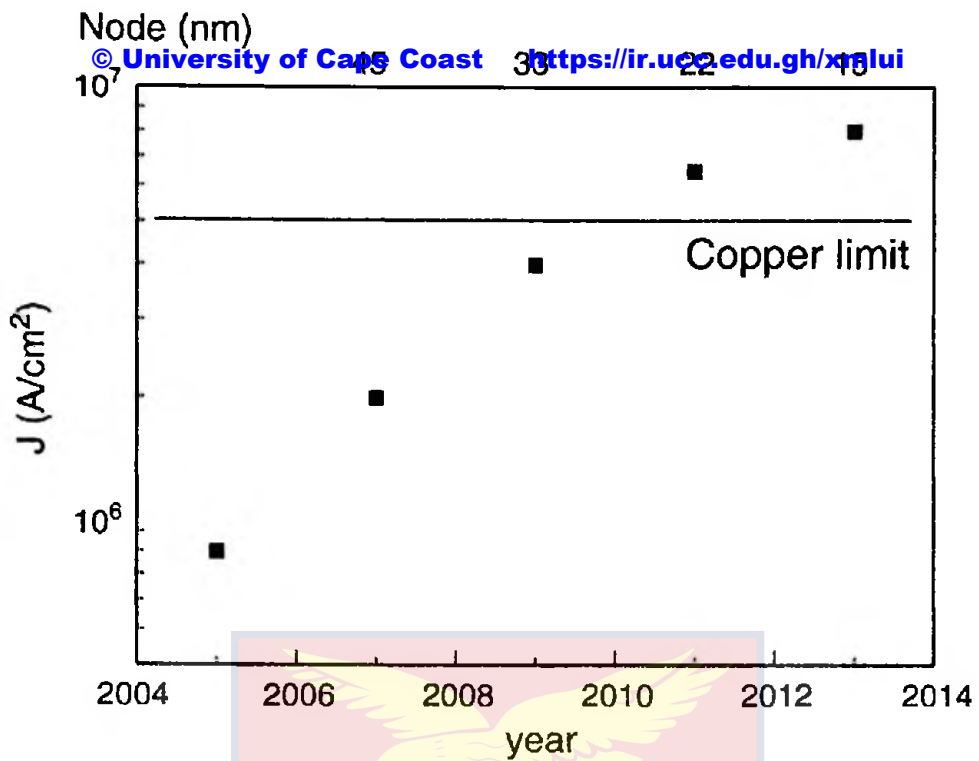


Figure 36: Current density as a function of year and technology node in the ITRS roadmap [173]

Carbon nanotubes (CNTs) are the only material (except graphene) which can carry a much higher current density up to $\sim 10^9$ A/cm² before failure [180,181]. The second reason is time delays in the integrated circuit. As dimensions have shrunk, the time delay is no longer dominated by the switching time constant of the transistor but to the RC time constant of the interconnect, due to the interconnect resistance R and its capacitance to the surroundings C as in figure 37.

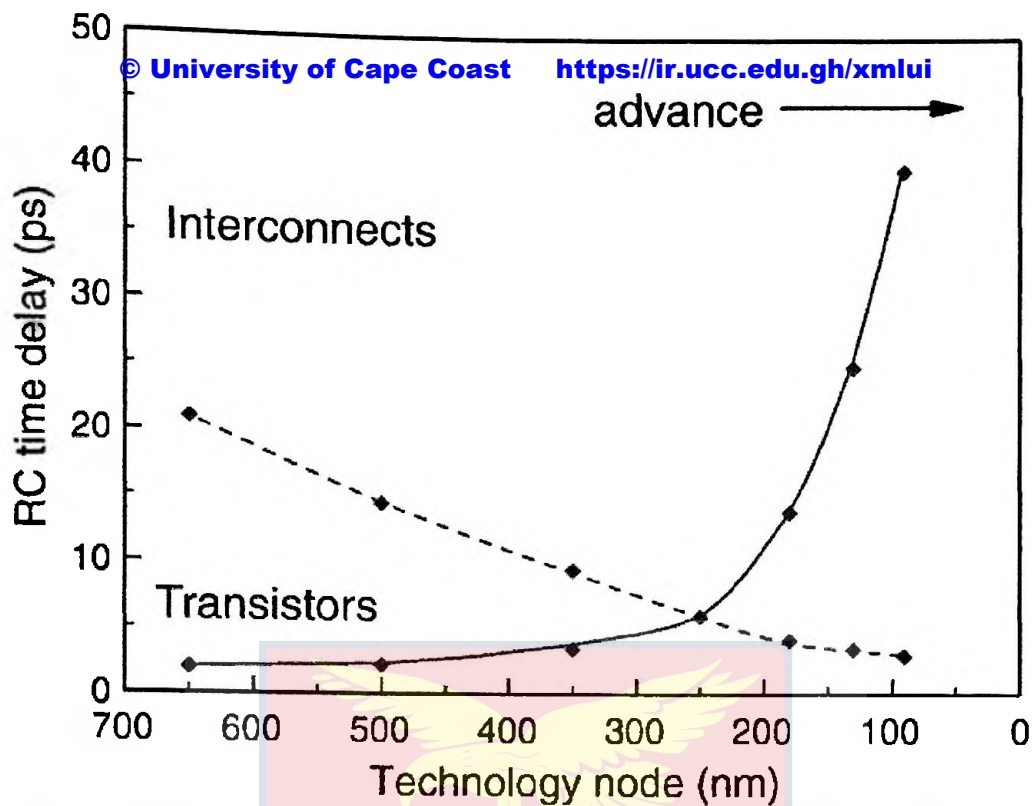


Figure 37: Time delays in integrated circuits as a function of technology node [173]

Long nanotubes can have lower resistances, which cuts down the RC time constant for long interconnects [173]. A third reason for possibly using nanotubes is the aspect ratio. It is difficult to make copper interconnects which have a large aspect ratio for putting into deep vertical holes [173]. Here, the interconnect (or Via) is not limited by its current density or resistance, just by its manufacturability. Despite these three advantages of carbon nanotubes, their use as interconnects is not trivial, because of quantum effects [173].

The resistance of a nanotube-based interconnect must be comparable or lower than that of the copper equivalent. Now, the resistivity of a copper wire increases as its diameter gets smaller, because of side-wall scattering, as shown in figure 38.

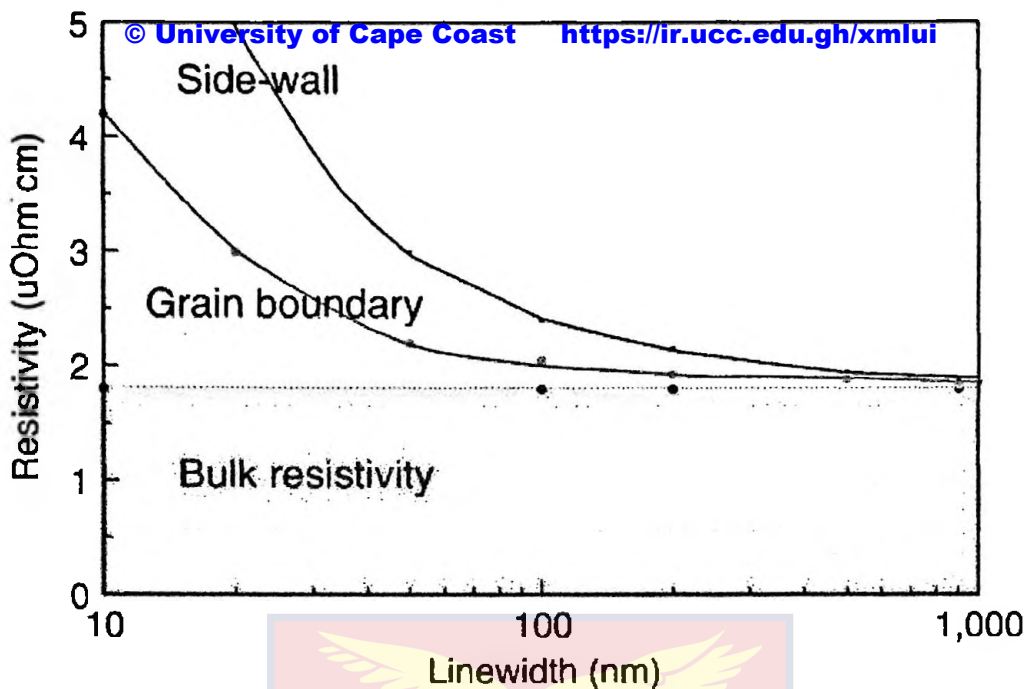


Figure 38: Copper resistivity vs. interconnects line-width [173]

This is equivalent to the copper wire becoming more like a one-dimensional conductor, bulk scattering continues, but side-wall scattering increases as a proportion. The conductivity of a one-dimensional conductor like a carbon nanotube is limited by one quantum of conductance G_0 /conducting channel. For nanotubes, there are two conducting channels/wall of the nanotube [173]. The factor two arises because in the band structure of any metallic nanotube wall, there are two bands that cross the Fermi level. The quantum of conductance appears as a series resistance in the overall equivalent circuit. Nanotubes are well known for having a ballistic conductance, which enhances their conductance at moderate lengths, but the quantum conductance limits their resistance at short lengths. Thus, the overall resistance of a nanotube interconnect is given by [173]

$$R = (R_q + rL)/2n \quad (23)$$

where R_q is the quantum of conductance, $R_q = 12.6k\Omega/\text{channel}$, r is the incremental resistivity/unit length of the nanotube, L is its length, and n is the number of walls in the interconnect. Clearly, in order to minimize the resistance of the interconnect and make it less than the Cu equivalent, the objective is to maximize the number of walls in the interconnect space.

There are two possibilities for nanotube interconnects to maximize n , use one or more multi-walled nanotubes (MWCNTs) or use a very high density of single walled nanotubes (SWCNTs). MWCNTs are always metallic because they always have one wall which is metallic. However, the problem with MWCNTs is that only the outer wall tends to carry current, unless the inner walls are properly contacted, and current is forced down them. On the other hand, SWCNTs can be either semiconducting or metallic, and it is essential that the fraction of metallic SWCNTs is maximized.

Also the applicability of carbon nanotube bundles as interconnects of the future has been analyzed by Naeemi A. et al., [174] while taking into account the practical limitations of this emerging technology. The performance of CNT-bundle interconnects has been compared to that of copper interconnects of future technology generations and their applicability at different metal tiers in a VLSI design is studied [174]. At the local interconnect level, CNT-bundles with imperfect contacts do not give much performance improvement. It is also shown that there exists an optimal density less than the maximum packing density of CNT bundles at which the interconnect propagation delay is minimum [174]. This is a useful finding in light of the fact that CNT-bundles fabricated till date do not have a very high density [177] and all the CNTs in a bundle may not have metallic nature.

Although this fact can be advantageous to the use of CNTs as interconnects, with technology scaling, it becomes imperative to also reduce the additional resistance associated with imperfect metal-nanotube contacts. In the case of long intermediate and global interconnects, densely packed CNT bundle interconnects show significant improvement in performance as compared to copper interconnects, in spite of imperfect metal-nanotube contacts [174, 182].

Diodes and Transistors

Diodes

Liu Chang-Hua et al., [183], demonstrate a fully tunable diode structure utilizing a fully suspended single-walled carbon nanotube (SWCNT) which incorporates several types of junction diodes within single device architecture by simply controlling gate voltages. Figure 39 illustrates the schematic of our fully suspended SWCNT p-n diode device.

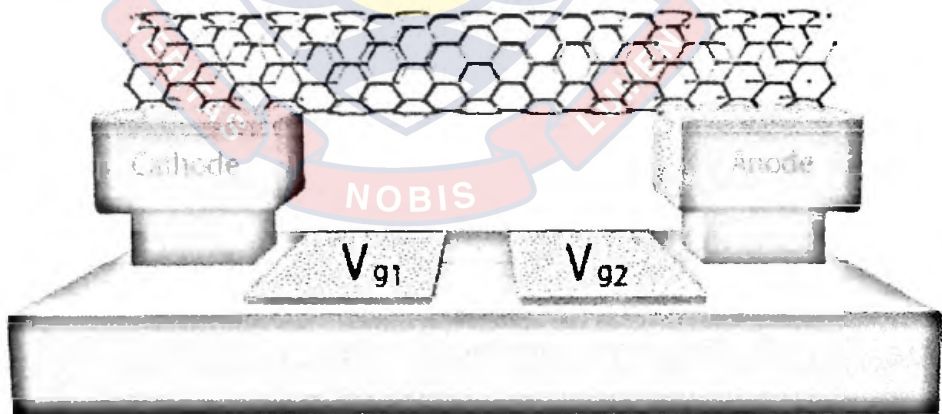


Figure 39: The schematic of our fully suspended SWCNT p-n diode device [183]

The device substrate is with pre-patterned cathode, anode, and two bottom split gate electrodes V_{g1} and V_{g2} . The electrostatic doping of the nanotube is achieved by controlling the two bottom split gate voltages, V_{g1} and V_{g2} . The diode's turn-on voltage under forward bias can be continuously tuned up to 4.3 V by controlling gate voltages, which is ~ 6 times the nanotube bandgap energy. Furthermore, the same device design can be configured into a backward diode by tuning the band-to-band tunneling current with gate voltages. A nanotube backward diode is demonstrated for the first time with nonlinearity exceeding the ideal diode. These results suggest that a tunable nanotube diode can be a unique building block for developing next generation programmable nanoelectronic logic and integrated circuits [183].

Integrated nanoelectronics [184] of the coming generation can benefit from actively tunable device components, where a single device can be programmed to embody different device concepts to achieve high packing density, diverse functionality, and low power consumption. However, electronic characteristics of conventional devices are pre-determined by material properties such as bandgap energy, doping level, metal-semiconductor interfaces, etc, and active tuning of individual device remains extremely challenging. For instance, a conventional diode has fixed rectification characteristics; the intrinsic doping levels across the junction determine the built-in potential and the turn-on voltage of the diode. To active modulate junction properties, including doping concentrations and doping profile in bulk devices, are limited mainly by the strong screening effect and the increasing 3-dimensional density-of-states (DOS) with increasing energy. To this regard, recent works address these issues by chemical or electrochemical doping and demonstrate the concept of tunable electronics [185-187]. But these device

structures and fabrication methodologies are difficult to be integrated with existing CMOS platform.

SWCNTs are quasi one-dimensional structures with promising electrical and optical properties [70, 188-189]. Because the DOS decreases with increasing energy in one-dimension, doping concentration in carbon nanotube can be easily modulated through electrostatic gating [190, 191]. Ideal diode behaviour has been demonstrated on suspended SWCNTs with electrostatic p-n doping [192-194], and efficient light emission and photocurrent generation have also been shown in SWCNT diodes [195-197]. In addition, strong band-to-band tunneling across nanotube Schottky junction or p-n junction [198-200] has lead to SWCNT tunneling diodes exhibiting negative differential resistance with high peak to valley ratio [201]. However, all previous nanotube diode design can only exhibit one specific diode concept among diverse types of junction diodes [10].

Figure 40 (a) shows I - V characteristics of a representative SWCNT diode with split gate separation of $4\ \mu\text{m}$ under different gate bias conditions. Positive V_{g1} and negative V_{g2} electrostatically dope nanotube sections above the split gates into n and p type, respectively. The formation of the p-n junction leads to the rectified I - V curves which turn on at forward bias direction. Interestingly, when holding V_{g2} at a constant voltage of $-4\ \text{V}$ and increasing V_{g1} from 2 to $9\ \text{V}$, the rectified I - V curves shift gradually toward higher turn-on voltages while maintaining the same nonlinearity. The extracted turn-on voltages show linear dependence on the split gate voltage V_{g2} (figure 40 (b)), with maximum value exceeding $4.3\ \text{V}$, corresponding to ~ 6 times the bandgap voltage of the nanotube. We also studied the diode characteristics under constant V_{g1} of $4\ \text{V}$ and varying V_{g2} from -2 to $-9\ \text{V}$ (figure 41 (a)). As V_{g2} decreases to more negative voltages, the turn-on voltages drop from $2.6\ \text{V}$ to $0.5\ \text{V}$. The extracted turn-on voltages again show

linear dependence on the amplitude of split gate voltage, V_{g2} , but with a negative slope (Figure 41 (b) 5). Importantly, the observed gate-controlled tunability and the beyond-bandgap voltage rectification are not possible in conventional diodes [183].

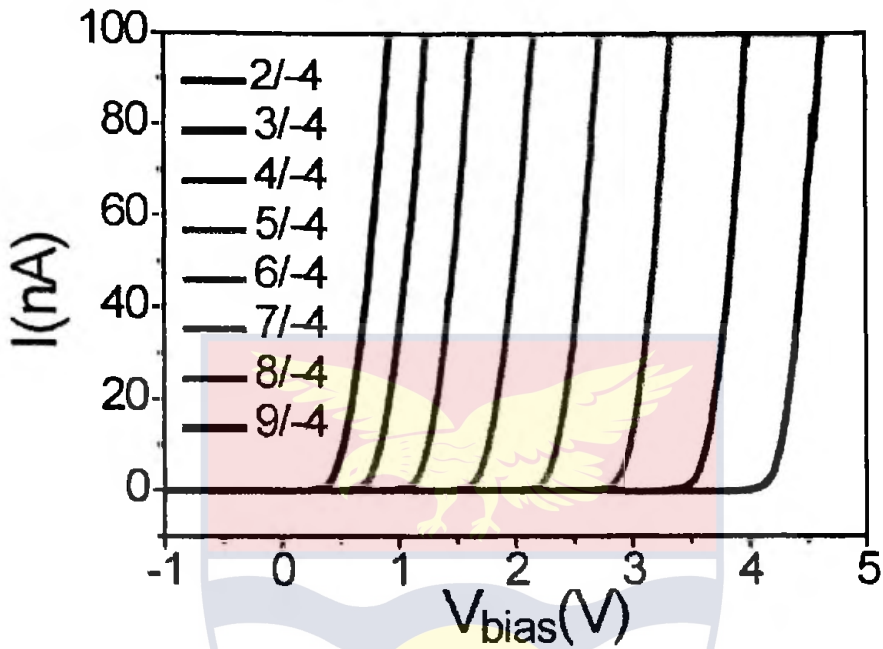


Figure 40: (a) 2 I-V characteristics of a representative SWCNT diode with split gate separation of 4 μm under different gate bias conditions [183]

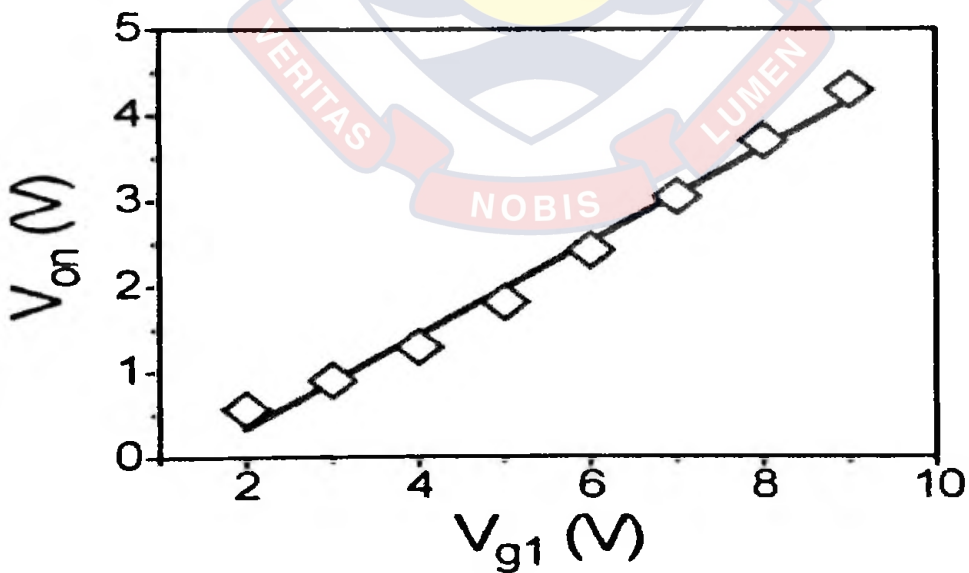


Figure 40: (b) The extracted turn-on voltages show linear dependence on the split gate voltage V_{g2} [183]

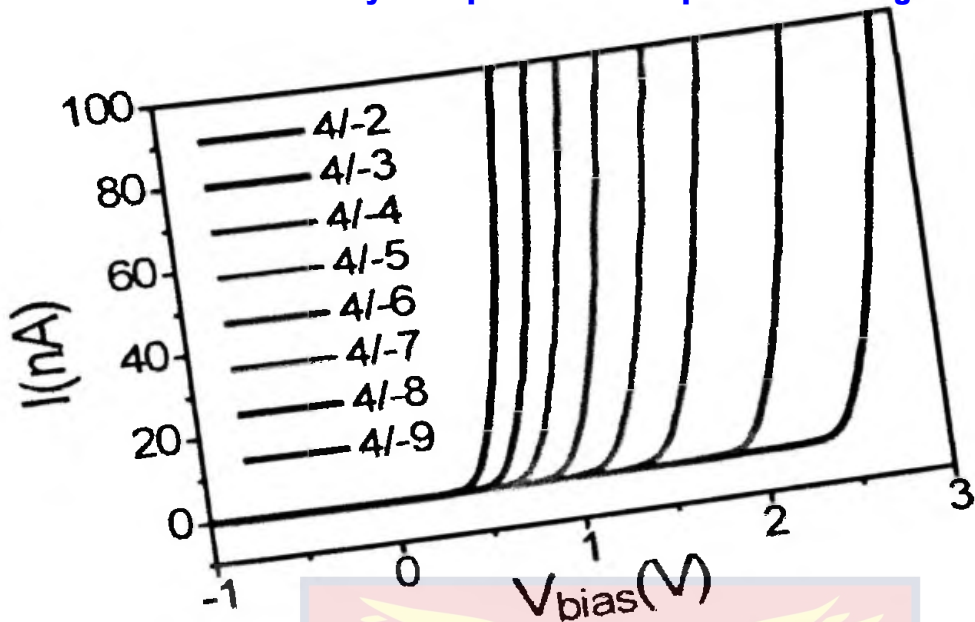


Figure 41: (a) The diode characteristics under constant V_{g1} of 4 V and varying V_{g2} from -2 to -9 V [183]

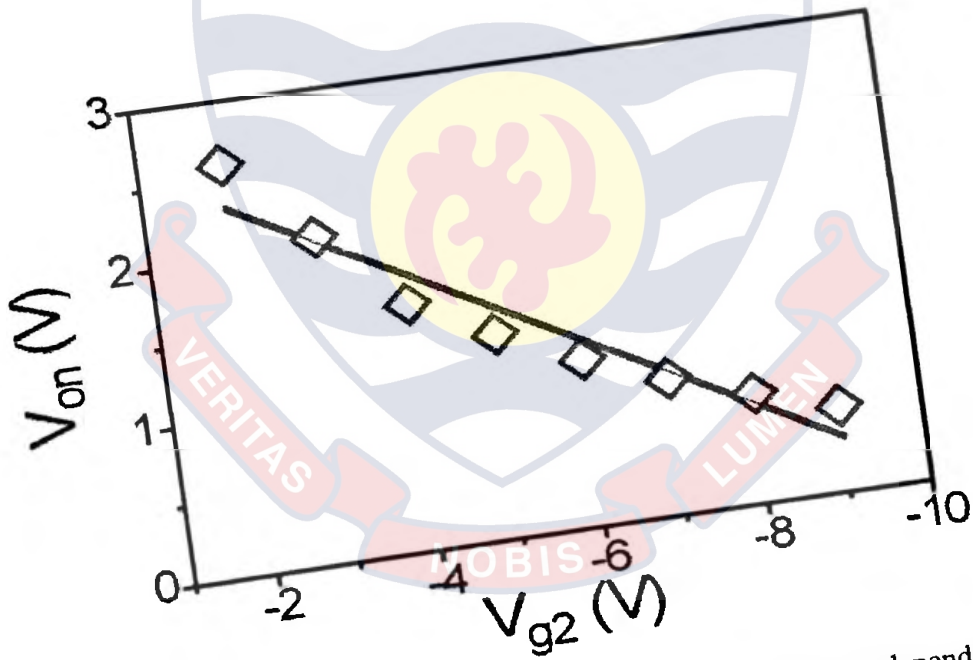


Figure 41: (b) The extracted turn-on voltages again show linear dependence on the amplitude of split gate voltage, $-V_{g2}$, but with a negative slope [183]

Carbon nanotubes are a new form of carbon with unique electrical and mechanical properties. Varying the diameter of the cylinder can control the band gap of semiconducting nanotubes. The width of the diameter of the carbon nanotube is inversely proportional to the size of the band gap [202]. Semiconducting nanotubes can be used to build molecular field-effect transistors (FETs) while metallic nanotubes can be used to build single-electron transistors [203].

According to Marani et al., [204], the aggressive scaling of Complementary metal oxide semiconductor (CMOS) led to higher and higher integration density in microcircuits, lower power consumption and increased performance. However, the scaling down will eventually reach its limit. As device sizes approach the nanoscale, new opportunities arise from harnessing the physical and chemical properties at the nanoscale. Carbon nanotubes (CNT) are considered as the most promising carbon nanostructures, and, in particular, the Carbon nanotube Field Effect Transistors (CNTFETs) are a new kind of molecular device, using a carbon nanotube as channel. Today CNTFETs are regarded as an important contending device to replace conventional metal oxide semiconductor field-effect transistors (MOSFETs) or silicon transistors [205]. Carbon nanotube field-effect transistors (CNFET) are similar to the MOSFETs of today. They require three terminals, source, drain, and gate. The gate is used to control the current across the source and drain terminal. Current is able to flow across the source and drain through a channel when the gate is on.

The main difference between CNTFETs and MOSFETs is that CNTFETs use one dimensional (1D) CNTs as the channel, while MOSFET's channel is made from heavily doped silicon.

Figure 42(a) shows the layout of the Carbon nanotube Field-Effect Transistors (CNTFET) and figure 42 (b) displays its I-V characteristics.

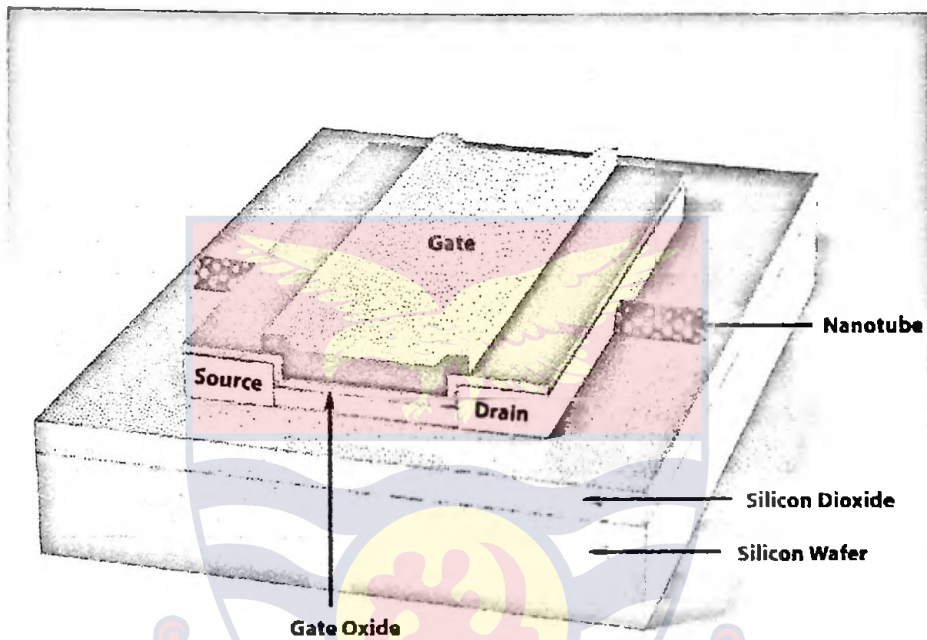


Figure 42: (a) Carbon nanotube Field-Effect Transistors (CNTFET) [206]

The SWCNT transistors consist of a semiconducting carbon nanotube about 1 nm in diameter bridging two closely separated metal electrodes on top a silicon surface coated with SiO_2 [207]. Applying an electric field to the silicon via the gate electrode turns on and off the flow of the current across the nanotube by controlling the movement of charge carriers onto it. SWCNT or MWCNT bridging two electrodes deposited on a 140 nm thick gate oxide films on a doped

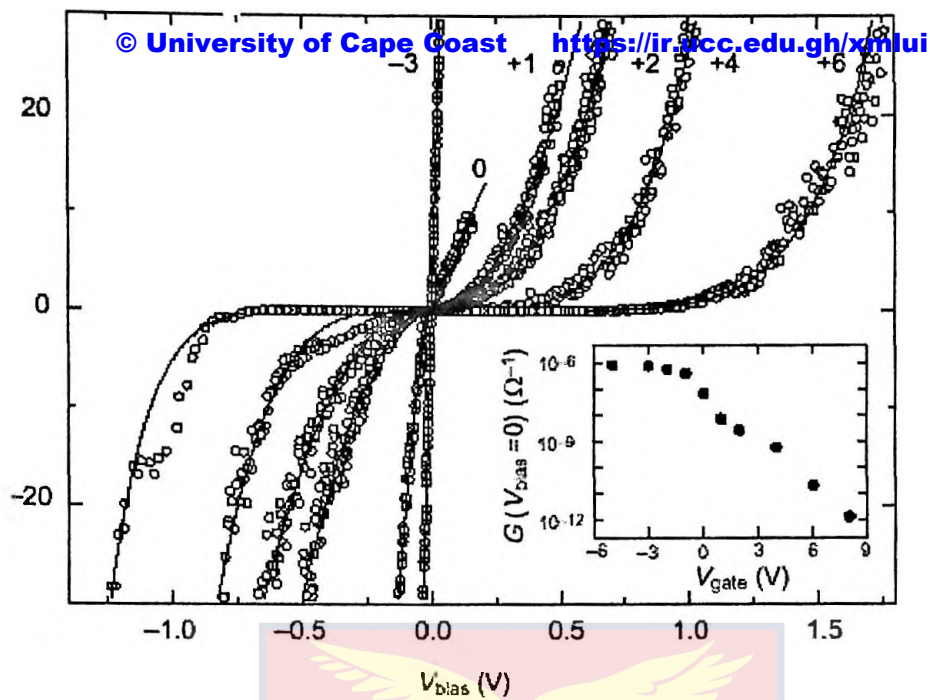


Figure 42: (b) I-V characteristics for Carbon nanotube transistor [203]

Figure 42 (b) shows the schematic of the CNT device. The field effect transistor consists of either an individual SI wafer. The Au electrodes were generated through electron beam lithography.

The behaviour of the CNT transistors is similar to that of a p-channel MOSFET. The I-V characteristics of the CNTs were measured at room temperature. Figure 42 (b) shows the I-VSD of a device consisting of a SWCNT with a diameter of 1.6 nm. The source-drain current decreases strongly with increasing gate voltage indicates that the CNT device operates as a field effect transistor and also that the transport through semiconducting SWCNT is dominated by positive carriers [203]. The source of these carriers is possibly from the carrier concentration inherent to the CNT or these carriers can be the majority carriers that were injected at the gold-nanotube contacts.

next generation of field effect transistors, which maintain the operating principles of the conventional semiconductor transistors currently used [204] because of the following differences : One of the difference is that carbon nanotube is one-dimensional which greatly reduces the scattering probability [208]. As a result, the devices may operate in the ballistic regime. Another difference is that the nanotube conducts essentially on the surface where the chemical bonds are saturated and stable [208]. The stable bond indicates that there is no need for careful passivation of the interface between the nanotube channel and the gate dielectric. The MOSFET devices do not have such an interface between the silicon/silicon dioxide interfaces. A third difference is that the Schottky barrier at the metal-nanotube contact is the active switching element in an intrinsic nanotube device [202]. The switching behaviour involves mostly the contacts as oppose to the bulk of the nanotube.

Recent research at IBM produced the highest nanotubes transistors that can output perform leading MOSFETs [208]. Through experiments with different device structures, the researchers achieve the highest transconductance, the measure of current carrying capability, of any carbon transistor to date [208]. This high transconductance implies that the transistors can operate faster. The IBM group also has produced large arrays of carbon nanotubes bypassing the need to meticulously separate metallic and semiconducting nanotubes.

Logic circuits have been realized through the production of both n-type and p-type CNTFETs. The n-type CNTFETs were generated by doping the p-type FETs with potassium. The modification at the contacts introduces an

increase of the barrier height for hole injection, leading to an n-type CNTFET.

There is an intermediate stage in which the Fermi level is around mid-gap. This intermediate stage leads to ambipolar behaviour of the CNTFET in which conduction of both holes and electrons are possible, thus making it both n-type and p-type [202]. Complementary CNTFETs are placed in circuit to operate simple logic functions. This kind of nanotube-based circuit is the analogue to the conventional CMOS based logic gates and has the same advantages. A simple example of this complementary CNTFET is the bonding of two ambipolar CNTFETs. An offset voltage between the isolated transistor back-gates allows adjustment of the threshold of the p- and n- CNTFET characteristic so that the inversion function is optimal [202].

High power electrochemical capacitors

According to Du et al., [209], of all the challenges facing human beings in the near future, energy related issues are likely to be the grandest. To achieve a more sustainable society with adequate renewable energy and less environmental pollution, more versatile, robust and efficient approaches in electric energy storage and conversion are needed. Electric energy storage devices (or electrochemical devices) may be broadly characterized by two parameters namely energy density (how long the device can last) and power density (how much of that energy can be delivered from the device over a certain period of time) [209]. Zhao et al., [210] stated that research efforts have mostly be focused on two types of electrochemical devices namely batteries and capacitors. Batteries suffer from low-power density although they have high-energy density, whereas conventional capacitors exhibit high power

but low-energy density [210]. Batteries have been the preferred electricity storage device because of their portability and relative high energy density for many applications requiring sustained power supply over a reasonable time period [209]. However, for other applications demanding a huge power surge or instantaneous power release like rocket launching, batteries become unsuitable due to their slow rate of energy release. Although new technologies such as the lithium-ion battery have been developed to improve the power performance (high-rate capability), they are still subject to the same intrinsic limits [209]. Supercapacitors, also called ultracapacitors or electrochemical capacitors, are thus emerging as the promising energy sources with exceptionally fast charge-discharge rates [209-211]. According to Halper et al., [211], supercapacitors are governed by the same fundamental equations as conventional capacitors, but utilize higher surface area electrodes and thinner dielectrics to achieve greater capacitances. This allows for energy densities greater than those of conventional capacitors and power densities greater than those of batteries.

Carbon nanotubes with their unique properties are a promising material for next generation supercapacitors [209]. Specifically, the use of nanotubes to construct supercapacitor electrodes can increase the power density and performance of supercapacitors relative to conventional dielectric capacitors [209, 211]. For supercapacitors, attaining a high power density is always the main goal. According to Du et al., [211], the maximum power density of a supercapacitor is given by $P_{max} = V_i^2/4R$ (where V_i is the initial voltage and R is the equivalent series resistance (ESR)) [211]. Thus, high power density requires low electrical resistance of the electrode itself and the contact

© University of Cape Coast <https://ir.ucc.edu.gh/xmlui>

resistance between the electrodes and current collectors. Clearly, there is a role for carbon nanotubes to play due to their remarkable specific surface area and electric conductivity. In addition, the unique structure of carbon nanotubes is another advantage over conventional carbon materials. As carbon nanotubes usually have an aspect ratio of more than 1000, they tend to entangle with each other to form a durable and porous nanotube skeleton. Such a porous structure formed by the open spaces between entangled nanotubes enables easy access of the electrolyte ions to the electrode/electrolyte interface, which is crucial for charging the electric double layer, thus exhibiting extremely small resistance of the electrode itself. Moreover, due to the durability of the nanotube skeleton, little or even no binder is needed, unlike conventional carbon materials [211].

The pioneering work of using carbon nanotubes for double layer supercapacitors was carried out by Niu, et al., [212], who developed supercapacitor electrodes with free-standing mats of MWCNTs. Unlike other types of carbon electrodes containing micropores including slit and dead end pores, the pores in the carbon nanotube electrode are spaces in the entangled nanotube network, and are thus all inter-connected. Such nanotube electrodes are essentially open structures, enabling almost all the surface area accessible to the electrolyte. In contrast, in an activated carbon electrode with a surface area of 1000 m²/g, only less than 1/3 of the surface area is available for the formation of an ionic double layer [212]. Consequently, a power density above 8 kW/kg was obtained using these nanotube electrodes. The encouraging electrochemical performance of carbon nanotube electrodes has led to extensive studies in this area. A systematic work was done by Frackowiak, et al., [213], to investigate the electrochemical characteristics and to correlate

© University of Cape Coast <https://ir.ucc.edu.gh/>
them with the microtexture and elemental composition of supercapacitors built from different type of MWCNTs and SWCNTs. It was found that, in addition to the presence of mesopores formed by the entanglement of carbon nanotubes, the central canals of the tubes also contribute to easy accessibility of the ions charging the electrical double layer.

In general, SWCNTs have been shown to have higher specific capacitance, due mainly to their large surface area. It has found, however, that MWCNTs could generate capacitance twice as high in comparison to SCWNTs under certain circumstance [209]. It has been suggested that the higher capacitance of MCWNTs in a study was attributed to the presence of mesopores due to the open central canal and the accessible network of entangled nanotubes, facilitating the transport of the ions from the solution to the charged interface [209].

High power density supercapacitors using carbon nanotube thin film electrodes are useful because of their high power density (at least about ten times larger than that of batteries) [209]. Several successful attempts to fabricate high power density supercapacitors have been reported. One group obtained a power density of 20 kW/kg in an electrolyte of 7.5 N KOH [214]. A polished nickel foil was used for lower contact resistance and a heat-treatment at high temperature was used to reduce the internal resistance of the SWCNT electrode. Direct growth of carbon nanotubes on metal current collectors is another way to reduce the contact resistance as realized by Yoon et al., [215], using hot filament plasma enhanced chemical vapor deposition (HFPECVD). A much higher discharge efficiency and good electrodynamic performance were obtained, resulting in higher power density.

The Pan group at University of California, Davis has developed two different approaches to lower the equivalent series resistance in fabricating carbon nanotube thin film electrodes [216]. One approach is to prepare thin films with coherent structures using highly concentrated colloidal suspension of carbon nanotubes, resulting in very high packing density and some local alignment.. This coherent and flexible film was a highly conductive nanotube network with drastically small electrode resistance. In addition, the nanotubes adhered directly to the current collector since no binder was added, thus the contact between them was very good and contact resistance was reduced as well.

Carbon nanotubes are likely to have several advantages over conventional carbon materials for supercapacitor electrodes. In particular, nanotube-based supercapacitors are likely to demonstrate better power performance over conventional devices [209, 211]. Multiwalled carbon nanotubes are now being manufactured in large quantities at reasonable prices, which open the possibility for cost-effective production of carbon nanotube-based supercapacitor electrodes. Yet, additional research and development is needed to bring nanotube-based supercapacitors to the market [209].

Data Storage Devices

The rapid expansion of portable consumer electronics has created a demand for new designs of data storage devices, which are devices for recording (storing) information (data), with improved performance characteristics. According to Bichoutskaia et al., [217], there are currently three commercially available families of memory namely dynamic random access memory (DRAM), static random access memory (SRAM), and Flash memory,

which requires no power to store data. Consumer products typically use combinations of these three memory families, each having its unique advantage. For example DRAM is cheap, SRAM is fast, and Flash is nonvolatile. In the semiconductor industry, increasing miniaturization is beginning to place strains on existing technologies for data storage and computer memory, which could soon reach fundamental physical limitations [217]. At the same time, rapid growth in mobile devices is creating a need to develop new memory technologies that can deliver low power operation and low standby battery drain. These trends have accelerated development efforts in universal memory products that integrate the best features of existing memory types into a single package and eliminate the growing technical challenges. A new universal memory chip should be cheap and compact, draw and dissipate little power, and switch in nanoseconds [217].

In an article by Bichoutskaia et al., [217], an insight is given into a new approach to storing memory bits that is based on carbon nanotubes (CNTs). It employs a simple electromechanical switching rule, according to which the device is held together by a balance of three major forces: electrostatic, elastostatic, and van der Waals. Technically elegant and innovative designs of CNT-based electromechanical data storage devices exploit CNTs as both molecular device elements and molecular wires for the read-write scheme. This is an emerging area in the universal memory market, in which only the fabrication of the first integrated working prototypes and single demonstrations of electromechanical devices for storing, reading, and writing information has been achieved so far [218-224]. However, CNTs hold great promise for future bottom-up approaches to the manufacture of electromechanical memory

devices, as the exceptional properties and well-characterized structures of CNTs allow for very high density memories and strong resilience of devices to fatigue and breakage [217]. The three of types electromechanical data storage devices based on carbon nanotubes are as follows: data storage based on cantilever carbon nanotubes, data storage based on suspended carbon nanotubes and data storage based on telescoping carbon nanotubes

Data storage based on cantilever carbon nanotubes

A three-terminal memory cell based on cantilever CNTs [225] is shown in figure 43. A conducting movable component, which could be a single- or multiwalled CNT, is connected to a source electrode and suspended above a stepped Si substrate containing drain and gate electrodes. In a nonconducting state '0' (figure 43 (a)), the nanotube is not in contact with the drain electrode.

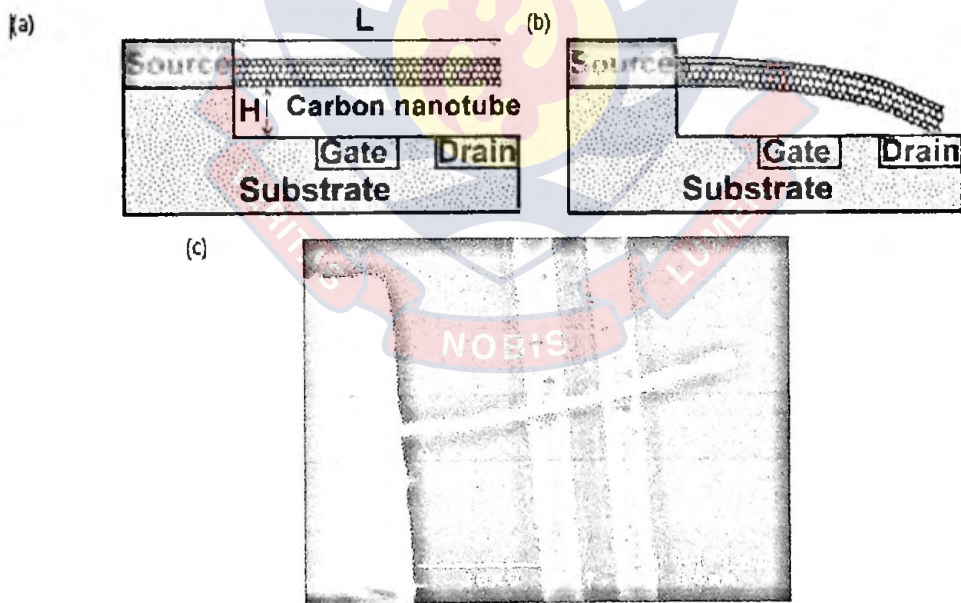


Figure 43: A three-terminal memory cell based on cantilever carbon nanotubes: (a) nonconducting state '0', (b) conducting state '1', and (c) scanning electron microscope (SEM) image. [217, 218]

When a voltage is applied between the source and the gate electrodes, charge is induced in the cantilever nanotube and it is deflected towards the substrate. At a certain, so-called 'pull in voltage', the nanotube comes into electric contact with the drain electrode. The device is now in a conducting state '1' (figure 43 (b)). If the device remains stable in state '1' after the voltage is turned off, it can be used as a nonvolatile memory cell. In such a nonvolatile device, an additional 'pull-out voltage' pulse is required to return it back to the '0' state. The voltage applied to the drain electrode is typically small, < 1 V, and does not affect the value of the pull-in voltage. It is used to control the current between the source and the drain electrodes.

The first prototypes of a three-terminal cantilever memory cell have been fabricated using Au electrodes and multiwalled CNTs [218] . In this device (figure 43(c)), multiple switching cycles have been achieved with the gate voltage ranging between 6 V and 20 V. The source–gate voltage– current characteristics have been measured in air at room temperature, demonstrating the suitability of CNTs for the development of data storage devices.

The operational characteristics of cantilever memory cells have been studied using continuum models based on linear and nonlinear beam theories, molecular dynamics, and combined molecular dynamics/continuum approaches [225-229]. It has been shown that van der Waals forces have a substantial effect on the performance of cantilever memory cells and introduce some design constraints [225, 227]. Devices with small diameter nanotubes have stiction and adhesion problems, i.e. a CNT, when in contact with the metal electrode, adheres to the surface with a high binding energy compared with the

nanotube's elastic energy. The effects are more profound for longer nanotubes
© University of Cape Coast <https://ir.ucc.edu.gh/xmlui>
positioned closer to the substrate [226]

Numerical simulations [227] reveal a significant difference in the write time for the '1→0' transition (0.02 ns) and the '0→1' transition (0.8 ns). In the '0→1' transition, although the nanotube bends quickly towards the drain electrode, it tends to bounce off the surface many times before coming to rest in position '1'. When the nanotube bounces, dissipative surface processes arising from phonon excitation in the drain electrode reduce the '0→1' transition time by two orders of magnitude [10].

Three-terminal memory cells have also been fabricated using vertically aligned multiwalled CNTs grown in a controlled manner from the pre-patterned catalyst dots on the device electrodes [220, 221] (figure 44).

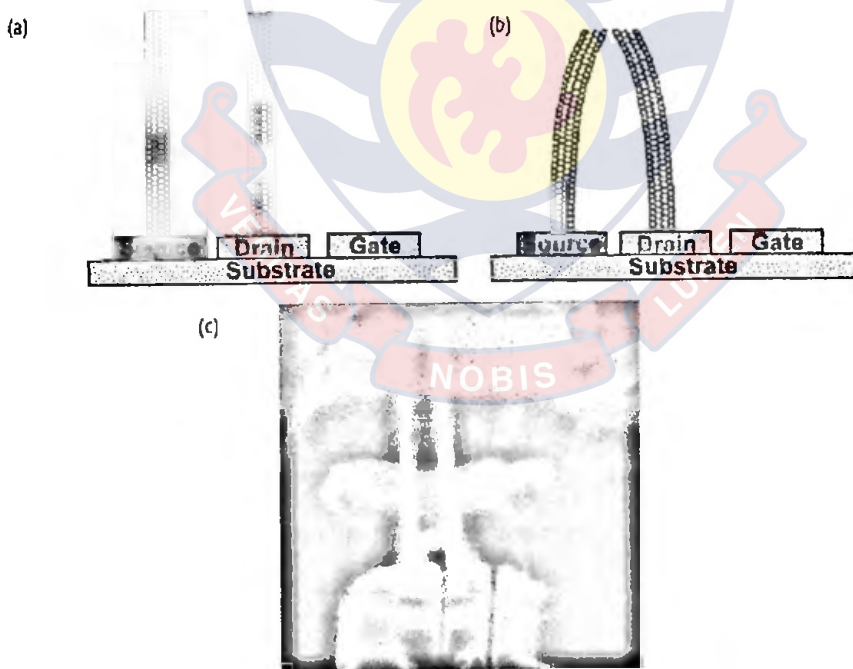


Figure 44: A three-terminal memory cell based on vertically aligned multiwalled carbon nanotubes: (a) nonconducting state '0', (b) conducting state '1', and (c) SEM image [217, 221]

technology, but also allows a dramatic increase in integration densities compared with conventional memory devices. In the design [221], the source electrode is electrically connected to earth ground. When the drain and gate electrodes are connected to a positive voltage supply, positive electrostatic charges build up in these electrodes, and negative charges build up in the source electrode. This leads to electrostatic repulsion, pushing the CNT at the drain electrode away from the gate electrode and towards the CNT at the source electrode. When the pull-in voltage is applied, the source and drain electrodes make electrical contact, establishing the state '1' of the device (figure 44 (b)).

It has been shown that once the voltage applied to the gate electrode is turned off, the source and drain electrodes can either remain held together in state '1' (typically for long nanotubes of $\sim 2 \mu\text{m}$ in length, for which the attractive van der Waals force is larger than the restoring elastostatic force), or alternatively return to the state '0' shown in figure 44 (a) (typically for shorter nanotubes of $1.4 \mu\text{m}$ in length and less). This allows the fabrication of two different types of memory device with either volatile or nonvolatile behaviour. Recently, the performance of memory cells with vertically aligned CNTs has been significantly improved by making a CNT-insulator-metal (CIM) capacitor on the source [230]. A CNT grown from the source electrode is coated with a dielectric layer of SiN_x and a metal layer of Cr to form a CIM structure similar to the capacitors used in conventional high-density DRAM [231] . The CNT grown on the drain electrode is the mechanical element of the cell that, under electrostatic forces, bends and makes contact with the CIM

capacitor. The CNT always snaps back after making contact and charging the outer electrode of the CIM capacitor in a write or read operation. A logic '1' ('0') is flagged by charge (no charge) on the outer electrode of the capacitor, not by the physical contact. Replacing the SiN_x layer with high dielectric constant materials, such as Ta₂O₅ or SrTiO₃ would increase the capacitance and bias of the device to the level needed for gigabit-level applications (~10–15 fF and ~60–80 mV, respectively) [231].

Data storage based on suspended carbon nanotubes

A new form of electromechanical memory based on suspended CNTs has been developed and manufactured by the start-up company Nantero, Inc. It is a high-density, nanotube-based nonvolatile random access memory (NRAM™) [219,232]. In NRAM, a CNT bundle is suspended across a gap and connected to the source and drain electrodes. A metal gate electrode is positioned at the bottom of the gap underneath the suspended CNTs, so that charge can be induced in the CNTs by applying a voltage to the gate electrode. The applied voltage causes the nanotubes to flex and come into van der Waals contact with the gate electrode. This switches the device into the state '1' (figure 45 (b)). The van der Waals forces make NRAM a nonvolatile device, as they hold the CNTs in the bent position until the pull-out voltage is applied to turn the device back to the '0' state (figure 45 (a)).

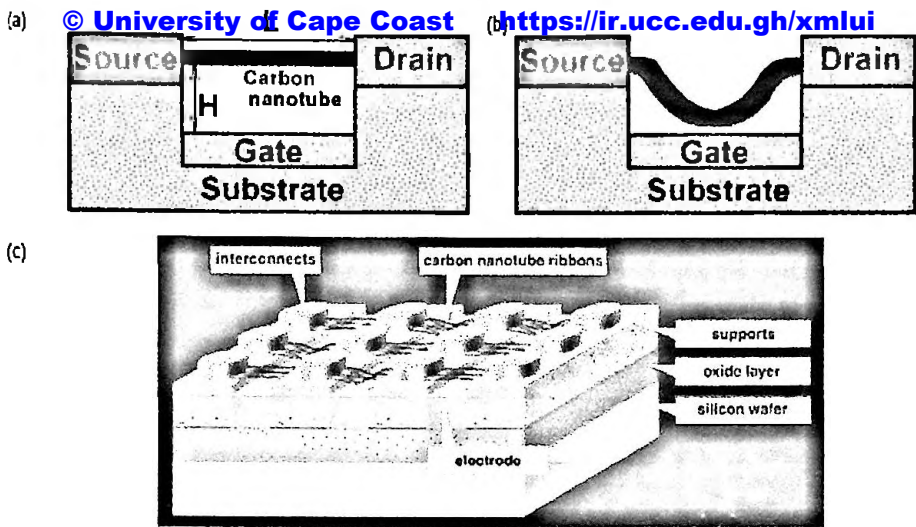


Figure 45: A three-terminal memory cell based on suspended carbon nanotubes: (a) nonconducting state ‘0’, (b) conducting state ‘1’, and (c) Nantero’s NRAM™ [217]

For nonvolatile conditions, the linear dimensions of the device are carefully chosen so that the ratio of the length of the suspended nanotubes over the depth of the gap is kept equal to ten [232].

The operational characteristics of NRAM have been modeled using molecular dynamics [218, 226], continuum models [218,233][1,16], as well as other static and dynamic approaches [234]. One study [226] suggested that the pull-in voltage of a memory cell based on suspended nanotubes is greater than that of a cell based on cantilever nanotubes with the same geometry, because CNTs fixed at both ends are stiffer and show smaller deflections. It also concluded that for a cell based on suspended nanotubes, the van der Waals interactions between the CNTs and the graphite gate were not significant. In the actual NRAM device, the van der Waals interaction between the CNTs and the oxide material of the gate electrode is a key parameter that defines the

performance and nonvolatility of the device [233, 234]. The nonvolatility of NRAM could be improved by increasing the length of suspended CNTs, decreasing the gap between the CNTs and the gate, or by selecting a type of oxide layer that increases the van der Waals interaction effects. Stronger van der Waals interactions would lead to a decrease in the pull-in voltage, while the pull-out voltage is increased. Therefore, the pull-in and pullout voltages should be carefully selected.

In NRAM, the tunneling resistance depends exponentially on the CNT deflection, invoking a sharp transition from the '0' to the '1' states when the voltage on the gate electrode is varied and the source-drain voltage is fixed [233-234]. For a given structural geometry and a fixed low voltage on the gate electrode, the '0→1' transition time increases with larger diameters of the suspended nanotube, and, at a certain diameter, NRAM stops operating as a memory device. Similarly, the '0→1' transition time increases with the depth of the gap. The diameter of the suspended CNT is another parameter that could potentially affect the operation of NRAM and its nonvolatility are temperature effects, such as thermal fluctuations of suspended nanotubes, and contact effects with the gate substrate.

Data storage based on telescoping carbon nanotubes

The achievement of the controlled and reversible telescopic extension of multiwalled CNTs [235] led to a suggestion for a route towards an electromechanical switch based on CNT telescopic extension [236][. The telescoping process has been found to be fully reversible and has been

repeated a number of times without apparent damage to the sliding surfaces [235]. Since then, the first nonvolatile device that operates using CNTs as low-friction bearings has been fabricated [222]. This device consists of two open-ended multiwalled CNTs attached to the source and the drain electrodes (figure 46 (c)). The CNTs are separated by a nanometer-scale gap with the gate electrode positioned between them. Switching occurs through the electrostatically initiated sliding of the inner core of a multiwalled CNT out of its sleeve. This closes the gap between the CNTs and establishes a conducting state '1'. The device has been shown to require <10 V of pull-in voltage on the drain electrode and <100 V of pull-out voltage on the gate electrode to produce robust and reversible '0 \rightarrow 1' conductance cycles with extremely high switching speeds. A number of further designs for data storage devices based on telescoping CNTs have been suggested that are based on double walled CNTs with a short, capped inner wall acting as a shuttle [237-240]. One of these is an all-carbon three-terminal memory cell [238] with a single-walled CNT attached to the drain electrode and a CNT with removed core attached to the gate electrode (figures 46 (a) and 46 (b)).

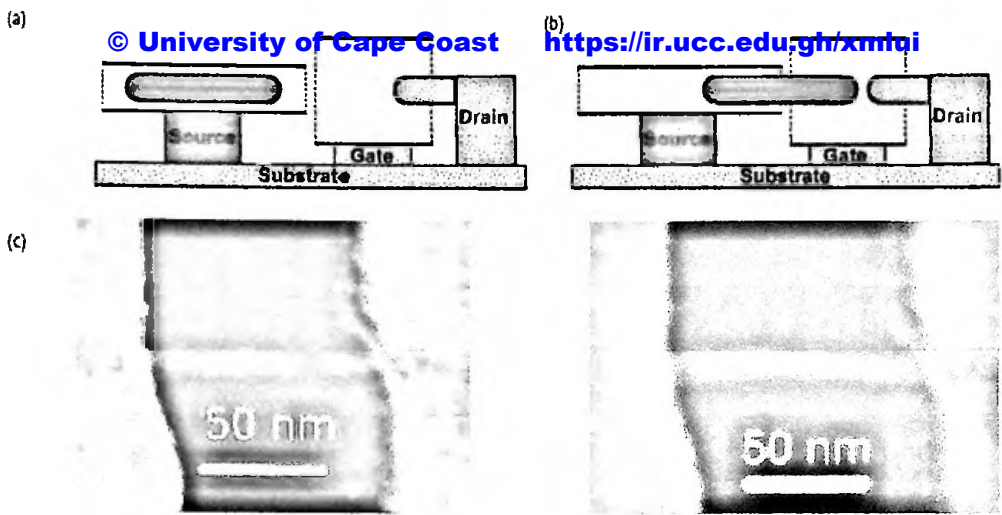


Figure 46: A three-terminal memory cell based on telescoping carbon nanotubes. An all-carbon memory cell with a CNT attached to the gate electrode: (a) in nonconducting state '0', and (b) in conducting state '1'. (c) SEM images of a memory cell with a flat gate electrode [217, 222].

The core of inner walls can be removed with the use of a nanomanipulator [235]. The balance of the forces that defines the performance of the device has been analyzed [241]. Electrostatic forces pull the shuttle out of the sleeve of a double-walled CNT attached to the source electrode, which comes into electric contact with the drain, thus establishing the connection (figure 46 (b)). After the power is switched off, the cell may remain held in state '1' by the van der Waals forces between the shuttle and the drain and the static friction force between the shuttle and the sleeve. This provides permanent contact and gives the nonvolatile capability of the device. At the same time, the capillary force of the weak van der Waals interaction between the walls of the double-walled CNT tends to retract the shuttle back into the sleeve, restoring the CNT to its original condition. When no voltage is applied, this force may provide a permanent gap between the CNT and the drain, keeping the cell in a

nonconducting '0' state (figure 46 (a)). Thus both nonvolatile and volatile behavior can be achieved in the device. The all-carbon memory cell has some advantages in terms of future high-bandwidth applications, as CNT-made electrodes have much smaller dimensions compared with metal electrodes. Uniformity of all-carbon memory cell characteristics can be achieved by using identical switches made of CNTs with the same chirality indices. The volatility of the device is defined by the strength of the static friction force applied to the shuttle, which depends on the structure and the length of double-walled CNT. If the friction force is small, the device is stable in state '1' only if a voltage is applied, thus allowing the operation of a volatile memory cell. In a nonvolatile memory cell with all-carbon electrodes, as a result of thermal fluctuations of the components, the minimum size of the device at $T = 300$ K should be an order of magnitude greater than that at $T = 0$ K. To achieve optimal miniaturization and the highest operation frequencies, the device should be fabricated and used at very low temperatures. Under these conditions, the write density and switching frequencies will be significantly greater than those of memory cells based on cantilever and suspended nanotubes.

In conclusion, the semiconductor industry is actively evaluating emerging memory technologies in the search of a new scalable technology [217]. Although existing memory technologies continue to advance, providing faster, smaller, and cheaper memory, they are not expected to scale down beyond a very few additional process technology nodes. The most widely used commercial nonvolatile memory – Flash – has a low write speed leading to slow random access. New memory technologies such as FRAM, MRAM, and

PRAM are currently in use in a number of applications where the limitations of Flash are an issue.

Memory devices based on CNTs also have the potential to be advantageous allowing, at least in theory, densities higher than those of DRAM. The power needed to write to these devices is much lower than in DRAM, which has to build up charge on the plates. This means that CNT-based memory devices could not only compete with existing memories in terms of speed, but would also require much less power to run. Nantero, Inc. has recently demonstrated a prototype of a 22 nm NRAM switch and suggested that the NRAM switch will continue to scale down to below the 5 nm technology node. All these advances, however, will become firm commercial reality only if radical changes in processing are found that gain precise control over the number and spatial location of CNTs over large areas. A production chip would require hundreds of millions of CNTs that are long enough to bend and have been manufactured cleanly and consistently. Additionally, new chemical processes will need to be proposed to align the CNTs better in the device, thus reducing the problem of reproducibility [217].

Field Emission Devices

Field emission (or Fowler-Nordheim tunneling) is a quantum mechanical process whereby electrons can tunnel through a potential barrier in the presence of a high electric field. Nanometric size, chemical stability, structural robustness and high conductivity are some of the vital properties of CNTs[23, 70, 242-245] . The right combination of these properties make them good emitters, better than the conventional ones (some examples are Mo or Si

tips, Cs-coated diamond, graphite powder)[242]. A good emitter should have a low emission threshold field and the capability to maintain a stable high current density. With respect to the emission threshold, CNTs are better than the conventional emitters.

Industrial and academic research activity on electronic devices has focused principally on using SWCNTs and MWCNTs as field emission electron sources [246, 247] for flat panel displays [248], gas discharge tubes providing surge protection [249], and x-ray [250] and microwave generators [251]. A potential applied between a carbon nanotube-coated surface and an anode produces high local fields, as a result of the small radius of the nanofiber tip and the length of the nanofiber. These local fields cause electrons to tunnel from the nanotube tip into the vacuum. Electric fields direct the field-emitted electrons toward the anode, where a phosphor produces light for the flat panel display application.

There is an intensive investigation of the emission properties of CNTs [252-263] for technological applications such as flat panel display and electron guns for various systems. Samsung has been developing a Field-Emission flat display, and has demonstrated a prototype of a 9-inch full color display (576 x 242 pixels) in 1999 [264]. The structure of a SWCNT based flat panel display is shown in figure 47. Each pixel in this device is primarily composed of two glasses: an anode glass, which is coated with a layer of indium-tin-oxide (ITO) phosphor, and a cathode glass that is coated with SWCNT [264]. The role of the SWCNT in this device is to generate an electron source. Assembling these pixels into a matrix creates the flat panel display [264]. Using the plasma-enhanced or conventional CVD on top of substrates prepatterned with

transitional metal catalysts yielded highly aligned arrays of carbon nanotubes growing vertically to the surface of the substrate [265].

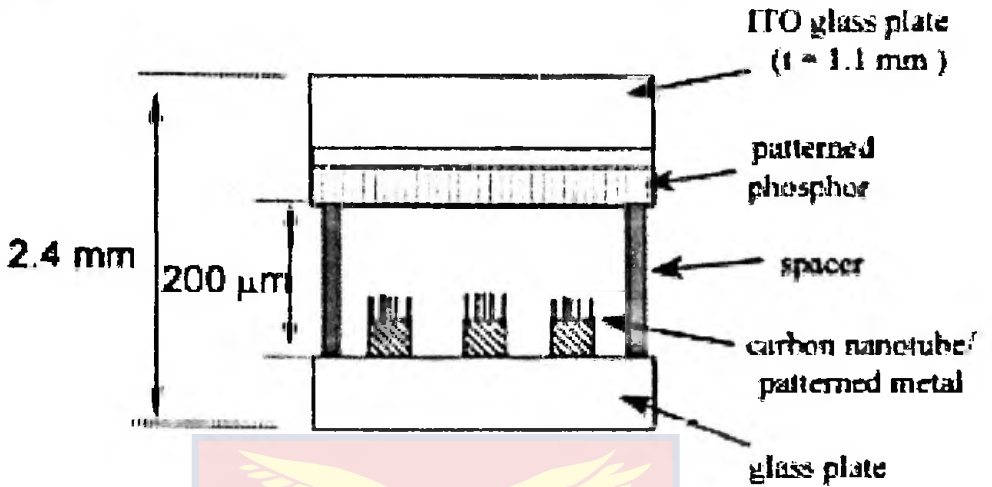


Figure 47: Schematic structure of nanotube flat panel display [264]



Figure 48: The Samsung 4.5" full-color nanotube display [264]

SWCNT displays could eventually displace liquid-crystal and plasma displays in large flat panels. Their advantages over standard liquid crystal displays include lower power consumption, higher brightness, a wider viewing angle, faster response rate, and a wide operating temperature range. But nanotube displays are technically complex and require concurrent advances in electronic-addressing circuitry, low voltage phosphors, methods to maintain the required vacuum, and the elimination of faulty pixels. Hence, according to Bonard Jean-

Marc et al. [266], carbon nanotubes have been recognized as one of the most promising electron field emitters currently available.

Terahertz Oscillators

The terahertz spectrum occurs within the frequency range of 0.1–1 THz and is bound by the microwave and optical spectral bands [267]. Although technology within each of these distinct bands is well developed, application of microwave and optical techniques to the generation and detection of terahertz radiation has proceeded slowly, creating a “terahertz Gap [268, 269]. The state of affairs is exemplified by the fact that at the present time a continuous wave, compact, efficient, high-power, and inexpensive terahertz source that operates at room temperature does not exist [267]. Extension of optical techniques into the terahertz gap is limited since terahertz energies are much smaller than typical semiconductor energy gaps and lie close to the room temperature thermal energy [267]. Furthermore, many optical sources and detectors are bulky and expensive [267]. The cascade laser is promising but must be cryogenically cooled [270]. However, more improvements are needed to further penetrate the terahertz gap [267]. Another difficulty is the fact that both electronic and optical sources suffer from a sharp reduction in output power within the terahertz regime [271].

For the effective use of diode oscillators in the terahertz regime, exploration of new materials may be profitable. Materials that are useful for oscillator diodes generally exhibit negative differential conductivity (NDC) [267]. Many properties of carbon nanotubes (CNTs) are well suited for use in

high frequency oscillator applications [267]. Experiments have shown that suspended metallic CNTs exhibit NDC [267]. Also Boltzmann transport theory has predicted NDC in both metallic and semiconducting single-walled CNTs (s-SWCNTs) [272-276]. The figure 49 below shows resonant circuit connected to a s-SWCNT oscillator of length L . Where R_r , C_r and L_r are resistance, capacitance, and inductance respectively connected in parallel across a dc source of voltage V , and electric field strength E

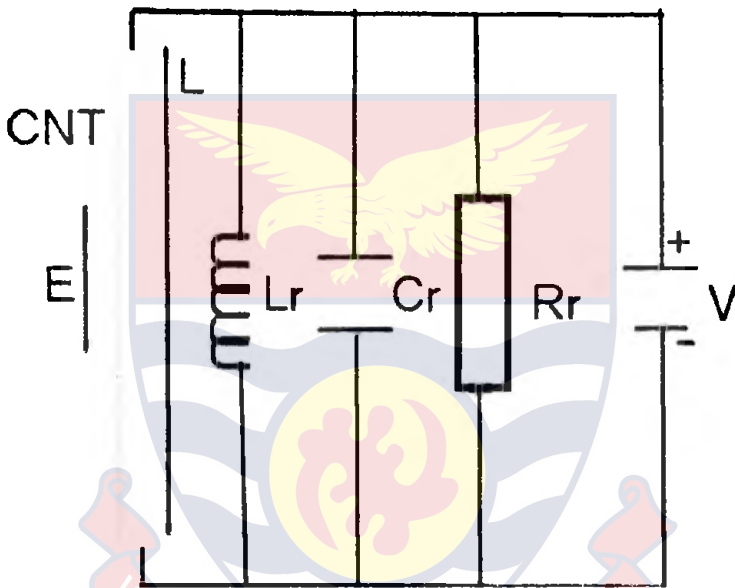
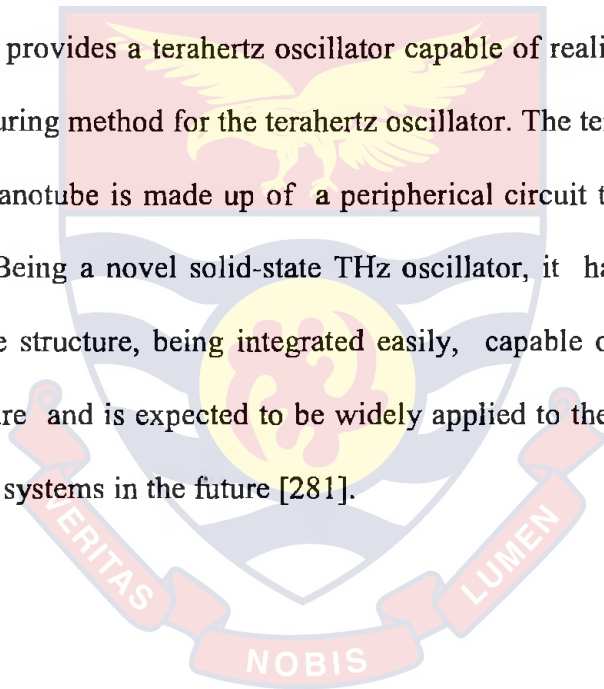


Figure 49: Resonant circuit connected to a s-SWCNT oscillator [281]

Furthermore, simulations of high field transport in s-SWCNTs have shown that nanotubes can generate terahertz frequency current oscillations [277, 278]. Additionally, the Monte Carlo simulations of Akturk et al., [279] predict that electrons in CNTs exhibit negative differential velocities (NDVs) or NDC, similar in that respect to GaAs, opening possibilities for their use in oscillators and, therefore, communication networks [280]. When used in circuits, their simulations indicate that they may oscillate at very high frequencies in the terahertz range, enabling data rates approaching terabits [277]. These

oscillations suggest that CNTs may be applicable for use in THz radio frequency circuits [277].

Invention of terahertz oscillator in 2009 by Wang C et al., [281] utilizes a terahertz oscillation method based on a CNT. Direct-current bias voltage is applied to two ends of a semiconductor carbon nanotube so that the drifting speed of the electrons in the semiconductor carbon nanotube is arranged in the negative differential drifting speed area (or the negative differential conductivity (NDC) region) , thus generating the oscillation current that changes periodically with time in the semiconductor carbon nanotube. Their invention provides a terahertz oscillator capable of realizing the method and a manufacturing method for the terahertz oscillator. The terahertz oscillator of the carbon nanotube is made up of a peripheral circuit that is connected with the chip. Being a novel solid-state THz oscillator, it has advantages of having a simple structure, being integrated easily, capable of running under room temperature and is expected to be widely applied to the spatial wireless communication systems in the future [281].



CHAPTER THREE

THEORETICAL MODELS OF CURRENT DENSITIES FOR CARBON NANOTUBES

Electron Transport in Carbon Nanotubes

Electron transport in a material is an important subject of experimental and theoretical investigations beginning from the pioneering paper of electron transport in semiconductor superlattices by Esaki and Tsu [282]. This chapter theoretically explores the electron transport in achiral carbon nanotubes. The Boltzmann transport equation is solved in the framework of momentum-independent relaxation time. The calculation is done using the semiclassical approach which provides us with the simplest route to this theory, supplying somewhat rough but quite tractable analytical results. We consider each achiral carbon nanotube exposed to dc field as well as dc-ac driven fields in the absence and presence of hot electrons source. An analytical expression for the current density of achiral carbon nanotubes in each case is derived. The results of these calculations are analysed in chapter 4 and the effect of hot electrons on the conductivity of carbon nanotube in each case is observed and theoretically investigated.

Phenomenological Model of a Carbon Nanotube

If a static electric field E_z is applied along a z - axis of an undoped single-walled carbon nanotube, electrons begin to move in accordance with the semiclassical Newton's law (neglecting scattering) [283] :

$$\frac{dP_z}{dt} = eE_z \quad (24)$$

where P_z and e are the axial component of the quasimomentum and the electronic charge of the propagating electrons respectively. For a CNT, If energy level spacing $\Delta\varepsilon$ ($\Delta\varepsilon = \pi\hbar V_F/L$, $\hbar = h/2\pi$, h is Planck constant, V_F is Fermi velocity and L is the length of the nanotube) is large enough and the scattering rate ν is small such that $\Delta\varepsilon \gg aeE_z$ and $h\nu < aeE_z$ ($zz -$ CNT, and $\Delta\varepsilon \gg a3aeE_z$ and $h\nu < a3aeE_z$, $ac -$ CNT), then the electrons oscillate inside the lower level with the so-called Bloch frequency Ω given by [275] :

$$\Omega_{zz} = \frac{aeE_z}{\hbar} \quad (25a)$$

and

$$\Omega_{ac} = \frac{aeE_z}{\sqrt{3}\hbar} \quad (25b)$$

for $zz -$ CNT and $ac -$ CNT respectively. Here, a is the lattice constant of the CNT. For an undoped achiral CNT exposed to a dc field with and without the presence of hot electrons source, the investigation is done within the

semiclassical approximation in which the motion of the π -electrons are considered as classical motion of free quasiparticles in the field of the crystalline lattice with dispersion law extracted from the quantum theory[275]

Taking into account the hexagonal crystalline structure of a rolled graphene in a form of CNTs and using the tight binding approximation, the energies for zz-CNT and ac-CNT are expressed as in equations (26a) and (26b), respectively [275]

$$\begin{aligned} \varepsilon(s\Delta p_\phi, p_z) &\equiv \varepsilon_s(p_z) \\ &= \pm\gamma_0 \left[1 + 4\cos(ap_z)\cos\left(\frac{a}{\sqrt{3}}s\Delta p_\phi\right) \right. \\ &\quad \left. + 4\cos^2\left(\frac{a}{\sqrt{3}}s\Delta p_\phi\right) \right]^{1/2} \end{aligned} \quad (26a)$$

$$\begin{aligned} \varepsilon(s\Delta p_\phi, p_z) &\equiv \varepsilon_s(p_z) \\ &= \pm\gamma_0 \left[1 + 4\cos(as\Delta p_\phi)\cos\left(\frac{a}{\sqrt{3}}p_z\right) \right. \\ &\quad \left. + 4\cos^2\left(\frac{a}{\sqrt{3}}p_z\right) \right]^{1/2} \end{aligned} \quad (26b)$$

where $\gamma_0 \approx 3.0\text{eV}$ is the overlapping integral, p_z is the axial component of quasi-momentum. Δp_ϕ is transverse quasimomentum level spacing and s is an integer. The expression for lattice constant a in equations (26a) and (26b) is given by

$$a = \frac{3a_{c-c}}{2\hbar} \quad (27)$$

where $a_{c-c} = 0.142\text{nm}$ is the C-C bond length

The - and + signs correspond to the valence and conduction bands, respectively. Due to the transverse quantization of the quasimomentum P , its transverse component p_ϕ can take n discrete values,

$$p_\phi = s\Delta p_\phi = \frac{\pi\sqrt{3}s}{an} \quad (s = 1, \dots, n)$$

Unlike transverse quasimomentum, p_ϕ , the axial quasimomentum p_z is assumed to vary continuously within the range $0 \leq p_z \leq 2\pi/a$, which corresponds to the model of infinitely long CNT ($L = \infty$). This model is applicable to the case under consideration because we are restricted to temperatures and/or voltages well above the level spacing [284], i.e.

$k_B T > \varepsilon_c \Delta \varepsilon$, where k_B is Boltzmann constant, T is the absolute temperature, ε_c is the charging energy. Considering the presence of hot electrons source, the motion of quasiparticles in an external axial electric field is described by the Boltzmann kinetic equation in the form as shown below [275, 283]

$$\frac{\partial f(p)}{\partial t} + v_z \frac{\partial f(p)}{\partial x} + eE(t) \frac{\partial f(p)}{\partial p_z} = - \frac{[f(p) - f_0(p)]}{\tau} + S(p) \quad (29)$$

where $S(p)$ is the hot electron source function, $f_0(p)$ is equilibrium Fermi distribution function, $f(p, t)$ is the distribution function, v_z is the quasiparticle group velocity along the z-axis of carbon nanotube and τ is the relaxation time. The relaxation term of equation (29) describes the electron-phonon scattering, electron-electron collisions [285, 286], etc. Using the method originally developed in the theory of quantum semiconductor superlattices [275], an exact solution of equation (29) can be constructed without assuming a weak electric field. Expanding the distribution functions of interest in Fourier series as

$$f(p, t) = \Delta p_\phi \sum_{s=1}^n \delta(p_\phi - s\Delta p_\phi) \sum_{r \neq 0} f_{rs} e^{iarp_z} \psi_v(t) \quad (30a)$$

and

$$f_0(p) = \Delta p_\phi \sum_{s=1}^n \delta(p_\phi - s\Delta p_\phi) \sum_{r \neq 0} f_{rs} e^{iarp_z} \quad (30b)$$

For zz-CNTs, and

$$f(p, t) = \Delta p_\phi \sum_{s=1}^n \delta(p_\phi - s\Delta p_\phi) \sum_{r \neq 0} f_{rs} e^{ibrp_z} \psi_v(t) \quad (31a)$$

and

$$f_0(p) = \Delta p_\phi \sum_{s=1}^n \delta(p_\phi - s\Delta p_\phi) \sum_{r \neq 0} f_{rs} e^{ibrp_z} \quad (31b)$$

For ac-CNTs

where $b = a/\sqrt{3}$ or $a = b\sqrt{3}$, $\delta(p_\phi - s\Delta p_\phi)$ is the Dirac delta function, f_{rs} is the coefficients of the Fourier series and $\psi_v(t)$ is the factor by which the Fourier transform of the nonequilibrium distribution function differs from its equilibrium distribution counterpart. For simplicity, we consider a hot electron source of the simplest form given by the expression,

$$S(p) = \frac{Qa}{\hbar} \delta(\varphi - \varphi') - \frac{aQ}{n_0} f_s(\varphi) \quad (32)$$

where $f_s(p)$ is the stationary (static and homogeneous) solution of equation(29), Q is the injection rate of hot electron, n_0 is the equilibrium particle density, φ and φ' are the dimensionless momenta of electrons and hot electrons respectively which are expressed as $\varphi_{zz} = ap_z/\hbar$ and $\varphi'_{zz} = ap'_z/\hbar$ for zz-CNTs and $\varphi_{ac} = ap_z/\sqrt{3}\hbar$ and $\varphi'_{ac} = ap'_z/\sqrt{3}\hbar$ for ac-CNTs,

Current Density for Zigzag Carbon Nanotubes (zz-CNT) in the Absence of Hot Electrons Source

We now determine the electric current density of the zz-CNT for the case when there is no hot electron source present. Substituting equation 30 (a) into equation 30 (b) and setting $S(p) = 0$, we get

© University of Cape Coast <https://ir.ucc.edu.gh/xmlui> (33)

$$\frac{\partial \psi_v(t)}{\partial t} + i\epsilon_s(p_z) \psi_v(t) = \frac{1}{\tau} \psi_v(t) \quad (33)$$

Solving the homogeneous differential equation corresponding to equation (33), we obtain

$$\psi_v(t) = \frac{v}{(v + ir\Omega)} \quad (34)$$

where $v = 1/\tau$

The expression for the coefficients f_{rs} of equation (30) is found to be

$$f_{rs} = \frac{a}{2\pi\Delta p_\phi} \int_0^{2\pi/a} \frac{\exp^{-iar p_z}}{1 + \exp\{\epsilon_s(p_z)/k_B T\}} dp_z \quad (35)$$

The surface current density is defined by

$$j_z = \frac{2e}{(2\pi\hbar)^2} \iint f(p, t) v_z(p) d^2p,$$

or

$$j_z = \frac{2e}{(2\pi\hbar)^2} \sum_{s=1}^n \int_0^{2\pi/a} f(p_z, s\Delta p_\phi, \psi_v(t)) v_z(p_z, s\Delta p_\phi) dp_z \quad (36)$$

where the integration is over the first Brillouin zone, v_z is given by

$$v_z(p_z, s\Delta p_\phi) = \frac{\partial \epsilon_s(p_z)}{\partial p_z} \quad (37)$$

Now we expand $\epsilon_s(p_z)/\gamma_0$ in Fourier series with coefficients ϵ_{rs} to be determined

$$\epsilon(p_z, s\Delta p_\phi) = \epsilon_s(p_z) = \gamma_0 \sum_{r \neq 0} \epsilon_{rs} \exp^{iar p_z} \quad (38)$$

The expression for the coefficients is found to be

$$\epsilon_{rs} = \frac{a}{2\pi\gamma_0} \int_0^{2\pi/a} \epsilon_s(p_z) \exp^{-iar p_z} dp_z \quad (39)$$

where $\varepsilon_s(p_z)$ is given by equation (26a), From equations (37) and (38)

$$v_z(p_z, s\Delta p_\phi) = \gamma_0 \sum_{r \neq 0} \frac{\partial(\varepsilon_{rs} \exp^{iar p_z})}{\partial p_z} = \gamma_0 \sum_{r \neq 0} iar \varepsilon_{rs} \exp^{iar p_z} \quad (40)$$

From equation(30) ,

$$f(p_z, s\Delta p_\phi, \psi_v(t)) = \Delta p_\phi \sum_{r \neq 0} f_{rs} \exp^{iar p_z} \psi_v(t) \quad (41)$$

Substituting equations(30) and (31) into equation (36), the current density in the absence of hot electron source for zz-CNTs (j_z^{zz}) is obtained as

$$j_z^{zz} = i \frac{4\sqrt{3} e^2 \gamma_0}{\hbar^2 n} \sum_{r=1}^{\infty} \frac{rv}{(v + ir\Omega_{zz})} \sum_{s=1}^n f_{rs} \varepsilon_{rs} \quad (42)$$

Current Density for Zigzag Carbon Nanotube (zz-CNT) in the Presence of Hot Electron Source

The stationary homogeneous distribution function $f_s(\varphi)$ in the presence of hot electron source is given by [283] :

$$f_s(\varphi) = f_E(\varphi) + f'(\varphi) \quad (43)$$

where $f_E(\varphi) = f(p) = \psi_v(t)$

Substituting equation(43) into equation(29)we get

$$\frac{\partial f'(\varphi)}{\partial \varphi} + \left(\frac{v}{\Omega} + \frac{Q}{n_o \Omega}\right) f'(\varphi) = \frac{aQ}{\Omega} \delta(\varphi - \varphi') - \frac{aQ}{\Omega n_o} f_E(\varphi) \quad (44)$$

Solving the above homogeneous differential equation , $f'(\varphi)$ is obtained as

$$f'(\varphi) = \eta_{zz} \frac{n_o}{2\pi} \cdot \sum_r \frac{\Omega_{zz}}{(ir\Omega_{zz} + v + \eta_{zz}\Omega_{zz})} \left\{ e^{-ir\varphi'} - \frac{v}{(v + ir\Omega_{zz})} \right\} \quad (45)$$

where introducing a dimensionless nonequilibrium parameter η_{zz} , given by

$$\eta_{zz} = Q/\Omega_{zz}n_o.$$

Substituting equations (34) and (45) into equation (43), $f_s(\varphi)$ is obtained as

$$f_s(\varphi) = \frac{v}{(v + ir\Omega)} + \eta_{zz} \frac{n_o}{2\pi} \cdot \sum_r \frac{\Omega_{zz}}{(ir\Omega_{zz} + v + \eta_{zz}\Omega_{zz})} \times \left(e^{-ir\varphi'} - \frac{v}{(v + ir\Omega_{zz})} \right) \quad (46)$$

The current density in the presence of hot electron source j_{zHE}^{zz} is given by

$$j_{zHE}^{zz} = i \sum_{s=1}^n j_{os} f_s(\varphi) \quad (47)$$

where

$$j_{os} = \frac{4\sqrt{3} e^2 \gamma_0}{\hbar^2 n} \sum_{r=1}^{\infty} r \sum_{s=1}^n f_{rs} \varepsilon_{rs}$$

Substituting equation (46) into equation (47), we obtain the current density in the presence of hot electron source for zz-CNTs (j_{zHE}^{zz}) given by

$$j_{zHE}^{zz} = i \frac{4\sqrt{3} e^2 \gamma_0}{\hbar^2 n} \sum_{r=1}^{\infty} \left\{ \frac{rv}{(v + ir\Omega_{zz})} + \eta_{zz} \frac{n_o}{2\pi} \sum_r \frac{r\Omega_{zz} e^{ir\varphi}}{(ir\Omega_{zz} + v + \eta_{zz}\Omega_{zz})} \left(e^{-ir\varphi'} - \frac{v}{(v + ir\Omega_{zz})} \right) \right\} \sum_{s=1}^n f_{rs} \varepsilon_{rs} \quad (48)$$

Current Density for Armchair Carbon Nanotube (ac-CNT) in the Absence of Hot Electrons Source

Determining the electric current density of the ac-CNT for the case when there is no hot electron source present. Substituting equations (31a) and (31b) into equation (29) and setting $S(p) = 0$, equation (49) is obtained as

$$\frac{\partial \psi_v(t)}{\partial t} + \left(iebrE_z + \frac{1}{\tau} \right) \psi_v(t) = \frac{1}{\tau} \quad (49)$$

Solving the homogeneous differential equation corresponding to equation (49), $\psi_v(t)$ is obtained

$$\psi_v(t) = \frac{v}{(v + ir\Omega_{ac})} \quad (50)$$

The expression for the coefficients f_{rs} of equation (48) is found to be

$$f_{rs} = \frac{a}{2\pi\Delta p_\phi} \int_0^{2\pi/a} \frac{\exp^{-ibrp_z}}{1 + \exp\{\varepsilon_s(p_z)/k_B T\}} dp_z \quad (51)$$

Now expanding $\varepsilon_s(p_z)/\gamma_0$ in Fourier series with coefficients ε_{rs} to be determined

$$\varepsilon(p_z, s\Delta p_\phi) = \varepsilon_s(p_z) = \gamma_0 \sum_{r \neq 0} \varepsilon_{rs} \exp^{ibrp_z} \quad (52)$$

The expression for the coefficients of equation (48) is found to be

$$\varepsilon_{rs} = \frac{a}{2\pi\gamma_0} \int_0^{2\pi/a} \varepsilon_s(p_z) \exp^{-ibrp_z} dp_z \quad (53)$$

where $\varepsilon_s(p_z)$ is given by equation (26b), From equations (37) and (52)


<https://ir.ucc.edu.gh/xmlui>

$$v_z(p_z, s\Delta p_\phi) = \gamma_0 \sum_{r \neq 0} \frac{\partial(\epsilon_{rs} \exp^{ibrp_z})}{\partial p_z} = \gamma_0 \sum_{r \neq 0} \frac{ir \epsilon_{rs} \exp^{ibrp_z}}{\epsilon_{rs}} \quad (54)$$

From equation (31b) ,

$$f(p_z, s\Delta p_\phi, \psi_v(t)) = \Delta p_\phi \sum_{r \neq 0} f_{rs} \exp^{ibrp_z} \psi_v(t) \quad (55)$$

Substituting equations (54) and (55) into equation (36), the current density in the absence of hot electron source for ac-CNTs (j_z^{ac}) is obtained as

$$j_z^{ac} = i \frac{4 e^2 \gamma_0}{\sqrt{3} \hbar^2 n} \sum_{r=1}^{\infty} \frac{rv}{(v + ir\Omega_{ac})} \sum_{s=1}^n f_{rs} \epsilon_{rs} \quad (56)$$

Current Density for Armchair Carbon Nanotube (ac- CNT) in the Presence of Hot Electron Source

Solving the homogeneous differential equation (44) for ac-CNT, $f'(\varphi)$ is obtained as

$$f'(\varphi) = \eta_{ac} \frac{n_o}{2\pi} \cdot \sum_r \frac{\Omega_{ac}}{(ir\Omega_{ac} + v + \eta_{ac})} \left\{ e^{-ir\varphi'} - \frac{v}{(v + ir\Omega_{ac})} \right\} \quad (57)$$

where the nonequilibrium parameter $\eta_{ac} = Q/\Omega_{ac}n_o$ for ac-CNT

Substituting equations (34) and (57) into equation (43) for ac-CNT , $f_s(\varphi)$ is obtained as

$$f_s(\varphi) = \frac{v}{(v + ir\Omega_{ac})} + \eta_{ac} \frac{n_o}{2\pi} \cdot \sum_r \frac{\Omega_{ac}}{(ir\Omega_{ac} + v + \eta_{ac}\Omega_{ac})} \times \left(e^{-ir\varphi'} - \frac{v}{(v + ir\Omega_{ac})} \right) \quad (58)$$

Current density for ac-CNTs in the presence of hot electron source j_z^{ac} is given by

Recall for ac-CNT

$$j_{os} = \frac{4 e^2 \gamma_0}{\sqrt{3} \hbar^2 n} \sum_{r=1}^{\infty} r \sum_{s=1}^n f_{rs} \epsilon_{rs} \quad (60)$$

Substituting equations (58) and (60) into equation (59), j_{zHE}^{ac} is obtained as

$$j_{zHE}^{ac} = i \frac{4\sqrt{3} e^2 \gamma_0}{\hbar^2 n} \sum_{r=1}^{\infty} \left\{ \frac{rv}{(v + ir\Omega_{ac})} + \eta_{ac} \frac{n_0}{2\pi} \sum_r \frac{r\Omega_{ac}}{(ir\Omega_{ac} + v + \eta\Omega_{ac})} \left\{ e^{-ir\varphi'} - \frac{v}{(v + ir\Omega_{ac})} \right\} \right\} \sum_{s=1}^n f_{rs} \epsilon_{rs} \quad (61)$$

High-Frequency Conductivity of Zigzag Carbon Nanotube (zz-CNT) in the Presence and Absence of Hot Electron Source

Now finding the high frequency conductivity in the nonequilibrium state for zz-CNT by considering perturbations with frequency ω and wave-vector κ of the form

$$E(t) = E_z + E_{\omega,\kappa} e^{-i\omega t + i\kappa z} \quad (62a)$$

$$f = f_s(\varphi) + f_{\omega,\kappa} e^{-i\omega t + i\kappa z} \quad (62b)$$

Substituting equations(62a) and (62b) into equation (29) and rearranging yields,

$$\frac{\partial f_{\omega,\kappa}}{\partial \varphi} + i[\alpha + \kappa v_z / \Omega_{zz}] f_{\omega,\kappa} = - \frac{E_{\omega,\kappa}}{E_z} \frac{\partial f_s(\varphi)}{\partial \varphi} \quad (63)$$

where $\alpha = -(\omega + iv_z)/\Omega_{zz}$

© University of Cape Coast <https://ir.ucc.edu.gh/xmlui>

Solving the homogeneous differential equation (63) and then introducing the

Jacobi-Anger expansion and averaging the current over time, the current

density for the zz-CNTs in the presence of hot electrons $j_z^{zz} E$ is obtained as

$$j_z^{zz} E = i \frac{4\sqrt{3}e^2\gamma_0}{n\hbar^2} \sum_{m, l=-\infty}^{\infty} \frac{i^l m l j_m(\beta) j_{m-l}(\beta) I_{m-l}(\beta) \Omega_{zz}}{\omega + iv - m\Omega_{zz}} \times$$

$$\sum_{r=1} \left\{ \eta_{zz} \frac{n_0}{2\pi} \cdot \sum_r \frac{r\Omega_{zz} e^{ir\varphi}}{(ir\Omega_{zz} + v + \eta\Omega_{zz})} \left(e^{-ir\varphi'} - \frac{v}{(v + ir\Omega_{zz})} \right) \right.$$

$$\left. + \frac{rv}{(v + ir\Omega_{zz})} \right\} \sum_{s=1}^n f_{rs} \varepsilon_{rs} \quad (64)$$

where $j_m(\beta)$ is the bessel function of order m

$I_{m-l}(\beta)$ is the modified bessel function of order m-l.

$\beta = \frac{\kappa\gamma_0 a}{\Omega_{zz}\hbar}$ is a normalized amplitude of ac field

In the absence of hot electrons, the nonequilibrium parameter for zz-CNT

$\eta_{zz} = 0$, hence the current density for zz-CNTs without hot electron source

j_z^{zz} could be obtained from equation (64) by setting $\eta_{zz} = 0$. Therefore, the

current density of zz-CNTs in the absence of hot electrons j_z^{zz} is given by

$$j_z^{zz}$$

$$= i \frac{4\sqrt{3}e^2\gamma_0}{n\hbar^2} \sum_{m, l=-\infty}^{\infty} \frac{i^l m l j_m(\beta) j_{m-l}(\beta) I_{m-l}(\beta) \Omega_{zz}}{\omega + iv - m\Omega_{zz}} \sum_{r=1} \frac{rv}{(v + ir\Omega_{zz})} \sum_{s=1}^n f_{rs} \varepsilon_{rs} \quad (65)$$

the Presence and Absence of Hot Electron Source

Similarly solving the homogeneous differential equation (63) for ac-CNTs, here $\alpha = -(\omega + i\nu_z)/\Omega_{ac}$ and then introducing the Jacobi-Anger expansion, and averaging the current over time, the current density for the ac-CNTs in the presence of hot electrons j_{zHE}^{ac} is obtained as

$$j_{zHE}^{ac} = i \frac{4 e^2 \gamma_0}{\sqrt{3} n \hbar^2} \sum_{m, l=-\infty}^{\infty} \frac{i^l m l j_m(\beta) j_{m-l}(\beta) I_{m-l}(\beta) \Omega_{ac}}{\omega + i\nu - m \Omega_{ac}} \times$$

$$\sum_r \left\{ \eta_{ac} \frac{n_0}{2\pi} \sum_r \frac{\Omega_{ac} e^{ir\varphi}}{(ir\Omega_{ac} + \nu + \eta_{ac})} \left(e^{-ir\varphi'} - \frac{\nu}{(\nu + ir\Omega_{ac})} \right) + \frac{\nu}{(\nu + ir\Omega_{ac})} \right\} \sum_{s=1}^n f_{rs} \epsilon_{rs} \quad (66)$$

In the absence of hot electrons, the nonequilibrium parameter for ac-CNT $\eta_{ac} = 0$, hence the current density for ac-CNTs without hot electron source j_z^{ac} could be obtained from equation (66) by setting $\eta_{ac} = 0$. Therefore, the current density of zz-CNTs in the absence of hot electrons j_z^{ac} is obtained as

$$j_z^{ac} = i \frac{4 \sqrt{3} e^2 \gamma_0}{n \hbar^2} \sum_{m, l=-\infty}^{\infty} \frac{i^l m l j_m(\beta) j_{m-l}(\beta) I_{m-l}(\beta) \Omega_{ac}}{\omega + i\nu - m \Omega_{ac}} \sum_{r=1}^n \frac{r\nu}{(\nu + ir\Omega_{ac})} \sum_{s=1}^n f_{rs} \epsilon_{rs} \quad (67)$$

CHAPTER FOUR

RESULTS AND DISCUSSION

In chapter 3, the Boltzmann transport kinetic equation was utilized to derive the mathematical expression for current density of each of the following:

- i. zigzag carbon nanotube (zz-CNT) without and with injection of hot electrons along its axis under the influence of the applied dc field,
- ii. armchair carbon nanotube (ac-CNT) without and with injection of hot electrons along its axis under the influence of the applied dc field,
- iii. zigzag carbon nanotube (zz-CNT) with and without injection of hot electrons exposed simultaneously to a high frequency ac and dc fields (i.e. the high frequency differential conductivity in zz-CNT)
- iv. armchair carbon nanotube (ac-CNT) with and without injection of hot electrons exposed simultaneously to a high frequency ac and dc fields (i.e. the high-frequency differential conductivity in ac- CNT)

This chapter will focus on the numerical analysis of the mathematical expression of each current density obtained in chapter 3. The stated aim of the work presented is not only to probe the effect of hot electrons on conductivity of CNTs, but also to find out whether there is some useful application of the effect.

Current density of a CNT as a function of the applied dc field

The behaviour of normalized current density as a function of the applied dc field in the absence as well as presence of hot electrons for each achiral CNT is shown in figure 50. It has been observed that the normalized

Furthermore, the behaviour of the normalized current density as a function of the dc field for the CNTs stimulated axially with the hot electrons, represented by the nonequilibrium parameter η has been displayed in figure 51.

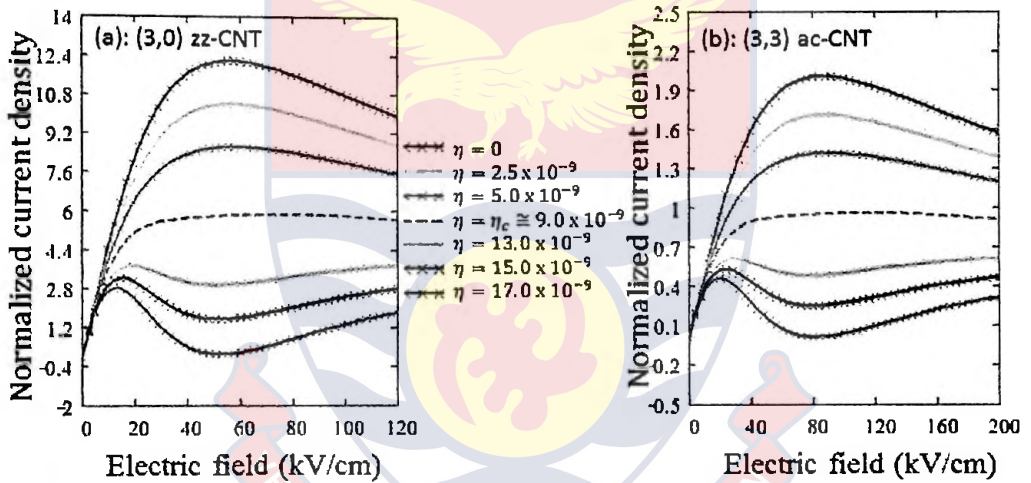


Figure 51: A plot of normalized current density versus electric field for (a) (3,0) zz-CNT and (b) (3,3) ac-CNT as the nonequilibrium parameter η increases from 0 to 17.0×10^{-9} , $T = 287.5$ K and $u = 1$ THz

As nonequilibrium parameter η increases from 0 to 17.0×10^{-9} , it has been observed as shown in figure 51 that the normalized current density has the highest intensity for $\eta = 0$ (no hot electrons). Upon increasing the hot electrons injection rate, the intensity of the current density decreases and shifts to the left (i.e., low electric fields). This stems from the scattering effects due

to the increase in electron-phonon interactions as well as the increase in the direct injection rate of the hot electrons [287].

As the injection rate of the hot electrons becomes strong enough, the current density up-turned, exhibiting a positive differential conductivity (PDC) near 50 kV/cm and 75 kV/cm for the zz-CNT and the ac-CNT, respectively. In this region, the hot electrons become the dominant determining factor [287]. The physical mechanism behind the switch from NDC to PDC is due to the interplay between the hot electrons pumping frequency (Q/n_0), which is a function of rate of hot electrons injection (Q), and the Bloch frequency (Ω), which depends on the electric field (E_z). At stronger electric field, the rate of scattering of the electrons by phonons is well pronounced resulting in the gradual decrease in the current density with increasing the dc field (NDC region). However, as the rate of hot electrons injection increases, the corresponding rise in the current density due to hot electrons injection now far exceeds the reduction in the current density due to scattering of electrons by phonons. Thus, the net effect on the current density from the two opposing sources (with the rate of hot electrons injection being dominant) gives rise to the PDC characteristics as shown in figure 51 for $\eta \geq 13.0 \times 10^{-9}$. The desirable effect of a switch from NDC to PDC takes place when η is larger than a critical value $\eta_c \cong 0.9 \times 10^{-8}$. Larger η can be achieved at low temperatures with a low equilibrium density n_0 . However, at higher temperatures (room temperature), η_c becomes smaller, therefore the effect of pumping is more pronounced. This gives hope in observing the effect at both low and high temperatures. When axial injection of hot electrons into the achiral CNTs is strong enough, the nonequilibrium parameter η exceeds the critical value

Also, the inversion of the differential conductivity in a nonequilibrium state as the nonequilibrium parameter η is further increased to 4.5×10^{-8} is shown in figure 52

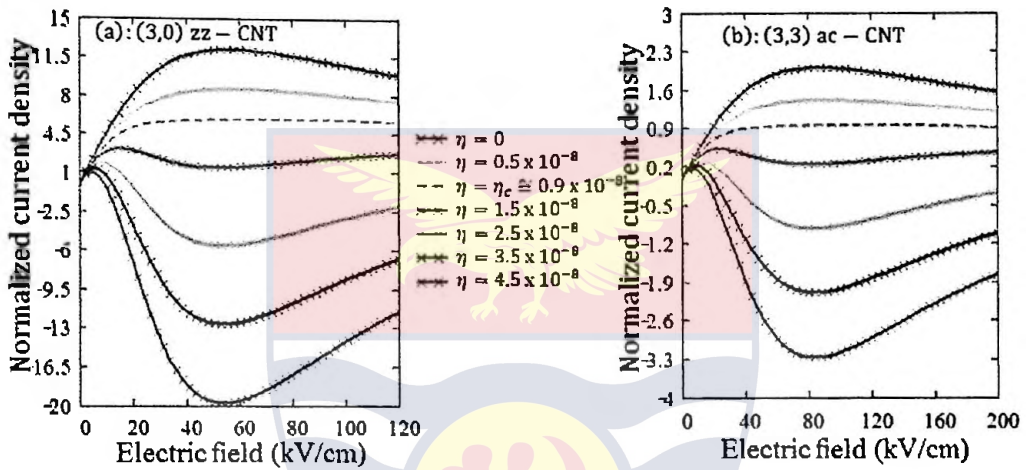


Figure 52: A plot of current density versus electric field for (a) (3,0) zz-CNT and (b) (3,3) ac-CNT as the nonequilibrium parameter η further increases to 4.5×10^{-8} , $T = 287.5$ K and $\nu = 1$ THz

There is a clear inversion of the differential conductivity in a nonequilibrium state as nonequilibrium parameter η exceeds a critical value $\eta_c \cong 0.9 \times 10^{-8}$. The PDC region shifts towards stronger electric fields, whereas the onset of the NDC shifts towards lower electric field upon increasing the hot electrons injection rate. As mentioned earlier, the upturn in the conductivity is due to the strong axial injection of the hot electrons which is significantly stronger than the fall in conductivity due to increase in electron-phonon scattering as the electric field increases, consequently there is a switch from NDC to PDC.

the normalized current density (J_z) as a function of the electric field (E_z) and nonequilibrium parameter (η) for each achiral CNT has been displayed in figures 53 and 54.

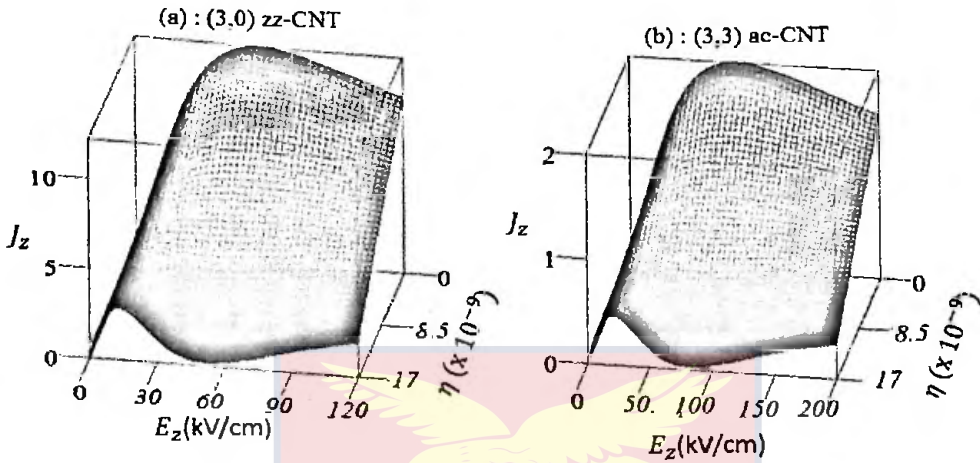


Figure 53: A 3D plot of normalized current density (J_z) versus electric field (E_z) and nonequilibrium parameter (η) for (a) (3,0) zz-CNT and (b) (3,3) ac-CNT, $T = 287.5$ K and $\nu = 1$ THz

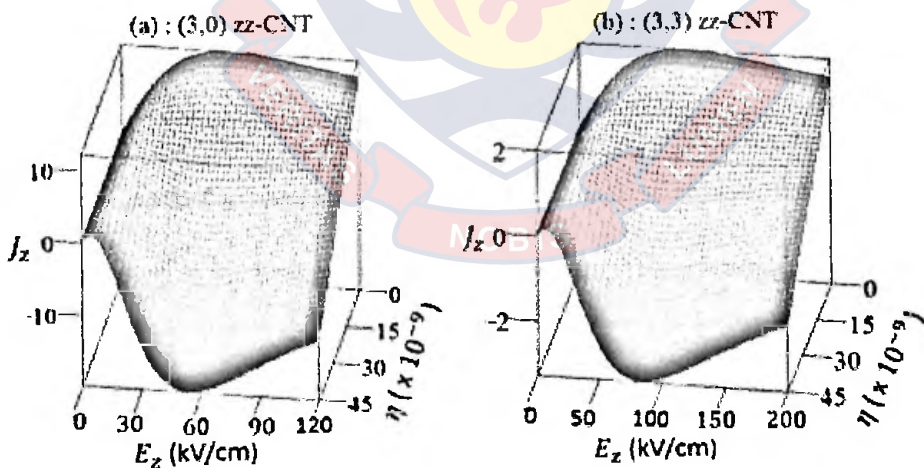


Figure 54: A 3D plot of normalized current density (J_z) versus electric field (E_z) and nonequilibrium parameter (η) showing inversion of the differential conductivity in a nonequilibrium state for (a) (3,0) zz-CNT and (b) (3,3) ac-CNT, $T = 287.5$ K and $\nu = 1$ THz

The differential conductivity as well as the peak of the current density attained the highest value when the nonequilibrium parameter is zero. For both zz-CNT and ac-CNT, as the nonequilibrium parameter gradually increases the differential conductivity and the peak current density decrease until the critical nonequilibrium parameter value $\eta_c \cong 0.9 \times 10^{-8}$ is reached, beyond which the NDC characteristics slowly changes to PDC characteristics as shown in figures 53 and 54. As can be seen in figure 54, the peak at the onset of the NDC shifts toward low electric fields whereas the onset of the PDC shifts towards the high electric fields with increasing the hot electron injection rate for both CNTs. So far these results have been published in "The European Physical Journal B" [288].

High Frequency Differential Conductivity in a CNT

A semiclassical theory of electron transport in a CNT exposed to dc-ac driven fields in the presence and absence of hot electrons is now presented. Given a suitable combination of the dc and ac operating conditions, high field domains are then unable to build up [289]. These domains are believed to be destructive for the Bloch gain [290]. After solving Boltzmann's transport equation, an analytical expression for current density which is a function of frequency of ac electric field ω , normalized amplitude β of high frequency ac electric field and also simultaneously applied dc field E_z is obtained when each achiral CNT is stimulated axially with the hot electrons ($\eta > 0$) and also in the absence of hot electrons ($\eta = 0$).

Ensuring that all other equally important parameters are kept constant, the behaviour of the normalized current density J_z as a function of each of the following:

- i. frequency of ac electric field ω
- ii. normalized amplitude β of the high frequency ac electric field
- iii. applied dc field E_z when frequency of ac field ω is
 - (a) much greater than scattering frequency ν (i.e. $\omega \gg \nu$ or $\omega\tau \gg 1$)
 - (b) much less than scattering frequency ν (i.e. $\omega \ll \nu$ or $\omega\tau \ll 1$)
 which is called Quasi-static case or state (where $\nu = \tau^{-1}$)

has been displayed.

Figure 55 is a plot of normalized current density (J_z) versus frequency of ac field (ω) displaying the effect of hot electrons on high frequency conductivity in achiral CNTs.

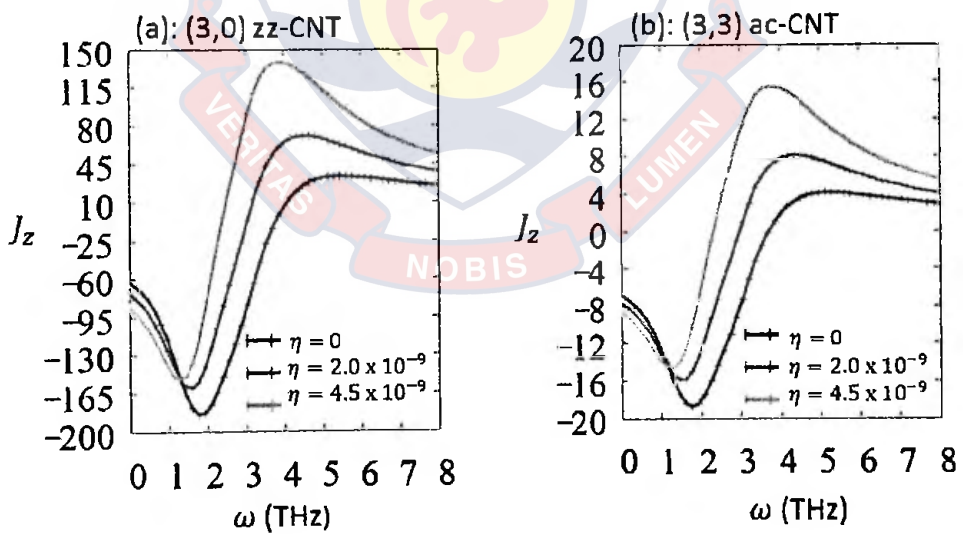


Figure 55: A plot of normalized current density (J_z) versus frequency of ac field (ω) as the nonequilibrium parameter (η) increases from 0 to 4.5×10^{-9} for (a) (3,0) zz-CNT and (b) (3,3) ac-CNT, $T = 287.5$ K and $\nu = 1$ THz

As nonequilibrium parameter η which is directly proportional to the rate of hot electrons injection increases from 0 (no hot electrons) to 4.5×10^{-9} (presence of hot electrons), the minimum peak decreases and shifts to the left (i.e., low frequency). In the contrary, the maximum peak increases and also shifts to the left (i.e., low frequency) as shown in figure 55.

Furthermore, the behaviour of normalized current density (J_z) as a function of frequency of ac field (ω) as the nonequilibrium parameter (η) is further increased to 23.0×10^{-9} is shown in figure 56

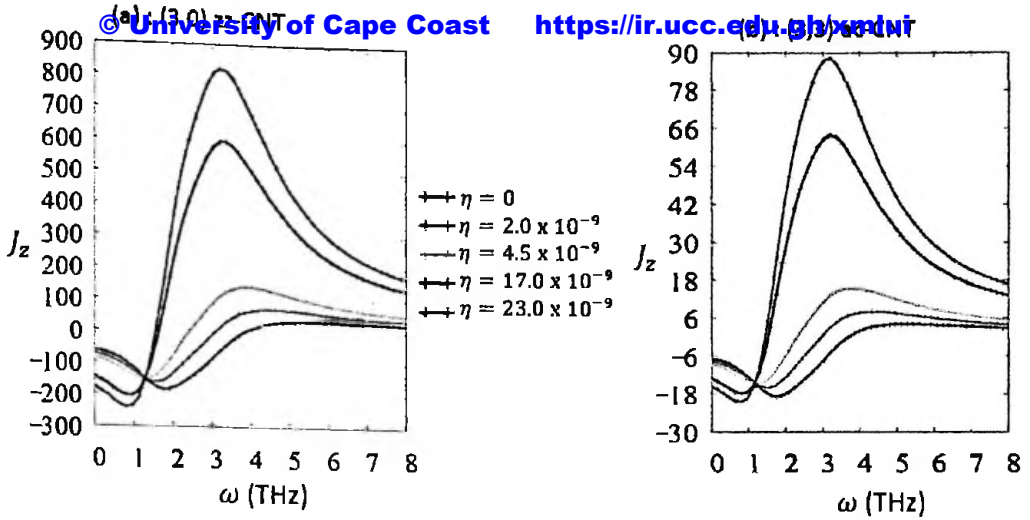


Figure 56: A plot of normalized current density (J_z) versus frequency of ac field (ω) as the nonequilibrium parameter (η) further increases to 23.0×10^{-9} for (a) (3,0) zz-CNT and (b) (3,3) ac-CNT, $T=287.5$ K and $v=1$ THz

As the nonequilibrium parameter η further increases to 23.0×10^{-9} (i.e, strong enough injection rate) , both the minimum and maximum peaks increase and shift to the left (i.e., low frequency) for $\eta \geq 17.0 \times 10^{-9}$. Hence the effect of strong enough injection of hot electrons on high frequency conductivity in CNTs is to increase both the minimum and maximum peaks of normalized current density at lower frequencies.

A 3-dimensional behaviour of the normalized current density (J_z) as a function of the frequency of ac field (ω) and nonequilibrium parameter (η) in order to put the observations in perspective has been displayed in figure 57 as well as figure 58.

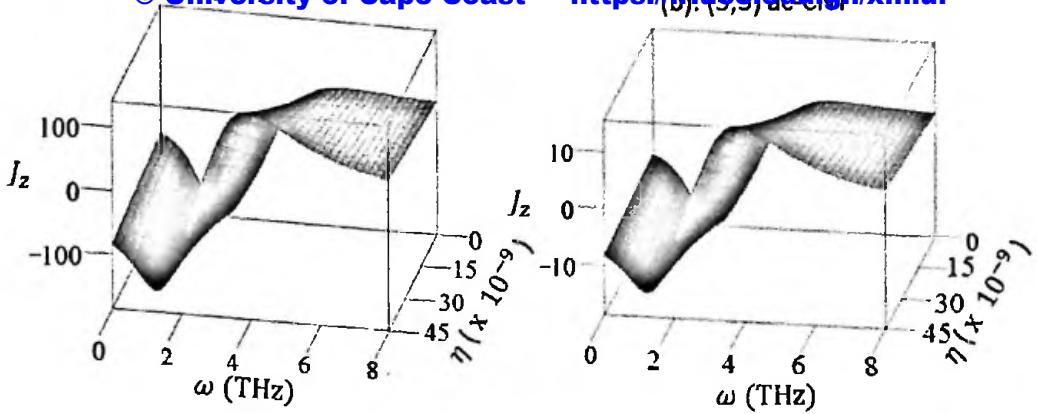


Figure 57: A 3D plot of normalized current density (J_z) versus frequency of ac field (ω) and nonequilibrium parameter (η) as η increases from 0 to 4.5×10^{-9} for (a) (3, 0) zz-CNT and (b) (3,3) ac-CNT, $T = 287.5$ K and $v = 1$ THz

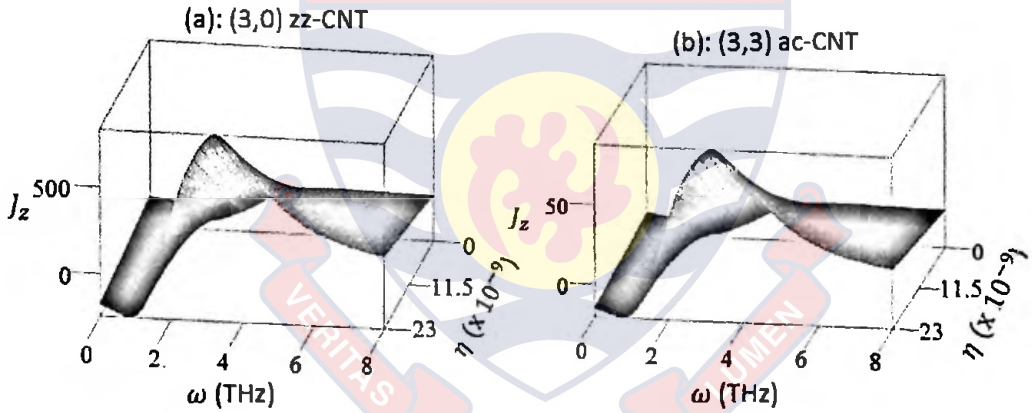
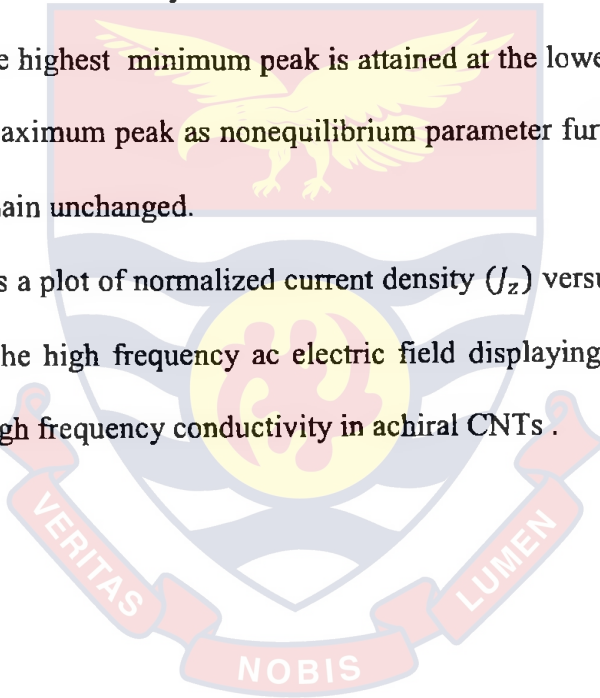


Figure 58 : A 3D plot of normalized current density (J_z) versus frequency of ac field (ω) and nonequilibrium parameter (η) as η further increases to 23.0×10^{-9} for (a) (3,0) zz-CNT and (b) (3,3) ac-CNT, $T = 287.5$ K and $v = 1$ THz

In figure 57, when nonequilibrium parameter η is zero, the minimum peak is the greatest at a relative high frequency while the maximum peak is the least also at high frequency. As nonequilibrium parameter η increases from 0 to 4.5×10^{-9} , the minimum peak gradually decreases and shifts towards left (i.e. low frequency) while the maximum peak slowly increases and also shift towards left (i.e. low frequency)

In figure 58, as nonequilibrium parameter η further increases from 0 to 23.0×10^{-9} , the minimum peak initially decreases and shifts towards left (i.e. low frequency) and then finally increases and shifts towards left (i.e. low frequency) until the highest minimum peak is attained at the lowest frequency. The trend of the maximum peak as nonequilibrium parameter further increases to 23.0×10^{-9} remain unchanged.

Figure 59 is a plot of normalized current density (J_z) versus normalized amplitude (β) of the high frequency ac electric field displaying the effect of hot electrons on high frequency conductivity in achiral CNTs .



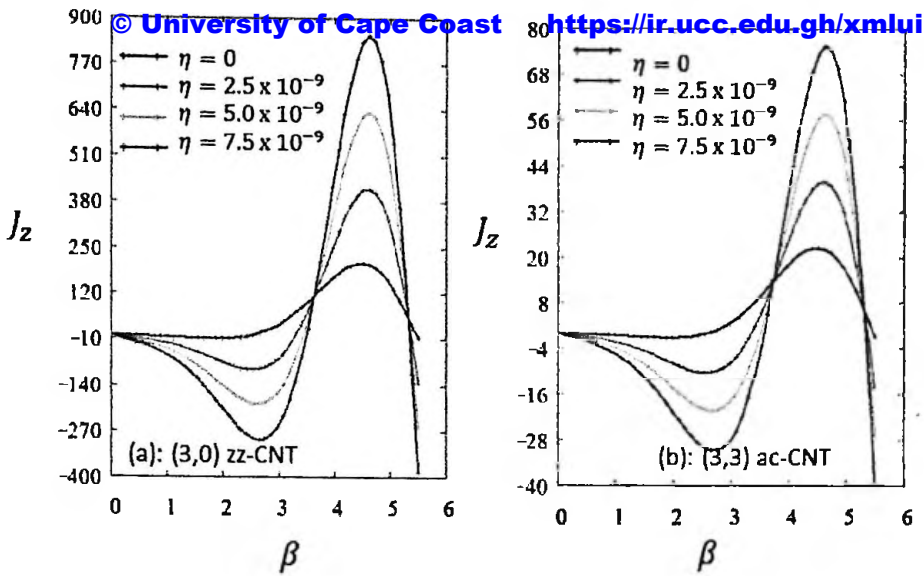


Figure 59: A plot of normalized current density (J_z) versus normalized amplitude (β) of the high frequency ac electric field for (a) (3,0) zz-CNT and (b) (3,3)ac-CNT as the nonequilibrium parameter η increases from 0 to 2.0×10^{-9} , $T = 287.5$ K and $\nu = 1$ THz

As nonequilibrium parameter η which is directly proportional to the rate of hot electrons injection increases from 0 (no hot electrons) to 2.0×10^{-9} (presence of hot electrons), both minimum and maximum peaks of normalized current density increase in magnitude. Therefore, the effect of axial hot electrons injection into achiral CNTs is to increase the magnitude of the peaks of the normalized current density. Consequently, there is an increase in high frequency conductivity as a result of the presence of hot electrons.

To put in perspective the observations, a 3-dimensional behaviour of the normalized current density (J_z) as a function of the normalized amplitude (β) of ac electric field and nonequilibrium parameter (η) is utilized in figure 60

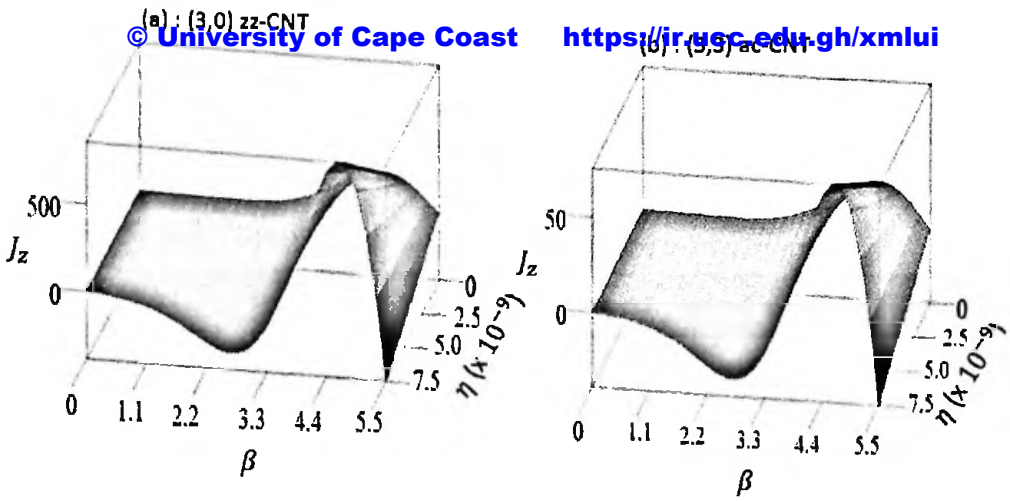


Figure 60: A 3D plot of normalized current density (J_z) versus normalized amplitude (β) of the high frequency ac electric field and nonequilibrium parameter (η) for (a) (3, 0) zz-CNT and (b) (3, 3) ac-CNT, $T = 287.5$ K and $\nu = 1$ THz

In figure 60 these observations are made. The magnitude of the minimum peak as well as maximum peak of the normalized current density (J_z) is at the lowest value when the nonequilibrium parameter $\eta = 0$ (no hot electrons). For both (3,0) zz-CNT and (3,3) ac-CNT, as the nonequilibrium parameter η gradually increases, the minimum peak as well as maximum peak of current density also increases until the highest value is attained when nonequilibrium parameter value $\eta = 7.5 \times 10^{-9}$ as shown in figure 60. Hence a 3 dimensional plot also illustrates the effect of hot electrons on both the minimum and maximum peaks of the normalized current density.

In figure 61, the behaviour of the normalized current density (J_z) as a function of the simultaneously applied dc field (E_z) when frequency of ac field ω is much greater than scattering frequency ν (i.e $\omega \gg \nu$ or $\omega\tau \gg 1$), where $\nu = \tau^{-1}$ for the CNTs stimulated axially with the hot electrons, represented by the nonequilibrium parameter η is now considered.

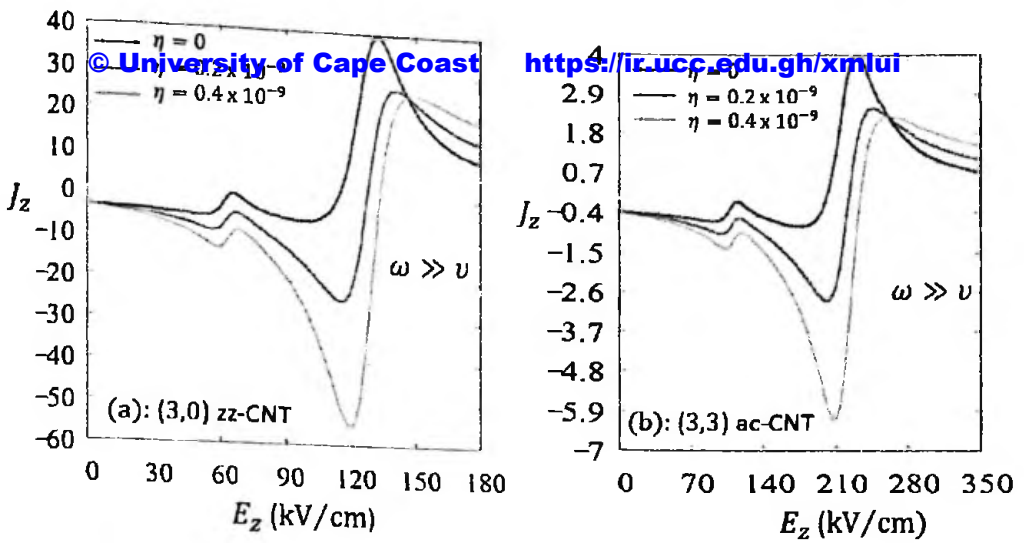


Figure 61: A plot of normalized current density (J_z) versus applied dc-field (E_z) as non equilibrium parameter (η) increases 0 to 0.4×10^{-9} when $\omega \gg \nu$ or $\omega\tau \gg 1$ for (a) (3, 0) zz-CNT and (b) (3, 3) ac-CNT , $T = 287.5 \text{ K}$, $\omega = 10 \text{ THz}$, $\nu = 1 \text{ THz}$ or $\tau = 1 \text{ ps}$ and $\omega\tau = 10$

In figure 61, the normalized current density of each CNT exhibits a non monotonic variation of the intensity as applied dc field E_z increases from 0 to 180 kV/cm and 350 kV/cm for zz-CNT and ac-CNT respectively either in the presence or absence of hot electrons. The dc differential conductivity is negative ($\partial J_z / \partial E_z < 0$) from 0 to about 60 kV/cm and 95 kV/cm for zz-CNT and ac-CNT respectively and then becomes positive ($\partial J_z / \partial E_z > 0$) from 60 kV/cm to about 70 kV/cm and from 95 kV/cm to 120 kV/cm for zz-CNT and ac-CNT respectively. These trends of alternating negative and positive dc-differential conductivities are repeated with different ranges of applied dc field as shown in figure 61. The following observations are made. The positive differential conductivity ($\partial J_z / \partial E_z > 0$) within each range of applied dc -field is nearly the same with or without hot electrons. However, negative differential conductivity ($\partial J_z / \partial E_z < 0$) within each range of applied dc field

increases as we increase nonequilibrium η from zero (no hot electrons) to 0.4×10^{-9} (presence of hot electrons) with exception of a slight decrease in differential conductivity when applied dc field exceeds about 130 kV/cm and 230 kV/cm for zz-CNT and ac-CNT respectively. Within these ranges for both zz-CNT and ac-CNT, the peak normalized current densities fall and shift towards right (i.e. high applied dc field) as nonequilibrium parameter η increases as shown in figure 61.

In figure 62, the rise and further shift towards right as nonequilibrium parameter is increased to 3.0×10^{-9} (i.e. $\eta \geq 2.0 \times 10^{-9}$) is noticed.

Therefore, with strong injection of hot electrons at relatively high applied dc field there is peak rise and further shift towards right as shown in figure 62.

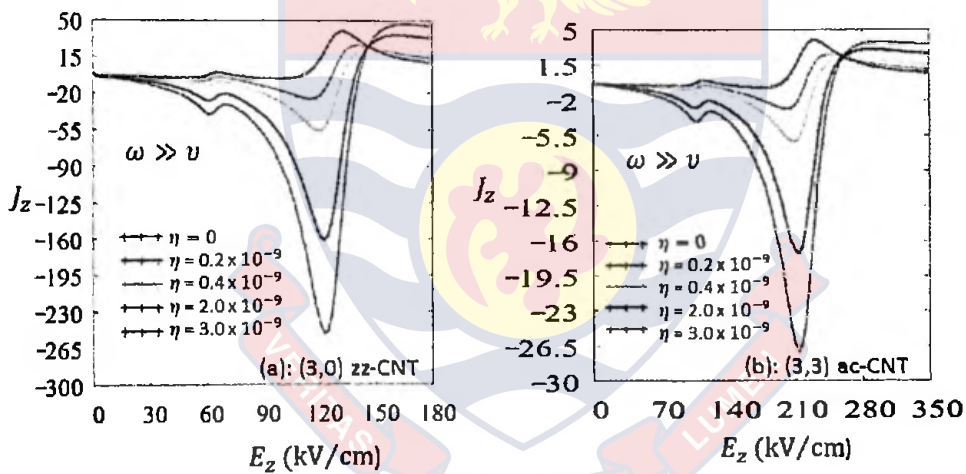


Figure 62: A plot of normalized current density (J_z) versus dc field (E_z) as the nonequilibrium parameter η further increases to 3.0×10^{-9} , when $\omega \gg \nu$ or $\omega\tau \gg 1$ for (a) (3,0) zz-CNT and (b) (3,3)ac-CNT, $T = 287.5$ K, $\omega = 10$ THz, $\nu = 1$ THz or $\tau = 1$ ps and $\omega\tau = 10$

To put these observations in perspective, a 3-dimensional behaviour of the normalized current density (J_z) as a function of the applied dc field (E_z) and nonequilibrium parameter (η) when $\omega \gg \nu$ or $\omega\tau \gg 1$, where $\nu = \tau^{-1}$ has been displayed in figure 63 as well as figure 64.

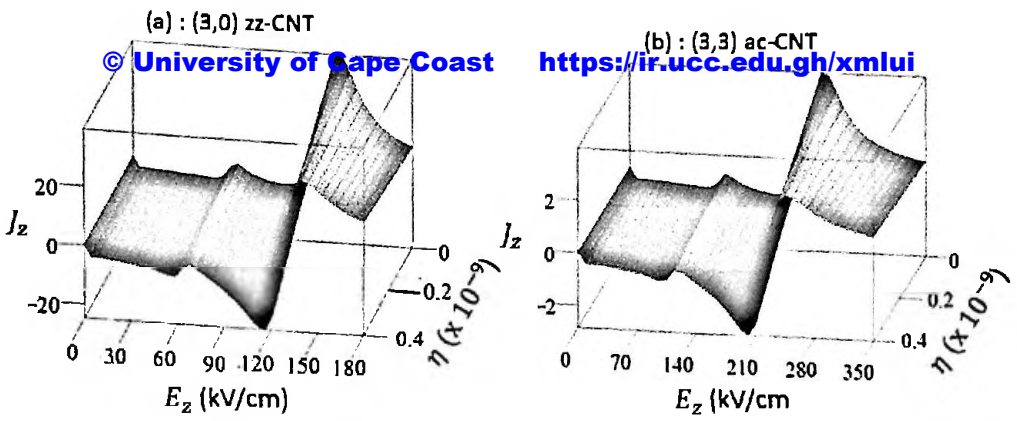


Figure 63: A 3D plot of normalized current density (J_z) versus dc field (E_z) and nonequilibrium parameter (η) when $\omega \gg \nu$ or $\omega\tau \gg 1$ for (a) (3, 0) zz-CNT and (b) (3, 3) ac-CNT, $T = 287.5$ K, $\omega = 10$ THz, $\nu = 1$ THz or $\tau = 1$ ps and $\omega\tau = 10$

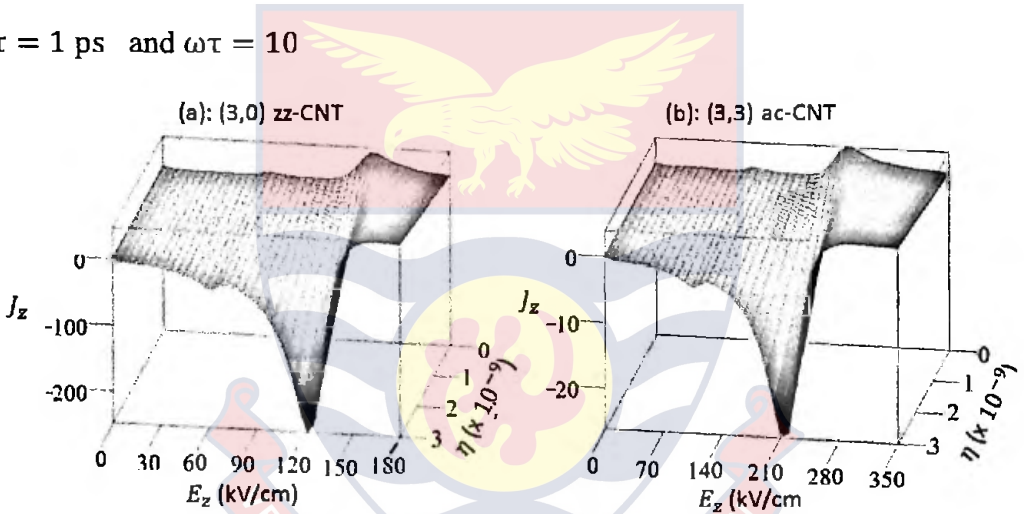


Figure 64: A 3D plot of normalized current density (J_z) versus dc field (E_z) and nonequilibrium parameter (η) when $\omega \gg \nu$ or $\omega\tau \gg 1$ as the rate of hot electrons injection is further increased for (a) (3,0) zz-CNT and (b) (3, 3) ac-CNT, $T = 287.5$ K, $\omega = 10$ THz, $\nu = 1$ THz or $\tau = 1$ ps and $\omega\tau = 10$

As mentioned earlier, as nonequilibrium parameter η increases from 0 to either 0.4×10^{-9} (figure 63) or 3.0×10^{-9} (figure 64), the normalized current density of the CNTs exhibits a non monotonic variation of the intensity as applied dc field increases from 0 to 180 kV/cm and 350 kV/cm for zz-CNT

and ac-CNT respectively. The trend of alternating negative and positive dc-

© University of Cape Coast <https://ir.ucc.edu.gh/xmlui>

differential conductivities with different ranges of applied dc field as

nonequilibrium parameter changes from 0 to 0.4×10^{-9} and 3.0×10^{-9} are displayed by 3D plots in figures 63 and 64 respectively. It has shown for either zz-CNT or ac- CNT, that the peak of the normalized current densities fall and shift towards right (i.e high applied dc field) as nonequilibrium parameter increases from 0 to 0.4×10^{-9} when applied dc field is either greater than 120 kV/cm(zz-CNT) or 210 kV/cm (ac-CNT) in figure 63. As nonequilibrium η further increases to 3.0×10^{-9} , the peak of the normalized current densities rise and shift towards right (i.e. high applied dc field) as shown in figure 64.

The current dynamics of a CNT under conditions where, in addition to the dc field causing a NDC, a similarly strong ac field is present, at a frequency ω somewhat much below the scattering frequency ν ($\omega \ll \nu$ or $\omega\tau \ll 1$, i. e a quasi – static ac electric field) is finally analysed theoretically. Here the ac field plays a twofold role: It suppresses the space-charge instability in CNT and simultaneously pumps an energy for generation and amplification of THz radiation at higher frequency [290]. Figure 65 displays the behaviour of the normalized current density (J_z) as a function of the applied dc field (E_z) when frequency of ac field ω is much less than scattering frequency ν (i.e $\omega \ll \nu$) for the CNTs stimulated axially with the hot electrons, represented by the nonequilibrium parameter η .

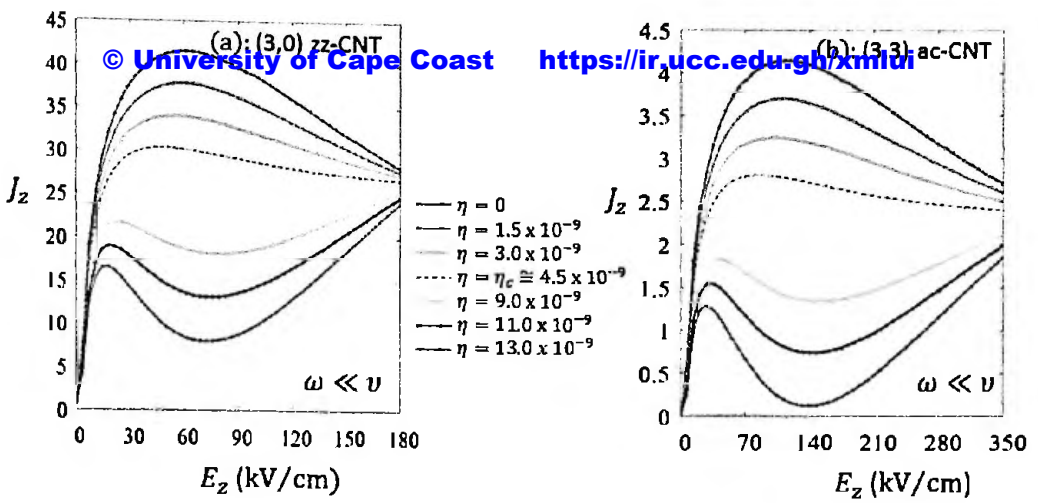


Figure 65: A plot of normalized current density (J_z) versus applied dc field (E_z) as the nonequilibrium parameter η increases from 0 to 13.0×10^{-9} when $\omega \ll \nu$ or $\omega\tau \ll 1$ (i.e. quasi – static case), for (a) (3, 0) zz-CNT and (b) (3, 3) ac-CNT, $T = 287.5$ K, $\omega = 10^{-4}$ THz, $\nu = 1$ THz or $\tau = 1$ ps and $\omega\tau = 10^{-4}$

As nonequilibrium parameter η increases from 0 to 13.0×10^{-9} , the following observations are made. The normalized current density has the highest intensity for $\eta = 0$ (no hot electrons). Upon increasing the hot electrons injection rate, the intensity of the current density decreases and shifts to the left (i.e., low dc fields). This is caused by the scattering effects due to the increase in electron-phonon interactions as well as the increase in the direct injection rate of the hot electrons [287].

Unlike when frequency of ac field ω is much greater than scattering frequency ν (i.e. $\omega \gg \nu$), the normalized current density (J_z) of the CNTs exhibits a linear monotonic dependence on the applied dc field (E_z) at weak field (i.e., the region of ohmic conductivity) when frequency of ac field ω is much less than scattering frequency ν (i.e. $\omega \ll \nu$). As the applied dc field

increases, the normalized current density increases and reaches a maximum, and drops off, experiencing a negative differential conductivity (NDC) for both the zz- CNT and the ac-CNT as shown in figures 16a and 16b, respectively.

As the injection rate of the hot electrons becomes strong enough, the current density up-turned, exhibiting a positive differential conductivity (PDC) near 70 kV/cm and 140 kV/cm for the zz-CNT and the ac-CNT, respectively. In this region, the hot electrons become the dominant determining factor [287]. The physical mechanism behind the switch from NDC to PDC is due to the interplay between the hot electrons pumping frequency (Q/n_0), which is a function of rate of hot electrons injection (Q), and the Bloch frequency (Ω), which depend on the dc field (E_z). At stronger dc field, the rate of scattering of the electrons by phonons is well pronounced resulting in the gradual decrease in the current density with increasing the dc field (NDC region). However, as the rate of hot electrons injection increases, the corresponding rise in the current density due to hot electrons injection now far exceeds the reduction in the current density due to scattering of electrons by phonons. Thus, the net effect on the current density from the two opposing sources (with the hot electrons being dominant) gives rise to the PDC characteristics as shown in figure 16 for $\eta \geq 9.0 \times 10^{-9}$. The desirable effect of a switch from NDC to PDC takes place when η is larger than a critical value $\eta_c \cong 4.5 \times 10^{-9}$. When axial injection of hot electrons into the achiral CNTs is strong enough, the nonequilibrium parameter η exceeds the critical value $\eta_c \cong 4.5 \times 10^{-9}$ and the NDC characteristics change to the PDC characteristics. Thus, the most important tough problem for NDC region which is the space charge instabilities that lead to electric field domains formation

resulting in non uniform electric field distribution which usually destroys the high-frequency Bloch gain can be suppressed due to the switch from the NDC behaviour to the PDC behaviour [289]. This is mainly because PDC is considered as one of the conditions for electric stability of the system necessary for suppressing electric field domains [289]. Hence a critical challenge for the successful observation of THz Bloch gain is the suppression of electric field domains by switching from NDC region to PDC region.

A 3-dimensional behaviour of the normalized current density (J_z) as a function of the applied dc field (E_z) and nonequilibrium parameter (η) when frequency of ac field ω is much less than scattering frequency ν (i.e $\omega \ll \nu$) for each achiral CNT has now been displayed in figure 66,

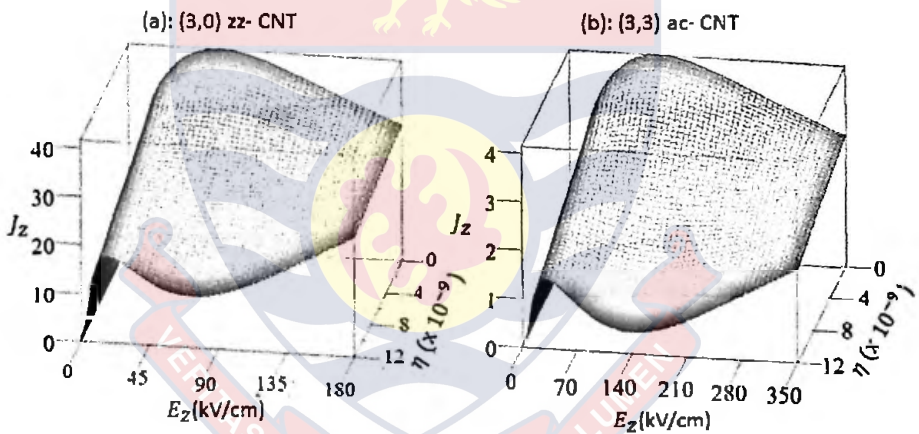


Figure 66: A 3D plot of normalized current density (J_z) versus dc field (E_z) and nonequilibrium parameter (η) when $\omega \ll \nu$ or $\omega\tau \ll 1$

(i. e. quasi – static case),for (a) (3, 0) zz-CNT and (b) (3, 3) ac-CNT,

$$T = 287.5K, \omega = 10^{-4} \text{ THz}, \nu = 1 \text{ THz or } \tau = 1\text{ps and } \omega\tau = 10^{-4}$$

The dc differential conductivity and the peak of the current density are at the highest when the nonequilibrium parameter is zero. For both zz-CNT and ac-CNT, as the nonequilibrium parameter gradually increases the dc differential

conductivity and the peak normalized current density decrease until the critical nonequilibrium parameter value $\eta_c \cong 4.5 \times 10^{-9}$ is reached, beyond which the NDC characteristics slowly changes to PDC characteristics as shown in figure 66

Finally, the behaviour of the normalized current density (J_z) as a function of the applied dc field (E_z) of dc-ac driven fields as $\omega\tau$ increasing from 0.01 to 0.15 when the nonequilibrium parameter $\eta = 0.9 \times 10^{-8}$ (presence of hot electrons) and $\eta = 0$ (absence of hot electrons) for each achiral CNT has been displayed in figure 67.

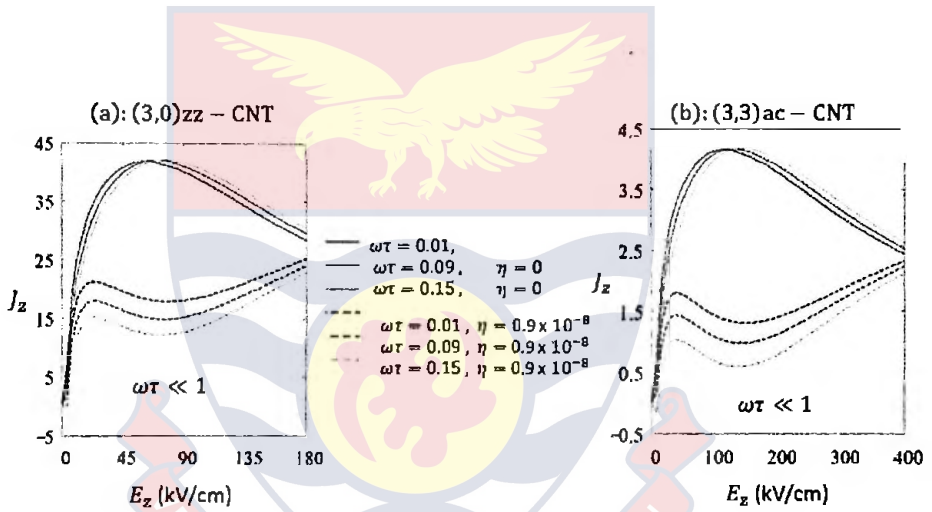
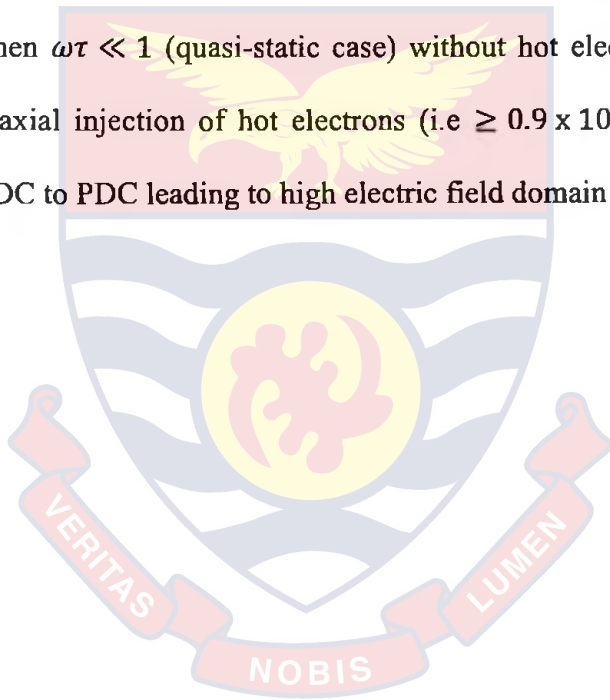


Figure 67: A plot of normalized current density (J_z) versus applied dc field (E_z) as $\omega\tau \ll 1$ increases from 0.01 to 0.17 for (a) (3, 0) zz-CNT and (b) (3, 3) ac-CNT when $\eta = 0$ and $\eta = 0.9 \times 10^{-8}$, $\nu = 1$ THz or $\tau = 1\text{ps}$

As $\omega\tau$ increases from 0.01 to 0.15, the following observations are made from figure 67. The normalized current density has the highest peak at $\omega\tau = 0.01$. Upon increasing the $\omega\tau$, the peak current density decreases until the least peak is attained when $\omega\tau = 0.15$. Furthermore, there is a switch from NDC to PDC

near 75 kV/cm and 140 kV/cm for zz-CNT and ac- CNT respectively so far as
 © University of Cape Coast <https://ir.ucc.edu.gh/xmlui>
 $\omega\tau \ll 1$ (i.e 0.01 to 0.15). Also the differential conductivity ($\partial J/\partial E_z$) in
 NDC region is fairly constant as $\omega\tau$ increases from 0.01 to 0.17. However in
 PDC region after the switch from NDC to PDC, differential conductivity
 ($\partial J/\partial E_z$) fairly increases as $\omega\tau$ increases from 0.01 to 0.15 as shown in figure
 67(a) and 67 (b) for zz-CNT and ac-CNT respectively. In the absence of hot
 electrons ($\eta = 0$), there is a shift of peak current density towards right (i.e
 high dc field) as $\omega\tau$ increases from 0.01 to 0.17 for each achiral CNT. Hence,
 the current density - dc field characteristic shows a negative differential
 conductivity when $\omega\tau \ll 1$ (quasi-static case) without hot electrons and with
 strong enough axial injection of hot electrons (i.e $\geq 0.9 \times 10^{-8}$), there is a
 switch from NDC to PDC leading to high electric field domain suppression.



CHAPTER FIVE

SUMMARY, CONCLUSION AND RECOMMENDATIONS

This chapter is organized into two main parts namely Conclusion and Recommendations. However, a summary of the entire thesis would be given first before conclusion and finally recommendations.

SUMMARY

In summary, within the course of the research that formed this thesis, a comprehensive theoretical model has been developed to compute and investigate the effect of hot electrons on the conductivity of carbon nanotubes. This model is based on utilizing the Boltzmann's transport equation to derive mathematical expression for current density. The current density is expressed as either a function of a homogeneous axial dc field (E_z) or a function of frequency of ac field (ω), normalized amplitude of ac field (β) and simultaneously applied dc field when considering dc-ac driven fields (i.e. high frequency conductivity) without and with axial injection of hot electrons in carbon nanotubes. In order to understand comprehensively the basis of the results, certain physical aspects of the carbon nanotubes have to be kept in mind.

They are:

- i. allotrope of carbon which are long, thin seamless hollow cylinders of graphene with extremely high length-to-diameter aspect ratio of 28000000:1 which is significantly larger than any other material

ii. atomic thick molecules, and the properties of the conducting types, are very uniform

iii. quasi-one dimensional crystals with translational periodicity along the tube axis and the motion of their conducting π electrons are considered as a classical motion of free quasi-particles in the field of crystalline lattice with dispersion law extracted from the quantum theory

By careful considering of the above points, the theoretical model was developed by adopting semiclassical approach. The results obtained by utilizing the model are analyzed and the effect of hot electrons on the conductivity of carbon nanotubes are summarized in the following subsections

- i. effect of hot electrons on the conductivity of carbon nanotubes under the influence of the applied dc field
- ii. effect of hot electrons on high frequency conductivity of carbon nanotubes

Effect of hot electrons on the conductivity of carbon nanotubes under the influence of the applied dc field

In summary, it has been demonstrated that an axial injection of hot electrons into undoped achiral CNTs under constant electric field stimulation leads to changes in the nature of the dc differential conductivity. That is dc differential conductivity switching from NDC characteristics to PDC characteristics near 50 kV/cm and 75 kV/cm for a zz- CNT and an ac- CNT, respectively when critical nonequilibrium parameter (η_c) is exceeded. Thus, the destructive electric domain instability associated with NDC can be suppressed, suggesting a potential generation of terahertz radiations which have enormous promising applications in very different areas of science and technology such

as space astronomy, wideband communications and biosecurity, to name a few [268].

The tunable nature of nonequilibrium parameter (η) due to the interplay between the injection rate of hot electrons (Q) and the Bloch frequency (Ω) suggests the possibility of observing the effect at both low and high (room) temperatures .

Effect of hot electrons on high frequency conductivity of carbon nanotubes

Furthermore, the effect of hot electrons on high frequency conductivity of a CNT under conditions where, in addition to the dc field causing NDC, a similarly strong ac field is applied has been analyzed theoretically. It has been shown that a suitable combination of the dc and ac operating conditions, unwanted electric domains are suppressed. The main dilemma in the realization of THz Bloch oscillation is finding operational conditions which allow simultaneously to achieve gain at THz frequencies and to avoid destructive space-charge instabilities. The electric domains are believed to be destructive for high frequency gain. The ac field plays twofold roles namely the suppression of the space-charge instability in CNT and simultaneously pumping of energy for generation and amplification of THz radiation at higher frequency [290]. It has been also observed that a strong enough injection of hot electrons caused both the minimum and maximum peaks of normalized current density to increase at lower frequencies.

A negative differential conductivity (NDC) is observed for a plot of normalized current density versus dc field of dc-ac driven fields on the condition that the frequency of ac field ω is much less than the scattering frequency ν ($\omega \ll \nu$ or $\omega\tau \ll 1$, $\nu = \tau^{-1}$ i. e. quasi – static case).

The desirable effect of dc differential conductivity switching from NDC characteristics to PDC characteristics in quasi-static state occurs as usual when critical nonequilibrium parameter (η_c) is exceeded. The switching occurs about 75 kV/cm and 140 kV/cm for a zz- CNT and an ac- CNT, respectively as compared to about 50 kV/cm and 75 kV/cm for a zz- CNT and an ac- CNT, respectively under the influence applied dc field only.

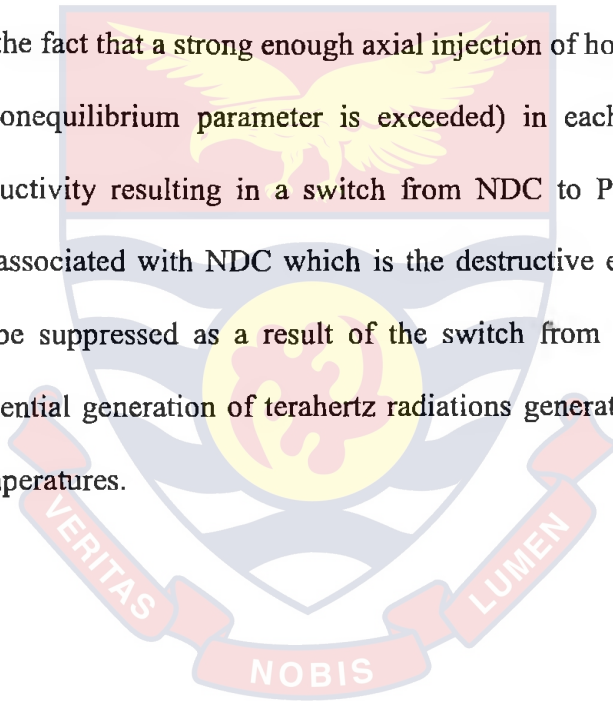
The observed notable differences between the desirable effect of switching from NDC to PDC under the influence of quasi-static case of dc-ac driven fields and dc field only are summarised as follows:

- i. the critical dc field at which NDC occurs is greater in the quasi-static case of dc-ac driven fields than that of dc field only
- ii. the differential conductivity ($\partial J_z / \partial E_z$) of the quasi-static case of dc-ac driven fields is higher than that of dc field only.
- iii. hot electrons injection rate beyond which there is a switch from NDC to PDC represented by critical nonequilibrium parameter (η_c) is lower for the quasi-static case of dc-ac driven fields than that of dc field only (i.e. $\eta_c \cong 4.5 \times 10^{-9}$ for quasi – static case of ac – dc driven fields and $\eta_c \cong 9.0 \times 10^{-9}$ for dc field only)

The differences are solely attributed to the presence of high frequency ac field.

CONCLUSION

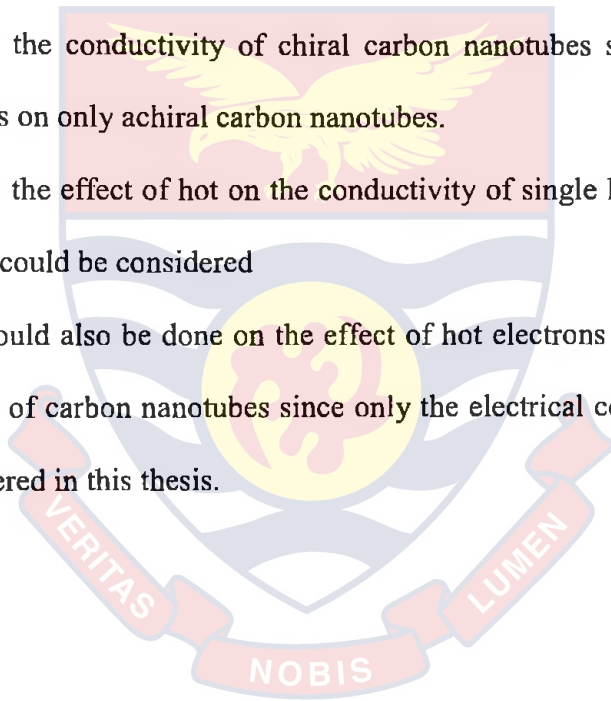
In conclusion, the main aspects of nonequilibrium hot electron phenomena in achiral carbon nanotubes have been studied and a comprehensive theoretical model developed to compute and investigate the effect of hot electrons on the conductivity of achiral carbon nanotubes. The effect of hot electrons on the conductivity of carbon nanotube is desirable although hot electron phenomena in many cases are nuisance [1]. This could be attributed to the fact that a strong enough axial injection of hot electrons (i.e. when critical nonequilibrium parameter is exceeded) in each achiral CNT affects its conductivity resulting in a switch from NDC to PDC. Thus, the tough problem associated with NDC which is the destructive electric domain instability can be suppressed as a result of the switch from NDC to PDC, predicting a potential generation of terahertz radiations generation at low and high (room) temperatures.



RECOMMENDATIONS

Research work presented in this thesis on the effect of hot electrons on the conductivity of carbon nanotubes opens up a range of possibilities for further research work in this area. Briefly, these possibilities are:

- i. this work could also be done using doped achiral carbon nanotubes instead of undoped types considered.
- ii. the extension of this work could probably be to investigate the effect of hot electrons on the conductivity of chiral carbon nanotubes since the work done so far is on only achiral carbon nanotubes.
- iii. the study of the effect of hot on the conductivity of single layer Graphene Nanoribbon could be considered
- iv. a research could also be done on the effect of hot electrons on the thermal conductivity of carbon nanotubes since only the electrical conductivity has been considered in this thesis.



REFERENCES

- [1] Balkan. N. *Hot electrons in semiconductors: physics and devices*. no. 5. Oxford University Press, 1998
- [2] Craighead H. G. "Nanoelectromechanical systems." *Science* 290, no. 5496 (2000): 1532-1535.
- [3] Roukes M.. "Nanoelectromechanical systems face the future." *Physics World* 14, no. 2 (2001): 25.
- [4] Burg B. R. and Poulidakos D. "Large-scale integration of single-walled carbon nanotubes and graphene into sensors and devices using dielectrophoresis: A review." *Journal of materials research* 26 no. 13 (2011): 1561-1571.
- [5] Luryi S. and Kastalsky A. "Hot-electron transport in heterostructure devices." *Physica B+ C* 134, no. 1-3 (1985): 453-465.
- [6] Xing D. Y. and Liu M. "Nonequilibrium statistical operator in hot electron transport theory." *International Journal of Modern Physics B* 6 no. 07 (1992): 1037-1057.
- [7] Mehrabova M. A. "The modeling of calculations of thermodynamic and electronic parameters of hot electrons in a quantum well ". *International Journal of Energy* 4, no. 04 (2010):63-70.
- [8] Conwell E. M. *High field transport in semiconductors*. no. 9

- [9] Kaganov M. I., Lifshitz I. M. and Tanatarov L. V. "Relaxation between electrons and the crystalline lattice." *Soviet Physics JETP-USSR* 4, no. 2 (1957): 173-178.
- [10] Sze S. M. and Ng K. K. *Physics of semiconductor devices*. John Wiley & Sons, 2006.
- [11] Sze S. M. *Semiconductor devices: physics and technology*. John Wiley & Sons, 2008.
- [12] Gunn J. B. "Microwave oscillations of current in III-V semiconductors." *Solid State Communications* 1, no. 4 (1963): 88-91.
- [13] Kroemer H. "Theory of the Gunn effect." *Proceedings of the IEEE* 52, no. 12 (1964): 1736-1736.
- [14] Ridley B. K. and Watkins T. B. "The possibility of negative resistance effects in semiconductors." *Proceedings of the Physical Society* 78, no. 2 (1961): 293
- [15] Hilsum C. "Transferred electron amplifiers and oscillators." *Proceedings of the IRE* 50, no. 2 (1962): 185-189.
- [16] Bosch B. G. and Richard Engelmann R. W. "Gunn-effect electronics." *New York, Halsted Press*, (1975): 445
- [17] Shur M. S. *GaAs devices and circuits*. Springer Science & Business Media, 2013.
- [18] Shur M. "Physics of Semiconductor Devices Prentice-Hall." *Inc., Englewood Cliffs, New Jersey* (1990): 680.
- [19] Frohman-Bentchkowsky D. "Memory behavior in a floating-gate avalanche-injection MOS (FAMOS) structure." *Applied Physics Letters* 165

- [20] Semenov A. D., Gol'tsman G. N. and Sobolewski R. "Hot electron effect in superconductors and its applications for radiation sensors." *Superconductor Science and Technology* 15, no. 4 (2002): R1.
- [21] Dresselhaus M. S., Dresselhaus G., Sugihara K., Spain I. L. and Goldberg H.A. *Graphite fibers and filaments*. Vol. 5. Springer Science & Business Media, 2013.
- [22] Wyckoff R. W. G. and Wyckoff R. W. *Crystal structures*. Vol. 1. New York: Interscience, 1960.
- [23] Saito R., Dresselhaus G. and Dresselhaus M. S. *Physical properties of carbon nanotubes*. Vol. 35. London: Imperial college press, 1998
- [24] Harris P. J. and Harris P. J. F. *Carbon nanotubes and related structures: new materials for the twenty-first century*. Cambridge university press, 2001.
- [25] Goel R. K. and Panwar A. "Carbon Nano Tubes: A New Approach in Material Science" *International Journal of Latest Research in Science and Technology* 1 no. 2 (2012):155-158.
- [26] Sagadevan S. "Recent Trends on Nanostructures Based Solar Energy Applications: A Review." *Rev. Adv. Mater. Sci* 34 (2013): 44-61.
- [27] Pan Z. W., Xie S. S., Chang B. H., Wang C. Y., Lu L., Liu W. , Zhou W. Y., Li W. Z. and Qian L. X. "Very long carbon nanotubes." *Nature* 394, no. 6694 (1998): 631-632.
- [28] Lichtfouse E, Schwarzbauer J and Robert D. eds. *Environmental chemistry for a sustainable world: volume 1: remediation of air and*

- [29] Mourachkine A. *Room-temperature superconductivity*. Cambridge Int Science Publishing, 2004.
- [30] Iijima S. "Helical microtubules of graphitic carbon." *nature* 354, no. 6348 (1991): 56-58
- [31] Ishikawa H. , Fudetani S. and Hirohashi M. "Mechanical properties of thin films measured by nanoindenters." *Applied surface science* 178, no. 1 (2001): 56-62.
- [32] Kracke B., and Damaschke B. "Measurement of nanohardness and nanoelasticity of thin gold films with scanning force microscope." *Applied Physics Letters* 77, no. 3 (2000): 361-363.
- [33] Chuan H.C. "Modeling and analysis of ballistic carbon nanotube field effect transistor (CNTFET) with quantum transport concept." PhD diss., Universiti Teknologi Malaysia, 2007.
- [34] Dresselhaus M. S., Dresselhaus G. and Jorio A. "Unusual properties and structure of carbon nanotubes." *Annu. Rev. Mater. Res.* 34 (2004): 247-278.
- [35] Martel R., Schmidt T., Shea H. R., Hertel T. and Avouris P "Single – and multi-wall carbon nanotube field-effect transistors." *Applied Physics Letters* 73, no. 17 (1998): 2447-2449.
- [36] Maruyama S., Kojima R. , Miyauchi Y., Chiashi S, and Kohno M "Low-temperature synthesis of high-purity single-walled carbon nanotubes from alcohol." *Chemical physics letters* 360, no. 3 (2002): 229-234.
- [37] Zhou Y., Gaur A., Hur S.H., Kocabas C., Meitl M.A., Shim M. and

Rogers J.A., "P-channel, n-channel thin film transistors and pn diodes based on single wall carbon nanotube networks." *Nano Letters* 4, no. 10 (2004): 2031-2035.

- [38] Sethi R. and Soni G., "Comparative Analysis of Si-MOSFET and CNFET-Based 28T Full Adder." In *Proceedings of Fifth International Conference on Soft Computing for Problem Solving*, pp. 439-451. Springer Singapore, 2016.
- [39] Forró L. and Schönenberger C "Carbon nanotubes, materials for the future." *europhysics news* 32, no. 3 (2001): 86-90.
- [40] Kroto H.W., Heath J.R., O'Brien S.C., Curl R.F. and Smalley R.E., "C 60: buckminsterfullerene." *Nature* 318, no. 6042 (1985): 162-163.
- [41] Kratschmer W., Lamb L.D., Fostiropoulos K. and Huffman D.R. "Solid C60: a new form of carbon." *Nature* 347 (1990): 27.
- [42] Haddon R.C., Hebard A.F., Rosseinsky M.J., Murphy D.W., Duclos S. J., Lyons K.B., Miller B., Rosamilia J.M., Fleming R.M., Kortan A.R and Glarum S.H. "Conducting films of C60 and C70 by alkali-metal doping." *Nature* 350, no. 6316 (1991): 320-322.
- [43] Aghabozorg H.R., Mousavi R., Asckari S. and Aghabozorg H. "Effects of synthesis methods of vanadium oxide nanotubes on the inter layer distances." *Journal of Nanoparticle Research* 9, no. 3 (2007): 497-500.
- [44] Saito R., Fujita M., Dresselhaus G. and Dresselhaus M.S. "Electronic structure of graphene tubules based on C 60." *Physical Review B* 46, no. 3 (1992): 1804.
- [45] Li Y., Mann D., Rolandi M., Kim W., Ural A., Hung S., Javey A., Cao

semiconducting single-walled carbon nanotubes by a plasma enhanced CVD method." *Nano Letters* 4, no. 2 (2004): 317-321.

- [46] Pal A.K., Roy R.K., Mandal S.K., Gupta S. and Deb B. "Electrodeposited carbon nanotube thin films." *Thin Solid Films* 476, no. 2 (2005): 288-294.
- [48] Iijima S. and Ichihashi T. "Single-shell carbon nanotubes of 1-nm diameter." (1993): 603-605.
- [49] Bethune D.S., Klang C.H., De Vries M.S., Gorman G., Savoy R., Vazquez J. and Beyers R. "Cobalt-catalysed growth of carbon nanotubes with single-atomic-layer walls." (1993): 605-607.
- [50] Ajayan P. M. "Nanotubes from carbon." *Chemical reviews* 99, no. 7 (1999): 1787-1800.
- [51] Guo T., Nikolaev P., Thess A., Colbert D.T. and Smalley R.E. "Catalytic growth of single-walled nanotubes by laser vaporization." *Chemical physics letters* 243, no. 1 (1995): 49-54.
- [52] Nikolaev P., Bronikowsk M.J., Bradley R.K., Rohmund F., Colbert D.T., Smith K.A. and Smalley R.E. "Gas-phase catalytic growth of single-walled carbon nanotubes from carbon monoxide." *Chemical physics letters* 313, no. 1 (1999): 91-97.
- [53] Bacon R. "Growth, structure, and properties of graphite whiskers." *Journal of Applied Physics* 31, no. 2 (1960): 283-290.
- [54] Liu B.C., Liang Q., Tang S.H., Guo L.Z., Zhang B.L., Qu M.Z. and Yu

using fluidized-bed reactor." *Chinese Chemical Letters* 11, no. 11
(2000): 1031-1034.

- [55] Weidenkaff A., Ebbinghaus S.G., Mauron P., Reller A., Zhang Y. and Züttel A. "Metal nanoparticles for the production of carbon nanotube composite materials by decomposition of different carbon sources." *Materials Science and Engineering: C* 19, no. 1 (2002): 119-123.
- [56] Mubarak N.M., Abdullah E.C., Jayakumar N.S. and Sahu J.N. "An overview on methods for the production of carbon nanotubes." *Journal of Industrial and Engineering Chemistry* 20, no. 4 (2014): 1186-1197.
- [57] Wiles P. G. and Abrahamson J. "Carbon fibre layers on arc electrodes: their properties and cool-down behaviour." *Carbon* 16, no. 5 (1978): 341-349.
- [58] Baker, R.T.K., Barber M.A., Harris P.S., Feates F.S. and Waite R.J.. "Nucleation and growth of carbon deposits from the nickel catalyzed decomposition of acetylene." *Journal of catalysis* 26, no. 1 (1972): 51-62.
- [59] Venegoni D., Serp P., Feurer R., Kihn Y., Vahlas C. and Kalck P. "Parametric study for the growth of carbon nanotubes by catalytic chemical vapor deposition in a fluidized bed reactor." *Carbon* 40, no. 10 (2002): 1799-1807.
- [60] Qian W., Yu H., Wei F., Zhang Q. and Wang Z. "Synthesis of

Carbon 40, no. 15 (2002): 2968-2970.

- [61] Zhang M. and Li J. "Carbon nanotube in different shapes." *Materials today* 12, no. 6 (2009): 12-18.
- [62] Zhang Q. ed. *Carbon nanotubes and their applications*. CRC Press, 2012.
- [63] Oberlin, A., Endo, M. and Koyama, T. "Filamentous growth of carbon through benzene decomposition." *Journal of crystal growth* 32, no. 3 (1976): 335-349.
- [64] Kürti J. and Zólyomi V. "Theoretical Investigation of Small Diameter Single-Wall Carbon Nanotubes." In *Molecular Nanostructures: XVII International Winterschool Euroconference on Electronic Properties of Novel Materials*, vol. 685, no. 1, AIP Publishing, (2003):456-459
- [65] Hirleka R., Yamagar M., Garse H., Vij M. and Kadam V. "Carbon nanotubes and its applications: a review." *Asian Journal of Pharmaceutical and Clinical Research* 2, no. 4 (2009): 17-27.
- [66] Pudlak M., Pincak R. and Osipov V.A. "Electronic structures of double-layer zig-zag carbon nanotube." In *Journal of Physics: Conference Series*, vol. 129, no. 1, p. 012011. IOP Publishing, 2008
- [67] Karniadakis, G.E., Beskok, A. and Aluru, N. *Microflows and nanoflows: fundamentals and simulation*. Vol. 29. Springer Science & Business Media, 2006.
- [68] Belin T. and Epron F. Epron. "Characterization methods of carbon

no. 2 (2005): 105-118

- [69] Wilder, J.W., Venema, L.C., Rinzler, A.G., Smalley, R.E. and Dekker, C.
"Electronic structure of atomically resolved carbon nanotubes." *Nature*
391, no. 6662 (1998): 59-62.
- [70] Dresselhaus M.S, Dresselhaus G, and Avouris P. *Carbon nanotubes: synthesis, structure, properties and applications*. Berlin: Springer-Verlag; 2001.
- [71] Charlier, J.C., Blase, X. and Roche, S. "Electronic and transport properties of nanotubes." *Reviews of modern physics* 79, no. 2 (2007): 677
- [72] Landi B.J., Ganter M.J., Cress C.D., DiLeo R.A. and Raffaele R.P.
"Carbon nanotubes for lithium ion batteries." *Energy & Environmental Science* 2, no. 6 (2009): 638-654.
- [73] El-Barbary A. "First principles characterisation of defects in irradiated graphitic materials." PhD diss., University of Sussex, 2005.
- [74] Clauss W., Bergeron D.J. and Johnson A.T. "Atomic resolution STM imaging of a twisted single-wall carbon nanotube." *Physical Review B* 58, no. 8 (1998): R4266.
- [75] Wilder J.W., Venema L.C., Rinzler A.G., Smalley R.E. and Dekker C.
"Electronic structure of atomically resolved carbon nanotubes." *Nature*
391, no. 6662 (1998): 59-62.
- [76] Odom T.W., Huang J.L., Kim P. and Lieber C.M. "Atomic structure and electronic properties of single-walled carbon nanotubes." *Nature*

- [77] Tans, S.J., Devoret, M.H., Dai, H., Thess, A., Smalley, R.E., Georlga, L.J. and Dekker, C. "Individual single-wall carbon nanotubes as quantum wires." *Nature* 386 no. 6624 (1997): 474-477
- [78] Sinha N. and Yeow J.T. "Carbon nanotubes for biomedical applications." *NanoBioscience, IEEE Transactions on* 4, no. 2 (2005): 180-195
- [79] Iijima S., Ajayan P.M. and Ichihashi T. "Growth model for carbon nanotubes." *Physical review letters* 69, no. 21 (1992): 3100.
- [80] Ebbesen T. W. and Ajayan P. M. "Large-scale synthesis of carbon nanotubes." *Nature* 358, no. 6383 (1992): 220-222.
- [81] Liu C., Cong H.T., Li F., Tan P.H., Cheng H.M., Lu K. and Zhou B.L. "Semi-continuous synthesis of single-walled carbon nanotubes by a hydrogen arc discharge method." *Carbon* 37, no. 11 (1999): 1865-1868.
- [82] Antisari M.V., Marazzi R. and Krsmanovic R. "Synthesis of multiwall carbon nanotubes by electric arc discharge in liquid environments." *Carbon* 41, no. 12 (2003): 2393-2401.
- [83] Zhu H.W., Jiang B., Xu C.L. and Wu D.H. "Synthesis of high quality single-walled carbon nanotube silks by the arc discharge technique." *The Journal of Physical Chemistry B* 107, no. 27 (2003): 6514-6518
- [84] Li, Huanjun, Lunhui Guan, Zujin Shi, and Zhennan Gu. "Direct synthesis of high purity single-walled carbon nanotube fibers by arc discharge." *The*

- [85] Journet C., Maser W.K., Bernier P., Loiseau A., De La Chapelle M.L., Lefrant D.L.S., Deniard P., Lee R. and Fischer J.E. "Large-scale production of single-walled carbon nanotubes by the electric-arc technique." *nature* 388, no. 6644 (1997): 756-758.
- [86] Thess A., Lee R., Nikolaev P. and Dai H. "Crystalline ropes of metallic carbon nanotubes." *Science-AAAS-Weekly Paper Edition* 273, no. 5274 (1996): 483-487.
- [87] Braidy N., El Khakani M.M. and Botton G.G. "Carbon nanotubular structures synthesis by means of ultraviolet laser ablation." *Journal of materials research* 17, no. 09 (2002): 2189-2192
- [88] Takahashi S., Ikuno T., Oyama T., Honda S.I., Katayama M., Hirao T. and Oura K. "Synthesis and characterization of carbon nanotubes grown on carbon particles by using high vacuum laser ablation," *J. Vac. Soc. Jpn.*, vol. 45, no. 7 (2002) : 609–61
- [89] Vander Wal R.L., Berger G.M. and Tichich T.M. "Carbon nanotube synthesis in a flame using laser ablation for in situ catalyst generation." *Applied Physics A* 77, no. 7 (2003): 885-889.
- [90] José-Yacamán M., Miki-Yoshida M., Rendon L. and Santiesteban J.G. "Catalytic growth of carbon microtubules with fullerene structure." *Applied physics letters* 62, no. 2 (1993): 202-204
- [91] Li W.Z., Xie S.S., Qian L. and Chang B.H. "Large-scale synthesis of aligned carbon nanotubes." *Science* 274, no. 5293 (1996): 1701–1703
- [92] Qin L. C. "CVD synthesis of carbon nanotubes." *Journal of materials science letters* 16, no. 6 (1997): 457-459.

- [93] Choi Y.C., Bae D.J., Lee Y.H., Lee B.S., Park G.S., Choi W.B., Lee N.S. and Kim J.M. "Growth of carbon nanotubes by microwave plasma-enhanced chemical vapor deposition at low temperature." *Journal of Vacuum Science & Technology A* 18, no. 4 (2000): 1864-1868.
- [94] Varadan V.K. and Xie J. "Large-scale synthesis of multi-walled carbon nanotubes by microwave CVD." *Smart materials and structures* 11, no. 4 (2002): 610.
- [95] Chatterjee A.K., Sharon M., Banerjee R. and Neumann-Spallart M. "CVD synthesis of carbon nanotubes using a finely dispersed cobalt catalyst and their use in double layer electrochemical capacitors." *Electrochimica Acta* 48, no. 23 (2003): 3439-3446.
- [96] Park D., Kim Y.H. and Lee J.K. "Synthesis of carbon nanotubes on metallic substrates by a sequential combination of PECVD and thermal CVD." *Carbon* 41, no. 5 (2003): 1025-1029.
- [97] Chaisitsak S., Yamada A. and Konagai M. "Hot filament enhanced CVD synthesis of carbon nanotubes by using a carbon filament." *Diamond and related materials* 13, no. 3 (2004): 438-444.
- [98] Mukhopadhyay K., Lal D., Ram K. and Mathur G.N. "Synthesis of two dimensional quasi-aligned carbon nanotube bundles by a catalytic chemical vapour deposition method— an inside story." *Smart materials and structures* 13, no. 1 (2004): N5.
- [99] Seidel R., Duesberg G.S., Unger E., Graham A.P., Liebau M. and Kreupl F. "Chemical vapor deposition growth of single-walled carbon nanotubes at 600 C and a simple growth model." *The Journal of*

- [100] Vohs J.K., Brege J.J., Raymond J.E., Brown A.E., Williams G.L. and Fahlman B.D. "Low-temperature growth of carbon nanotubes from the catalytic decomposition of carbon tetrachloride." *Journal of the American Chemical Society* 126, no. 32 (2004): 9936-9937.
- [101] Koziol K., Boskovic B.O. and Yahya N. "Synthesis of carbon nanostructures by CVD method." In *Carbon and Oxide Nanostructures*, pp. 23-49. Springer Berlin Heidelberg, 2010.
- [102] Ebbesen T.W. "Production and purification of carbon nanotubes." *Carbon Nanotubes: Preparation and Properties* (1997): 139-162.
- [103] Dai, H. "Nanotube growth and characterization." In *Carbon Nanotubes*, pp. 29-53. Springer Berlin Heidelberg, 2001.
- [104] Popov V. N. "Carbon nanotubes: properties and application." *Materials Science and Engineering: R: Reports* 43, no. 3 (2004): 61-102.
- [105] Dai H. "Carbon nanotubes: opportunities and challenges." *Surface Science* 500, no. 1 (2002): 218-241.
- [106] Thiên-Nga L., Bonard J.M., Gáal R., Forró L. and Hernadi K. "Comparison of catalytically grown and arc-discharge carbon nanotube tips." *Applied physics letters* 80, no. 5 (2002): 850-852.
- [107] Ebbesen T.W., Ajayan P.M. and Tanigaki K. "Purification of nanotubes." *Nature* 367, no. 6463 (1994): 519-519.
- [108] Gajewski S., Maneck H.E., Knoll U., Neubert D., Dörfel I., Mach R., Strauss B. and Friedrich J.F. "Purification of single walled carbon nanotubes by thermal gas phase oxidation." *Diamond and related*

- [109] Hiura H., Ebbesen T.W. and Tanigaki K. "Opening and purification of carbon nanotubes in high yields." *Advanced Materials* 7, no. 3 (1995): 275-276.
- [110] Vaccarini L., Goze C., Aznar R., Micholet V., Journet C. and Dernier P. "Purification procedure of carbon nanotubes." *Synthetic Metals* 103, no. 1 (1999): 2492-2493.
- [111] Kim H.Y., Choi W.B., Lee N.S., Chung D.S., Kang J.H., Han I.T., Kim J.M., Moon M.H. and Kim J.S. "Purification and characterization of single-walled carbon nanotubes." In *MRS Proceedings*, vol. 593, p. 123. Cambridge University Press, 1999.
- [112] Bandow S., Rao A.M., Williams K.A., Thess A., Smalley R.E. and Eklund P.C. "Purification of single-wall carbon nanotubes by microfiltration." *The Journal of Physical Chemistry B* 101, no. 44 (1997): 8839-8842.
- [113] Xu C., Flahaut E., Bailey S.R., Brown G., Sloan J., Coleman K.S., Williams V.C. and Green M.L. "Purification of single-walled carbon nanotubes grown by a chemical vapour deposition (CVD) method." *Chemical Research in Chinese Universities* 18, no. 2 (2002): 130-132
- [114] Biro L.P., Khanh N.Q., Vertesy Z., Horvath Z.E., Osvath Z., Koos A., Gyulai J., Kocsonya A., Konya Z., Zhang X.B. and Van Tendeloo G. "Catalyst traces and other impurities in chemically purified carbon nanotubes grown by CVD." *Materials Science and Engineering: C* 19, no. 1 (2002): 9-13.

- [115] Shelimov K.B., Esenaliev R.O., Rinzler A.G., Huffman C.B. and © University of Cape Coast <https://ir.ucc.edu.gh/xmlui> Smalley R.E. "Purification of single-wall carbon nanotubes by ultrasonically assisted filtration." *Chemical Physics Letters* 282, no. 5 (1998): 429-434.
- [116] Dujardin E., Ebbesen T.W., Krishnan A. and Treacy M.M. "Purification of single-shell nanotubes." *Advanced Materials* 10, no. 8 (1998): 611-613.
- [117] Harutyunyan A.R., Pradhan B.K., Chang, J., Chen G. and Eklund P.C. "Purification of single-wall carbon nanotubes by selective microwave heating of catalyst particles." *The Journal of Physical Chemistry B* 106, no. 34 (2002): 8671-8675.
- [118] Ko C.J., Lee C.Y., Ko F.H., Chen H.L. and Chu T.C. "Highly efficient microwave-assisted purification of multiwalled carbon nanotubes." *Microelectronic engineering* 73 (2004): 570-577.
- [119] Guo T., Nikolaev P., Thess A., Colbert D.T. and Smalley R.E. "Catalytic growth of single-walled nanotubes by laser vaporization." *Chemical physics letters* 243, no. 1 (1995): 49-54.
- [120] José-Yacamán M., Miki-Yoshida M., Rendon L. and Santiesteban J.G. "Catalytic growth of carbon microtubules with fullerene structure." *Applied physics letters* 62, no. 2 (1993): 202-204.
- [121] Saito R., Takeya T., Kimura T., Dresselhaus G. and Dresselhaus M.S. "Raman intensity of single-wall carbon nanotubes." *Physical Review B* 57, no. 7 (1998): 4145.
- [122] Dresselhaus M., Dresselhaus G., Eklund P. and Saito R. "Carbon

- [123] Dresselhaus M.S., Dresselhaus G. and Eklund P.C. *Science of fullerenes and carbon nanotubes: their properties and applications*. Academic press, 1996.
- [124] Grove-Rasmussen K. and Jorgensen T. "Electrical properties of carbon nanotubes." *Bachelor thesis, Niels Bohr Institute* (2000).
- [125] White C.T. and Mintmire J.W. "Density of states reflects diameter in nanotubes." *Nature* 394, no. 6688 (1998): 29-30.
- [126] Venema L.C., Wildöer J.W.G., Dekker C., Rinzler G.A. and Smalley R.E. "STM atomic resolution images of single-wall carbon nanotubes." *Applied Physics A: Materials Science & Processing* 66 (1998): S153-S155.
- [127] Kittel C. *Introduction to solid state physics*. Wiley, 2005.
- [128] Seidel R. V. "Carbon Nanotube Devices" PhD Thesis (2004)
- [129] Collins, P.G. and Avouris, P. "Nanotubes for electronics." *Scientific american* 283, no. 6 (2000): 62-69.
- [130] Saito R., Fujita M., Dresselhaus G. and Dresselhaus M.S. "Electronic structure of graphene tubules based on C 60." *Physical Review B* 46, no. 3 (1992): 1804.
- [131] Suenaga K., Okazaki T., Wang C.R., Bandow S., Shinohara H. and Iijima, S. "Direct Imaging of Sc₂@C₈₄ Molecules Encapsulated Inside Single-Wall Carbon Nanotubes by High Resolution Electron Microscopy with Atomic Sensitivity." *Physical review letters* 90, no. 5 (2003): 055506.

- [132] Wallace P.R. The band structure of graphite. *Phys. Rev* 71, no. 9 (1947): 622-634.
- [133] Mintmire J.W., Dunlap B.I. and White C.T. "Are fullerene tubules metallic?" *Physical Review Letters* 68, no. 5 (1992): 631.
- [134] Hamada N., Sawada S.I. and Oshiyama A. "New one- dimensional conductors: graphitic microtubules." *Physical Review Letters* 68, no. 10 (1992): 1579.
- [135] Saito R., Fujita M., Dresselhaus G. and Dresselhaus U.M. "Electronic structure of chiral graphene tubules." *Applied physics letters* 60, no. 18 (1992): 2204-2206.
- [136] White C.T. and Mintmire J.W. "Density of states reflects diameter in nanotubes." *Nature* 394, no. 6688 (1998): 29-30.
- [137] Charlier J.C. and Lambin P. "Electronic structure of carbon nanotubes with chiral symmetry." *Physical Review B* 57, no. 24 (1998): R15037.
- [138] Mintmire J. W. and White C. T. "Universal density of states for carbon nanotubes." *Physical Review Letters* 81, no. 12 (1998): 2506.
- [139] Stahl H. "Electronic transport in ropes of single wall carbon nanotubes." PhD diss., Bibliothek der RWTH Aachen, 2000.
- [140] Delaney P., Choi H.J., Ihm J., Louie S.G. and Cohen M.L. "Broken symmetry and pseudogaps in ropes of carbon nanotubes." *Nature* 391, no. 6666 (1998): 466-468.
- [141] Ahuja R., Auluck S., Wills J.M., Alouani M., Johansson B. and Eriksson O. "Optical properties of graphite from first-principles

- [142] Avouris P. "Carbon nanotube electronics and optoelectronics." *Mrs Bulletin* 29, no. 06 (2004): 403-410
- [145] Saito R., Fujita M., Dresselhaus G. and Dresselhaus M.S. "Electronic structure of graphene tubules based on C 60." *Physical Review B* 46, no. 3 (1992): 1804.
- [146] Saito R. and Kataura H. "Optical properties and Raman spectroscopy of carbon nanotubes." In *Carbon nanotubes*, Springer Berlin Heidelberg, (2001) :213-247
- [147] Biró L.P., Bernardo C., Tibbetts G.G. and Lambin P. eds. *Carbon Filaments and Nanotubes: Common Origins, Differing Applications?*. Vol. 372. Springer Science & Business Media, 2012.
- [148] White C.T. and Todorov T.N. "Carbon nanotubes as long ballistic conductors." *Nature* 393, no. 6682 (1998): 240-242.
- [149] Ventra M., Evoy S. and Heflin J.R. eds. *Introduction to nanoscale science and technology*. Springer Science & Business Media, 2006.
- [150] Dresselhaus M. S. "Nanotechnology: New tricks with nanotubes." *Nature* 391, no. 6662 (1998): 19-20.
- [151] Kleiner A. and Eggert S. "Curvature, hybridization, and STM images of carbon nanotubes." *Physical Review B* 64, no. 11 (2001): 113402.
- [152] Orlikowski D., Nardelli M.B., Bernholc J. and Roland C. "Theoretical STM signatures and transport properties of native defects in carbon nanotubes." *Physical Review B* 61, no. 20 (2000): 14194.

- [153] Meunier V. and Lambin P. "Tight-binding computation of the STM image of carbon nanotubes." *Physical review letters* 81, no. 25 (1998): 5588.
- [154] Delaney P., Choi H.J., Ihm J., Louie S.G., and Cohen M.L. "Broken symmetry and pseudogaps in ropes of carbon nanotubes." *Nature* 391, no. 6666 (1998): 466-468.
- [155] Kane, C.L. and Mele, E.J. "Size, shape, and low energy electronic structure of carbon nanotubes." *Physical Review Letters* 78, no. 10 (1997): 1932.
- [156] Odom T.W., Huang J.L., and Lieber C.M. "STM studies of single-walled carbon nanotubes." *Journal of Physics: Condensed Matter* 14, no. 6 (2002): R145.
- [157] Lemay S.G., Janssen J.W., van den Hout M., Mooij M. and Bronikowski M.J. *Nature* 412 (2001): 17.
- [158] Venema L.C., Wildöer J.W., Janssen J.W., Tans S.J., Tuinstra H.L.T., Kouwenhoven L.P. and Dekker C. "Imaging electron wave functions of quantized energy levels in carbon nanotubes." *Science* 283, no. 5398 (1999): 52-55.
- [159] Maltezopoulos T., Kubetzka A., Morgenstern M., Wiesendanger R., Lemay S.G., and Dekker C. "Direct observation of confined states in metallic single-walled carbon nanotubes." *Applied physics letters* 83,

- [160] LeRoy B.J., Lemay S.G., Kong J. and Dekker C. "Erratum: "Scanning tunneling spectroscopy of suspended single-wall carbon nanotubes" [Appl. Phys. Lett. 84, 4280(2004)]." *Applied Physics Letters* 85, no. 18 (2004): 4246-4246.
- [161] Gröning O., Küttel, O.M., Emmenegger C., Gröning P. and Schlapbach L. "Field emission properties of carbon nanotubes." *Journal of Vacuum Science & Technology B* 18, no. 2 (2000): 665-678.
- [162] Wilder J.W., Venema L.C., Rinzler A.G., Smalley R.E. and Dekker C. "Electronic structure of atomically resolved carbon nanotubes." *Nature* 391, no. 6662 (1998): 59-62.
- [163] Venema L.C., Wildöer J.W.G., Tuinstra H.T., Dekker C., Rinzler A.G and Smalley R.E. "Length control of individual carbon Nanotubes by nanostructuring with a scanning tunnelling microscope ." *Applied physics letters* 71, no. 18 (1997): 2629-2631.
- [164] Sagadevan S and Varatharajan R " Cuurent trends in carbon nanotubes and their applications ." *American Journal of Nanoscience and Nanotechnology* 1 , no. 4 (2013):79-82
- [165] Dai H. "Carbon nanotubes: opportunities and challenges." *Surface Science* 500, no. 1 (2002): 218-241.
- [166] Rotkina L., Lin J.F. and Bird J.P. "Nonlinear current-voltage

by electron-beam deposition." *Applied Physics Letters* 83, no. 21
(2003): 4426-4428.

- [167] Tans S.J., Verschueren A.R. and Dekker C. "Room- temperature transistor based on a single carbon nanotube." *Nature* 393, no. 6680 (1998): 49-52.
- [168] Emmenegger C., Mauron P., Sudan P., Wenger P., Hermann V., Gallay R. and Züttel A. "Investigation of electrochemical double-layer (ECDL) capacitors electrodes based on carbon nanotubes and activated carbon materials." *Journal of Power Sources* 124, no. 1 (2003): 321-329.
- [169] Fuhrer M.S., Kim B.M., Dürkop T. and Brintlinger T. "High-mobility nanotube transistor memory." *Nano Letters* 2, no. 7 (2002): 755-759
- [170] Lee N.S., Chung D.S., Han, I.T., Kang J.H., Choi Y.S., Kim H.Y., Park S.H., Jin Y.W., Yi W.K., Yun M.J. and Jung, J.E. "Application of carbon nanotubes to field emission displays." *Diamond and related materials* 10, no. 2 (2001): 265-270.
- [171] Saito Y., Nishiyama T., Kato T.A., Kondo S.I., Tanaka T., Yotani J. and Uemura S. "Field emission properties of carbon nanotubes and their application to display devices." *Molecular Crystals and Liquid Crystals* 387, no. 1 (2002): 79-86.
- [172] Yoon J., Ru C.Q. and Mioduchowski A. "Terahertz wave propagation in multiwall carbon nanotubes." In *Mems, Nano and*

- [173] Robertson J., Zhong G., Hofmann S., Bayer B.C., Esconjauregui C.S., Telg H. and Thomsen C. "Use of carbon nanotubes for VLSI interconnects." *Diamond and Related Materials* 18, no. 5 (2009): 957-962.
- [174] Naeemi A., Sarvari R. and Meindl J.D. "Performance comparison between carbon nanotube and copper interconnects for gigascale integration (GSI)." *Electron Device Letters, IEEE* 26, no. 2 (2005): 84-86.
- [175] S. M. Rosnagel and T. S. Kaun, "Alteration of Cu conductivity in the size effect regime," *J. Vac. Sci. Technol B*, no. 1(2004): 240–247.
- [176] Ravindra, N. "International Technology Roadmap for Semiconductors (ITRS). Symposium." *Journal of electronic materials* 30, no. 12 (2001): 1478-1627.
- [177] White C.T. and Todorov T.N. "Carbon nanotubes as long ballistic conductors." *Nature* 393, no. 6682 (1998): 240-242.
- [178] Zhirnov V., Herr D. and Meyyappan M. "Electronic applications of carbon nanotubes become closer to reality." *Journal of Nanoparticle Research* 1, no. 1 (1999): 151-152.
- [179] Li J., Ye Q., Cassell A., Ng H.T., Stevens R., Han J. and Meyyappan M. "Bottom-up approach for carbon nanotube interconnects." *Applied Physics Letters* 82, no. 15 (2003): 2491-2493
- [180] Yao Z., Kane C.L. and Dekker C. "High-field electrical transport in

(2000): 2941

- [181] Kong J., Yenilmez E., Tomblor T.W., Kim W., Dai H., Laughlin R.B., Liu L., Jayanthi C.S. and Wu S.Y. "Quantum interference and ballistic transmission in nanotube electron waveguides." *Physical review letters* 87, no. 10 (2001): 106801.
- [182] Joshi A. and Soni G. "A Comparative Analysis of Copper and Carbon Nanotubes-Based Global Interconnects in 32 nm Technology." In *Proceedings of Fifth International Conference on Soft Computing for Problem Solving*, Springer Singapore (2016): 425-437
- [183] Liu C.H., Wu C.C. and Zhong Z. "A fully tunable single-walled carbon nanotube diode." *Nano letters* 11, no. 4 (2011): 1782-1785.
- [184] Chau R., Doyle B., Datta S., Kavalieros J. and Zhang K. "Integrated nanoelectronics for the future." *Nature materials* 6, no. 11 (2007): 810-812.
- [185] Lonergan M. C. "A tunable diode based on an inorganic semiconductor conjugated polymer interface." *Science* 278, no. 5346 (1997): 2103-2106.
- [186] Zhou Y., Gaur A., Hur S.H., Kocabas C., Meitl M.A., Shim M. and Rogers J.A. "P-channel, n-channel thin film transistors and pn diodes based on single wall carbon nanotube networks." *Nano Letters* 4, no. 10 (2004): 2031-2035.
- [187] Boettcher S. W., Strandwitz N.C., Schierhorn M., Lock N., Lonergan M.C. and Stucky G.D. "Tunable electronic interfaces between bulk

- [188] Avouris P., Chen Z. and Perebeinos V. "Carbon- based electronics." *Nature nanotechnology* 2, no. 10 (2007): 605-615.
- [189] Avouris P., Freitag M. and Perebeinos V. "Carbon- nanotube photonics and optoelectronics." *Nature photonics* 2, no. 6. (2008): 341-350
- [190] Lee J.U., Gipp P.P. and Heller C.M. "Carbon nanotube pn junction diodes." *Applied Physics Letters* 85 (2004): 145.
- [191] Bosnick K., Gabor N. and McEuen P. "Transport in carbon nanotube pin diodes." *Applied physics letters* 89, no. 16 (2006): 163121.
- [192] Lee J. U. "Photovoltaic effect in ideal carbon nanotube diodes." *Applied physics letters* 87, no. 7 (2005): 73101-73101.
- [193] Lee J. U. "Band-gap renormalization in carbon nanotubes: Origin of the ideal diode behavior in carbon nanotube p– n structures." *Physical Review B* 75, no. 7 (2007): 075409.
- [194] Wu C.C., Liu C.H. and Zhong Z. "One-step direct transfer of pristine single-walled carbon nanotubes for functional nanoelectronics." *Nano letters* 10, no. 3 (2010): 1032-1036.
- [195] Chen J., Perebeinos V., Freitag M., Tsang J., Fu Q., Liu J. and Avouris P. "Bright infrared emission from electrically induced excitons in carbon nanotubes." *Science* 310, no. 5751 (2005): 1171-1174.
- [196] Mueller T., Kinoshita M., Steiner M., Perebeinos V., Bol A.A., Farmer D.B. and Avouris P. "Efficient narrow-band light emission from a single carbon nanotube p–n diode." *nature nanotechnology* 5, no. 1 (2010): 27-

- [197] Gabor N.M., Zhong Z., Bosnick K., Park J. and McEuen P.L.
"Extremely efficient multiple electron-hole pair generation in carbon nanotube photodiodes." *Science* 325, no. 5946. (2009): 1367-1371.
- [198] Appenzeller J., Lin Y.M., Knoch J. and Avouris P. "Band-to-band tunneling in carbon nanotube field-effect transistors." *Physical Review Letters* 93, no. 19 (2004): 196805.
- [199] Appenzeller J., Knoch J., Radosavljević M. and Avouris P..
"Multimode transport in Schottky-barrier carbon-nanotube field-effect transistors." *Physical Review Letters* 92, no. 22 (2004): 226802.
- [200] Jena D., Fang T., Zhan, Q. and Xing H. "Zener tunneling in semiconducting nanotube and graphene nanoribbon p-n junctions." *Applied Physics Letters* 93, no. 11 (2008): 112106.
- [201] Léonard F. and Tersoff J. "Negative differential resistance in nanotube devices." *Physical review letters* 85, no. 22 (2000): 4767.
- [202] Martel R., Derycke V., Appenzeller J., Wind S. and Avouris P. .
"Carbon nanotube field-effect transistors and logic circuits." In *Design Automation Conference, 2002. Proceedings. 39th*, pp. 94-98. IEEE, 2002.
- [203] Martel R., Schmidt T., Shea H.R., Hertel T. and Avouris, P.
"Single- and multi-wall carbon nanotube field-effect transistors."
Applied Physics Letters 73, no. 17 (1998): 2447-2449.
- [204] Marani R. and Perri A.G. "A Simple IV Model Of Carbon Nanotube Field Effect Transistors." *International Journal of Advances in Engineering & Technology* 6, no. 3 (2013): 1076.

- [205] Avouris P., Rao S.A., Jorio A.P., Filho A.C., Filho M. and Wind S.J. "Carbon Nanotube Electronics and Optoelectronics", in "Applied Physics of Carbon Nanotubes: Fundamentals of Theory, Optics and Transport Devices", editors Rotkin S.V., Subramone S. Berlin Heidelberg; Springer-Verlag; ISBN: 978-3-540-23110-3. (2005)
- [206] Avouris P. "Molecular electronics with carbon nanotubes." *Accounts of Chemical Research* 35, no. 12 (2002): 1026-1034.
- [207] Kane C.L., Mele E.J., Lee R.S., Fischer J.E., Petit P., Dai H., Thess A. and Smalley R.E. "Arm Verschueren, SJ Tans, and C." *Dekker, Europhys. Lett* 41 (1998): 683.
- [208] Zhang D. and Lin C.L. "Carbon Nanotube Final Report." (2003).
- [209] Du C. and Pan N. "Carbon nanotube-based supercapacitors." *Nanotech. L. & Bus.* 4 (2007): 3.
- [210] Zhao C. and Zheng W. "A review for aqueous electrochemical supercapacitors." *Frontiers in Energy Research* 3 (2015): 23.
- [211] Halper M.S. and Ellenbogen J.C. "Supercapacitors: A brief overview." *The Mitre Corporation, McLean, Virginia, USA* (2006):1-34.
- [212] Niu C., Sichel E.K., Hoch R., Moy D. and Tennent H. "High power electrochemical capacitors based on carbon nanotube electrodes." *Applied Physics Letters* 70, no. 11 (1997): 1480-1482.
- [213] Frackowiak E., Metenier K., Bertagna V. and Beguin F. "Supercapacitor electrodes from multiwalled carbon nanotubes." *Applied Physics Letters* 77, no. 15 (2000): 2421-2423.
- [214] An K.H., Kim W.S., Park Y.S., Choi Y.C., Lee S.M., Chung D.C., Bae

- Supercapacitors using single-walled carbon nanotube electrodes." *Advanced Materials* 13, no. 7 (2001): 497-500.
- [215] Yoon B.J., Jeong S.H., Lee K.H., Kim H.S., Park C.G. and Han J.H. "Electrical properties of electrical double layer capacitors with integrated carbon nanotube electrodes." *Chemical Physics Letters* 388, no. 1 (2004): 170-174.
- [216] Du C., Yeh J. and Pan N. "High power density supercapacitors using locally aligned carbon nanotube electrodes." *Nanotechnology* 16, no. 4 (2005): 350.
- [217] Bichoutskaia E., Popov A.M. and Lozovik Y.E. "Nanotube-based data storage devices." *Materials Today* 11, no. 6 (2008):38-43
- [218] Lee S.W., Lee D.S., Morjan R.E., Jhang S.H., Sveningsson M., Nerushev O.A., Park Y.W. and Campbell E.E. "A three-terminal carbon nanorelay." *Nano letters* 4, no. 10 (2004): 2027-2030.
- [219] Rueckes T., Kim, K., Joselevich E., Tseng G.Y., Cheung C.L. and Lieber C.M. "Carbon nanotube-based nonvolatile random access memory for molecular computing." *science* 289, no. 5476 (2000): 94-97.
- [220] Kim P. and Lieber C.M. "Nanotube nanotweezers." *Science* 286, no. 5447 (1999): 2148-2150.
- [221] Jang J.E., Cha S.N., Choi Y., Amaratunga G.A., Kang D.J., Hasko D.G., Jung J.E. and Kim J.M. "Nanoelectromechanical switches with vertically aligned carbon nanotubes." *Applied Physics Letters* 87, no. 16 (2005): 163114.

- [222]  <https://ir.ucc.edu.gh/xmlui>
Deshpande V.V., Chiu H.Y., Postma H.C., Miko C., Porro L. and Bockrath M., 2006. "Carbon nanotube linear bearing nanoswitches." *Nano Letters* 6, no. 6 (2006): 1092-1095.
- [223] Dujardin E., Derycke V., Goffman M.F., Lefevre R. and Bourgoin J.P. "Self-assembled switches based on electroactuated multiwalled nanotubes." *Applied Physics Letters* 87, no. 19 (2005): 193107.
- [224] Axelsson S., Campbell E.E., Jonsson L.M., Kinaret J., Lee, S., Park Y. and Sveningsson M. "Theoretical and experimental investigations of three-terminal carbon nanotube relays." *New Journal of Physics* 7, no. 1 (2005): 245.
- [225] Kinaret J. M., T. Nord, and S. Viefers. "A carbon-nanotube-based nanorelay." *Applied Physics Letters* 82, no. 8 (2003): 1287-1289.
- [226] Dequesnes M., Rotkin S.V. and Aluru N.R. "Calculation of pull-in voltages for carbon-nanotube-based nanoelectromechanical switches." *Nanotechnology* 13, no. 1 (2002): 120.
- [227] Jonsson L.M., Nord T., Kinaret J.M. and Viefers S. "Effects of surface forces and phonon dissipation in a three-terminal nanorelay." *Journal of applied physics* 96, no. 1 (2004): 629-635.
- [228] Dequesnes M., Tang Z. and Aluru N.R. "Static and dynamic analysis of carbon nanotube-based switches." *Journal of engineering materials and technology* 126, no. 3 (2004): 230-237.
- [229] Ke C., Espinosa H.D. and Pugno N. "Numerical analysis of nanotube based NEMS devices—Part II: Role of finite kinematics, stretching and charge concentrations." *Journal of applied mechanics* 72, no. 5 (2005): 726-731.

- [230] © **University of Cape Coast** <https://ir.ucc.edu.gh/xmlui>
Jang J.E., Cha S.N., Choi Y.J., Kang D.J., Butler T.P., Hasko D.G.,
Jung J.E., Kim J.M. and Amaratunga G.A. "Nanoscale memory cell
based on a nanoelectromechanical switched capacitor." *Nature
Nanotechnology* 3, no. 1 (2008): 26-30.
- [231] Prince B. *Semiconductor memories: a handbook of design,
manufacture and application*. New York: Wiley, 1991.
- [232] Rueckes T., Segal B.M., Vogeli B., Brock D.K., Jaiprakash V.C. and
Bertin C.L. "NRAM bit selectable two-device nanotube array." U.S.
Patent 6,944,054, issued September 13, 2005.
- [233] Kang J.W., Lee J.H., Lee H.J., Kwon O.K. and Hwang H.J.
"Electromechanical modeling and simulations of nanobridge memory
device." *Physica E: Low-dimensional Systems and Nanostructures*
28, no. 3 (2005): 273-280.
- [234] Kang J.W., Kwon O.K., Lee J.H., Lee H.J., Song Y.J., Yoon Y.S. and
Hwang H.J. "Nanoelectromechanical carbon nanotube memory
analysis." *Physica E: Low-dimensional Systems and Nanostructures*
33, no. 1 (2006): 41-49.
- [235] Cumings J. and Zettl A. "Low-friction nanoscale linear bearing realized
from multiwall carbon nanotubes." *Science* 289, no. 5479 (2000):
602-604.
- [236] Forró L. "Beyond gedanken experiments." *Science* 289, no. 5479 (200)
: 560-561.
- [237] Maslov L. "Concept of nonvolatile memory based on multiwall
carbon nanotubes." *Nanotechnology* 17, no. 10 (2006): 2475.
- [238] Popov A.M., Bichoutskaia E., Lozovik Y.E. and Kulish A.S.

- nanothermometer, nanorelay, and nanoactuator." *physica status solidi (a)* 204, no. 6 (2007): 1911-1917.
- [239] Bichoutskaia E., Popov A.M. and Lozovik Y.E. "Nanotube-based data storage devices." *Materials Today* 11, no. 6 (2008): 38-43.
- [240] Kang J.W. and Jiang Q. "Electrostatically telescoping nanotube nonvolatile memory device." *Nanotechnology* 18, no. 9 (2007): 095705
- [241] Bichoutskaia E., Heggie M.I., Popov A.M. and Lozovik Y.E. "Interwall interaction and elastic properties of carbon nanotubes." *Physical Review B* 73, no. 4 (2006): 045435.
- [242] Ajayan P.M. and Zhou O.Z. "Applications of carbon nanotubes." In *Carbon nanotubes*, Springer Berlin Heidelberg, (2001): 391-425.
- [243] Bernholc, J., Brenner, D., Buongiorno Nardelli, M., Meunier, V. and Roland, C. "Mechanical and electrical properties of nanotubes." *Annual Review of Materials Research* 32, no. 1 (2002): 347-375.
- [244] Qian D., Wagner G.J., Liu W.K., Yu M.F. and Ruoff R.S. "Mechanics of carbon nanotubes." *Applied mechanics reviews* 55, no. 6 (2002): 495-533.
- [245] Kasumov A.Y., Deblock R., Kociak M., Reulet B., Bouchiat H., Khodos I.I., Gorbatov Y.B., Volkov V.T. "Supercurrents through single-walled carbon nanotubes." *Science* 284, no. 5419 (1999): 1508-1511.
- [246] De Heer W.A., Chatelain A. and Ugarte D. "A carbon nanotube field-emission electron source." *Science* 270, no. 5239 (1995): 1179-

- [247] Rinzler A. G., Hafner J. H., Nikolaev P. "Unraveling nanotubes: field emission from an atomic wire." *Science* 269, no. 5230 (1995): 1550.
- [248] Lee N.S., Chung D.S., Han I.T., Kang J.H., Choi Y.S., Kim H.Y., Park S.H., Jin Y.W., Yi W.K., Yun M.J. and Jung J.E. "Application of carbon nanotubes to field emission displays." *Diamond and related materials* 10, no. 2 (2001): 265-270.
- [249] Rosen R., Simendinger W., Debbault C., Shimoda H., Fleming L., Stoner B. and Zhou O. "Application of carbon nanotubes as electrodes in gas discharge tubes." *Applied Physics Letters* 76, no. 13 (2000): 1668-1670.
- [250] Sugie H., Tanemura M., Filip V., Iwata K., Takahashi K. and Okuyama F. "Carbon nanotubes as electron source in an x-ray tube." *Applied Physics Letters* 78, no. 17 (2001): 2578-2580.
- [251] Baughman R.H., Zakhidov A.A. and de Heer W.A. "Carbon nanotubes--the route toward applications." *Science* 297, no. 5582 (2002): 787-792
- [252] Rinzler A.G., Hafner J.H., Nikolaev P. and Lou L. "Unraveling nanotubes: field emission from an atomic wire." *Science* 269, no. 5230 (1995): 1550.
- [253] Ajayan, P. M., O. Stephan, C. Colliex, and D. Trauth. "Aligned carbon nanotube arrays formed by cutting a polymer resin-nanotube composite." *Science-New York Then Washington-* (1994): 1212

- [254] Walt A. "de Heer, A. Châtelain, and D. Ugarte." *Science* 270 (1995): 1179.
- [255] Dean K. A. and Chalamala B.R. "Current saturation mechanisms in carbon nanotube field emitters." *Applied Physics Letters* 76, no. 3 (2000): 375-377.
- [256] Dean K.A. and Chalamala B.R. "Field emission microscopy of carbon nanotube caps." *Journal of applied physics* 85, no. 7 (1999): 3832-3836.
- [257] Eletskaa A.V. and Bocharov G.S. "Emission properties of carbon nanotubes and cathodes on their basis." *Plasma Sources Science and Technology* 18, no. 3 (2009): 034013.
- [258] Tong Y., Lim S.C., Park K.A., Jeong H.J., Jeong S.Y., Lee Y.H., Liu C., Cheng H.M. and Choi Y. "Controlling field-emission patterns of isolated single-walled carbon nanotube rope." *Applied Physics Letters* 87, no. 4 (2005): 043114.
- [259] Heo J.N., Lee J.H., Jeong T.W., Lee C.S., Kim W.S., Jin Y.W., Kim J.M., Yu S., Yi W.K., Park S.H. and Oh T.S. "Electron emission from carbon nanotube-dispersed MgO layer." *Applied Physics Letters* 87, no. 11 (2005): 114105.
- [260] Smith R.C., Cox D.C. and Silva S.R.P. "Electron field emission from a single carbon nanotube: Effects of anode location." *Applied Physics Letters* 87, no. 10 (2005).

[262] Bonard J.M., Salvétat J.P., Stöckli T., de Heer W.A., Forró L. and Châtelain A. "Field emission from single-wall carbon nanotube films." *Applied physics letters* 73 (1998): 918.

[263] Küttel O.M., Groening O., Emmenegger C. and Schlapbach L. L. "Electron field emission from phase pure nanotube films grown in a methane/hydrogen plasma." *Applied physics letters* 73, no. 15 (1998):

[264] Choi W.B., Chung D.S., Kang J.H., Kim H.Y., Jin Y.W., Han I.T., Lee Y.H., Jung J.E., Lee N.S., Park G.S. and Kim J.M. "Fully sealed, high-brightness carbon-nanotube field-emission display." *Applied physics letters* 75, no. 20 (1999): 3129-3131.

[265] Govyadinov A, Mardilovich P, Routkevitch D. Field emission devices from aligned arrays of carbon nanotubes. In *Cold Cathodes Proceedings of the First International Symposium* (Vol. 2000), The Electrochemical Society, (2001): 74

[266] Bonard J.M., Croci M., Klinke C., Kurt R., Noury O. and Weiss N. "Carbon nanotube films as electron field emitters." *Carbon* 40, no. 10 (2002): 1715-1728.

[267] Pennington G. and Wickenden A .E. "Efficient terahertz generation by carbon nanotubes within the limited space-charge accumulation regime." *Journal of Applied Physics* 105, no. 9 (2009): 094316.

[269] Lee M. and Wanke M.C. "Searching for a solid-state terahertz technology." *Science* 316, no. 5821 (2007): 64-65.

[270] Köhler R., Tredicucci A., Beltram F., Beere H.E., Linfield E.H., Davies A.G., Ritchie D.A., Iotti R.C. and Rossi F. "Terahertz semiconductor-heterostructure laser." *Nature* 417, no. 6885 (2002): 156-159.

[271] Crowe T.W., Bishop W.L., Porterfield D.W., Hesler J.L. and Weikle R.M. "Opening the terahertz window with integrated diode circuits." *Solid-State Circuits, IEEE Journal of* 40, no. 10 (2005): 2104-2110.

[272] Pennington G. and Goldsman N. "Monte Carlo study of electron transport in a carbon nanotube." *Ieice Transactions on Electronics* 86, no. 3 (2003): 372-378.

[273] Léonard F. and Tersoff J. "Negative differential resistance in nanotube devices." *Physical review letters* 85, no. 22 (2000): 4767.

[274] Pennington G. and Wickenden A.E. "Efficient terahertz generation by carbon nanotubes within the limited space-charge accumulation regime" *Journal of Applied Physics* 105, no. 9 (2009): 094316.

[275] Maksimenko, A.S. and Slepyan, G.Y. "Negative differential conductivity in carbon nanotubes." *Physical review letters* 84, no. 2 (2000): 362.

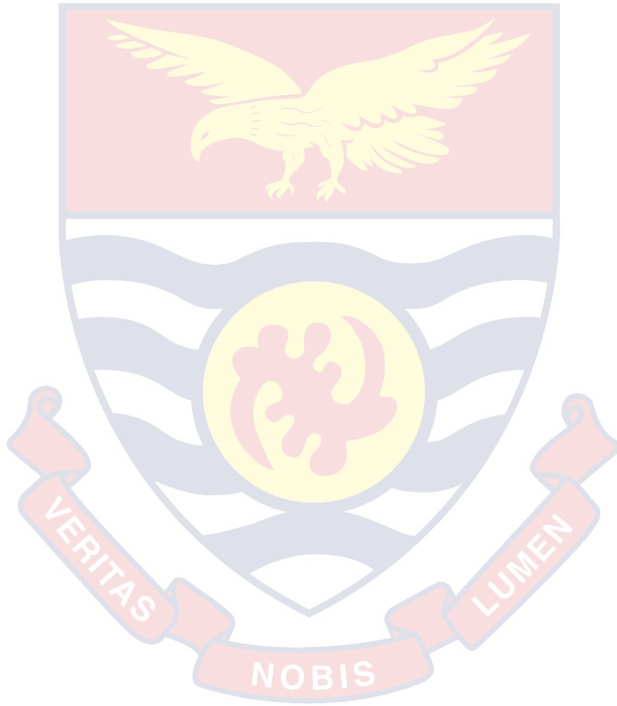
- [276] Perebeinos V., Terzoff L. and Aronoff P. "Electron-phonon interaction and transport in semiconducting carbon nanotubes." *Physical review letters* 94, no. 8 (2005): 086802.
- [277] Akturk A., Pennington G.W., Goldsman N. and Wickenden A.E. "Quantum electron transport in carbon nanotubes: Velocity oscillations and length dependence." In *Simulation of Semiconductor Processes and Devices, 2006 International Conference* , IEEE, (2006):31-34.
- [278] Verma A. , Kauser M. Z., and Ruden P. P. "Ensemble Monte Carlo transport simulations for semiconducting carbon nanotubes." *Journal of applied physics* 97, no. 11 (2005): 114319.
- [279] Akturk A., Pennington G., Goldsman N. and Wkicenden A. "Electron transport and velocity oscillations in a carbon nanotube." *Nanotechnology, IEEE Transactions on* 6, no. 4 (2007): 469-474
- [280] Kondo H., Hieda M., Nakayama M., Tanaka T., Osakabe K. and Mizuno K. "Millimeter and submillimeter wave quasi-optical oscillator with multi-elements." *IEEE transactions on microwave theory and techniques* 40, no. 5 (1992): 857-863.
- [281] Wang C., and Cao J. C. "Terahertz generation and chaotic dynamics in single-walled zigzag carbon nanotubes." *Chaos: An Interdisciplinary Journal of Nonlinear Science* 19, no. 3 (2009): 033136.
- [282] Esaki, L. and Tsu, R. "Superlattice and negative differential conductivity in semiconductors." *IBM Journal of Research and Development* 14, no. 1 (1970): 61-65.

- Superlattice with hot electron injection: an approach to a Bloch oscillator." *Physical Review B* 67, no. 3 (2003): 033305.
- [284] Lin M.F. and Shung K.W.K. "Magnetization of grapheme tubules." *Physical Review B* 52, no. 11 (1995): 8423.
- [285] Jishi R.A., Dresselhaus M.S. and Dresselhaus G. "Electron-phonon coupling and the electrical conductivity of fullerene nanotubes." *Physical review B* 48, no. 15 (1993): 11385.
- [286] Kane C.L. and Mele E.J. "Ratio problem in single carbon nanotube fluorescence spectroscopy." *Physical review letters* 90, no. 20 (2003): 207401.
- [287] Bass F. G. "Nonlinear galvanomagnetic effects, negative resistance regions of current-voltage characteristics, and runaway electrons (Semiconductor galvanomagnetism, volt-ampere characteristics with negative differential conductivity and escaping electrons)." *Soviet Physics-JETP* 21 (1965): 181-189.
- [288] Amekpewu M., Abukari S. S., Adu K. W., Mensah S.Y. and Mensah N. G. "Effect of hot electrons on the electrical conductivity of carbon nanotubes under the influence of applied dc field." *The European Physical Journal B* 88, no. 2 (2015):1-6.
- [289] Kroemer H. "Large-amplitude oscillation dynamics and domain suppression in a superlattice Bloch oscillator." *arXiv preprint cond-mat/0009311* (2000).

N.V. and Shorokhov A.V. "Suppressed absolute negative conductance and generation of high-frequency radiation in semiconductor superlattices." *EPL (Europhysics Letters)* 73, no. 6 (2006): 934.

[291] Hyart T., Alekseev K.N., Leppänen A. and Thuneberg E.V.

"Terahertz Bloch oscillator with suppressed electric domains: Effect of elastic scattering." *International Journal of Modern Physics B* 23, no. 20n21 (2009): 4459-4472.



APPENDIX A

CURRENT DENSITY FOR ZIGZAG CARBON NANOTUBE IN THE ABSENCE OF HOT ELECTRON SOURCE

Motion of electrons using the semiclassical Newton’s law (neglecting scattering), if a static electric field E_z is applied along a z- axis of an undoped single-wall carbon nanotube is given by

$$\frac{dP_z}{dt} = eE_z \tag{A1}$$

where P_z and e are the axial component of the quasimomentum and the electronic charge of the propagating electrons respectively

Bloch frequency Ω for zz – CNT is given by [275] :

$$\Omega_{zz} = \frac{aeE_z}{\hbar} \tag{A2}$$

where a is the lattice constant of the zz-CNT.

The energy for zz-CNT is expressed as [275]

$$\begin{aligned} \varepsilon(s\Delta p_\phi, p_z) &\equiv \varepsilon_s(p_z) \\ &= \pm\gamma_0 \left[1 + 4\cos(ap_z)\cos\left(\frac{a}{\sqrt{3}}s\Delta p_\phi\right) \right. \\ &\quad \left. + 4\cos^2\left(\frac{a}{\sqrt{3}}s\Delta p_\phi\right) \right]^{1/2} \end{aligned} \tag{A3}$$

where $\gamma_0 \approx 3.0\text{eV}$ is the overlapping integral, Δp_ϕ is transverse quasimomentum level spacing and s is an integer.

The - and + signs correspond to the valence and conduction bands respectively.

The expression for lattice constant a in equation (A3) is given by

$$a = \frac{3a_{c-c}}{2\hbar} \tag{A4}$$

where $a_{c-c} = 0.142$ nm is the C-C bond length.

Due to the transverse quantization of the quasimomentum P , its transverse component p_ϕ can take n discrete values,

$$p_\phi = s\Delta p_\phi = \frac{\pi\sqrt{3}s}{an} \quad (s = 1, \dots, n) \quad (A5)$$

Considering the presence of hot electrons source, the motion of quasiparticles in an external axial electric field is described by the Boltzmann kinetic equation in the form as shown below [275, 283]

$$\frac{\partial f(p)}{\partial t} + v_z \frac{\partial f(p)}{\partial x} + eE_z(t) \frac{\partial f(p)}{\partial p_z} = -\frac{[f(p) - f_0(p)]}{\tau} + S(p) \quad (A6)$$

where $S(p)$ is the hot electron source function, $f_0(p)$ is equilibrium Fermi distribution function, $f(p, t)$ is the distribution function, v_z is the quasiparticle group velocity along the z-axis of carbon nanotube and τ is the relaxation time. Expanding the distribution functions of interest in Fourier series as

$$f(p, t) = \Delta p_\phi \sum_{s=1}^n \delta(p_\phi - s\Delta p_\phi) \sum_{r \neq 0} f_{rs} e^{iarp_z} \psi_v(t) \quad (A7)$$

and

$$f_0(p) = \Delta p_\phi \sum_{s=1}^n \delta(p_\phi - s\Delta p_\phi) \sum_{r \neq 0} f_{rs} e^{iarp_z} \quad (A8)$$

for zz-CNTs,

where $\delta(p_\phi - s\Delta p_\phi)$ is the Dirac delta function, f_{rs} is the coefficient of the Fourier series and $\psi_v(t)$ is the factor by which the Fourier transform of the nonequilibrium distribution function differs from its equilibrium distribution counterpart.

For simplicity, a hot electron source $S(p)$ of the simplest form given by the expression (A9) is considered,

© University of Cape Coast <https://is.ucc.edu.gh/xmlui> (A9)

$$S(p) = \frac{Qa}{\hbar} \delta(\varphi - \varphi') - \frac{aq}{n_0} f_s(\varphi) \quad (A9)$$

where $f_s(p)$ is the stationary (static and homogeneous) solution of equation (A6), Q is the injection rate of hot electrons, n_0 is the equilibrium particle density, φ and φ' are the dimensionless momenta of electrons and hot electrons respectively which are expressed as $\varphi_{zz} = ap_z/\hbar$ and $\varphi'_{zz} = ap'_z/\hbar$ for zz-CNTs. We now determine the electric current density of the zz-CNT for the case when there is no hot electron source present. Substituting equations (A7) and (A8) into equation (A6) and setting $S(p) = 0$, (A10) is obtained as

$$\frac{\partial \psi_v(t)}{\partial t} + \left(iearE_z + \frac{1}{\tau} \right) \psi_v(t) = \frac{1}{\tau} \quad (A10)$$

Solving the homogeneous differential equation (A10), $\psi_v(t)$ is obtained as

$$\psi_v(t) = C(t) e^{-\int [iearE_z + \frac{1}{\tau}] dt} = C(t) \exp^{-iearE_z t} \cdot \exp^{-\frac{t}{\tau}} \quad (A11)$$

Then by differentiating equation (A11), (A12) is obtained as

$$\frac{\partial \psi_v(t)}{\partial t} = \left[\frac{\partial C(t)}{\partial t} - \left(iearE_z + \frac{1}{\tau} \right) C(t) \right] \exp^{-iearE_z t} \cdot \exp^{-\frac{t}{\tau}} \quad (A12)$$

Substituting (A12) and (A11) in eq (A10), $C(t)$ is finally obtained as in (A13)

$$\begin{aligned} \frac{\partial C(t)}{\partial t} \exp^{-iearE_z t} \cdot \exp^{-\frac{t}{\tau}} &= \frac{1}{\tau} \\ C(t) &= \int \frac{1}{\tau} \exp^{iearE_z t} \cdot \exp^{\frac{t}{\tau}} dt \\ &= \frac{\exp^{iearE_z t} \cdot \exp^{\frac{t}{\tau}}}{(1 + iearE_z \tau)} \end{aligned} \quad (A13)$$

Substituting equation (A13) into equation (A11), $\psi_v(t)$ is obtained as

$$\psi_v(t) = \frac{1}{(1 + iearE_z \tau)} \quad (A14)$$

Therefore

$$\psi_v(t) = \frac{v}{(v + ir\Omega_{zz})} \quad (A15)$$

where $\Omega_{zz} = aeE_z$, $v = 1/\tau$ and $\hbar = 1$

To find the coefficients f_{rs} , both sides of equation (A8) is multiplied by \exp^{-iampz} , and then integrate over the periodic interval $0 \leq p_z \leq 2\pi/a$.

Thus

$$\begin{aligned} & \int_0^{2\pi/a} f_0(\mathbf{p}) e^{-iampz} dp_z \\ &= \Delta p_\phi \sum_{s=1}^n \delta(p_\phi - s\Delta p_\phi) \sum_{r \neq 0} f_{rs} \int_0^{2\pi/a} \exp^{-ia(r-m)p_z} dp_z \\ &= \Delta p_\phi \sum_{r \neq 0} f_{rs} \frac{2\pi}{a} \delta_{r,m} \\ & f_{rs} = \frac{a}{2\pi\Delta p_\phi} \int_0^{2\pi/a} f_0(\mathbf{p}) \exp^{-iar p_z} dp_z \end{aligned} \quad (A16)$$

But,

$$f_0(\mathbf{p}) = \frac{1}{1 + \exp\{\varepsilon_s(p_z)/k_B T\}}$$

Therefore, from equation (A16),

$$f_{rs} = \frac{a}{2\pi\Delta p_\phi} \int_0^{2\pi/a} \frac{\exp^{-iar p_z}}{1 + \exp\{\varepsilon_s(p_z)/k_B T\}} dp_z \quad (A17)$$

Now we apply the surface current density which is generally defined by

$$j_z = \frac{2e}{(2\pi\hbar)^2} \iint f(p, t) v_z(p) d^2p,$$

or

$$j_z = \frac{2e}{(2\pi\hbar)^2} \sum_{s=1}^n \int_0^{2\pi/a} f(p_z, s\Delta p_\phi, \psi_v(t)) v_z(p_z, s\Delta p_\phi) dp_z \quad (A18)$$

Where the integration is over the first Brillouin zone, v_z is given by

© University of Cape Coast <https://ir.ucc.edu.gh/xmlui>

$$v_z(p_z, s\Delta p_\phi) = \frac{\partial \varepsilon_s(p_z)}{\partial p_z} \quad (A19)$$

Now expanding $\varepsilon_s(p_z)/\gamma_0$ in Fourier series with coefficients ε_{rs} to be determined

$$\begin{aligned} \varepsilon(p_z, s\Delta p_\phi) &= \varepsilon_s(p_z) \\ &= \gamma_0 \sum_{r \neq 0} \varepsilon_{rs} \exp^{iar p_z} \end{aligned} \quad (A20)$$

Multiplying both sides of equation (A20) by $\exp(-iam p_z)$ and integrating over $0 \leq p_z \leq 2\pi/a$, ε_{rs} is obtained as in (A21)

$$\begin{aligned} \int_0^{2\pi/a} \varepsilon_s(p_z) \exp^{-iam p_z} dp_z &= \gamma_0 \sum_{r \neq 0} \varepsilon_{rs} \int_0^{2\pi/a} \exp^{ia(r-m)p_z} dp_z \\ &= \gamma_0 \sum_{r \neq 0} \varepsilon_{rs} \frac{2\pi}{a} \delta_{r,m} \end{aligned}$$

$$\begin{aligned} \text{Therefore } \int_0^{2\pi/a} \varepsilon_s(p_z) \exp^{-iar p_z} dp_z &= \gamma_0 \varepsilon_{rs} \frac{2\pi}{a} \\ \varepsilon_{rs} &= \frac{a}{2\pi \gamma_0} \int_0^{2\pi/a} \varepsilon_s(p_z) \exp^{-iar p_z} dp_z \end{aligned} \quad (A21)$$

where $\varepsilon_s(p_z)$ is given by equation (A3)

From equations (A19) and (A20)

$$\begin{aligned} v_z(p_z, s\Delta p_\phi) &= \gamma_0 \sum_{r \neq 0} \frac{\partial (\varepsilon_{rs} \exp^{iar p_z})}{\partial p_z} \\ &= \gamma_0 \sum_{r \neq 0} iar \varepsilon_{rs} \exp^{iar p_z} \end{aligned} \quad (A22)$$

From equation (A7),

$$f(p, t) = \Delta p_\phi \sum_{r \neq 0} f_{rs} \exp^{iar p_z} \psi_v(t)$$

$$f(p_z, s\Delta p_\phi, \psi_v(t)) = \Delta p_\phi \sum_{r \neq 0} f_{rs} \exp^{iar p_z} \psi_v(t) \quad (\text{A23})$$

Substituting equation (A23) and (A22) into equation (A18), the current density for zz-CNTs j_z^{zz} is obtained as

$$j_z^{zz} = \frac{2e}{(2\pi\hbar)^2} i\gamma_0 a \Delta p_\phi \sum_{s=1}^n \int_0^{\frac{2\pi}{a}} \left(\sum_{r \neq 0} f_{rs} e^{iar p_z} \psi_v(t) \right) \left(\sum_{r' \neq 0} ia r' \epsilon_{rs} e^{iar' p_z} \right) dp_z \quad (\text{A24})$$

But current density for zz-CNTs j_z^{zz} can also be written as

$$j_z^{zz} = i \sum_{s=1}^n j_{os} \psi_v(t) \quad (\text{A25})$$

So from equations (A24) and (A25), j_{os} obtained as

$$\begin{aligned} j_{os} &= \frac{2e}{(2\pi\hbar)^2} \gamma_0 a \Delta p_\phi \sum_{s=1}^n \int_0^{\frac{2\pi}{a}} \left(\sum_{r \neq 0} f_{rs} e^{iar p_z} \right) \left(\sum_{r' \neq 0} ia r' \epsilon_{rs} e^{iar' p_z} \right) dp_z \\ &= \frac{2e}{(2\pi\hbar)^2} \gamma_0 a \Delta p_\phi \sum_{s=1}^n \int_0^{\frac{2\pi}{a}} \left(\sum_{r \neq 0} f_{rs} e^{iar p_z} \right) \left(\sum_{r' \neq 0} ia r' \epsilon_{rs} e^{iar' p_z} \right) dp_z \\ &= \frac{2e}{(2\pi\hbar)^2} \gamma_0 a \Delta p_\phi \sum_{s=1}^n \sum_{r \neq 0} \sum_{r' \neq 0} r' f_{rs} \epsilon_{rs} \int_0^{\frac{2\pi}{a}} e^{ia(r+r')p_z} dp_z \end{aligned} \quad (\text{A26})$$

Noting that each of r and r' is summation from $-\infty$ to $+\infty$, equation (A26) is integrated and j_{os} is obtained as

$$j_{os} = \frac{2e}{(2\pi\hbar)^2} \gamma_0 a \Delta p_\phi \sum_{s=1}^n 2 \sum_{r=1}^{\infty} 2 \sum_{r'=1}^{\infty} r' f_{rs} \epsilon_{rs} \frac{2\pi}{a} \delta_{r,-r'}$$

Here, the r and r' summations are taken over $1 \leq r \leq \infty$ and $1 \leq r' \leq \infty$, therefore a factor of 2 is required to account for each of r and r' summation from $-\infty$ to $+\infty$.

© University of Cape Coast <https://ir.ucc.edu.gh/xmlui>

$$j_{os} = \frac{2e}{(2\pi\hbar)^2} \gamma_0 a \Delta p_\phi \sum_{s=1}^n \sum_{r=1}^{\infty} r f_{rs} \epsilon_{rs} \frac{2\pi}{a}$$

$$= \frac{2e}{(2\pi\hbar)^2} \frac{2\pi}{a} \gamma_0 a \Delta p_\phi \sum_{s=1}^n \sum_{r=1}^{\infty} r f_{rs} \epsilon_{rs} \quad (A27)$$

Simplifying the constant terms in (A27)

$$\frac{2e^2}{(2\pi\hbar)^2} \frac{2\pi}{a} \gamma_0 a^2 \Delta p_\phi^4 = \frac{4e^2}{\pi\hbar^2} \gamma_0 a \Delta p_\phi = \frac{4e^2}{\pi\hbar^2} \gamma_0 a \frac{\pi\sqrt{3}}{an} = \frac{4\sqrt{3} e^2 \gamma_0}{\hbar^2 n} \quad (A28)$$

$$j_{os} = \frac{4\sqrt{3} e^2 \gamma_0}{\hbar^2 n} \sum_{r=1}^{\infty} r \sum_{s=1}^n f_{rs} \epsilon_{rs} \quad (A29)$$

Substituting equations(A29) and (A14) into equation (A25), j_z^{zz} is obtained

as

$$j_z^{zz} = i \frac{4\sqrt{3} e^2 \gamma_0}{\hbar^2 n} \sum_{r=1}^{\infty} \frac{rv}{(v + ir\Omega_{zz})} \sum_{s=1}^n f_{rs} \epsilon_{rs} \quad (A30)$$

Considering only the real part of equation (A30), j_z^{zz} is obtained as

$$\begin{aligned} j_z^{zz} &= \frac{4\sqrt{3} e^2 \gamma_0}{\hbar^2 n} \sum_{r=1}^{\infty} \frac{r^2 a e E_z \tau}{1 + (r a e E_z \tau)^2} \sum_{s=1}^n f_{rs} \epsilon_{rs} \\ &= \frac{4\sqrt{3} e^2 \gamma_0}{\hbar^2 n} \sum_{r=1}^{\infty} \frac{r^2 \Omega_{zz} \tau}{1 + (r \Omega_{zz} \tau)^2} \sum_{s=1}^n f_{rs} \epsilon_{rs} \\ j_z^{zz} &= \frac{4\sqrt{3} e^2 \gamma_0}{\hbar^2 n} \sum_{r=1}^{\infty} \frac{r^2 \Omega_{zz} v}{v^2 + r^2 (\Omega_{zz})^2} \sum_{s=1}^n f_{rs} \epsilon_{rs} \end{aligned} \quad (A31)$$

where, $v = 1/\tau$, $\Omega_{zz} = a e E_z$ and $\hbar = 1$

CURRENT DENSITY FOR ZIGZAG CARBON NANOTUBE IN THE PRESENCE OF HOT ELECTRON SOURCE

Considering the presence of hot electrons source, the motion of quasiparticles in an external axial electric field is described by the Boltzmann kinetic equation in the form as shown below [275, 283]

$$\frac{\partial f(p)}{\partial t} + v_z \frac{\partial f(p)}{\partial x} + eE_z(t) \frac{\partial f(p)}{\partial p_z} = - \frac{[f(p) - f_0(p)]}{\tau} + S(p) \quad (B1)$$

where $S(p)$ is the hot electron source function, $f_0(p)$ is equilibrium Fermi distribution function, $f(p, t)$ is the distribution function, v_z is the quasiparticle group velocity along the z-axis of carbon nanotube and τ is the relaxation time. The stationary homogeneous distribution function $f_s(\varphi)$ in the presence of hot electron source is given by

$$f_s(\varphi) = f_E(\varphi) + f'(\varphi) \quad (B2)$$

$$\text{where } f_E(p) = f(p) = \psi_v(t) = rv/(v + ir\Omega_{zz}) \quad (B3)$$

Substituting equation (B2) into equation (B1), (B4) is obtained as

$$\frac{\partial f'(\varphi)}{\partial \varphi} + \left(\frac{v}{\Omega_{zz}} + \frac{Q}{n_o \Omega_{zz}} \right) f'(\varphi) = \frac{aQ}{\Omega_{zz}} \delta(\varphi - \varphi') - \frac{aQ}{\Omega_{zz} n_o} f_E(\varphi) \quad (B4)$$

Solving the homogeneous differential equation (B4), $f'(\varphi)$ is obtained as

$$\begin{aligned} f'(\varphi) &= C(\varphi) e^{-\int \left[\frac{v}{\Omega_{zz}} + \frac{Q}{n_o \Omega_{zz}} \right] d\varphi} \\ &= C(\varphi) e^{-\left[\frac{v}{\Omega_{zz}} + \frac{Q}{n_o \Omega_{zz}} \right] \varphi} \end{aligned} \quad (B5)$$

Then by differentiating equation (B5), (B6) is obtained as

$$\frac{\partial f'(\varphi)}{\partial \varphi} = \left[\frac{\partial C(\varphi)}{\partial \varphi} - \left(\frac{v}{\Omega_{zz}} + \frac{Q}{n_o \Omega_{zz}} \right) C(\varphi) \right] e^{-\left[\frac{v}{\Omega_{zz}} + \frac{Q}{n_o \Omega_{zz}} \right] \varphi} \quad (B6)$$

Substituting for $f'(\varphi)$ and $\partial f'(\varphi)/\partial \varphi$ in equation (B4), $C(\varphi)$ is obtained as in

(B7)

© University of Cape Coast <https://ir.ucc.edu.gh/xmlui>

$$\frac{\partial C(\varphi)}{\partial \varphi} e^{-\left[\frac{v}{\Omega_{zz}} + \frac{q}{n_0 \Omega_{zz}}\right] \varphi} = \frac{aQ}{\Omega} \delta(\varphi - \varphi') - \frac{aQ}{\Omega n_0} f_E(\varphi)$$

$$\Rightarrow C(\varphi) = \int \left\{ \frac{aQ}{\Omega_{zz}} \delta(\varphi - \varphi') - \frac{aQ}{\Omega_{zz} n_0} f_E(\varphi) \right\} e^{\left[\frac{v}{\Omega_{zz}} + \frac{q}{n_0 \Omega_{zz}}\right] \varphi} \partial \varphi \quad (B7)$$

Introducing Dirac-delta transformation

$$\delta(\varphi - \varphi') = \frac{1}{2\pi} \sum_r e^{ir(\varphi - \varphi')} \quad (B8)$$

Substituting equations (B3) and (B8) into equation (B7) to obtain equation (B9)

$$\begin{aligned} C(\varphi) &= \frac{aQ}{2\pi \Omega_{zz}} \cdot \frac{n_0}{n_0} \int \left\{ \sum_r e^{ir(\varphi - \varphi')} - \frac{Q}{\Omega_{zz} n_0} f_E(\varphi) \right\} e^{\left[\frac{v}{\Omega_{zz}} + \frac{q}{n_0 \Omega_{zz}}\right] \varphi} \partial \varphi \\ &= \frac{aQ}{2\pi \Omega_{zz}} \cdot \frac{n_0}{n_0} \int \left\{ \sum_r e^{-ir\varphi'} - \frac{v}{(v + ir\Omega_{zz})} \right\} e^{\left[\frac{v}{\Omega_{zz}} + \frac{q}{n_0 \Omega_{zz}}\right] \varphi} \partial \varphi \\ &= \frac{aQ}{2\pi \Omega_{zz}} \cdot \frac{n_0}{n_0} \sum_r \frac{\Omega_{zz}}{(ir\Omega_{zz} + v + \frac{q}{n_0})} \left\{ e^{-ir\varphi'} \right. \\ &\quad \left. - \frac{v}{(v + ir\Omega_{zz})} \right\} e^{\left[\frac{v}{\Omega_{zz}} + \frac{q}{n_0 \Omega_{zz}}\right] \varphi} \quad (B9) \end{aligned}$$

Substituting equation (B9) into equation (B5), $f'(\varphi)$ is obtained as

$$f'(\varphi) = \eta_{zz} \frac{n_0}{2\pi} \cdot \sum_r \frac{\Omega_{zz} e^{ir\varphi}}{(ir\Omega_{zz} + v + \eta_{zz} \Omega_{zz})} \left\{ e^{-ir\varphi'} - \frac{v}{(v + ir\Omega_{zz})} \right\} \quad (B10)$$

where the nonequilibrium parameter $\eta_{zz} = Q/\Omega_{zz} n_0$ (B11)

Current density for zz- CNTs in the presence of hot electron source j_z^{zz} is given by

$$j_z^{zz} = i \sum_{s=1}^n j_{os} f_s(\varphi) \quad (B12)$$

Recall for zz-CNTs,

© University of Cape Coast <https://ir.ucc.edu.gh/xmlui> (B13)

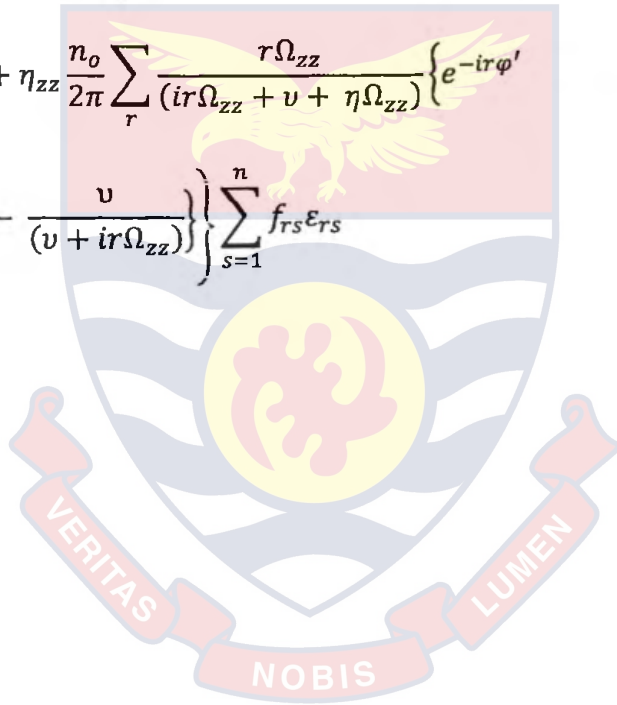
$$j_{os} = \frac{4\sqrt{3} e^2 \gamma_0}{\hbar^2 n} \sum_{r=1}^{\infty} r \sum_{s=1}^n f_{rs} \epsilon_{rs}$$

Substituting equation (B2) into equation (B12)

$$j_z^{zz} = i \sum_{s=1}^n j_{os} [f_E(\varphi) + f'(\varphi)] \quad (B14)$$

Substituting equations (B3), (B10) and (B13) into equations (B14), j_{zHE}^{zz} is obtained as

$$j_{zHE}^{zz} = i \frac{4\sqrt{3} e^2 \gamma_0}{\hbar^2 n} \sum_{r=1}^{\infty} \left\{ \frac{rv}{(v + ir\Omega_{zz})} + \eta_{zz} \frac{n_0}{2\pi} \sum_r \frac{r\Omega_{zz}}{(ir\Omega_{zz} + v + \eta\Omega_{zz})} \left\{ e^{-ir\varphi'} - \frac{v}{(v + ir\Omega_{zz})} \right\} \sum_{s=1}^n f_{rs} \epsilon_{rs} \right\} \quad (B15)$$



CURRENT DENSITY FOR ARMCHAIR CNT IN THE ABSENCE OF HOT ELECTRON SOURCE

Motion of electrons using the semiclassical Newton's law (neglecting scattering) if a static electric field E_z is applied along a z- axis of an undoped single-walled carbon nanotube is given by

$$\frac{dP_z}{dt} = eE_z \quad (C1)$$

where P_z and e are the axial component of the quasimomentum and the electronic charge of the propagating electrons respectively

Bloch frequency Ω for ac-CNT is given by [275] :

$$\Omega_{ac} = \frac{aeE_z}{\sqrt{3}\hbar} \quad (C2)$$

Here, a is the lattice constant of the ac-CNT.

The energy for ac-CNT is expressed as [275].

$$\begin{aligned} \varepsilon(s\Delta p_\phi, p_z) &\equiv \varepsilon_s(p_z) \\ &= \pm\gamma_0 \left[1 + 4\cos(as\Delta p_\phi)\cos\left(\frac{a}{\sqrt{3}}p_z\right) \right. \\ &\quad \left. + 4\cos^2\left(\frac{a}{\sqrt{3}}p_z\right) \right]^{1/2} \end{aligned} \quad (C3)$$

where $\gamma_0 \approx 3.0\text{eV}$ is the overlapping integral, Δp_ϕ is transverse quasimomentum level spacing and s is an integer. The - and + signs correspond to the valence and conduction bands respectively. The expression for lattice constant a in equation (C3) is given by

$$a = \frac{3a_{c-c}}{2\hbar} \quad (C4)$$

where $a_{c-c} = 0.142\text{nm}$ is the C-C bond length

Due to the transverse quantization of the quasimomentum P , its transverse component p_ϕ can take n discrete values,

$$p_\phi = s\Delta p_\phi = \frac{\pi\sqrt{3}s}{an} \quad (s = 1, \dots, n) \quad (C5)$$

Considering the presence of hot electrons source, the motion of quasiparticles in an external axial electric field is described by the Boltzmann kinetic equation in the form as shown below [275 283]

$$\frac{\partial f(p)}{\partial t} + v_z \frac{\partial f(p)}{\partial x} + eE_z(t) \frac{\partial f(p)}{\partial p_z} = -\frac{[f(p) - f_0(p)]}{\tau} + S(p) \quad (C6)$$

where $S(p)$ is the hot electron source function, $f_0(p)$ is equilibrium Fermi distribution function, $f(p, t)$ is the distribution function, v_z is the quasiparticle group velocity along the z-axis of carbon nanotube and τ is the relaxation time.

$$\text{let } b = a/\sqrt{3} \text{ or } a = b\sqrt{3}$$

Hence expanding the distribution functions of interest in Fourier series as

$$f(p, t) = \Delta p_\phi \sum_{s=1}^n \delta(p_\phi - s\Delta p_\phi) \sum_{r \neq 0} f_{rs} e^{ibrp_z} \psi_v(t) \quad (C7)$$

and

$$f_0(p) = \Delta p_\phi \sum_{s=1}^n \delta(p_\phi - s\Delta p_\phi) \sum_{r \neq 0} f_{rs} e^{ibrp_z} \quad (C8)$$

for ac-CNTs

where $\delta(p_\phi - s\Delta p_\phi)$ is the Dirac delta function, f_{rs} is the coefficients of the Fourier series and $\psi_v(t)$ is the factor by which the Fourier transform of the nonequilibrium distribution function differs from its equilibrium distribution counterpart. For simplicity, a hot electron source $S(p)$ of the simplest form given by the expression (C9) is considered

where $f_s(p)$ is the stationary (static and homogeneous) solution of equation (C6), Q is the injection rate of hot electrons, n_0 is the equilibrium particle density, φ and φ' are the dimensionless momenta of electrons and hot electrons respectively which are expressed as

$$\varphi_{zz} = ap_z/\sqrt{3}\hbar \text{ and } \varphi'_{zz} = ap'_z/\sqrt{3}\hbar \text{ for ac-CNTs}$$

The electric current density of the ac-CNT for the case when there is no hot electron source present is now determined. Substituting equations (C7) and (C8) into equation (C6) and setting $S(p) = 0$, (C10) is obtained as

$$\frac{\partial \psi_v(t)}{\partial t} + \left(i e b r E_z + \frac{1}{\tau} \right) \psi_v(t) = \frac{1}{\tau} \quad (C10)$$

Solving the homogeneous differential equation (C10), $\psi_v(t)$ is obtained as

$$\psi_v(t) = C(t) e^{-\int \left(i e b r E_z + \frac{1}{\tau} \right) dt} = C(t) \exp^{-i e r b E_z t} \cdot \exp^{-\frac{t}{\tau}} \quad (C11)$$

Then by differentiating equation (C11), (C12) is obtained as

$$\frac{\partial \psi_v(t)}{\partial t} = \left[\frac{\partial C(t)}{\partial t} - \left(i e r b E_z + \frac{1}{\tau} \right) C(t) \right] \exp^{-i e r b E_z t} \cdot \exp^{-\frac{t}{\tau}} \quad (C12)$$

Substituting equations (C12) and (C11) in equation (C10), $C(t)$ is obtained as in (C13)

$$\begin{aligned} \frac{\partial C(t)}{\partial t} \exp^{-i e r b E_z t} \cdot \exp^{-\frac{t}{\tau}} &= \frac{1}{\tau} \\ \Rightarrow C(t) &= \int \frac{1}{\tau} \exp^{i e r b E_z t} \cdot \exp^{\frac{t}{\tau}} dt \\ C(t) &= \frac{\exp^{i e r b E_z t} \cdot \exp^{\frac{t}{\tau}}}{(1 + i e b r E_z \tau)} \end{aligned} \quad (C13)$$

Recall, $b = a/\sqrt{3}$ or $a = b\sqrt{3}$

Hence substituting equation (C13) into equation (C1), $\psi_v(t)$ is obtained as

© University of Cape Coast <https://ir.ucc.edu.gh/xmlui/> (C14)

$$\psi_v(t) = \frac{1}{(1 + ir \frac{a}{\sqrt{3}} e E_z \tau)} \quad (C14)$$

Therefore

$$\psi_v(t) = \frac{v}{(v + ir \Omega_{ac})} \quad (C15)$$

where $\Omega_{ac} = aeE_z/\sqrt{3}$, $v = 1/\tau$ and $\hbar = 1$

To find the coefficients f_{rs} , both sides of equation(C8) is multiplied by \exp^{-ibmp_z} , and then integrate over the periodic interval $0 \leq p_z \leq 2\pi/a$.

Thus

$$\begin{aligned} & \int_0^{2\pi/a} f_0(\mathbf{p}) e^{-ibmp_z} dp_z \\ &= \Delta p_\phi \sum_{s=1}^n \delta(p_\phi - s\Delta p_\phi) \sum_{r \neq 0} f_{rs} \int_0^{2\pi/a} \exp^{-ib(r-m)p_z} dp_z \\ &= \Delta p_\phi \sum_{r \neq 0} f_{rs} \frac{2\pi}{a} \delta_{r,m} \\ & f_{rs} = \frac{a}{2\pi \Delta p_\phi} \int_0^{2\pi/a} f_0(\mathbf{p}) \exp^{-ibrp_z} dp_z \end{aligned} \quad (C16)$$

But,

$$f_0(\mathbf{p}) = \frac{1}{1 + \exp \{ \epsilon_s(p_z)/k_B T \}}$$

Therefore, from equation (C16),

$$f_{rs} = \frac{a}{2\pi \Delta p_\phi} \int_0^{2\pi/a} \frac{\exp^{-ibrp_z}}{1 + \exp \{ \epsilon_s(p_z)/k_B T \}} dp_z \quad (C17)$$

Surface current density is generally defined by

$$j_z = \frac{2e}{(2\pi\hbar)^2} \iint f(p, t) v_z(p) d^2p,$$

or

©2019 University of Cape Coast <https://ir.ucc.edu.gh/xmlui>

$$j_z = \frac{1}{(2\pi\hbar)^2} \sum_{s=1}^n \int_0^{\frac{2\pi}{a}} f(p_z, s\Delta p_\phi, \psi_v(t)) v_z(p_z, s\Delta p_\phi) dp_z \quad (C18)$$

Where the integration is over the first Brillouin zone, v_z is given by

$$v_z(p_z, s\Delta p_\phi) = \frac{\partial \varepsilon_s(p_z)}{\partial p_z} \quad (C19)$$

Now expanding $\varepsilon_s(p_z)/\gamma_0$ in Fourier series with coefficients ε_{rs} to be determined

$$\begin{aligned} \varepsilon(p_z, s\Delta p_\phi) &= \varepsilon_s(p_z) \\ &= \gamma_0 \sum_{r \neq 0} \varepsilon_{rs} \exp^{ibrp_z} \quad (C20) \end{aligned}$$

Multiplying both sides of equation(C20) by $\exp(-ibmp_z)$ and integrating over $0 \leq p_z \leq 2\pi/a$, we have,

$$\begin{aligned} \int_0^{2\pi/a} \varepsilon_s(p_z) \exp^{-ibmp_z} dp_z &= \gamma_0 \sum_{r \neq 0} \varepsilon_{rs} \int_0^{2\pi/a} \exp^{ib(r-m)p_z} dp_z \\ &= \gamma_0 \sum_{r \neq 0} \varepsilon_{rs} \frac{2\pi}{a} \delta_{r,m} \end{aligned}$$

Therefore $\int_0^{2\pi/a} \varepsilon_s(p_z) \exp^{-ibrp_z} dp_z = \gamma_0 \varepsilon_{rs} \frac{2\pi}{a}$

$$\varepsilon_{rs} = \frac{a}{2\pi\gamma_0} \int_0^{2\pi/a} \varepsilon_s(p_z) \exp^{-ibrp_z} dp_z \quad (C21)$$

where $\varepsilon_s(p_z)$ is given by equation (C3), From equations (C19) and (C20)

$$v_z((p_z, s\Delta p_\phi) = \gamma_0 \sum_{r \neq 0} \frac{\partial(\varepsilon_{rs} \exp^{ibrp_z})}{\partial p_z} = \gamma_0 \sum_{r \neq 0} ibr \varepsilon_{rs} \exp^{iarp_z} \quad (C22)$$

From equation (C7)

$$f(p, t) = \Delta p_\phi \sum_{r \neq 0} f_{rs} \exp^{ibrp_z} \psi_v(t)$$

or

$$f(p_z, s\Delta p_\phi, \psi_v(t)) = \Delta p_\phi \sum_{r \neq 0} f_{rs} \exp^{ibrp_z} \psi_v(t) \quad (C23)$$

Substituting equations (C23) and (C22) into equation (C18), the current density for ac-CNTs j_z^{ac} is obtained as

$$j_z^{ac} = \frac{2e}{(2\pi\hbar)^2} i\gamma_0 b \Delta p_\phi \sum_{s=1}^n \int_0^{\frac{2\pi}{a}} \left(\sum_{r \neq 0} f_{rs} e^{iar p_z} \psi_v(t) \right) \left(\sum_{r' \neq 0} ib r' \epsilon_{rs} e^{ibr' p_z} \right) dp_z \quad (C24)$$

But current density for ac-CNTs j_z^{ac} can also be written as

$$j_z^{ac} = i \sum_{s=1}^n j_{os} \psi_v(t) \quad (C25)$$

So from equation (C24) and (C25), expression for j_{os} is obtained as

$$j_{os} = \frac{2e}{(2\pi\hbar)^2} \gamma_0 b \Delta p_\phi \sum_{s=1}^n \int_0^{\frac{2\pi}{a}} \left(\sum_{r \neq 0} f_{rs} e^{ibr p_z} \right) \left(\sum_{r' \neq 0} ib r' \epsilon_{rs} e^{ibr' p_z} \right) dp_z$$

$$j_{os} = \frac{2e}{(2\pi\hbar)^2} \gamma_0 b \Delta p_\phi \sum_{s=1}^n \int_0^{\frac{2\pi}{a}} \left(\sum_{r \neq 0} f_{rs} e^{ibr p_z} \right) \left(\sum_{r' \neq 0} ib r' \epsilon_{rs} e^{ibr' p_z} \right) dp_z$$

$$j_{os} = \frac{2e}{(2\pi\hbar)^2} \gamma_0 b^2 \Delta p_\phi \sum_{s=1}^n \sum_{r \neq 0} \sum_{r' \neq 0} r' f_{rs} \epsilon_{rs} \int_0^{\frac{2\pi}{a}} e^{ia(r+r')p_z} dp_z \quad (C26)$$

Noting that each of r and r' is summation from $-\infty$ to $+\infty$ and integrating equation (C26) and j_{os} is obtained as

Here, the r and r' summations are taken over $1 \leq r \leq \infty$ and $1 \leq r' \leq \infty$, therefore a factor of 2 is required to account for each of r and r' summation from $-\infty$ to $+\infty$,

$$j_{os} = \frac{2e}{(2\pi\hbar)^2} \gamma_0 b^2 \Delta p_\phi \sum_{s=1}^n 4 \sum_{r=1}^{\infty} r f_{rs} \epsilon_{rs} \frac{2\pi}{a}$$

$$j_{os} = \frac{2e}{(2\pi\hbar)^2} \frac{2\pi}{a} \gamma_0 b^2 \Delta p_\phi 4 \sum_{s=1}^n \sum_{r=1}^{\infty} r f_{rs} \epsilon_{rs} \quad (C27)$$

Simplifying the constant terms in (C27)

$$\frac{2e^2}{(2\pi\hbar)^2} \frac{2\pi}{a} \gamma_0 b^2 \Delta p_\phi 4 = \frac{2e^2}{(2\pi\hbar)^2} \frac{2\pi}{a} \gamma_0 \left(\frac{a}{\sqrt{3}}\right)^2 \Delta p_\phi 4 = \frac{4e^2}{(\sqrt{3})^2 \pi \hbar^2} \gamma_0 a \Delta p_\phi$$

$$= \frac{4e^2}{(\sqrt{3})^2 \pi \hbar^2} \gamma_0 a \frac{\pi \sqrt{3}}{a n} = \frac{4e^2 \gamma_0}{\sqrt{3} \hbar^2 n} \quad (C28)$$

$$j_{os} = \frac{4e^2 \gamma_0}{\sqrt{3} \hbar^2 n} \sum_{r=1}^{\infty} r \sum_{s=1}^n f_{rs} \epsilon_{rs} \quad (C29)$$

Substituting equations (C29) and (C14), into equation (C25), j_z^{ac} is obtained as

$$j_z^{ac} = i \frac{4e^2 \gamma_0}{\sqrt{3} \hbar^2 n} \sum_{r=1}^{\infty} \frac{r v}{(v + ir \Omega_{ac})} \sum_{s=1}^n f_{rs} \epsilon_{rs} \quad (C30)$$

Considering only the real part of equation (C30), j_z^{ac} is given by

$$j_z^{ac} = \frac{4e^2 \gamma_0}{\sqrt{3} \hbar^2 n} \sum_{r=1}^{\infty} \frac{r^2 a e E_z \tau}{1 + (r a e E_z \tau)^2} \sum_{s=1}^n f_{rs} \epsilon_{rs}$$

© University of Cape Coast <https://ir.ucc.edu.gh/xmlui>

$$j_z^{ac} = \frac{4 e^{-\gamma_0}}{\sqrt{3} \hbar^2 n} \sum_{r=1}^n \frac{r^2 \Omega_{ac} \tau}{1 + (r \Omega_{ac} \tau)^2} \sum_{s=1}^n f_{rs} \epsilon_{rs}$$

$$= \frac{4 e^2 \gamma_0}{\sqrt{3} \hbar^2 n} \sum_{r=1}^n \frac{r^2 \Omega_{ac} v}{v^2 + r^2 (\Omega_{ac})^2} \sum_{s=1}^n f_{rs} \epsilon_{rs} \quad (C31)$$

where, $v = 1/\tau$, $\Omega_{ac} = aeE_z/\sqrt{3}$ and $\hbar = 1$



CURRENT DENSITY FOR ARMCHAIR CARBON NANOTUBE IN THE PRESENCE OF HOT ELECTRON SOURCE

Considering the presence of hot electrons source, the motion of quasiparticles in an external axial electric field is described by the Boltzmann kinetic equation in the form as shown below [275 283]

$$\frac{\partial f(p)}{\partial t} + v_z \frac{\partial f(p)}{\partial x} + eE_z(t) \frac{\partial f(p)}{\partial p_z} = -\frac{[f(p) - f_0(p)]}{\tau} + S(p) \quad (D1)$$

where $S(p)$ is the hot electron source function, $f_0(p)$ is equilibrium Fermi distribution function, $f(p, t)$ is the distribution function, v_z is the quasiparticle group velocity along the z-axis of carbon nanotube and τ is the relaxation time. The stationary homogeneous distribution function $f_s(\varphi)$ in the presence of hot electron source is given by

$$f_s(\varphi) = f_E(\varphi) + f'(\varphi) \quad (D2)$$

where $f_E(p) = f(p) = \psi_v(t) = rv/(v + ir\Omega_{ac}) \quad (D3)$

Substituting equation (D2) into equation (D1), (D4) is obtained as

$$\frac{\partial f'(\varphi)}{\partial \varphi} + \left(\frac{v}{\Omega_{ac}} + \frac{Q}{n_o \Omega_{ac}} \right) f'(\varphi) = \frac{aQ}{\Omega_{ac}} \delta(\varphi - \varphi') - \frac{aQ}{\Omega_{ac} n_o} f_E(\varphi) \quad (D4)$$

Solving the homogeneous differential equation (D4), $f'(\varphi)$ is obtained as

$$f'(\varphi) = C(\varphi) e^{-\int \left[\frac{v}{\Omega_{ac}} + \frac{Q}{n_o \Omega_{ac}} \right] d\varphi} = C(\varphi) e^{-\left[\frac{v}{\Omega_{ac}} + \frac{Q}{n_o \Omega_{ac}} \right] \varphi} \quad (D5)$$

Then by differentiating equation (D5), (D6) is obtained as

$$\frac{\partial f'(\varphi)}{\partial \varphi} = \left[\frac{\partial C(\varphi)}{\partial \varphi} - \left(\frac{v}{\Omega_{ac}} + \frac{Q}{n_o \Omega_{ac}} \right) C(\varphi) \right] e^{-\left[\frac{v}{\Omega_{ac}} + \frac{Q}{n_o \Omega_{ac}} \right] \varphi} \quad (D6)$$

Substituting for $f'(\varphi)$ and $\partial f'(\varphi)/\partial \varphi$ in equation (D4), $C(\varphi)$ is obtained as in (D7).

$$\Rightarrow C(\varphi) = \int \left\{ \frac{aQ}{\Omega_{ac}} \delta(\varphi - \varphi') - \frac{aQ}{\Omega_{ac} n_o} f_E(\varphi) \right\} e^{\left[\frac{v}{\Omega_{ac}} + \frac{q}{n_o \Omega_{ac}} \right] \varphi} \partial \varphi \quad (D7)$$

Introducing Dirac-delta transformation

$$\delta(\varphi - \varphi') = \frac{1}{2\pi} \sum_{\tau} e^{i\tau(\varphi - \varphi')} \quad (D8)$$

Substituting equations (D3) and (D8) into equation (D7) to obtain equation (D9)

$$\begin{aligned} C(\varphi) &= \frac{aQ}{2\pi\Omega_{ac}} \cdot \frac{n_o}{n_o} \int \left\{ \sum_{\tau} e^{i\tau(\varphi - \varphi')} - \frac{q}{\Omega_{ac} n_o} f_E(\varphi) \right\} e^{\left[\frac{v}{\Omega_{ac}} + \frac{q}{n_o \Omega_{ac}} \right] \varphi} \partial \varphi \\ &= \frac{aQ}{2\pi\Omega_{ac}} \cdot \frac{n_o}{n_o} \int \left\{ \sum_{\tau} e^{-i\tau\varphi'} - \frac{v}{(v + i\tau\Omega_{ac})} \right\} e^{\left[\frac{v}{\Omega_{ac}} + \frac{q}{n_o \Omega_{ac}} \right] \varphi} \partial \varphi \\ &= \frac{aQ}{2\pi\Omega_{ac}} \cdot \frac{n_o}{n_o} \sum_{\tau} \frac{\Omega_{ac}}{(i\tau\Omega_{ac} + v + \frac{q}{n_o})} \left\{ e^{-i\tau\varphi'} \right. \\ &\quad \left. - \frac{v}{(v + i\tau\Omega_{ac})} \right\} e^{\left[\frac{v}{\Omega_{ac}} + \frac{q}{n_o \Omega_{ac}} \right] \varphi} \quad (D9) \end{aligned}$$

Substituting equation (D9) into equation (D5), $f'(\varphi)$ is obtained

$$f'(\varphi) = \eta_{ac} \frac{n_o}{2\pi} \sum_{\tau} \frac{\Omega_{ac}}{(i\tau\Omega_{ac} + v + \eta_{ac})} \left\{ e^{-i\tau\varphi'} - \frac{v}{(v + i\tau\Omega_{ac})} \right\} \quad (D10)$$

Where the nonequilibrium parameter $\eta_{ac} = Q/\Omega_{ac} n_o$ (D11)

Current density for ac-CNTs in the presence of hot electron source j_z^{ac} is given by

$$j_z^{ac} = i \sum_{s=1}^n j_{os} f_s(\varphi) \quad (D12)$$

Recall

© University of Cape Coast <https://ir.ucc.edu.gh/xmlui> (D13)

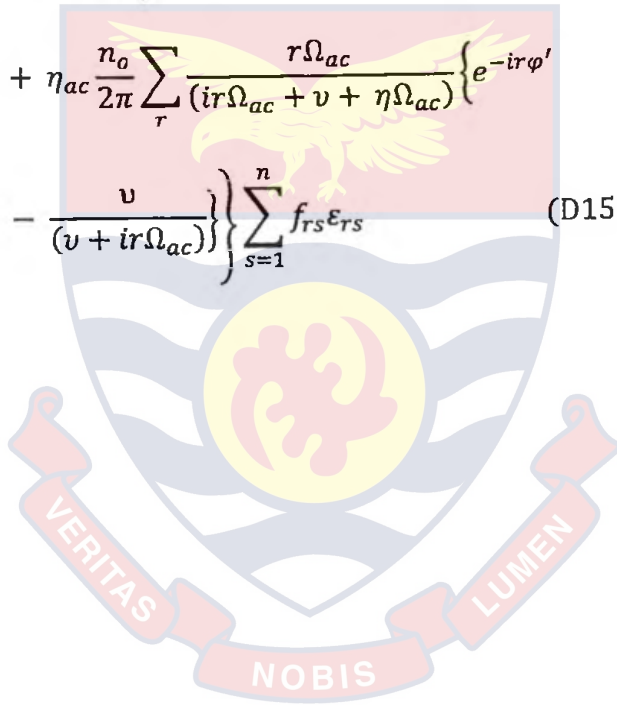
$$j_{os} = \frac{4\sqrt{3} e^2 \gamma_0}{\hbar^2 n} \sum_{r=1}^{\infty} r \sum_{s=1}^n f_{rs} \epsilon_{rs}$$

Substituting equation (D2) into equation (D12)

$$j_z = i \sum_{s=1}^n j_{os} [f_E(\varphi) + f'(\varphi)] \quad (D14)$$

Substituting equations (D3), (D10) and (D13) into equation (D14), j_{zHE}^{ac} is obtained as

$$j_{zHE}^{ac} = i \frac{4\sqrt{3} e^2 \gamma_0}{\hbar^2 n} \sum_{r=1}^{\infty} \left\{ \frac{rv}{(v + ir\Omega_{ac})} + \eta_{ac} \frac{n_0}{2\pi} \sum_r \frac{r\Omega_{ac}}{(ir\Omega_{ac} + v + \eta\Omega_{ac})} \left\{ e^{-ir\varphi'} - \frac{v}{(v + ir\Omega_{ac})} \right\} \sum_{s=1}^n f_{rs} \epsilon_{rs} \right\} \quad (D15)$$



HIGH FREQUENCY CONDUCTIVITY OF ZIGZAG CARBON NANOTUBES IN THE PRESENCE AND ABSENCE OF HOT ELECTRON SOURCE

Boltzmann kinetic equation is given as shown below [275 283]

$$\frac{\partial f(p)}{\partial t} + v_z \frac{\partial f(p)}{\partial x} + eE(t) \frac{\partial f(p)}{\partial p_z} = -\frac{[f(p) - f_0(p)]}{\tau} + S(p) \quad (E1)$$

Finding the high frequency conductivity in the nonequilibrium state for zz-CNT by considering perturbations with frequency ω and wave-vector κ of the form

$$E(t) = E_z + E_{\omega,\kappa} e^{-i\omega t + i\kappa z} \quad (E2)$$

$$f = f_s(\varphi) + f_{\omega,\kappa} e^{-i\omega t + i\kappa z} \quad (E3)$$

Substituting equations(E2) and (E3) into equation (E1), the expression below is obtained

$$\begin{aligned} \frac{\partial f_s(\varphi)}{\partial t} - i\omega f_{\omega,\kappa} e^{-i\omega t + i\kappa z} + v_z \frac{\partial f_s(\varphi)}{\partial x} + i\kappa f_{\omega,\kappa} e^{-i\omega t + i\kappa z} + eE_z \frac{\partial f_s(\varphi)}{\partial \varphi} \\ + eE_z \frac{\partial f_{\omega,\kappa} e^{-i\omega t + i\kappa z}}{\partial \varphi} + E_{\omega,\kappa} e^{-i\omega t + i\kappa z} \frac{\partial f_s(\varphi)}{\partial \varphi} \\ = -v_z [f_s(\varphi) + f_{\omega,\kappa} e^{-i\omega t + i\kappa z} - f_0(\varphi)] \end{aligned}$$

Rearranging yield

$$\begin{aligned} eE_z \frac{\partial f_{\omega,\kappa} e^{-i\omega t + i\kappa z}}{\partial \varphi} + i\kappa f_{\omega,\kappa} e^{-i\omega t + i\kappa z} - i\omega f_{\omega,\kappa} e^{-i\omega t + i\kappa z} + v f_{\omega,\kappa} e^{-i\omega t + i\kappa z} = \\ E_{\omega,\kappa} e^{-i\omega t + i\kappa z} \frac{\partial f_s(\varphi)}{\partial \varphi} + f_0(\varphi) \end{aligned}$$

$$\text{Therefore, } \frac{\partial f_{\omega,\kappa}}{\partial \varphi} + i[\alpha + (\kappa v_z / \Omega_{zz})] f_{\omega,\kappa} = -\frac{E_{\omega,\kappa}}{E_z} \frac{\partial f_s(\varphi)}{\partial \varphi} \quad (E4)$$

where $\alpha = -(\omega + i v_z) / \Omega_{zz}$

The velocity of the zigzag carbon nanotube is expressed as:
 © University of Cape Coast <https://ir.ucc.edu.gh/xmlui>

$$v_z(p_z, s\Delta p_\phi) = \frac{\partial \varepsilon_s(p_z)}{\partial p_z}$$

Now expanding $\varepsilon_s(p_z)/\gamma_0$ in Fourier series

$$\varepsilon(p_z, s\Delta p_\phi) = \varepsilon_s(p_z) = \gamma_0 \sum_{r \neq 0} \varepsilon_{rs} e^{ir\varphi}$$

where

$$\varphi = \frac{ap_z}{\hbar}$$

$$v_z(p_z, s\Delta p_\phi) = \gamma_0 \sum_{r \neq 0} \frac{\partial(\varepsilon_{rs} e^{ir\varphi})}{\partial p_z} = \frac{\gamma_0 a}{\hbar} \sum_{r \neq 0} ir \varepsilon_{rs} e^{ir\varphi}$$

$$v_z = \frac{\gamma_0 a}{\hbar} \sum_{r \neq 0} ir \varepsilon_{rs} [\cos(r\varphi) + i\sin(r\varphi)] \quad (E5)$$

Substituting equation (E5) into equation (E4)

$$\frac{\partial f_{\omega, \kappa}}{\partial \varphi} + i \left\{ \alpha + \frac{\kappa \gamma_0 a}{\Omega_{zz} \hbar} \sum_{r \neq 0} ir \varepsilon_{rs} [\cos(r\varphi) + i\sin(r\varphi)] \right\} f_{\omega, \kappa}$$

$$= -\frac{E_{\omega, \kappa}}{E_z} \frac{\partial f_s(\varphi)}{\partial \varphi}$$

For simplicity, considering the first term by putting $r=1$ and $s=1$

$$\frac{\partial f_{\omega, \kappa}}{\partial \varphi} + i \left\{ \alpha + i \frac{\kappa \gamma_0 a}{\Omega_{zz} \hbar} [\cos(\varphi) + i\sin(\varphi)] \right\} f_{\omega, \kappa} = -\frac{E_{\omega, \kappa}}{E_z} \frac{\partial f_s(\varphi)}{\partial \varphi} \quad (E6)$$

Solving the homogeneous differential equation (E6), $f_{\omega, \kappa}$ is obtained as

$$f_{\omega, \kappa} = C(\varphi) e^{-i \int [\alpha + i\beta [\cos(\varphi) + i\kappa \sin(\varphi)]] d\varphi}$$

$$= C(\varphi) e^{-i[\alpha + i\beta [\sin(\varphi) - i\kappa \cos(\varphi)]]} \quad (E7)$$

Where

$$\beta = \frac{\kappa \gamma_0 a}{\Omega_{zz} \hbar}$$

Then by differentiating equation (E7), (E8) is obtained

$$\times e^{i\{\alpha+\beta[\sin(\varphi)-i\kappa\cos(\varphi)]\}\varphi} \quad (E8)$$

Substituting equations (E7) and (E8) in equation (E4), $C(\varphi)$ is obtained as shown below

$$\frac{\partial C(\varphi)}{\partial \varphi} e^{-i\{\alpha+\beta[\sin(\varphi)-i\kappa\cos(\varphi)]\}\varphi} = -\frac{E_{\omega,\kappa}}{E_z} \frac{\partial f_s(\varphi)}{\partial \varphi}$$

$$\Rightarrow C(\varphi) = \int -\frac{E_{\omega,\kappa}}{E_z} \frac{\partial f_s(\varphi)}{\partial \varphi} e^{i\{\alpha+\beta[\sin(\varphi)-i\kappa\cos(\varphi)]\}\varphi} d\varphi \quad (E9)$$

Introducing the Jacobi-Anger expansion which is an expansion of exponentials of trigonometric functions in the basis of their harmonics:

$$(i) e^{-i\kappa\cos\theta} = \sum_{k=-\infty}^{\infty} i^{-k} k j_k(x) e^{-ik\theta}$$

$$(ii) e^{i\kappa\cos\theta} = \sum_{k=-\infty}^{\infty} i^k k j_k(x) e^{ik\theta}$$

$$(iii) e^{x\cos\theta} = \sum_{m=-\infty}^{\infty} I_m(x) e^{im\theta}$$

$$(iv) e^{x\cos\theta+y\sin\theta} = \sum_{m=-\infty}^{\infty} I_m(\sqrt{x^2+y^2}) e^{im\theta}$$

$$(v) e^{x\cos\varphi+y\sin\theta} = \sum_{m=-\infty}^{\infty} I_m(\sqrt{x^2+y^2}) e^{im(\theta+\varphi)}$$

$$(vi) e^{x\sin\theta} = \sum_{m=-\infty}^{\infty} I_m(x) e^{im\theta} \quad (E10)$$

$$C(\varphi) = \int \frac{E_{\omega,\kappa}}{E_z} \frac{\partial f_s(\varphi)}{\partial \varphi} \sum_{m=-\infty}^{\infty} i^m m j_m(\beta) e^{im\theta} \sum_{m=-\infty}^{\infty} I_m(\beta) e^{im\theta} e^{-i\alpha\varphi} d\varphi$$

where $\theta = a p_z$

$$C(\varphi) = \int_{E_z} \frac{E_{\omega,\kappa} \partial(f_E(\varphi) + f'(\varphi))}{\partial\varphi} \sum_{m=-\infty}^{\infty} i^m m j_m(\beta) I_m(\beta) e^{i[-\alpha+m]\varphi} d\varphi$$

$$C(\varphi) = \int \frac{E_{\omega,\kappa} \partial(f_E(\varphi) + f'(\varphi))}{\partial\varphi} \sum_{m=-\infty}^{\infty} i^m m j_m(\beta) I_m(\beta) e^{i[-\alpha+m]\varphi} d\varphi$$

(E11)

Substituting (E11) into (E7) yields

$$f_{\omega,\kappa} = \sum_{m=-\infty}^{\infty} \frac{i^{m-1} m j_m(\beta) I_m(\beta) \Omega_{zz}}{\omega + i\nu - m\Omega_{zz}} \int e^{[\beta[\sin\theta - i\cos\theta] - im]\varphi} \frac{E_{\omega,\kappa} \partial(f_E(\varphi) + f'(\varphi))}{\partial\varphi} d\varphi \quad (E12)$$

Using the Jacobi-Anger expansion (E10)

$$f_{\omega,\kappa} = \sum_{m=-\infty}^{\infty} \sum_{k=-\infty}^{\infty} \frac{i^m i^{-k} k m j_m(\beta) j_k(\beta) I_k(\beta) I_m(\beta) \Omega_{zz}}{\omega + i\nu - m\Omega_{zz}} \int \frac{E_{\omega,\kappa} \partial(f_E(\varphi) + f'(\varphi))}{\partial\varphi} d\varphi \quad (E13)$$

Putting expression (B3) and (B10) into the integrand in equation (E13), expression below is obtained

$$\int \frac{E_{\omega,\kappa} \partial(f_E(\varphi) + f'(\varphi))}{\partial\varphi} d\varphi = \frac{E_{\omega,\kappa}}{E_z} \left\{ \eta_{zz} \frac{n_o}{2\pi} \sum_r \frac{\Omega_{zz} e^{ir\varphi}}{(ir\Omega_{zz} + \nu + \eta\Omega_{zz})} \left(e^{-ir\varphi'} - \frac{\nu}{(\nu + ir\Omega_{zz})} \right) + \frac{\nu}{(\nu + ir\Omega_{zz})} \right\}$$

Introducing indices $m = k + l$ into equation (E13)

$$\Rightarrow f_{\omega,\kappa} = \sum_{m, l=-\infty}^{\infty} \frac{i^l m l j_m(\beta) j_{m-l}(\beta) I_{m-l}(\beta) \Omega_{zz}}{\omega + i\nu - m\Omega_{zz}} \times$$

© University of Cape Coast <https://ir.ucc.edu.gh/xmlui>

$$\left\{ \eta_{zz} \frac{n_0}{2\pi} \sum_r \frac{e^{ir\varphi}}{(ir\Omega_{zz} + v + \eta\Omega_{zz})} \left(e^{-ir\varphi'} - \frac{v}{v + ir\Omega_{zz}} \right) + \frac{v}{(v + ir\Omega_{zz})} \right\} \quad (E14)$$

But current density for zz-CNTs in the presence of hot electrons j_{zHE}^{zz} can also be written as

$$j_{zHE}^{zz} = i \sum_{s=1}^n j_{os}(f_{\omega,\kappa}) \quad (E15)$$

For zz-CNTs, recall from equation (A27) that

$$j_{os} = \frac{4\sqrt{3} e^2 \gamma_0}{n\hbar^2} \sum_{l=1}^n r \sum_{s=1}^n f_{rs} \epsilon_{rs} \quad (E16)$$

Substituting equations (E14) and (E16) into equation (E15), j_{zHE}^{zz} is obtained as

$$j_{zHE}^{zz} = i \frac{4\sqrt{3} e^2 \gamma_0}{n\hbar^2} \sum_{m, l=-\infty}^{\infty} \frac{i^l m l j_m(\beta) j_{m-l}(\beta) I_{m-l}(\beta) \Omega_{zz}}{\omega + iv - m\Omega_{zz}} \times \sum_r \left\{ \eta_{zz} \frac{n_0}{2\pi} \sum_r \frac{r\Omega_{zz} e^{ir\varphi}}{(ir\Omega_{zz} + v + \eta\Omega_{zz})} \left(e^{-ir\varphi'} - \frac{v}{(v + ir\Omega_{zz})} \right) + \frac{rv}{(v + ir\Omega_{zz})} \right\} \sum_{s=1}^n f_{rs} \epsilon_{rs} \quad (E17)$$

In the absence of hot electrons, the nonequilibrium parameter for zz-CNT $\eta_{zz} = 0$, hence the current density for zz-CNTs without hot electron source j_z^{zz} could be obtained from equation (E17) by setting $\eta_{zz} = 0$. Therefore, the current density of zz-CNTs in the absence of hot electrons j_z^{zz} is given by

$$= i \frac{4\sqrt{3}e^2\gamma_0}{n\hbar^2} \sum_{r=1}^{\infty} \frac{rv}{(v + ir\Omega_{zz})} \sum_{m, l=-\infty}^{\infty} \frac{i^l m l j_m(\beta) j_{m-l}(\beta) I_{m-l}(\beta) \Omega_{zz}}{\omega + iv - m\Omega_{zz}} \sum_{s=1}^n f_{rs} \varepsilon_{rs}$$

(E18)



APPENDIX F

HIGH FREQUENCY CONDUCTIVITY OF ARMCHAIR CARBON NANOTUBES IN THE PRESENCE AND ABSENCE OF HOT ELECTRONS

Boltzmann kinetic equation is given as shown below [275, 283]

$$\frac{\partial f(p)}{\partial t} + v_z \frac{\partial f(p)}{\partial x} + eE(t) \frac{\partial f(p)}{\partial p_z} = -\frac{[f(p) - f_0(p)]}{\tau} + S(p) \quad (F1)$$

Finding the high frequency conductivity in the nonequilibrium state for ac-CNT by considering perturbations with frequency ω and wave-vector κ of the form

$$E(t) = E_z + E_{\omega,\kappa} e^{-i\omega t + i\kappa z} \quad (F2)$$

$$f = f_s(\varphi) + f_{\omega,\kappa} e^{-i\omega t + i\kappa z} \quad (F3)$$

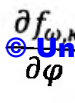
Substituting equations(F2) and (F3) into equation (F1), expression below is obtained

$$\begin{aligned} \frac{\partial f_s(\varphi)}{\partial t} - i\omega f_{\omega,\kappa} e^{-i\omega t + i\kappa z} + v_z \frac{\partial f_s(\varphi)}{\partial x} + i\kappa f_{\omega,\kappa} e^{-i\omega t + i\kappa z} + eE_z \frac{\partial f_s(\varphi)}{\partial \varphi} \\ + eE_z \frac{\partial f_{\omega,\kappa} e^{-i\omega t + i\kappa z}}{\partial \varphi} + E_{\omega,\kappa} e^{-i\omega t + i\kappa z} \frac{\partial f_s(\varphi)}{\partial \varphi} \\ = -v_z [f_s(\varphi) + f_{\omega,\kappa} e^{-i\omega t + i\kappa z} - f_0(\varphi)] \end{aligned}$$

Rearranging yield

$$\begin{aligned} eE_z \frac{\partial f_{\omega,\kappa} e^{-i\omega t + i\kappa z}}{\partial \varphi} + i\kappa f_{\omega,\kappa} e^{-i\omega t + i\kappa z} - i\omega f_{\omega,\kappa} e^{-i\omega t + i\kappa z} + v f_{\omega,\kappa} e^{-i\omega t + i\kappa z} = \\ E_{\omega,\kappa} e^{-i\omega t + i\kappa z} \frac{\partial f_s(\varphi)}{\partial \varphi} + f_0(\varphi) \end{aligned}$$

Therefore


 University of Cape Coast <https://ic.ac.edu.gh/xmlui> (F4)

$$\frac{\partial f_{\omega, \kappa}}{\partial \varphi} + i \left\{ \alpha + \frac{\kappa \gamma_0 a}{\Omega_{ac} \hbar} \sum_{r \neq 0} ir \varepsilon_{rs} [\cos(r\varphi) + i \sin(r\varphi)] \right\} f_{\omega, \kappa} = - \frac{E_{\omega, \kappa}}{E_z} \frac{\partial f_s(\varphi)}{\partial \varphi}$$

where $\alpha = -(\omega + i\nu_z)/\Omega_{ac}$

The velocity of the zigzag carbon nanotube is expressed as

$$v_z(p_z, s\Delta p_\phi) = \frac{\partial \varepsilon_s(p_z)}{\partial p_z}$$

Now we expanding $\varepsilon_s(p_z)/\gamma_0$ in Fourier series

$$\varepsilon(p_z, s\Delta p_\phi) = \varepsilon_s(p_z) = \gamma_0 \sum_{r \neq 0} \varepsilon_{rs} e^{ir\varphi}$$

where $\varphi = ap_z/\hbar\sqrt{3}$

$$v_z(p_z, s\Delta p_\phi) = \gamma_0 \sum_{r \neq 0} \frac{\partial(\varepsilon_{rs} e^{ir\varphi})}{\partial p_z} = \frac{\gamma_0 a}{\hbar} \sum_{r \neq 0} ir \varepsilon_{rs} e^{ir\varphi}$$

$$v_z = \frac{\gamma_0 a}{\Omega_{ac} \hbar} \sum_{r \neq 0} ir \varepsilon_{rs} [\cos(r\varphi) + i \sin(r\varphi)] \quad (F5)$$

Substituting equation (F5) into equation (F4)

$$\frac{\partial f_{\omega, \kappa}}{\partial \varphi} + i \left\{ \alpha + \frac{\kappa \gamma_0 a}{\Omega_{ac} \hbar} \sum_{r \neq 0} ir \varepsilon_{rs} [\cos(r\varphi) + i \sin(r\varphi)] \right\} f_{\omega, \kappa} = - \frac{E_{\omega, \kappa}}{E_z} \frac{\partial f_s(\varphi)}{\partial \varphi}$$

For simplicity, considering the first term by putting $r=1$ and $s=1$

$$\frac{\partial f_{\omega, \kappa}}{\partial \varphi} + i \left\{ \alpha + i \frac{\kappa \gamma_0 a}{\Omega_{ac} \hbar} [\cos(\varphi) + i \sin(\varphi)] \right\} f_{\omega, \kappa} = - \frac{E_{\omega, \kappa}}{E_z} \frac{\partial f_s(\varphi)}{\partial \varphi} \quad (F6)$$

Solving the homogeneous differential equation (F6), $f_{\omega, \kappa}$ is obtained as

$$f_{\omega, \kappa} = C(\varphi) e^{-i \int \{ \alpha + i\beta [\cos(r\varphi) + i \sin(r\varphi)] \} d\varphi}$$

$$= C(\varphi) e^{-i(\alpha + i\beta[\sin(r\varphi) - i \cos(r\varphi)])} \quad (F7)$$

where

$$\beta = \frac{\kappa \gamma_0 a}{\Omega_{ac} \hbar}$$

Then by differentiating equation (F7) and (F8) it is obtained as shown below

$$\frac{\partial f_{\omega,\kappa}}{\partial \varphi} = \left[\frac{\partial C(\varphi)}{\partial \varphi} - \iota\{\alpha + \iota\beta[\sin(r\varphi) - \iota\kappa\cos(r\varphi)]\}C(\varphi) \right] \times e^{i\{\alpha + \beta[\sin(r\varphi) - \iota\kappa\cos(r\varphi)]\}\varphi} \quad (F8)$$

Substituting equations (F7) and (F8) in equation (F4), $C(\varphi)$ is obtained as shown below

$$\frac{\partial C(\varphi)}{\partial \varphi} e^{-i\{\alpha + \beta[\sin(r\varphi) - \iota\kappa\cos(r\varphi)]\}\varphi} = -\frac{E_{\omega,\kappa}}{E_z} \frac{\partial f_s(\varphi)}{\partial \varphi}$$

$$\Rightarrow C(\varphi) = \int -\frac{E_{\omega,\kappa}}{E_z} \frac{\partial f_s(\varphi)}{\partial \varphi} e^{i\{\alpha + \beta[\sin(r\varphi) - \iota\kappa\cos(r\varphi)]\}\varphi} d\varphi \quad (F9)$$

Introducing the Jacobi-Anger expansion which is an expansion of exponentials of trigonometric functions in the basis of their harmonics:

$$(i) e^{-ix\cos\theta} = \sum_{k=-\infty}^{\infty} i^{-k} k j_k(x) e^{-ik\theta}$$

$$(ii) e^{ix\cos\theta} = \sum_{k=-\infty}^{\infty} i^k k j_k(x) e^{ik\theta}$$

$$(iii) e^{x\cos\theta} = \sum_{m=-\infty}^{\infty} I_m(x) e^{im\theta}$$

$$(iv) e^{x\cos\theta + y\sin\theta} = \sum_{m=-\infty}^{\infty} I_m(\sqrt{x^2 + y^2}) e^{im\theta}$$

$$(v) e^{x\cos\varphi + y\sin\theta} = \sum_{m=-\infty}^{\infty} I_m(\sqrt{x^2 + y^2}) e^{im(\theta + \varphi)}$$

$$(vi) e^{x\sin\theta} = \sum_{m=-\infty}^{\infty} I_m(x) e^{im\theta} \quad (F10)$$

$$C(\varphi) = \int \frac{E_{\omega,\kappa}}{E_s} \frac{\partial f_s(\varphi)}{\partial \varphi} \sum_{m=-\infty}^{\infty} i^m m j_m(\beta) e^{im\theta} \sum_{m=-\infty}^{\infty} I_m(\beta) e^{im\theta} e^{-i\alpha\varphi} d\varphi$$

where $\theta = ar\rho_z$

$$C(\varphi) = \int \frac{E_{\omega,\kappa}}{E_z} \frac{\partial (f_E(\varphi) + f'(\varphi))}{\partial \varphi} \sum_{m=-\infty}^{\infty} i^m m j_m(\beta) I_m(\beta) e^{i[-\alpha+m]\varphi} d\varphi$$

$$C(\varphi) = \int \frac{E_{\omega,\kappa}}{E_z} \frac{\partial (f_E(\varphi) + f'(\varphi))}{\partial \varphi} \sum_{m=-\infty}^{\infty} i^m m j_m(\beta) I_m(\beta) e^{i[-\alpha+m]\varphi} d\varphi$$

Substituting(F11) into (F7) yields

$$f_{\omega,\kappa} = \sum_{m=-\infty}^{\infty} \frac{i^{m-1} m j_m(\beta) I_m(\beta) \Omega_{ac}}{\omega + i\nu - m\Omega_{ac}} \int e^{[\beta[\sin\theta - i\cos\theta] - im]} \frac{E_{\omega,\kappa}}{E_z} \frac{\partial (f_E(\varphi) + f'(\varphi))}{\partial \varphi} d\varphi \quad (F12)$$

Using the Jacobi-Anger expansion (E10) in (F12)

$$f_{\omega,\kappa} = \sum_{m=-\infty}^{\infty} \sum_{k=-\infty}^{\infty} \frac{i^m i^{-k} k m j_m(\beta) j_k(\beta) I_k(\beta) I_m(\beta) \Omega_{ac}}{\omega + i\nu - m\Omega_{ac}} \int \frac{E_{\omega,\kappa}}{E_s} \frac{\partial (f_E(\varphi) + f'(\varphi))}{\partial \varphi} d\varphi \quad (F13)$$

Substituting expressions (D3) and (D10) into the integrand in equation (E13), expression below is obtained

$$\begin{aligned} & \int \frac{E_{\omega,\kappa}}{E_z} \frac{\partial (f_E(\varphi) + f'(\varphi))}{\partial \varphi} d\varphi \\ &= \eta_{ac} \frac{n_o}{2\pi} \sum_r \frac{\Omega_{ac} e^{ir\varphi}}{(ir\Omega_{ac} + \nu + \eta\Omega_{ac})} \left\{ e^{-ir\varphi'} - \frac{\nu}{(\nu + ir\Omega_{ac})} \right\} \\ &+ \frac{\nu}{(\nu + ir\Omega_{ac})} \end{aligned}$$

Introducing indices $m = k + l$ into equation (F13)

© University of Cape Coast <https://ir.ucc.edu.gh/xmlui>

$$\Rightarrow f_{\omega,\kappa} = \sum_{m, l=-\infty}^{\infty} \frac{i^l m l j_m(\beta) j_{m-l}(\beta) I_{m-l}(\beta) \Omega_{ac}}{\omega + i\nu - m\Omega_{ac}} \times$$

$$\left\{ \eta_{ac} \frac{n_0}{2\pi} \cdot \sum_r \frac{\Omega_{ac} e^{ir\varphi}}{(ir\Omega_{ac} + \nu + \eta\Omega_{ac})} \left(e^{-ir\varphi'} - \frac{\nu}{\nu + ir\Omega_{ac}} \right) + \frac{\nu}{(\nu + ir\Omega_{ac})} \right\} \quad (F14)$$

But current density for ac-CNT in the presence of hot electrons j_{zHE}^{ac} can also be written as

$$j_{zHE}^{ac} = i \sum_{s=1}^n j_{os}(f_{\omega,\kappa}) \quad (F15)$$

For ac-CNTs, recall from equation (C27) that

$$j_{os} = \frac{4 e^2 \gamma_0}{\sqrt{3} n \hbar^2} \sum_{l=1}^n r \sum_{s=1}^n f_{rs} \varepsilon_{rs} \quad (F16)$$

Substituting equations (F14) and (F16) into equation (F15), j_{zHE}^{ac} is obtained as

$$j_{zHE}^{ac} = i \frac{4 e^2 \gamma_0}{\sqrt{3} n \hbar^2} \sum_{m, l=-\infty}^{\infty} \frac{i^l m l j_m(\beta) j_{m-l}(\beta) I_{m-l}(\beta) \Omega_{ac}}{\omega + i\nu - m\Omega_{ac}} \times$$

$$\sum_r \left\{ \eta_{ac} \frac{n_0}{2\pi} \cdot \sum_l \frac{r \Omega_{ac} e^{ir\varphi}}{(ir\Omega_{ac} + \nu + \eta\Omega_{ac})} \left(e^{-ir\varphi'} - \frac{\nu}{\nu + ir\Omega_{ac}} \right) + \frac{r\nu}{(\nu + ir\Omega_{ac})} \right\} \sum_{s=1}^n f_{rs} \varepsilon_{rs} \quad (F17)$$

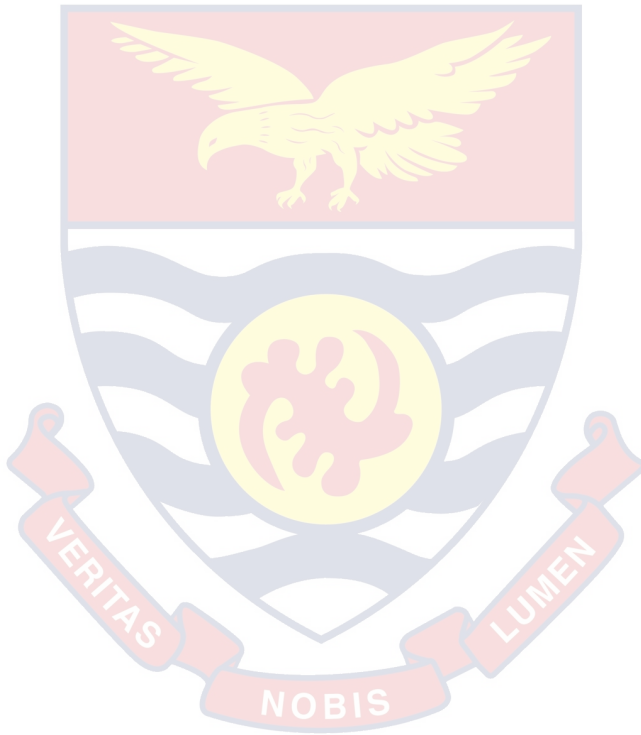
In the absence of hot electrons, the nonequilibrium parameter for ac-CNTs $\eta_{ac} = 0$, hence the current density for ac-CNTs without hot electron source j_z^{ac} could be obtained from equation (E17) by setting $\eta_{ac} = 0$.

© University of Cape Coast <https://ir.ucc.edu.gh/xmlui> j_z^{ac} is

Therefore, the current density of ac-CNTs in the absence of hot electrons j_z^{ac} is given by

$$j_z^{ac} = i \frac{4 e^2 \gamma_0}{\sqrt{3} n \hbar^2} \sum_m \sum_{l=-\infty}^{\infty} \frac{i^l m l j_m(\beta) j_{m-l}(\beta) I_{m-l}(\beta) \Omega_{ac}}{\omega + i\nu - m \Omega_{cc}} \sum_{r=1}^{\infty} \frac{\nu r}{(\nu + i r \Omega_{ac})} \sum_{s=1}^n f_{rs} \mathcal{E}_{rs}$$

(F18)



**PUBLICATIONS FROM THIS DOCTORAL THESIS ON THE
EFFECT OF HOT ELECTRONS ON THE CONDUCTIVITY OF
CARBON NANOTUBES**

1. **Amekpewu M.**, Abukari S.S., Adu K.W., Mensah S.Y., and Mensah N.G. "Effect of hot electrons on the electrical conductivity of carbon nanotubes under the influence of applied dc field." *The European physical journal B:Condensed Matter and Complex Systems* 88, no. 2 (2015): 1-6.
2. **Amekpewu M.**, Mensah S. Y., Musah R., Mensah N. G., Abukari S. S. and Dompseh K. A.. "High frequency conductivity of hot electrons in carbon nanotubes." *Physica B: Condensed Matter* , no. 488 (2016): 83–87
3. **Amekpewu M.**, Mensah S. Y., Musah R., Mensah N. G., Abukari S. S. and Dompseh, K. A. "Hot electrons injection in carbon nanotubes under the influence of quasi-static ac-field".*Physica E: Low-dimensional Systems and Nanostructures* , no. 81 (2016):145–149